Autonomous Monitoring System

Autonomní monitorovací systém

Doctoral degree program: Engineering Informatics
Supervisor: doc. Mgr. Milan Adámek, Ph.D.

Doctoral thesis
2013

Tomas Bata University in Zlín
Faculty of Applied Informatics

ABSTRACT

In this dissertation thesis, selected parts of the design issues on construction and controlling of a small airship are discussed.

The main topic is focused on a construction of a small Autonomous monitoring system that consists of a small airship filled with helium, its propelling and controlling systems and several monitoring devices like a camera etc. This system is intended for an indoor operation, which increases the demands on its precise control.

Whereas the topic is quite complex, special considerations were given to the following topics: hardware design, effective power supply, propelling and basic dynamical model of the system.

Keywords: airship, autonomous operation, indoor operation, obstacles detection, RFID, dynamic model

ABSTRAKT

V rámci této dizertační práce jsou rozebírány některé z problémů týkajících se návrhu konstrukce a řízení malé vzducholodi.

Hlavním tématem práce je konstrukce malého Autonomního monitorovacího systému, který sestává z malé heliem plněné vzducholodi, jejího pohonného mechanismu, řídicích obvodů různých monitorovacích zařízení, například kamery atd. Diskutovaný monitorovací systém je určen k provozu uvnitř uzavřených místností, což zvyšuje nároky na jeho přesné řízení.

Vzhledem k tomu, že se jedná o velmi rozsáhlé téma, byla pozornost autora zaměřena jen na vybraná témata: návrh řídicího hardwaru, efektivní napájení jednotlivých komponent, pohon a dynamický model soustavy.

Klíčová slova: vzducholoď, autonomní provoz, provoz v uzavřených prostorách, detekce překážek, RFID, dynamický model

ACKNOWLEDGEMENT

Herewith, I would like to thank to my parents and Iva for their patience in times when my good mood abandoned me, for their support and for their understanding that I must have divided my time among them and this thesis. I would also like to thank to my supervisor Milan Adámek and to the head of my department, Karel Vlček. They were always willing to help me and gave me a great support. Finally, I would like to thank to the management of the faculty for their superior backing of doctoral students, to my colleagues for their great cooperation and last, but not least, to our Lord who never let me down and helped me to write this thesis to the end.

TABLE OF CONTENT

Abstract 1
Abstrakt 2
Acknowledgement 3
Table of Content 4
1 Introduction 8
2 State of art 10
3 Objectives and methods 11
4 Theory 12
4.1 Distance measurement 12
4.1.1 Ultrasonic distance meter 12
4.1.2 Reflexive optical distance meters 16
4.1.2.1 Continuous mode reflexive distance meter 16
4.1.2.2 Optical distance meter utilizing a semitransparent mirror 17
4.1.2.3 Coincidence distance meter 18
4.1.3 Triangular optical distance meter 18
4.1.4 Laser distance meters 19
4.1.5 Distance measuring cameras 19
4.2 Motors and swivelling mechanisms 20
4.2.1 Commutator DC motors with permanent magnets 20
4.2.2 Brushless DC motors 24
4.2.3 Stepper motors 25
4.2.3.1 Stepper motors driving 28
4.2.3.2 Continuous operation of stepper motors improvement 32
4.2.4 Approach to stepper or BLDC motors driving when used for the propulsion 32
4.2.5 Swivelling mechanisms 33
4.2.5.1 Servo 33
4.3 Propellers 34
4.4 Airship's model 40
4.4.1 Deployment of the forces in the airship's coordinate system 48
4.4.2 Linearized and simplified model of the airship's rotation 50

4.4.3 Linearized and simplified model of the airship propulsion in forward direction 52
4.4.4 Airship's behaviour modelling 53
4.5 Electrical components 55
4.5.1 Microcontroller 55
4.5.2 RFID reader 56
4.5.3 Switching mode power supply source driver 59
5 Experimental part 60
5.1 Minor hardware modules 60
5.1.1 Module for communication with the ground station 60
5.1.1.1 IP Relay Charon I 61
5.1.1.2 IP Camera 62
5.1.1.3 WiFi Router 63
5.1.2 Module for obstacles detection 63
5.1.2.1 AT-9 board electrical connection 65
5.1.2.2 LED-9/1 board electrical connection 66
5.1.2.3 LED-9/2 electrical connection 66
5.1.2.4 Software of the module for obstacles detection 67
5.1.2.5 Mechanical construction of the Module for obstacles detection 68
5.1.2.6 Results of the Module for obstacles detection testing 69
5.1.3 Module for driving of the motors 72
5.1.3.1 Main board electrical circuitry 73
5.1.3.2 Motor control logic 76
5.1.3.3 Circuitry for external commands receiving 77
5.1.3.4 Controlling algorithm 79
5.1.3.5 Module for driving the motors control 81
5.1.3.6 Practical implementation 82
5.1.4 RFID tags detector 83
5.1.4.1 RFID tags detector main board circuitry 84
5.1.4.2 Communication with the RFID reader 86
5.1.4.3 Controlling algorithm 88
5.1.4.4 Linear voltage regulator circuitry 88
5.1.4.5 Switched-mode operating voltage regulator 90

5.1.4.6 Antenna 92
5.2 Software application 92
5.3 Final hardware design 94
5.3.1 Power supply source 95
5.3.1.1 Voltage regulators time synchronisation principle 98
5.3.1.2 Accumulator disconnector 104
5.3.1.3 Measuring of the lower cell voltage 105
5.3.1.4 Generator of Warning and Emergency shutdown signals 107
5.3.1.5 Voltage regulators design 109
5.3.1.6 Time synchronization 121
5.3.1.7 Complex power source circuitry 122
5.3.2 Motherboard 125
5.3.2.1 Motherboard circuit diagram 126
5.3.2.2 Motherboard connectors 128
5.3.2.3 List of motherboard devices 130
5.4 Airship's behaviour modelling 132
5.4.1 Operation with no elevation 135
5.4.1.1 Simulation 1: short force pulse 139
5.4.1.2 Simulation 2: propelling differences for various speeds are respected 141
5.4.1.3 Simulation 3: lowered power and fast braking 144
5.4.2 Operation with Fast Elevation 148
5.4.3 Change of flight direction 151
5.4.3.1 Simulation 5: yawig without braking 153
5.4.3.2 Simulation 6: yawing with braking 156
6 Conclusion 160
7 References 164
8 List of figures 169
9 List of tables 174
List of author's activities 175
Papers in reviewed journals 175
Papers in conference proceedings 176
Other publications 181

Intership abroad 181
Functional samples / constructions 181
Software 182
Author’s CV 183
List of variables 184
List of abbreviations 190
Appendix A 191
Appendix B 196
Appendix C 202
Appendix D 203

1 INTRODUCTION

After substantial increases of the airships' importance at the beginning of the 20th century it was considered for a long time that the technology of airships has been going to be fallen into forgetingness. There are no doubts that within the contemporary technologies the utilization of airships in applications for which they were developed in past (transport of persons and/or materials) is not effective. Therefore it is not surprising that traditional airships were replaced by modern aircrafts that produce significantly better transport performances.

However, concurrently with the development of traditional aircrafts also the research on the field of unmanned flying vehicles has arisen for various purposes. These vehicles are intended not only for military use, but also for peaceful purposes like landscapes photographing, fire fighting, monitoring of wild animals etc. Precisely in this field of tasks there exist jobs requiring the monitoring system to comply with the following properties:

- Low power consumption to ensure operation without movement,
- Low noise generation,
- Low vibrations (that could disturb photographing),
- Low cruise speed and a capability of staying still at one position,
- Small landing or starting area.

All the above mentioned features are well fulfilled by autonomous airships and currently there are real applications of airships for the purposes named in the text above, for example of monitoring of wildlife in Africa.

Apart from the above mentioned tasks that can be considered as "traditional" there currently arise new applications for which the application of airships is advantageous. In relation to the development of communication systems there occurs a need for static translation stations that acts like satellites, but are operated in considerably lower heights and for the purpose of covering of considerably smaller area. For example, there runs a project of Google Loons, utilizing balloons to bear wireless internet translating stations for areas with infrequent infrastructure. Another project is now run at Tomas Bata University in Zlin, dealing with a construction of small translating stations that would enable radio communication among firemen at the place of a larger fire.

Generally, the airships can be divided into two groups. One group consists of the airships that are large enough and can be operated outdoors. In the second group there are smaller airships the load capacity of whose is insufficient to bear motors and batteries powerful enough to cope with outdoor weather conditions. These airships can only be operated indoors, but, despite their small load capacity they provide such advantage like extremely small power consumption and high manoeuvrability in restricted areas. While the big airships operating outdoors are controlled by means of cooperation among the Global Positioning System, their central processing unit and radio connection with the operator, the

controlling of the small airships must be ensured by other methods due to the need of more accurate location of their position.

In this paper technical possibilities of construction of a small airship are discussed. Because the whole topic is quite large and complex, exceeding the framework of one paper, only selected parts are described in details.

2 STATE OF ART

Currently the issues on construction and controlling of large airships operating outdoors are being quite satisfactorily solved. As an example the project of AURORA [2] can be mentioned. It deals with a development of an airship that is capable of flying range larger than 100 km bearing a load exceeding 100 kg. This construction utilizes the Global Positioning System. The operator sets the required trajectory that is being kept by a set of controlling mechanisms during the whole flight. Another system is developed by Chinese Shanghai University [1] that deals with driving an airship the length of which is approximately 12 m.

The dynamics of large airships is quite difficult to be described as their behaviour is affected by a lot of influences from the selected construction up to the weather conditions. The complex description of the airship's dynamics is still a subject to study and partial pieces of information are published continuously. Relevant description of these issues can be found for example in [3]. In 2008 a non-linear model of stratospheric airship being as long as 200 m was published in [4]. It is expected to reach heights up to 20 000 m using motors of the total power of 100 kW. The purpose of its application is a set of measurements operated in stratosphere.

For the purpose of translating of radio communication signals, new Google Loon project has been launched in 2013. The idea is to put a set of static balloons into atmosphere. The balloons are intended to bear repeaters of wireless internet signals. Their position is stabilised by setting the proper height according to actual airflows in the atmosphere [45].

On the other hand the issues on construction and controlling of the small airships that are intended to be operated indoors are still marginalized. Operating at small areas they cannot be controlled on the basis of Global Positioning System. The combination of the following approaches appears satisfactory:

- Optical orientation using optical signs [3],
- Repeating the known trajectory on the basis of a set of sensors giving the appropriate feedback,
- Inertial controlling using the known point of taking off and the refined dynamic model of the airship,
- Navigation according to radio beacon or RFID tags spread around the trajectory,
- Anti-collision system using ultrasonic obstacle detectors.

3 OBJECTIVES AND METHODS

The objectives of this thesis are to propose a construction of an easy employable Autonomous monitoring system that utilizes a small airship bearing various monitoring components. Due to high complexity of the task the following topics are discussed in details:

1. Anti-collision system, detection of obstacles around the airship.
2. Description of a dynamic behaviour of an airship that would serve as a basis for programming of its inertial controlling. This point includes also the estimation of power consumption and efficiency of the propellers and the airship's operation.
3. Monitoring possibilities – transfer of picture from an on-board camera to a server and bidirectional transfer of small data amounts (manual control, transfer of information from embedded sensors).
4. Proposals on hardware solution of:
   a) Communication with the ground station
   b) Anti-collision system
   c) RFID navigation
   d) Motors' controller
   e) Effective power source with low electromagnetic radiation
   f) Central controlling unit

To reach the objectives of the thesis the following methods were chosen:

1. Theoretical design of individual components of the Autonomous monitoring system on the basis of general theoretical principles.
2. Practical realization of main electrical blocks and testing of their operation.
3. Simulations of more complex electrical circuits by means of the appropriate software.
4. Creating of the dynamic model of the airship in Matlab Simulink.

4 THEORY

This thesis includes theoretical knowledge from many technical disciplines. The following chapter describes the most important theoretical background.

4.1 Distance measurement

In order the basic orientation of the airship could be ensured, it must be capable of measuring its distance from the obstacles in its surroundings.. Distance measurements belong to the oldest tasks of the mankind. However, it is still an evolving discipline that includes up to 25 % of all industrial measurements performed under discrete processes.

Currently, many physical principles are employed. For the proper operation of the airship only contactless distance measurements are suitable; these are predominantly based on ultrasound or various rays of light.

4.1.1 Ultrasonic distance meter

The main advantages of ultrasonic distance meters are as follows:

- contactless measurement in dusty, foggy or (partly) noisy environment,
- performance is not dependent on the colour and type of the material the distance of which is measured.

Usually, ceramic resonant transducers operating with the frequency of approximately 40 kHz are employed, using a narrowband signal. Their bandwidth is usually limited to no more than 2.5 kHz [9]. Several periods of sonic signal are emitted to the obstacle and reflected back to the receiver within a delay that is defined by the velocity of the sound in the air and the distance between the meter and the obstacle. The received signal is then analysed so that it can be decided whether it is the reflection of the transmitted signal or a mere noise from the surroundings.

In the ceramic resonant transducers the piezoelectric effect is employed, being based on the fact that crystal deformation results in the change of its surface charge and vice versa. This effect is quite intensive in crystals that are not centrally symmetrical. The required resonant frequency can be achieved by optimization of the crystal dimensions. Therefore, synthetic ceramic is widely used for these purposes as its characteristics can be determined during its production. Currently, materials on the basis of solid solutions of leaded zirconate ($PbZrO_2$) and leaded titanate ($PbTiO_2$) with the addition of Sr, Ba, Ca, Bi, Sb and W are most widely used. [9]

Of course, there are also several disadvantages arising from the ultrasonic distance meters utilization. Firstly, the sound velocity in the air differs in accordance with elevation and temperature. It can also be affected by atmospheric pressure variations. Secondly, accurate clock source must be employed in the ultrasonic distance meter because the distance (length) is generally a function of the sound velocity and time. Considering the air to be an

ideal gas, the following equation can be applied in order to determine the measured distance l_m:

$$l_m = \frac{\sqrt{\kappa \frac{p_{g0}}{\rho_{g0}}}\left(1 + \frac{\gamma_g \cdot t_g}{2}\right)}{2} \cdot T \quad [m] \tag{1}$$

Where:
κ - Poisson's constant,
ρ_{g0} - gas (air) density at 0°C (273.15 K) [$kg \cdot m^{-3}$],
p_{g0} - gas (air) pressure at 0°C (273.15 K) [Pa],
γ_g - coefficient of the gas (air) thermal expansiveness [$m \cdot K^{-1}$],
t_g - air temperature [K],
T - time period between the sent and the received signal [s].

A partial compensation of the measurement error caused by the changes of the above mentioned parameters can be established when there also is an accurate temperature measurement. The approximation described in the following text can be applied: Considering the zero elevation and typical air pressure and density, the equation (1) can be approximated as follows:

$$l_m = \frac{331.51 + 0.607 t_g}{2} \cdot T \quad [m] \tag{2}$$

According to (2) it can be deduced that once the temperature changes by 25 °C, the measurement error increases by 5 %.

Other problems occurring during this method of measurement are caused by the shape of the emitted signal. In a plane, instead of an ideal straight line, the energy of the emitted signal is displaced in front of the transmitter according to Fig. 1. In practice this leads to the effect depicted in Fig. 2. In case the detector does not form a right angle with the measured surface, the shortest way of the emitted and received signals is not the expected red line but the blue linelocated at the border of the transmitting diagram. The situation can be analysed by means of the Sine theorem. Provided the transmitting angle of the ultrasonic distance meter is α and the angle between the detector orientation and the measured surface is β, then a triangle consisting of red and blue lines and part of the surface (black) can be identified. Based on the triangle theory the angles inside the triangle are $\alpha/2$, β and $\gamma = 180 - (\beta+\alpha/2)$. When the Sine theorem is applied, the equation (3) can be used to estimate the distance that was really measured. However, this is only a rough approximation which does not allow for the real shape of the emitted acoustical signal. Moreover, the approximation is valid only if $\gamma = 180 - (\beta+\alpha/2) > 90°$. Otherwise the measurement will not be correct.

$$l_{real} = l_m \cdot \frac{\sin\left(180 - \frac{\alpha}{2} - \beta\right)}{\sin(\beta)} \; [m] \tag{3}$$

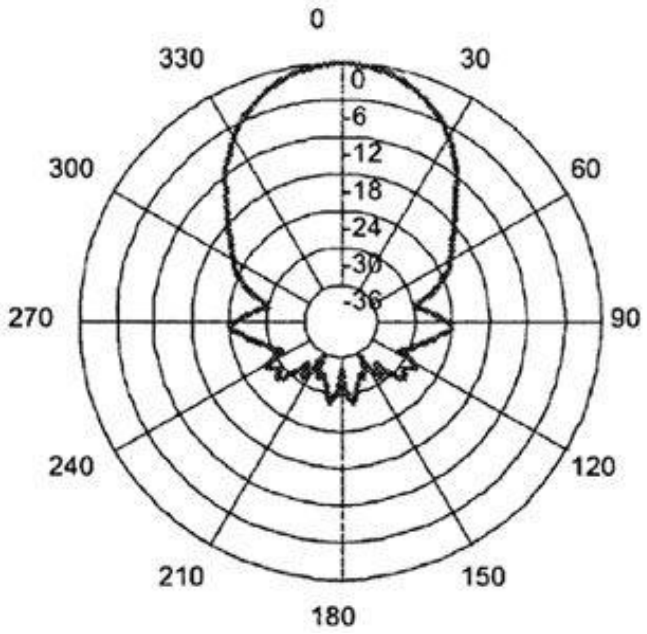

Fig. 1 – Typical ultrasonic transmitter radiation diagram [68]

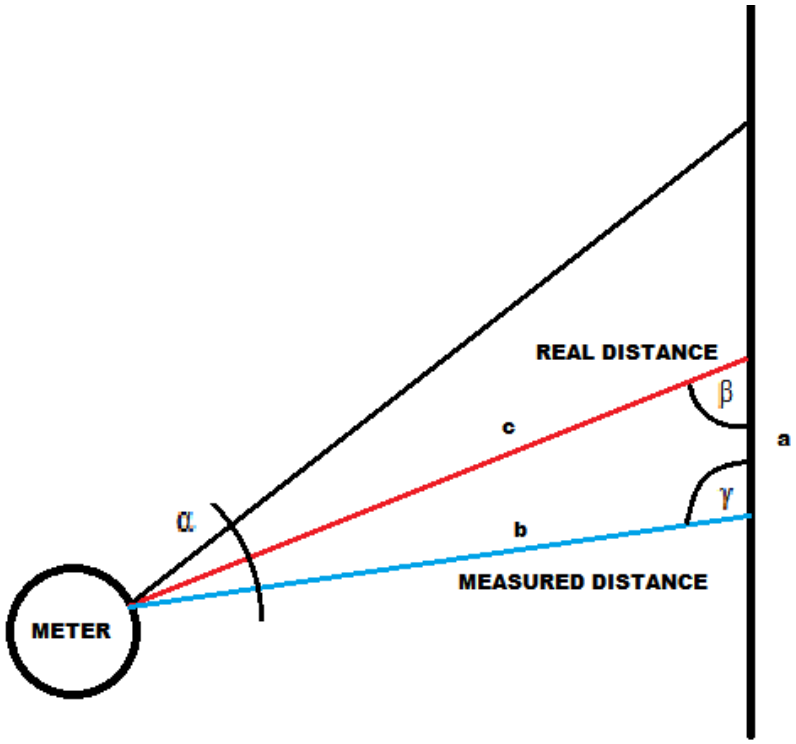

Fig. 2 – Measurement error caused by non-perpendicular reflection

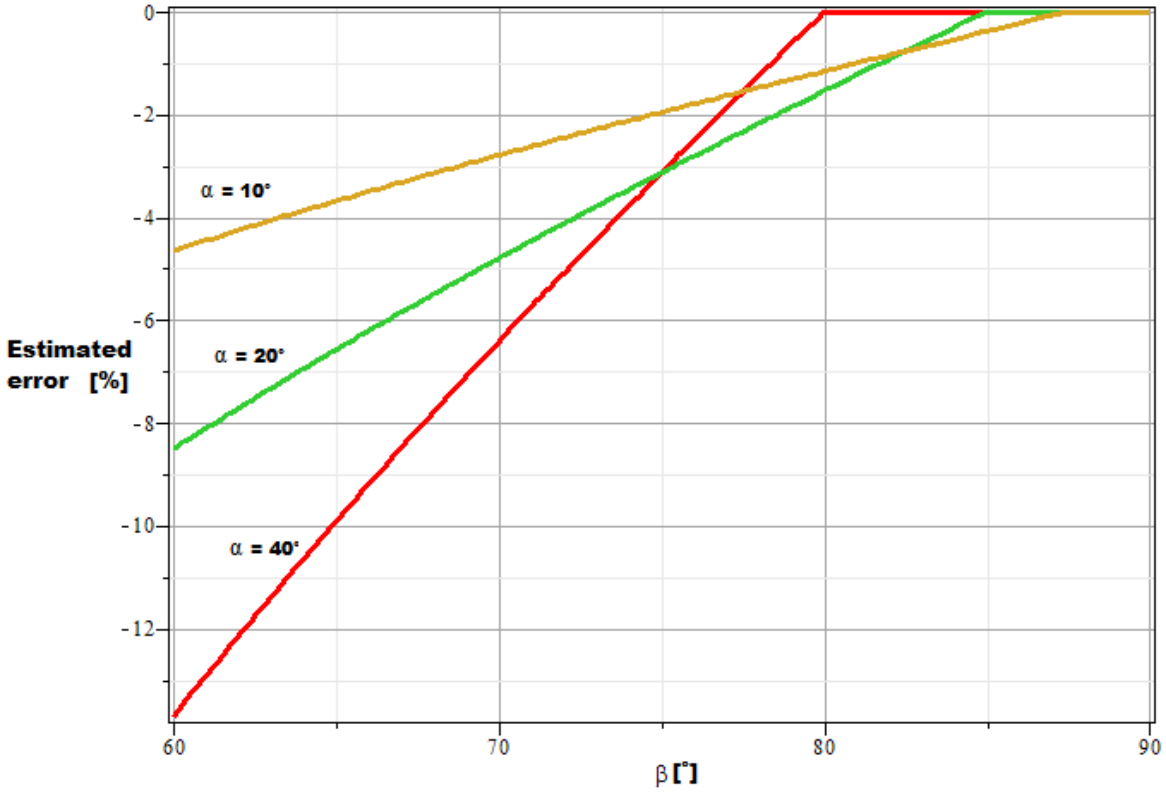

Fig. 3 – Error caused by the mutual geometry of the measured object and the surface of the obstacle (computed in mathematical software, see text)

In Fig. 3 practical issues arising from equation (3) are depicted. On the x-axis the angle between the detector plane and the surface is considered, on the y-axis the estimated error according to (3) is depicted for ultrasonic detectors of different radiation angles (10°, 20° and 40°). It is obvious that detectors with wider radiation angles allow to measure in a wider angle with almost no error (± 10°), but once the critical angle is overpassed, the error increases rapidly. Advanced detectors employ a complex algorithm that allows, by changing the irradiation power, to change the shape of the emitted signal and consequently obtain better accuracy when the measurement is processed under various angles.

Another disadvantage that must be considered at the orientation system of the airship is the fact that the performance of the ultrasonic detectors is dependent on the attenuation of the signal caused by the structure of the measured material. Almost all materials reflect the sound properly but the surface geometry of some of them may cause the reflections are directed not back to the receiver, but in other direction. Therefore, poor performance may be observed if the obstacles have cylindrical or conical surface. In addition, the length of 40 kHz sound waves is only approximately 8.5 mm, which can lead to high attenuation of the sound in corrugated or perforated surfaces.

Provided several ultrasonic detectors are employed, their time synchronization is crucial. Usually, it is obtained by a microcontroller that also evaluates the outputs of the detectors.

Current detectors usually achieve a good performance in the distance range within 0.1 to 6 m, with the linearity better than 0.2 % and the uncertainty in the order of percents. Connection between the microcontroller and the set of the detectors is usually established by means of the I^2C bus. An example of SRF05 ultrasonic detector is depicted in Fig. 4.

Fig. 4 – Ultrasonic detector example

4.1.2 Reflexive optical distance meters

Nowadays, there exist various constructions of reflexive optical distance meters [9]. Usually, they operate in a pulse mode employing infrared region with wavelengths within 850 to 1,000 nm, which minimizes the influence of ambient light on the measurement. Some of them achieve better accuracy than the previously mentioned ultrasonic detectors but none of them was intended to be used within the project of the autonomous airship for their disadvantages, which are more complex design and maintenance. However, a brief description of the most common constructions is provided below in order to enable the comparison with the ultrasonic detectors.

4.1.2.1 Continuous mode reflexive distance meter

This device operates on the basis of evaluation of the amount of reflected light. Although its principle is quite simple, it is inapplicable in the Autonomous monitoring system because it operates only in surfaces whose amount of reflection is known. The operation principle is depicted in Fig. 5. Common LED or laser diode usually serves as the light source (1). The light is emitted to the obstacle (2) from which it is reflected, striking a photodiode (3). The active zone

of the distance meter is depicted in dark grey colour; it is dependent on the mutual angle of the emitting diode and the photodiode that is marked as α. The only advantage of this method is its rapid response. The disadvantages consist in the frequent calibration (the characteristics of emitting and receiving diodes may be unstable in time) and the need for the constant reflection index of the measured object.

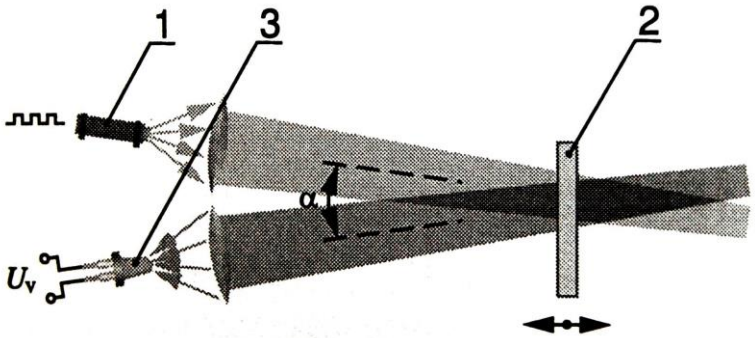

Fig. 5 – Continuous mode reflexive distance meter principle [9]

4.1.2.2 Optical distance meter utilizing a semitransparent mirror

By employing a semitransparent mirror, the measurement range of the continuous mode reflexive distance meter can be improved. The source (1) generates an infrared light that passes through the semitransparent mirror (2) and reflects from the obstacle (3). The reflection is reflected by the semitransparent mirror (2) to the detector (4). Obviously, the effect of the mutual angle α is cancelled but other features of this distance meter are comparable to the previously mentioned one.

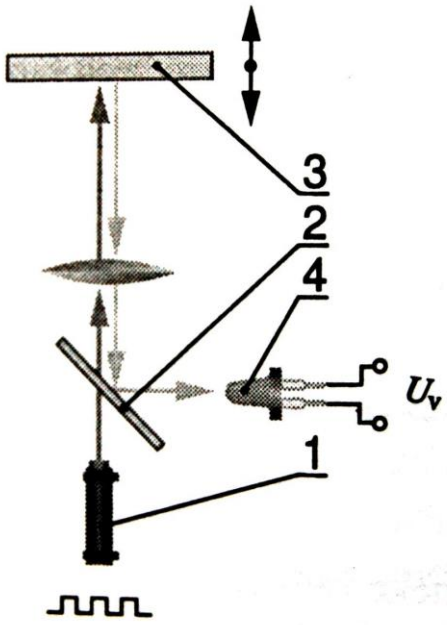

Fig. 6 - Optical distance meter utilizing a semitransparent mirror principle [9]

4.1.2.3 Coincidence distance meter

The coincidence distance meter is based on the improvement of the distance meter that employs the semitransparent mirror. The improvement consists in cancelling the influence of the light emitter and detector calibration for the measured distance. The infrared light is generated by the source (1) and passes through the optical system to the obstacle (2) from which it is reflected on the inclinable lens (3). The feedback loop implemented in the device attempts to set the angle α at which the detector (4) detects the highest light intensity. The distance can be then determined from the angle α, and the known distance d:

$$l_m = d \cdot tg(\alpha)\ [m] \tag{4}$$

Theoretically, this construction could be used within the Autonomous monitoring system because it is not affected by the characteristic drift of the light emitter and detector, neither is it affected by the reflexivity of the measured object provided sufficient amount of light is being reflected, which allows the operation of the device However, this device is expensive due to its complex mechanical construction and therefore inconvenient for the project of the Autonomous monitoring system.

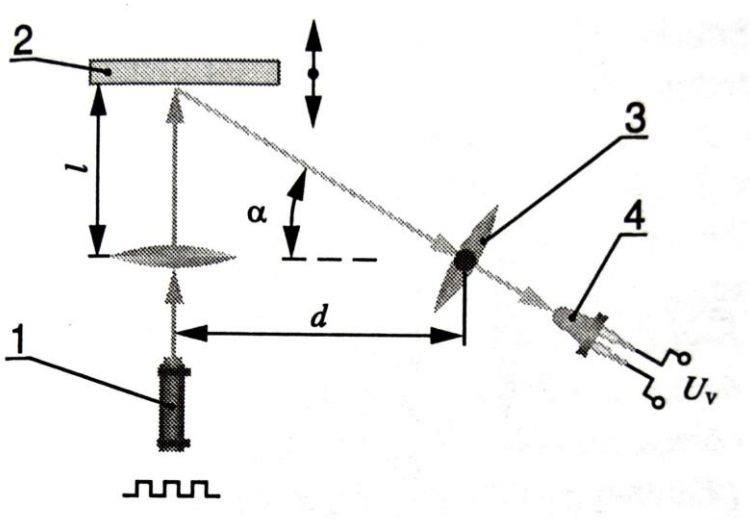

Fig. 7 – Coincidence distance meter operating principle [9]

4.1.3 Triangular optical distance meter

The triangular optical distance meter is of simple construction but operates within insufficient measurement range. It employs a strip of CCD or PSD sensors, as depicted in Fig. 8. The light ray emitted by the diode (1) creates its picture on the surface of the measured object (2). Lenses of the device project this point to the CCD or PSD sensor. At various distances of the obstacle the

point is projected at various pixels of the sensor. Therefore, direct digital signal, easily processed by the microcontroller, is obtained. However, the set of lenses is rather difficult to calibrate and the measurement range is usually within 20 to 400 mm, which makes this device insufficient for the Autonomous monitoring system.

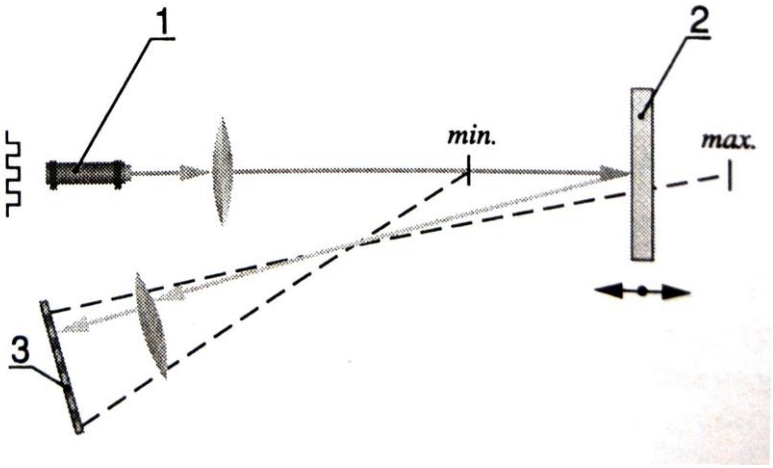

Fig. 8 – Triangular optical distance meter principle [9]

4.1.4 Laser distance meters

Laser distance meters operate on similar principles as the previously mentioned optical meters but employ frequency-stabilized lasers that serve as light emitters. Two main conceptions are usually utilized:

- optical characteristics of the received signal evaluation,
- two coherent rays interference evaluation.

None of these methods is suitable for the Autonomous monitoring system.

4.1.5 Distance measuring cameras

Specialised cameras are also available to measure distances but this solution is not suitable for the Autonomous monitoring system similarly to other methods based on the processing optical signals. There are three reasons why the cameras cannot be employed:

- weight,
- image processing computational complexity associated with high energy consumption,
- high price given by the complexity of the whole solution.

4.2 Motors and swivelling mechanisms

As electric motors and swivelling mechanisms are employed in the Autonomous monitoring system, some issues of the phenomena related to them are discussed in this chapter. Commutator DC motors or brushless DC motors can be used as the airship propellers. In order the elevation could be controlled, there is a need for positioning the propellers by a swivelling mechanism, based either on a servo or on a stepper motor.

4.2.1 Commutator DC motors with permanent magnets

These motors are easily achievable and affordable. They also offer high power at small dimensions. They are easy to control, as described below. Their main disadvantage is the presence of the commutator – the object that wears out. However, for the construction of the Autonomous monitoring system these motors are the preferred ones. The construction of a typical permanent magnet DC motor (PMDC) is depicted in Fig. 9.

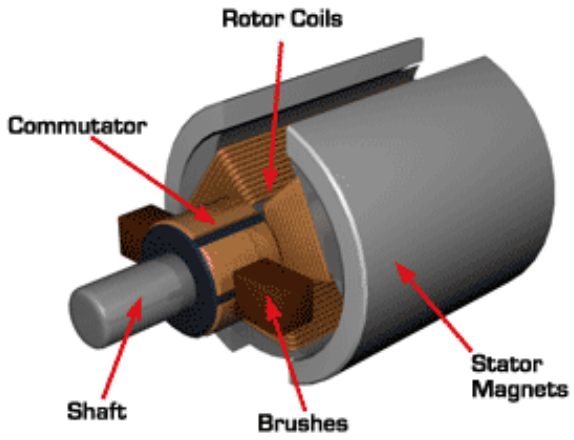

Fig. 9 – Permanent magnet DC motor construction (Internet)

The principle of operation of the PMDC motors is also described in Fig. 10. The stator magnets create a permanent magnetic field across the rotor coils. The commutator together with brushes operates as a positional-driven switch that connects one of the coils that is at that time the most parallel one to the magnetic field lines. If the motor and therefore the appropriate coil are fed by electrical current, the coil in the magnetic field generates force that can be observed as a torque moment on the shaft of the motor. Generally, the following expression can be applied:

$$M_m = 2 \cdot I_a \cdot l_w \cdot B_{pm} \cdot \frac{w_w}{2} \cdot \cos\alpha \ \ [Nm] \qquad (5)$$

Where:

M_m - torque force on the motor shaft [Nm],
I_a - current through the active winding [I],
l_w - rotor winding length [m],
B_{pm} - magnetic induction induced by the permanent magnets [T],
w_w - rotor winding diameter [m],
α - angle between the rotor and magnetic field lines [°]

From the equation (5) it is obvious that the torque force can be controlled by the current fed into the motor. It is also evident that the torque fluctuates during the shaft rotation. In practice, this fluctuation is eliminated by the mass persistence of the mechanism. However, the real torque moment is dependent on the number of the coils in the winding and therefore on the range of the angles α in which the appropriate coil is active.

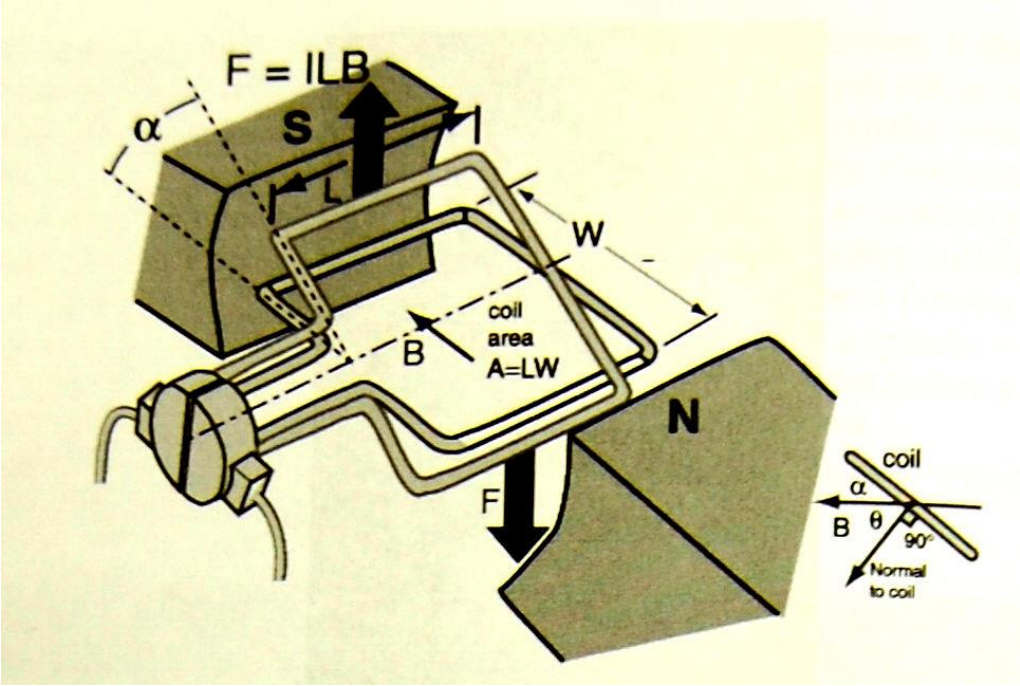

Fig. 10 – PMDC motor operating principle [7]

Generally, three methods of PMDC motor controlling have been introduced in the past:

- controlling on the basis of the supply voltage change,
- controlling on the basis of the magnetic flux change,
- controlling on the basis of the serial resistance change.

For the purposes of the Autonomous monitoring system only the controlling on the basis of the supply voltage is worth applying. The magnetic flux change

is not easily realizable on the motors with permanent magnets and the serial resistance decreases the power efficiency of the propulsion.

According to [7] the controlling characteristic of the PMDC motor is easy to be deduced. The equation (5) can be approximated by the equation for the electromagnetic torque moment:

$$M_m = c_m \cdot \phi_m \cdot I_a \; [Nm] \tag{6}$$

Where:

c_m - constant of the machine (determined by its construction etc.),
ϕ_m - magnetic flux (constant in PMDC) [Wb],
I_a - current through the motor winding [A].

When the rotor is running, some internal voltage is also induced in it. Therefore, the total voltage across the motor winding can be described as:

$$U_a = U_i + R_a I_a = \; c_m \cdot \phi_m \cdot \omega_m + R_a I_a \; [V] \tag{7}$$

Where:

U_a - total voltage across the motor winding [V],
R_a - resistance of the winding [Ω],
I_a - current through the winding [A],
ω_m - angular velocity of the shaft rotation [rad/s].

The relation between the number of turns of the shaft per minute n_m and the angular velocity of the shaft ω_m can be expressed as follows:

$$\omega_m = \frac{2\pi \cdot n_m}{60} \; [\mathrm{rad} \cdot \mathrm{s}^{-1}] \tag{8}$$

Based on the above mentioned equations, the following expression among the shaft rotation velocity, torque moment and current consumption can be deduced:

$$\omega_m = \frac{U_a}{c_m \cdot \phi_m} - \frac{R_a I_a}{c_m \cdot \phi_m} = \frac{U_a}{c_m \cdot \phi_m} - \frac{R_a M_L}{(c_m \cdot \phi_m)^2} = \omega_{m0} - \Delta\omega_m \left[\frac{\mathrm{rad}}{s}\right] \tag{9}$$

Where:

ω_{m0} - angular velocity of the shaft rotation under no load $[\mathrm{rad} \cdot \mathrm{s}^{-1}]$,
$\Delta\omega_m$ - change of the angular velocity of the shaft rotation when loaded with the moment M_L $[\mathrm{rad} \cdot \mathrm{s}^{-1}]$.

The above mentioned theory confirms that for the better determination of the shaft angular velocity, voltage-based controlling is more convenient than

current-based one. If the current source is used for controlling the motors only, according to equation (5), the angular velocity of their shafts would be strongly dependent on their load. On the contrary, if the controlled voltage source is applied, the shafts of the engine rotate with the angular velocity ω_0 determined only by the voltage U_a supplied to the motor (see (9)). When unloaded, the motors consume only a little current needed to cover the mechanical losses. If the load is increased, the current consumption rises correspondingly and also a minor decrease in the shafts rotation velocity can be observed as the current through the motors winding is limited by their serial resistance. This rotation velocity decrease can be described as follows:

$$\Delta\omega_m = \frac{R_a}{(c_m \cdot \Phi_m)^2} \cdot M_L \left[\frac{\text{rad}}{s}\right] \tag{10}$$

In the figure below the difference between the current-based and voltage-based motors driving is expressed. In case a), the source voltage remains on one level and its internal resistance is increased. In case b), the internal resistance of the power source remains the same but the voltage level is changed.

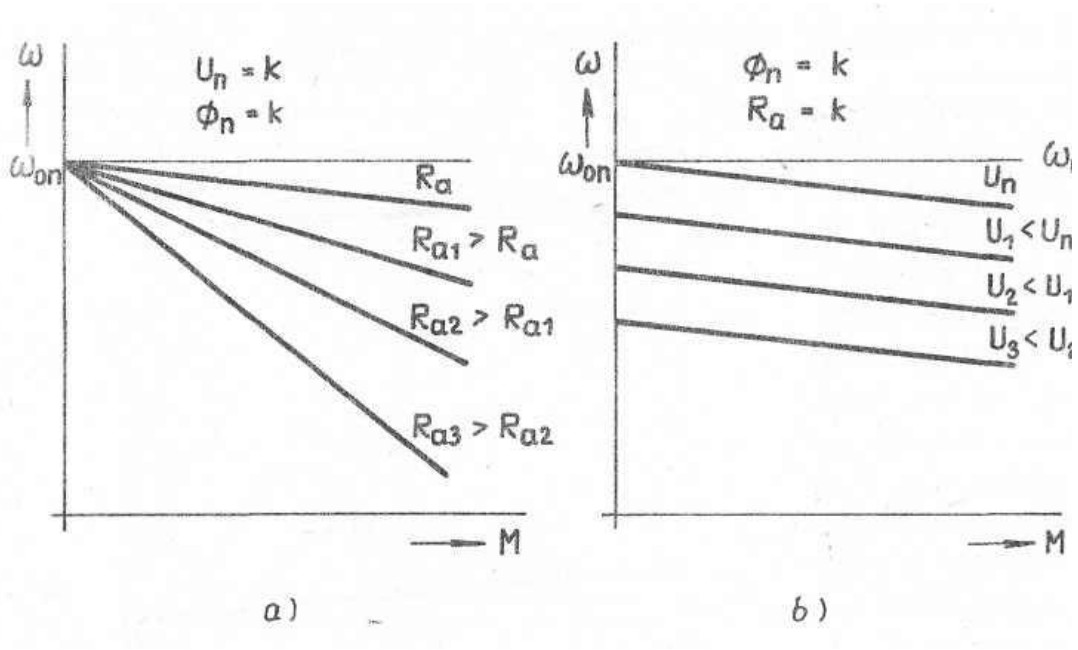

Fig. 11 – Current-based (a) versus voltage-based (b) PMDC motor controlling [24]

In the Autonomous monitoring system the motors are expected to be loaded with propellers that are, including their mechanical characteristics, described in the text below. Generally, the torque moment M needed for driving the propellers is not linearly dependent on their angular velocity.

4.2.2 Brushless DC motors

Brushless DC motors (BLDC) can also be applied to the Autonomous monitoring system propulsion. Currently, the applications employing BLDC motors are quite popular for their long lifespan. Generally, the BLDC motor construction is very similar to the synchronous AC motor. Usually, the rotor is made of permanent magnets while the active coils are displaced in the stator part of the motor. In the basic conception, three coils displaced by 120° are employed, similarly to the three-phase synchronous motor.

The most important advantage of the BLDC motors is that the critical part of the DC motors – commutator – has been replaced by electronic AC current generator. Not only is the lifespan of such motors increased but their EMC is improved and the arcing on the commutator contacts has been eliminated.

On the other hand, drawbacks with the BLDC motors tare higher price, complex construction and need for special electrical circuitry providing control of these motors. In order to apply electrical commutation, the relative position of the rotor and coils must always be known. This can be ensured by several methods. For example, Hall sensors, selfsynchrons, or other rotational encoders can be applied [7]. However, these solutions are too expensive to be used in cost-effective applications. According to [7], the method of back EMF sensing can be applied, determining the position of the rotor by checking the voltage induction on the currently unused coil of the stator. The principles of controlling BLDC motor are described in [7] and [34].

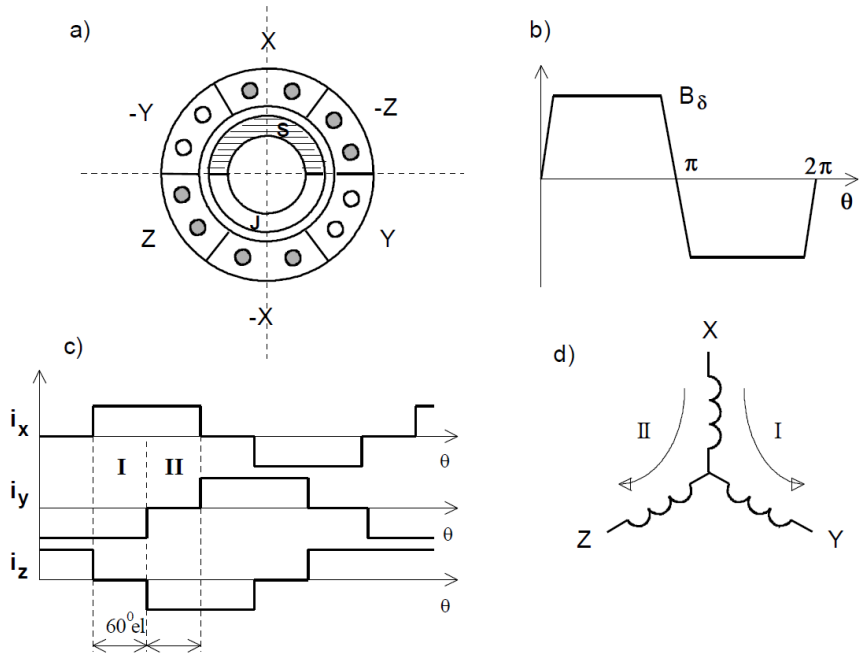

Fig. 12 – BLDC motor: a) cross-section, b) induction in the air gap, c) currents through the coils according to the rotor position, d) stator coils connection [34]

For the application in the Autonomous monitoring system several BLDC motors for RC models are worth considering but there is always a need for their external controller. Unfortunately, the controllers are ready to be used together with the RC receivers; in other words, if the BLDC motor is used, the controller has to be used as well and the communication protocol of this controller has to be known and implemented into the Autonomous monitoring system controlling algorithm. Therefore, the BLDC motors are not primarily intended to be employed in the Autonomous monitoring system.

4.2.3 Stepper motors

The stepper motors are the simplest actuators converting the digital signal to a position [23]. There are various constructions of the stepper motors. If it is ensured that all required steps are processed by the motor, no feedback is needed to determine its shaft position. Therefore, the stepper motors are perfectly suitable for driving the swivelling mechanisms. Nevertheless, they can also be used for the Autonomous monitoring system propulsion, especially in the tail position, as their controlling mechanism allows precise control of their angular velocity and effective deceleration. According to their construction, the following groups of stepper motors are distinguished:

- reluctance – having poles on the stator as well as on the rotor,
- with permanent magnets – the rotor is composed of permanent magnets,
- hybrid – combining the above mentioned constructions.

The stepper motors are designated by their static characteristics that describe the relation between the torque moment and the controlling frequency. Usually, the nominal load moment M_n and the maximum load moment M_{max} are considered. If the maximum load moment M_{max} is exceeded, the motor falls out of synchronism.

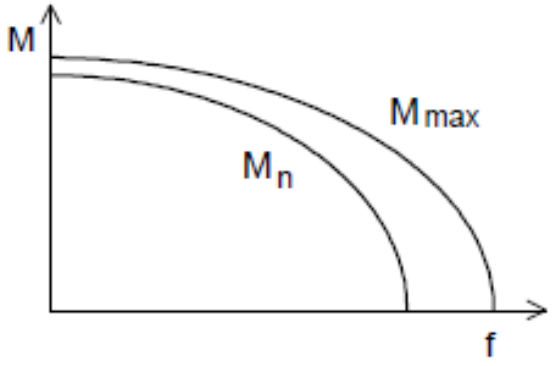

Fig. 13 – Typical static characteristics of the stepper motor [23]

The construction of the reluctance motor is depicted in Fig. 14 a). It is a three-phase motor consisting of six stator poles and four rotor poles. The pole couples are driven by the DC current in the consecutive way. In each step, the rotor turns by a half of the pole distance. Therefore, it enables to process 12 steps per one

shaft turn. Generally, the size of one step is determined according to the following equation:

$$\Delta\phi_m = \frac{2\pi}{n_{ph} \cdot N_n} \ [°] \tag{11}$$

Where:

n_{ph} - number of stator phases,

N_n - number of notches on the rotor.

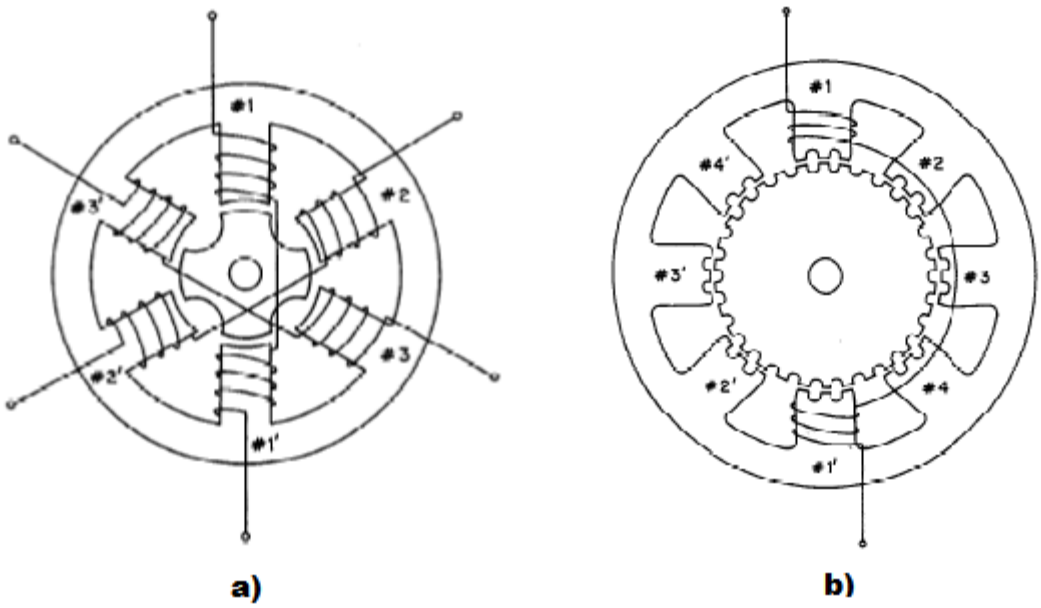

Fig. 14 – Reluctance stepper motors: a) three phase reluctance stepper motor, b) four phase reluctance stepper motor with increased number of steps per one turn. [23]

If more steps per one shaft turn are required, the construction in compliance with Fig. 14 b) is applied. The number of phases is increased reasonably and fine notches are created around the rotor. Additional notches are also created on the stator poles. This construction allows reaching approximately hundreds of steps per one shaft turn. Assuming more precision is required, a method called microstepper can be employed. This method consists in combination of driving several poles with different currents. According to displacement of currents in particular coils, practically unlimited position between two steps can be reached. However, advanced controlling techniques and microcontroller-aided hardware are needed to implement this method.

When permanent magnets are used in the rotor construction, an increased torque moment is reached. Moreover, the motor employing permanent magnet also shows the so called steady state moment. The rotor is then fixed in its position even if the motor is not driven by the power supply. The construction of the stepper motor employing the permanent magnet is depicted in Fig. 15. The permanent magnet is placed on the rotor shaft and the pole extensions are created by magnetically soft materials. The displacement of the pole extensions

differs for the northern and the southern pole of the magnet. The motors usually employ bifilar winding that allows polarity switching.

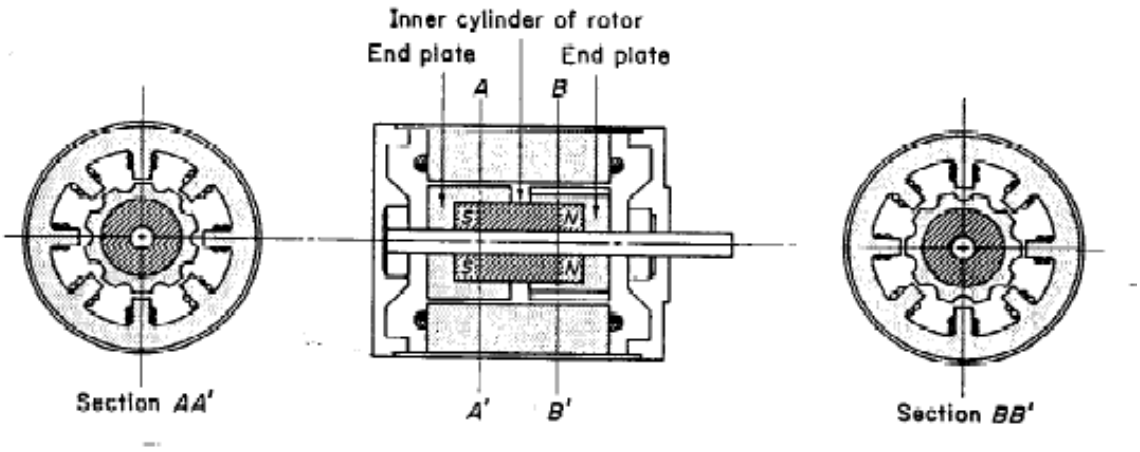

Fig. 15 - Stepper motor employing permanent magnet, cross-section [23]

According to [23], the mathematical model of the stepper motors can be deduced from the power balance equation:

$$u_e \cdot i = M_m \frac{d\phi_m}{dt} + \frac{d}{dt}\left(\frac{1}{2} i^2 L_m(\phi_m)\right) \; [W] \tag{12}$$

Where:

u_e - voltage across the active stator phase [V],
i - current consumed by the active stator phase [A],
M_m - electromagnetic torque moment of the motor [$N \cdot m$],
$\frac{d\phi_m}{dt}$ - shaft angular velocity [$rad \cdot s^{-1}$],
$L_m(\phi_m)$ - motor coil inductance as a function of rotor to stator angle [H].

In (12) the expression $\frac{d}{dt}\left(\frac{1}{2} i^2 L_m(\phi_m)\right)$ refers to the change of the magnetic energy and the expression $M_m \frac{d\phi}{dt}$ refers to the mechanical output power of the motor.

The induction $L_m(\phi_m)$ can be approximately expressed by the following equation:

$$L_m(\phi_m) = L_0 + L_{mn} \cdot \cos(2p_p\phi_m) \; [H] \tag{13}$$

Where:

p_p - number of the stator pole parts,
ϕ_m - rotor to stator displacement angle [rad],
L_0 - inceptive inductance, general constant [H],
L_{mn} - nominal inductance [H]

The voltage inducted in the active coil can be expressed as follows:

$$u_e = \frac{d}{dt}(L_m(\phi_m) \cdot i) \ [V] \tag{14}$$

Then the torque moment of the reluctance stepper motor can be expressed by the following equation:

$$M_m = \frac{1}{2} i^2 \frac{dL_m(\phi_m)}{d\phi_m} \ [Nm] \tag{15}$$

Finally, one can express the motion equation as follows:

$$M_m = J_m \frac{d^2\phi_m}{dt^2} + B_v \frac{d\phi_m}{dt} + M_L \ [Nm] \tag{16}$$

Where:

J_m - total persistence moment on the shaft [$\mathrm{kg} \cdot m^2$],
B_v - viscous friction coefficient [$\mathrm{kg} \cdot s^{-1}$],
M_L - external load torque [$\mathrm{N} \cdot \mathrm{m}$],
M_m - moment generated by the motor [$\mathrm{N} \cdot \mathrm{m}$].

4.2.3.1 Stepper motors driving

Unlike PMDC and BLDC motors, the stepper motors are more efficient when driven by a current-source. This phenomenon is discussed below.

Specialized integrated circuits have been developed for such purposes. Depending on the construction of the motor coils, bipolar and unipolar motors are distinguished. The principle of driving both of them is depicted in Fig. 16. The internal construction of the drivers is depicted in Fig. 17. According to [23], the bipolar motors deliver 40 % more torque compared to the unipolar ones of the same dimensions. This is due to their higher power loss limit, because the coils are simpler and capable of being wound by a thinner wire.

Generally, there are three methods of driving the stepper motors:

- by controlled voltage,
- by imposed current,
- by pulse source.

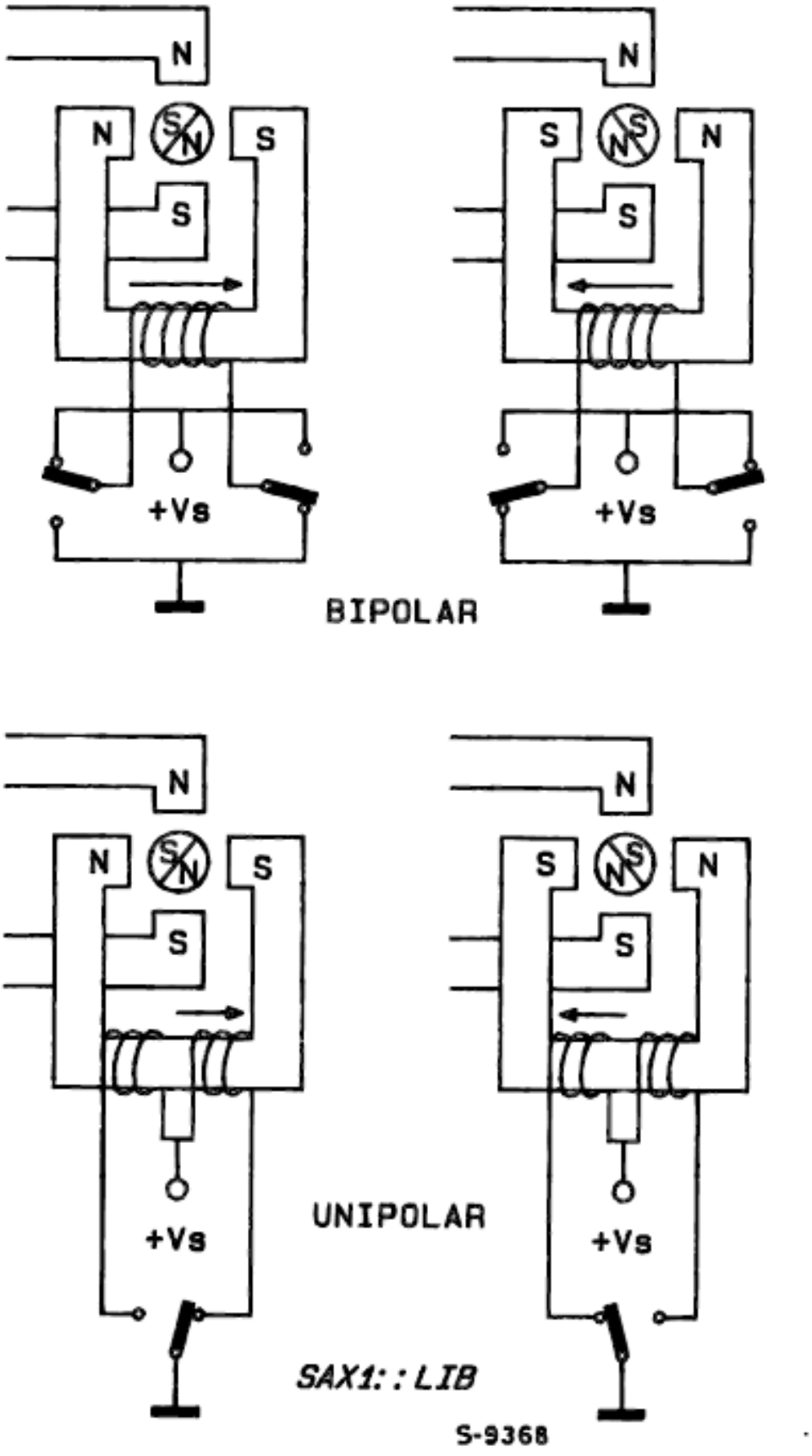

Fig. 16 – Bipolar versus unipolar stepper motor driving [23]

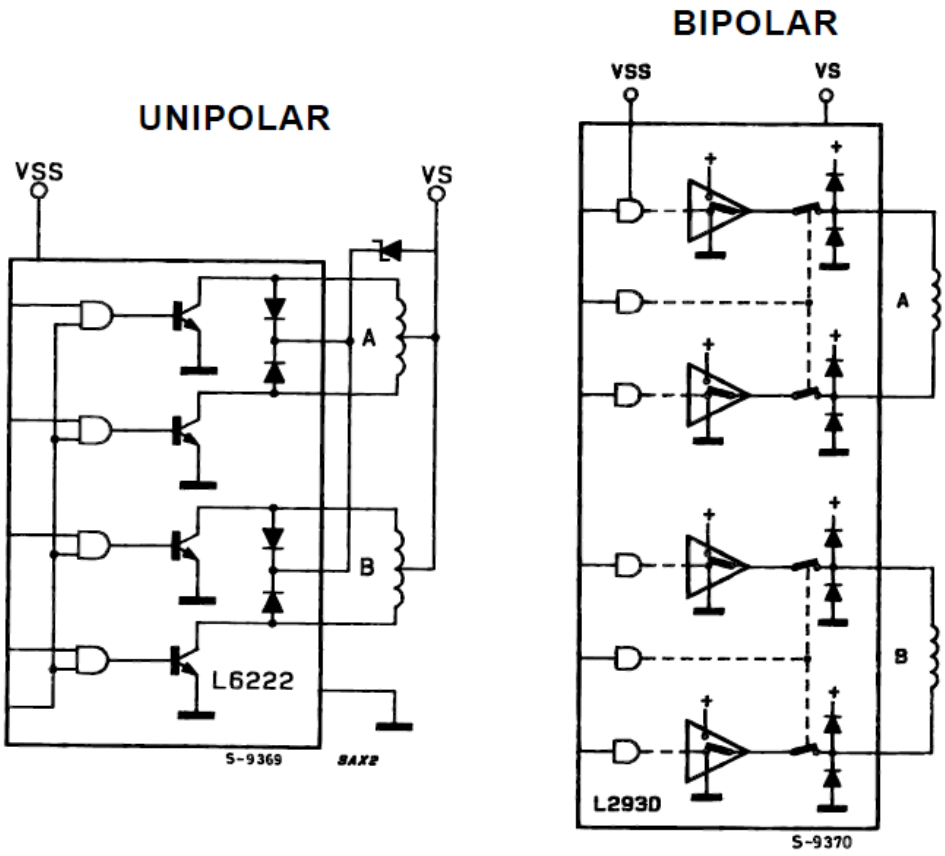

Fig. 17 – Example of internal stepper motors drivers – unipolar (L6222) and bipolar (L293D) [23]

When the fixed source generating voltage U_a is used for the motors driving, the problems occur at higher frequencies due to the inductance of the winding coils. The coils show a finite time constant τ that is defined as follows:

$$\tau = \frac{L_a}{R_a} \ [s] \tag{17}$$

Where:
L_a - coil inductance [H],
R_a - coil resistance [Ω].

When considering damped increase of the current after the appropriate coil is connected to the supply, the expression for the torque moment (15) shall involve following impact on the current i:

$$M(t) = \frac{1}{2}\left(\frac{U_a}{R_a}\left(1 - e^{-\frac{t}{\tau}}\right)\right)^2 \frac{d^2 L_m(t)}{dt^2} \ [Nm] \tag{18}$$

The equation (15) is valid provided the time in which each of the coils is operated is much higher than the time constant τ.

A partial improvement at high frequencies is achieved if the motor is driven by the imposed current. A higher voltage is applied and an auxiliary resistor is connected in series with the coil. By increasing the total resistance the time constant τ is lowered (see (17)). However, this solution is inefficient because of power losses in the serial resistors.

Therefore, pulse current sources are currently employed in order to achieve optimal efficiency and high torque moment at high shaft velocities. The aim is to feed the coils of the motor with a constant current, which eliminates the above mentioned phenomenon and improves the static characteristics of the motor at higher frequencies. A block diagram of driving one of the motor coils with switching mode current regulation is depicted in Fig. 18.

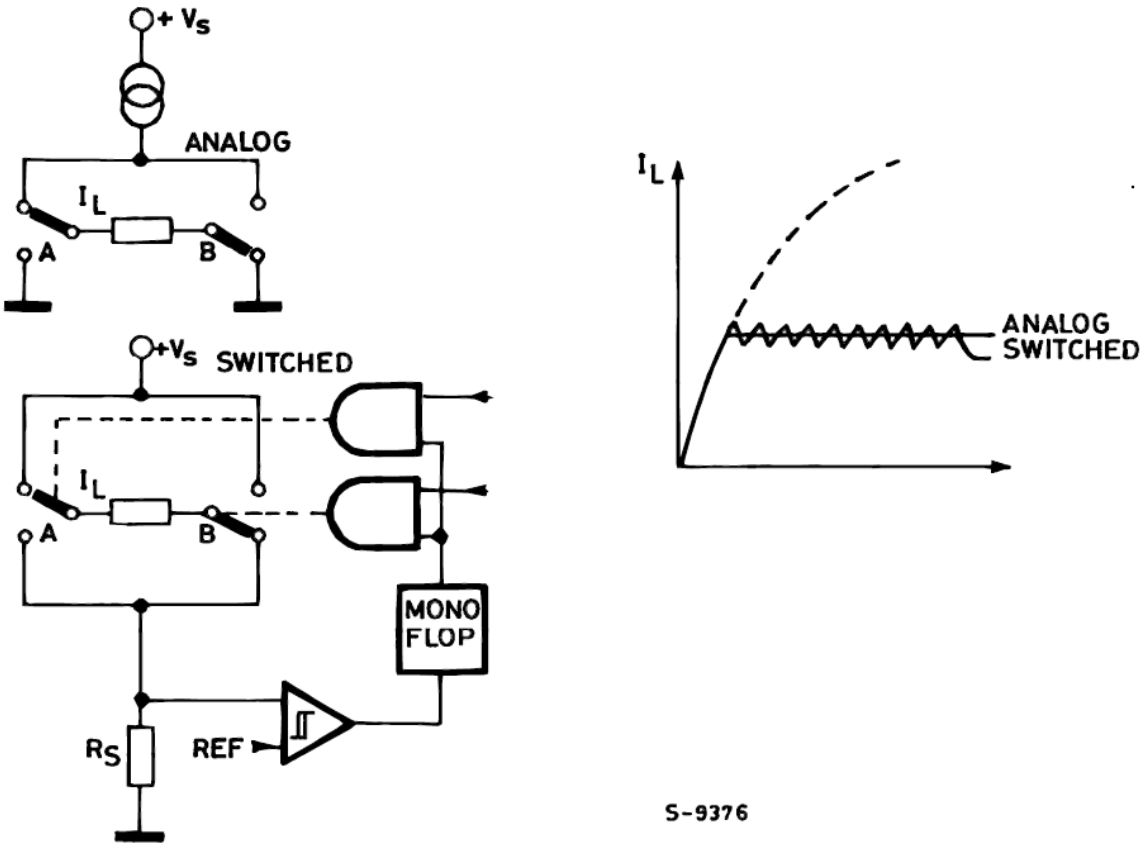

Fig. 18 – Switching mode current regulation of the motor coil [23]

As depicted in Fig. 18, the active coil of the motor is switched rapidly in order to ensure the required current flow through the motor. The current is sensed by the R_s resistor.

4.2.3.2 Continuous operation of stepper motors improvement

Provided the stepper motors are used for the purposes of propulsion of the Autonomous monitoring system, the improvement mentioned below is possible to be introduced.

The improvement consists in driving the motor in the same way as the BLDC motor – by feeding the winding coils with the sinusoidal current. Under such operation the motor will rather glide than step, which brings the following advantages [23]:

- no resonance problems,
- noise reduction,
- smooth run,
- position resolution is resumed.

When connected according to Fig. 18, the sinusoidal voltage reference would be connected to the REF input. Microcontroller can be used for generating the quasi-sinusoidal reference signal. According to [23] it has been proven that resolution of the sinusoidal up to 5 bits is sufficient and higher resolution does not bring any measurable advantages.

4.2.4 Approach to stepper or BLDC motors driving when used for the propulsion

As previously mentioned, the PMDC motors were primarily intended to be used for the Autonomous monitoring system propulsion. However, the small BLDC motors for RC models without electronic commutation can be treated as permanent magnet stepper motors with very little steps per turn. Their angular velocity can be driven by the clocking frequency while their torque moment can be driven by the coils current and controlled by the switching regulator.

Considering this type of propulsion, the torque moment needed by the propellers must be known for the whole range of the operating velocities and the driving current must be always set accordingly so that the power consumption is not too extensive and the motor still operates in the synchronous mode. Also, when acceleration or deceleration is required, the driving current must be increased prospectively in accordance with the motion equation (16). An example of the driving current modulation according to the operational mode (at one speed) is depicted in Fig. 19. Provided this method of regulation is applied, there is no need to determine the position of the BLDC motor’s stator. Moreover, fast deceleration can be achieved by feeding the coils of the motors with high DC current for a while. Such deceleration methods are convenient especially in the tail motor driving where it is necessary to start and stop the propeller quickly, so that the mechanical persistence of the propeller does not cause errors in inertial orientation of the Autonomous monitoring system.

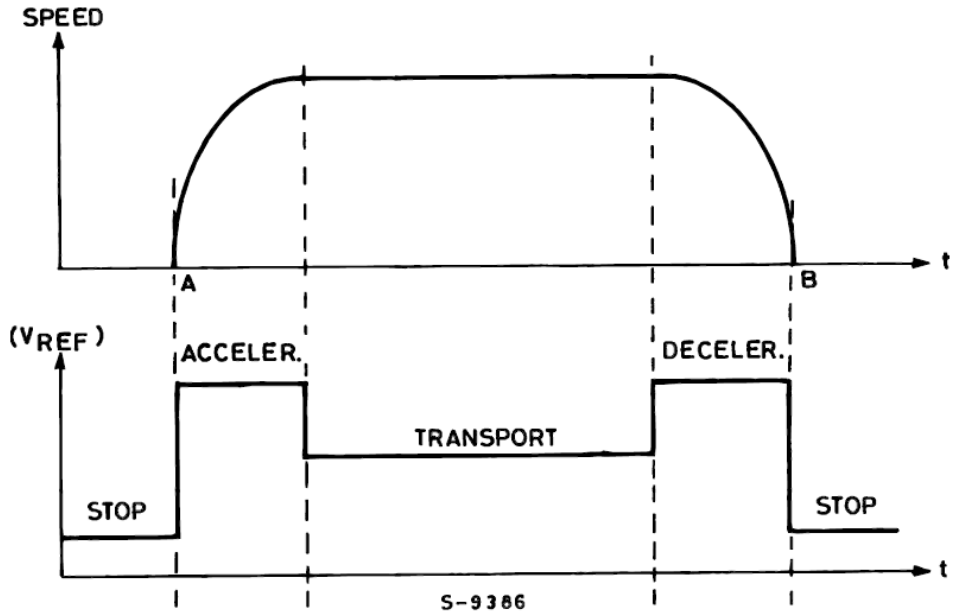

Fig. 19 – Switching mode current regulator reference voltage modulation example for different modes of the motor's operation [23]

4.2.5 Swivelling mechanisms

The propulsion of the Autonomous monitoring system considers two main motors mounted on a rotational shaft whose swivelling enables to control elevation of the airship. The swivelling can be driven by two different mechanisms:

- stepper motor,
- servo.

Stepper motors are described above. However, for the purpose of the main motors holder the servo used in RC models was intended to be used. Due to its internal construction it is quite easy to drive.

4.2.5.1 Servo

Servo is a mechanism that enables swivelling of complex mechanisms processed by a conventional motor. The motor is usually of the PMDC type operating together with a gearbox. However, BLDC or stepper motors may be used as well for more complex operations where the improved lifetime is worth higher costs. In order to determine the position a feedback must be obtained. This feedback can be given either by a potentiometer or by an optical position detector.

The conventional servo intended to be used in RC models usually employ a PMDC motor together with a small gearbox and a potentiometer as a position detector. These devices are organized in accordance with the following figure.

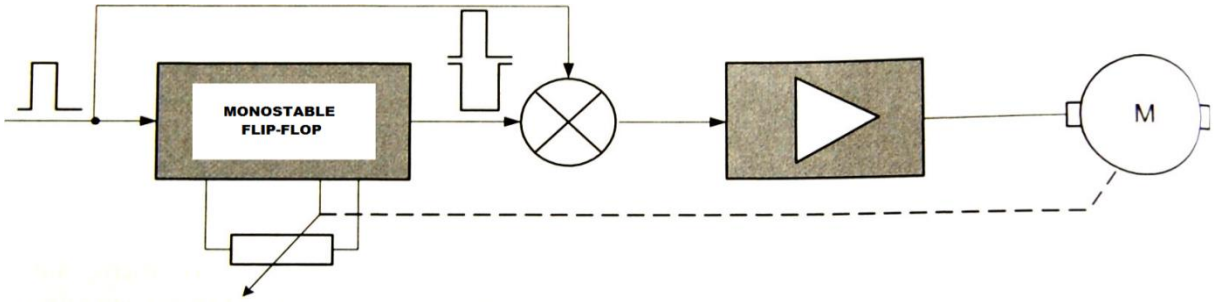

Fig. 20 – Internal organization of a conventional low-power servo [7]

The monostable flip-flop generates a negative pulse the length of which is proportional to the position of the servo shaft. It is triggered by the controlling pulse that is of the positive polarity and the length of which is proportional to the desired position of the shaft. The triggering pulse is then added to the pulse from the output of the flip-flop circuit, which results in either positive or negative pulse (according to the relative position of the current and the desired state) causing the motor to rotate in desired direction. Once the pulses are equally long, the desired state is achieved and the motor does not operate any more. As the controlling pulses are generated repeatedly, with the period of 20 ms, the feedback is still active; the position is being corrected constantly even if external forces are impacting on the output shaft of the servo. The length of the pulses varies from 1 to 2 ms according to the programmed position (1.5 ms refers to the centre of the shaft trajectory). The speed of such servos is usually quite low; several seconds are required to move the shaft from one marginal position to the other (usually 180° of shaft rotation). Such long time makes the delay the most significant parameter of the servo. Dynamical parameters can be neglected. The torque moment of the servo depends on the period in which the controlling pulses are repeated.

4.3 Propellers

The propellers are necessary to be used in order to ensure the Autonomous monitoring system propulsion. A minor propeller theory as described in [26], [27], [39] is needed so that the power of the motors as well as their current consumption could be determined approximately.

In order to analyse performance of the propeller, the following parameters must be known:

- propeller diameter D_p [m],
- propeller rotation velocity n_p [rpm],
- torque moment M_p [$N \cdot m$],
- thrust generated by the propeller F_T [N],
- gas (air, fluid) density ρ_g [$kg \cdot m^{-3}$],
- gas (air, fluid) viscosity μ_g [$m^2 \cdot s^{-1}$],
- gas (air, fluid) bulk elasticity modulus K_g [$N \cdot m^2$],

- flight velocity v_f $[m \cdot s^{-1}]$.

According to [26] the thrust generated by the propeller can be expressed as follows:

$$F_T = const. \cdot \rho_g n_p^2 D_p^4 \cdot f\left[\left(\frac{\mu_g}{D_p^2 n_p}\right)^f ; \left(\frac{K_g}{\rho_g n_p^2 D_p^2}\right)^g ; \left(\frac{v_f}{D_p n_p}\right)^h\right] \quad (19)$$

In (19) the coefficients f, g, h refer to the appropriate power of the expressions so that the dimensions of the parameters are in accordance. The terms in the brackets can be described as follows:

a) in $\left(\frac{\mu_g}{D_p^2 n_p}\right)$ the product $D_p^2 n_p$ is proportional to the speed of the tip, therefore it can be treated like:

$$\frac{\mu_g}{length\ x\ velocity} \propto \frac{1}{Re} \quad (20)$$

Where:
Re - Reynold's number [-].

b) in $\left(\frac{K_g}{\rho_g n_p^2 D_p^2}\right)$ the expression $\left(\frac{K_g}{\rho_g}\right) = c_s^2$ where c_s is the speed of sound in the air. This is like:

$$\frac{c_s^2}{(tip\ speed)^2} \propto \frac{1}{M_{tip}^2} \quad (21)$$

Where:
M_{tip} - Mach number of the tip [-].

c) in $\left(\frac{v_f}{D_p n_p}\right)$ the ratio $\left(\frac{v_f}{n_p}\right)$ refers to the distance advanced by the propeller in one revolution. The ratio is non-dimensionalised by the propeller diameter D_p. This coefficient is typically called the advance ratio and given the symbol J_p.

Finally, it can be claimed that the thrust generated by the propeller is a function of a constant, its diameter, number of revolutions per minute, air density, Reynold's number, Mach number of the propeller's tip and the advance ratio:

$$F_T = const. \cdot \rho_g n_p^2 D_p^4 \cdot f\left[Re; M_{tip}; J_p\right] \quad (22)$$

The expression (22) is usually simplified by employing the thrust coefficient k_T that is, in general, a function of the propeller design, Re, M_{tip} and J_p. The simplified expression is as follows:

$$F_T = k_T \rho_g n_p^2 D_p^4 \ [N] \tag{23}$$

By the same way the torque moment coefficient can be deduced. As the torque moment is a force multiplied by a length, the torque moment can be expressed as:

$$M_p = k_Q \rho_g n_p^2 D_p^5 \ \ [Nm] \tag{24}$$

Where:

k_Q - torque coefficient that is in general a function of the propeller design, Re, M_{tip} and J_p.

The power supplied to the propeller is proportional to its torque moment and the velocity of its rotation. This power is expected to be supplied by the motors and its knowledge is necessary in order to dimension the motor drivers for the proper performance. By using the above mentioned theory, it can be expressed as:

$$P_p = 2\pi n_p M_p \ [W] \tag{25}$$

From (24) and (25) it is obvious that

$$P_p \propto \ n_p^3 \tag{26}$$

The airship of the Autonomous monitoring system enters into operation by means of the mechanical output power generated by the propellers. The following equation applies to the useful output power generated by one propeller:

$$P_p' = \ F_T v_f \ [W] \tag{27}$$

The efficiency of the propeller can be expressed as:

$$\eta_p = \frac{P_p'}{P_p} = \frac{F_T v_f}{2\pi n_p M_p} = \frac{k_T \rho_g n_p^2 D_p^4 v_f}{2\pi n_p k_Q \rho_g n_p^2 D_p^5} = \frac{1}{2\pi}\frac{k_T}{k_Q} J_p \ [-] \tag{28}$$

In practice a variable called the power coefficient is employed:

$$C_{pow} = 2\pi k_Q \; [-] \tag{29}$$

Provided the power coefficient is known, the power required to drive the propeller as well as the efficiency can be expressed in the following way:

$$P_p = C_{pow}\rho_g n_p^3 D_p^5 \; [W] \tag{30}$$

$$\eta_p = J_p \left(\frac{k_T}{C_{pow}}\right) [-] \tag{31}$$

Knowledge of the above mentioned equations is needed so the relationship among the propulsion force, airship speed and motors load could be expressed. Moreover, the propellers should operate at revolutions at which their efficiency is optimal. The methods of measurement of propellers' characteristics are described in [27]. The literature [39] provides detailed information on more than 100 propellers for small aircrafts so that it can be used as a catalogue.

Naturally, the propeller's performance is dependent on its geometry, including the blade angle. The complete description of all the phenomena is beyond the scope of this paper; however, Fig. 21 can be used as a guideline. It shows typical propeller efficiency curves for different blade angles as functions of the advance ratio.

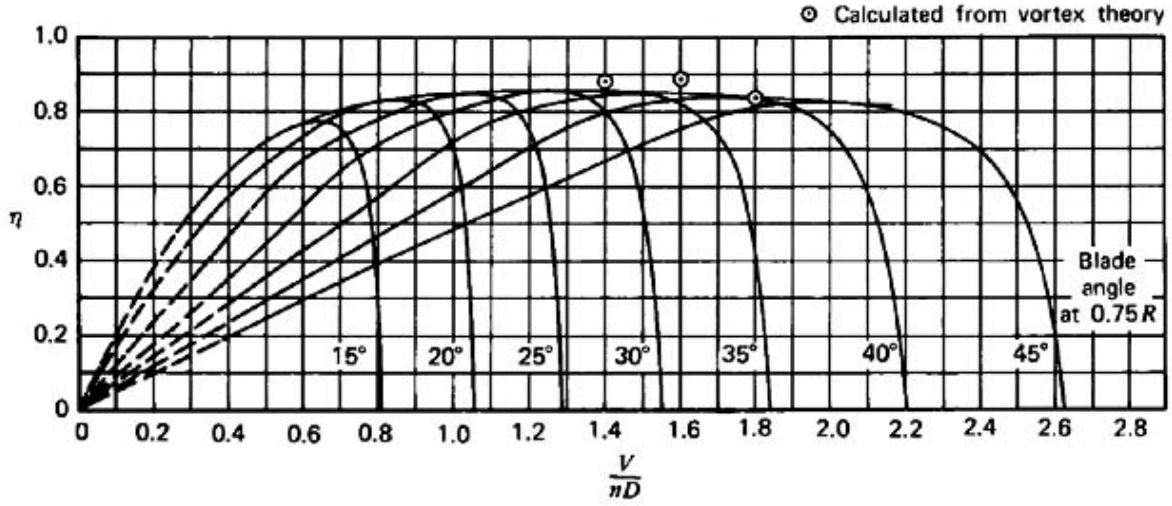

Fig. 21 – Typical propeller efficiency curves for different blade angles as functions of the advance ratio [27]

As the airship is expected to be operated at low speeds, propellers with small blade angles shall be employed. Let us consider the usage of APC Slow Flyer 8" x 3.8" propeller as an example. Its static efficiency characteristics for different motor speeds are depicted in Fig. 22. The optimum efficiency reached for J = 0.36 and the propeller's diameter is 0.2 m. For the expected maximum speed of the airship 2 m/s, the optimum shaft revolutions are 27.8 rev/s (≈ 1,667 rpm).

For obtaining the proper propulsion force this value is too low. The expected force at these revolutions is according to (23) expected to be at least 0.08 N. This force can be raised by increasing the speed of the motor. When increased 5 times, at 8,335 rpm the propeller delivers up to 4 N but its efficiency drops to approximately 15 %. The power delivered by the motor will increase from approximately 0.35 W to 27 W. This illustrates how crucial it is to adjust the propeller according to the needs of the airship. The fact that the airship moves slowly limits the possibility of efficient use of propellers suitable for RC models. Therefore, propellers with reasonably high diameter operating at low J_P should be employed.

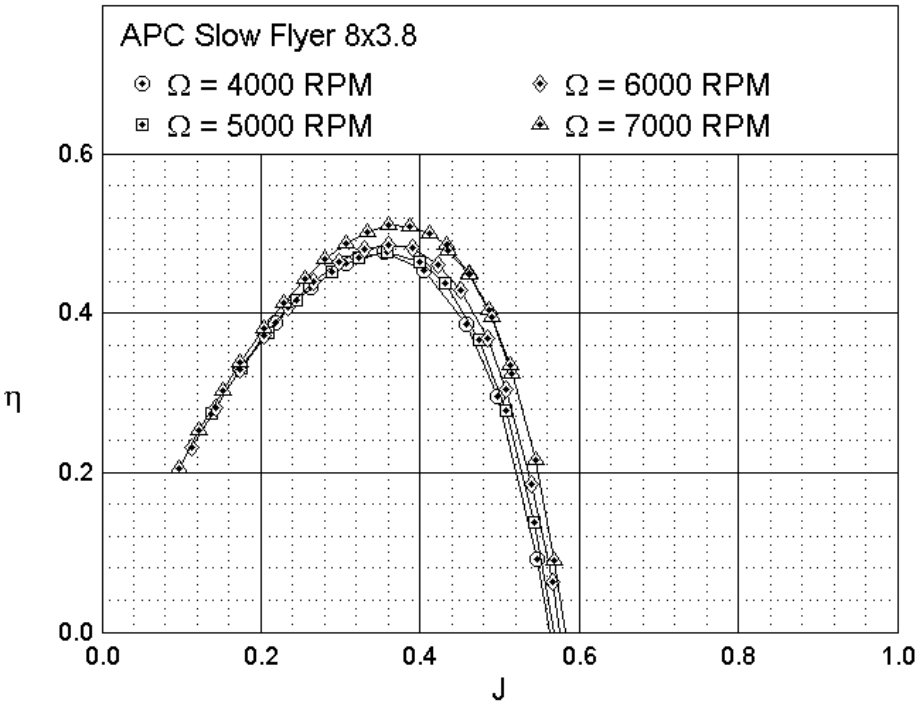

Fig. 22 – Static efficiency characteristics of the propeller APC Slow Flyer (8x3.8)" [39]

In figures below the estimated power consumption, propelling force and efficiency of the APC Slow Flyer (8 x 3.8)" propeller are depicted.

The static parameters, the propelling force and the consumed power, dependent on the motor shaft revolutions are depicted in Fig. 23 and Fig. 24. In Fig. 23 the propelling force generated by the propeller while the airship is in motion is depicted. For high rpm it is identical to the static propelling, but at low rpm rate, the propelling is decreased in dependence on the airship velocity. If rotating is too slow compared to the airship velocity, the propeller can even decelerate the airship (at the velocity of 2 m/s and 1,000 rpm it decelerates with the force of 5.6 mN). In Fig. 25 the efficiency versus motor revolutions is depicted for different airship speeds (physically, it makes no sense to measure the power efficiency if the airship does not move because according to (27), for the zero velocity it will always be zero).

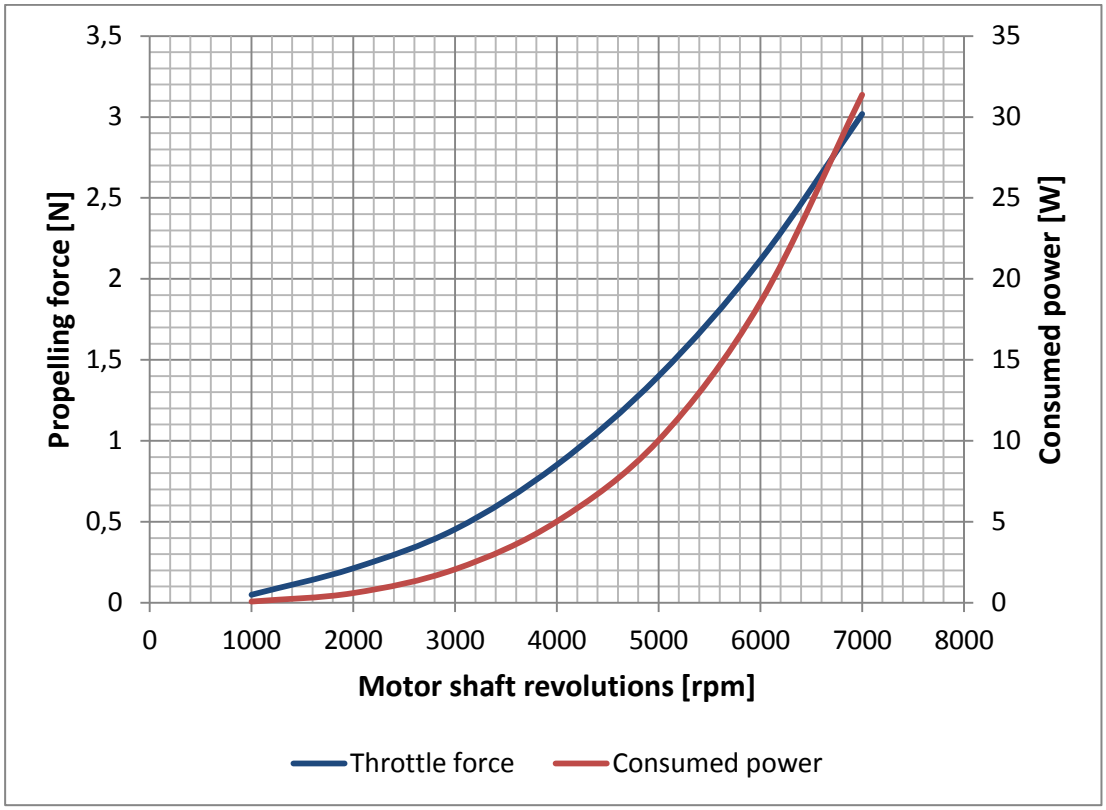

Fig. 23 – Estimated propelling force and consumed power of the propeller APC Slow Flyer (8x3.8)"

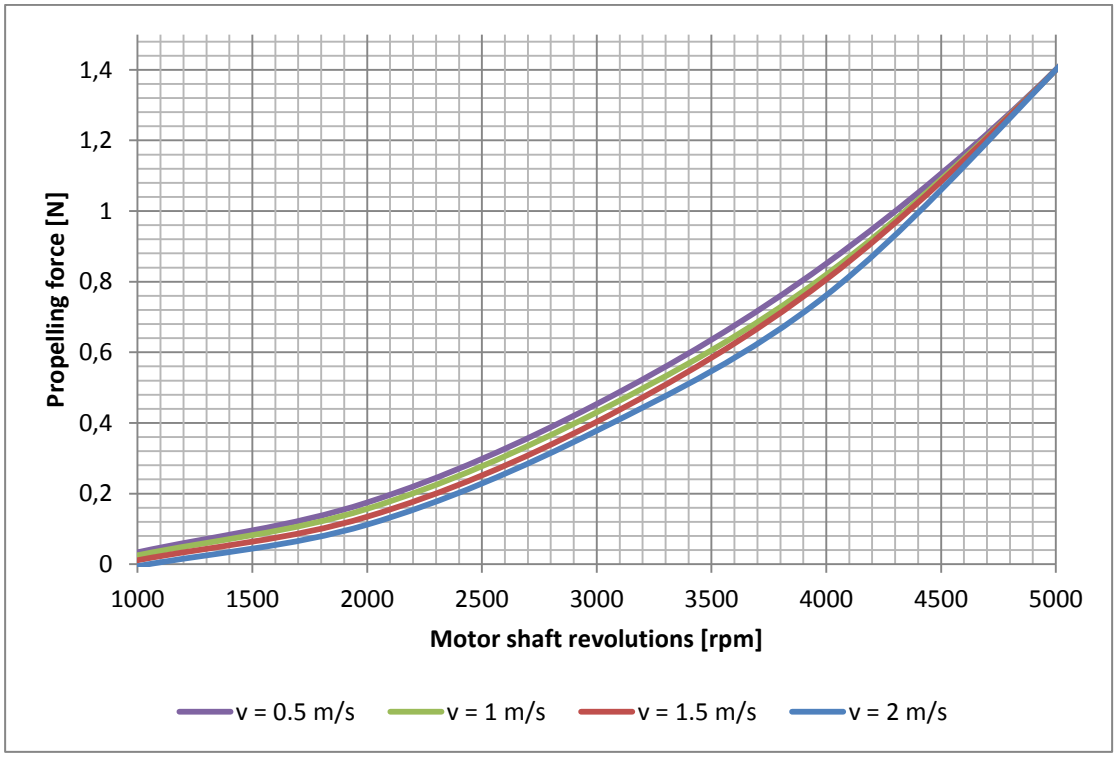

Fig. 24 – Propelling force at different airship velocities (propeller APC Slow Flyer (8x3.8)"

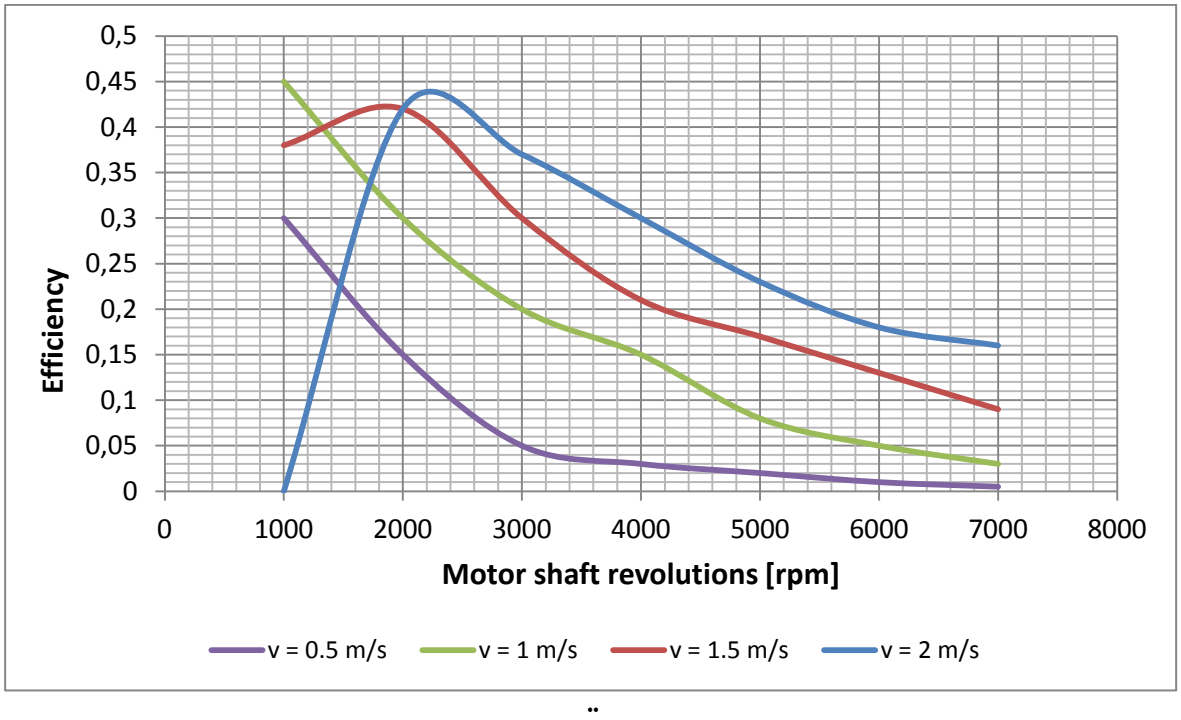

Fig. 25 - Propeller efficiency at different airship velocities and different motor shaft revolutions (propeller APC Slow Flyer (8x3.8)")

4.4 Airship's model

In order to discuss the controlling of the airship, its mathematical model must be known. This topic is well described in [46] and [50]. The main ideas are cited below.

Firstly, it is convenient to define two coordinate systems, one (stationary) referring to the ground and the second (moving) referring to the airship's centre of gravity. Let us consider the fixed coordinate system to be signed with the **w** sign while the airship's coordinate system is signed with the **a** sign. The transformation of the **a** system to the **w** system then can be done by rotating the airship around all three axes, x, y and z. The schematics description of the systems is depicted in Fig. 26. The matrixes of the airship's rotation are listed below:

$$\boldsymbol{R_x} = \begin{bmatrix} 1 & 0 & 0 \\ 0 & \cos(\phi) & -\sin(\phi) \\ 0 & \sin(\phi) & \cos(\phi) \end{bmatrix} \tag{32}$$

$$\boldsymbol{R_y} = \begin{bmatrix} \cos(\theta) & 0 & \sin(\theta) \\ 0 & 1 & 0 \\ -\sin(\theta) & 0 & \cos(\phi\theta) \end{bmatrix} \tag{33}$$

$$\boldsymbol{R_z} = \begin{bmatrix} \cos(\psi) & -\sin(\psi) & 0 \\ \sin(\psi) & \cos(\psi) & 0 \\ 0 & 0 & 1 \end{bmatrix} \tag{34}$$

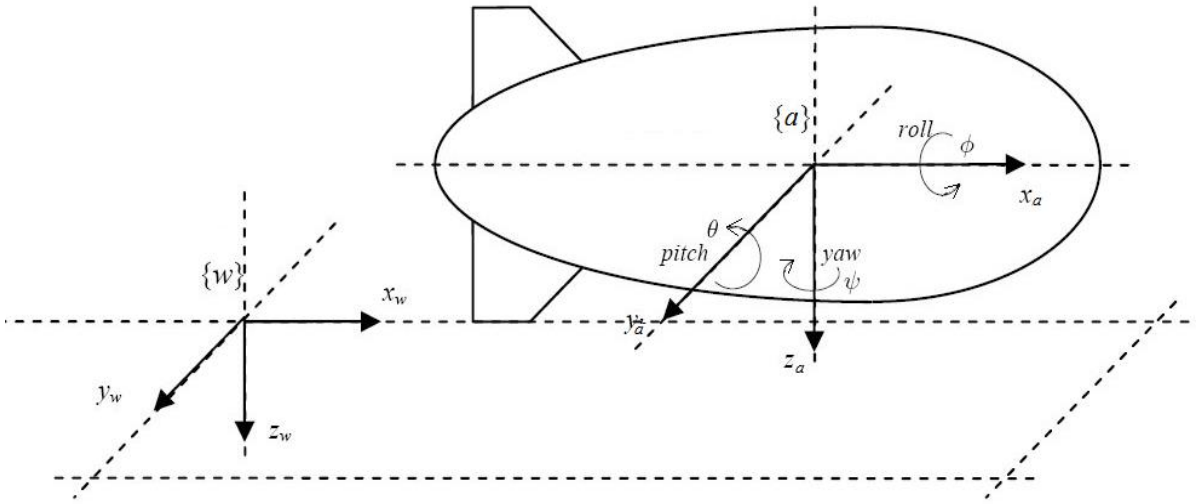

Fig. 26 – Schematic description of the coordinate systems used for the airship's trajectory description [50]

The matrix of rotation can be obtained as a product of the partial rotation matrixes (32), (33), (34):

$$\boldsymbol{R} = \boldsymbol{R_X} \cdot \boldsymbol{R_y} \cdot \boldsymbol{R_Z} \tag{35}$$

$$\boldsymbol{R} = \tag{36}$$
$$\begin{bmatrix} \cos(\psi)\cos(\theta) & -\sin(\psi)\cos(\theta) + \cos(\psi)\sin(\theta)\sin(\phi) & \sin(\psi)\sin(\theta) + \cos(\psi)\sin(\theta)\cos(\phi) \\ \sin(\psi)\cos(\theta) & \cos(\psi)\cos(\theta) + \sin(\psi)\sin(\theta)\sin(\phi) & -\cos(\psi)\sin(\theta) + \sin(\psi)\sin(\theta)\cos(\phi) \\ -\cos(\phi) & \cos(\psi)\sin(\phi) & \cos(\theta)\cos(\phi) \end{bmatrix}$$

In order to make the calculation more synoptic, the following vectors are introduced:

a) The $\vec{\imath}$ vector represents the coordinates of the airship according to the **w** coordinate system, where x, y and z are the appropriate coordinates:

$$\vec{\imath} = [x, y, z]^T \tag{37}$$

b) The $\vec{\vartheta}$ vector represents the airship's angles of rotation according to all axes of the **w** coordinate system, where ϕ, θ and ψ are the appropriate rotational angles:

$$\vec{\vartheta} = [\phi, \theta, \psi]^T \tag{38}$$

c) By connecting the (37) and (38) vectors into one vector $\vec{\varsigma}$ one obtains complete information on the position and rotation of the **a** coordinate system according to the **w** coordinate system:

$$\vec{\varsigma} = \left[\vec{\imath}^T, \vec{\vartheta}^T\right]^T \tag{39}$$

On the same principle the velocity vector $\vec{\varpi}$ can be obtained, including three components of sliding velocity and three components that determine the appropriate angular velocity:

$$\vec{v} = \left[v_x, v_y, v_z\right]^T \tag{40}$$

$$\vec{\xi} = \left[\omega_x, \omega_y, \omega_z\right]^T \tag{41}$$

$$\vec{\varpi} = \left[\vec{v}^T, \vec{\xi}^T\right]^T \tag{42}$$

Where:

$\vec{v}$ - vector of sliding velocities v_x, v_y and v_z, representing the velocity according to the x, y and z axes of the **w** coordinate system,

$\vec{\xi}$ - vector of angular velocities ω_x, ω_y and ω_z, representing the angular velocity of the airship's rotation according to the x, y and z axes of the **w** coordinate system.

In addition, for the mathematical description of the airship's movement one more matrix is needed, describing the transformation of the angular velocity from the airship's coordinate system **a** to the ground (world's) coordinate system **w**. This matrix is marked as $\mathbf{J_2}$ and its detailed description is included in [6]. The $\mathbf{J_2}$ matrix expression can be found below:

$$J_2^{-1}\left(\vec{\vartheta}\right) = \begin{bmatrix} 1 & 0 & -\sin(\theta) \\ 0 & \cos(\phi) & \sin(\phi)\cos(\theta) \\ 0 & -\sin(\phi) & \cos(\phi)\cos(\theta) \end{bmatrix} \tag{43}$$

$$J_2(\vec{\vartheta}) = \begin{bmatrix} 1 & \sin(\phi)\tan(\theta) & \cos(\phi)\tan(\theta) \\ 0 & \cos(\phi) & -\sin(\phi) \\ 0 & \dfrac{\sin(\phi)}{\cos(\theta)} & \dfrac{\cos(\phi)}{\cos(\theta)} \end{bmatrix} \tag{44}$$

Finally, the transformation between the vectors $\vec{\varsigma}$ and $\vec{\varpi}$ is as follows:

$$\begin{bmatrix} \dot{\vec{l}} \\ \dot{\vec{\vartheta}} \end{bmatrix} = \begin{bmatrix} \boldsymbol{R} & [\mathbf{0}]_{3x3} \\ [\mathbf{0}]_{3x3} & \boldsymbol{J_2}(\vec{\vartheta}) \end{bmatrix} \begin{bmatrix} \vec{v} \\ \vec{\xi} \end{bmatrix} \Leftrightarrow \dot{\vec{\xi}} = \boldsymbol{J}(\vec{\varsigma})\vec{\varpi} \tag{45}$$

In the coordinate system of the airship **a,** the dynamics of the airship can be described as follows:

$$(\boldsymbol{M}_{RB} + \boldsymbol{M}_{\boldsymbol{A}})(\dot{\vec{\varpi}}_a) + (\boldsymbol{C}_{RB} + \boldsymbol{C}_A)\vec{\varpi}_a + \boldsymbol{D}(\vec{\varpi}_a)\vec{\varpi}_a + \vec{g}(\vec{\varsigma}_a) = \vec{\tau}_b \tag{46}$$

Where:

$\mathbf{M}_{\mathrm{RB}}$	- mass weight matrix,
$\mathbf{M}_{\mathrm{A}}$	- additional weight matrix, caused by friction, propulsion, gravity etc.,
$\mathbf{C}_{\mathrm{RB}}$	- centripetal and Corliss's forces relative to the fixed point of a rigid body of the airship,
$\mathbf{C}_{\mathrm{A}}$	- centripetal and Corliss's forces relative to the additional weights,
$\boldsymbol{D}(\vec{\varpi}_a)$	- hydrodynamic damping force,
$\vec{g}(\vec{\varsigma}_a)$	- vector of reaction forces and moments respecting the gravity and the lift force generated by helium,
$\vec{\tau}_b$	- vector of propelling force and moment generated by the motors
$\vec{\varpi}_a$	- velocity vector recalculated to the **a** coordinate system,
$\vec{\varsigma}_a$	- position vector recalculated to the **a** coordinate system.

The model described by all above mentioned values is too complex to be processed further. In order to design the controlling algorithm , simplification of this model is necessary. According to [46] the following simplification is used so that the linear control theory can be applied.

The first step in the model simplifying consists in determining the point of operation at which the simplified model refers to the complex one. Not only must this be processed for the velocity but also for the position. The position of the point of operation can be expressed by means of the following vectors:

$$\vec{\varsigma}_0(t) = [x_0(t), y_0(t), z_0(t), \phi_0(t), \theta_0(t), \psi_0(t)] \tag{47}$$

$$\vec{\varpi}_0(t) = \left[v_{x0}(t), v_{y0}(t), v_{z0}(t), \omega_{x0}(t), \omega_{y0}(t), \omega_{z0}(t)\right] \tag{48}$$

The misalignment can then be described as:

$$\delta\vec{\varsigma}_0(t) = \vec{\varsigma}(t) - \vec{\varsigma}_0(t) \tag{49}$$

$$\delta\vec{\varpi}_0(t) = \vec{\varpi}(t) - \vec{\varpi}_0(t) \tag{50}$$

The expressions (47), (48), (49) and (50) can be utilized for the linearization of the expression (46). A substitution (47) described below is needed in order to replace the parameter $\vec{\varsigma}$.

$$\begin{aligned}(\boldsymbol{M}_{RB} + \boldsymbol{M}_A)\delta\dot{\vec{\varpi}} + \left.\frac{\partial(\boldsymbol{C}_{RB} + \boldsymbol{C}_A)\vec{\varpi}}{\partial\vec{\varpi}}\right|_{\vec{\varpi}_0} \delta\vec{\varpi} \\ + \left.\frac{\partial \boldsymbol{D}(\vec{\varpi})\vec{\varpi}}{\partial\vec{\varpi}}\right|_{\vec{\varpi}_0} \delta\vec{\varpi} + \left.\frac{\partial\vec{g}(\vec{\varsigma})}{\partial\vec{\varsigma}}\right|_{\vec{\varsigma}_0} \delta\vec{\varsigma} = \vec{\tau}\end{aligned} \tag{51}$$

$$\begin{aligned}\dot{\vec{\zeta}} + \delta\dot{\vec{\zeta}} &= \boldsymbol{J}(\zeta_0 + \delta\zeta)(\varpi_0 + \delta\varpi) \\ \delta\dot{\vec{\zeta}} &= \boldsymbol{J}(\zeta_0 + \delta\zeta)(\varpi_0 + \delta\varpi) - \boldsymbol{J}(\zeta_0)\varpi_0 \\ \delta\dot{\vec{\zeta}} &= \boldsymbol{J}(\zeta_0 + \delta\zeta)\delta\varpi + \big(\boldsymbol{J}(\zeta_0 + \delta\zeta) - \boldsymbol{J}(\zeta_0)\big)\varpi_0 \\ \delta\dot{\vec{\zeta}} &\approx \boldsymbol{J}(\zeta_0)\delta\varpi + \big(\boldsymbol{J}(\zeta_0 + \delta\zeta) - \boldsymbol{J}(\zeta_0)\big)\varpi_0\end{aligned} \tag{52}$$

For the equation (51) the following states can be defined:

$$\vec{x}_1 = \delta\varpi \tag{53}$$

$$\vec{x}_2 = \delta\zeta \tag{54}$$

$$\boldsymbol{B}\vec{\chi} = \vec{\tau} \tag{55}$$

Then the equation (51) can further be rewritten as follows:

$$\boldsymbol{M}\dot{\vec{x}}_1 + \boldsymbol{C}(t)\vec{x}_1 + \boldsymbol{D}(t)\vec{x}_1 + \boldsymbol{G}(t)\vec{x}_2 = \boldsymbol{B}\vec{\chi} \tag{56}$$

$$\dot{\vec{x}}_2 = \boldsymbol{J}(t)\vec{x}_1 + \boldsymbol{J}^*(t)\vec{x}_2 \tag{57}$$

The description of the matrixes applied above is as follows:

$$\boldsymbol{M} = \boldsymbol{M}_{RB} + \boldsymbol{M}_A \tag{58}$$

$$\boldsymbol{C}(t) = \boldsymbol{C}_{RB}(t) + \boldsymbol{C}_A(t) = \left.\frac{\partial \boldsymbol{C}(\vec{\varpi})\vec{\varpi}}{\partial \vec{\varpi}}\right|_{\vec{\varpi}_0(t)} \tag{59}$$

$$\boldsymbol{D}(t) = \left.\frac{\partial \boldsymbol{D}(\vec{\varpi})\vec{\varpi}}{\partial \vec{\varpi}}\right|_{\vec{\varpi}_0(t)} \tag{60}$$

$$\boldsymbol{G}(t) = \left.\frac{\partial \vec{g}(\vec{\zeta})\vec{\zeta}}{\partial \vec{\zeta}}\right|_{\vec{\zeta}_0(t)} \tag{61}$$

$$\boldsymbol{J}(t) = \boldsymbol{J}\left(\vec{\zeta}_0(t)\right) \tag{62}$$

$$\boldsymbol{J}^*(t) = \boldsymbol{J}\left(\vec{\zeta}_0(t) + \delta\vec{\zeta}(t)\right) - \boldsymbol{J}\vec{\zeta}_0(t) \tag{63}$$

The matrix **B** and the vector $\vec{\chi}$ are related to the propelling force generated by the motors and described below. Generally, **B** is dependent on the tilting angle of the motors and $\vec{\chi}$ is the vector representing propelling forces generated by the motors of the airship.

Finally, the following set of simplified equations can be created in order to describe the dynamics of the airship:

$$\begin{bmatrix} \boldsymbol{M}\dot{\vec{x}}_1 \\ \dot{\vec{x}}_2 \end{bmatrix} = \begin{bmatrix} -\left(\boldsymbol{C}(t) + \boldsymbol{D}(t)\right) & -\boldsymbol{G}(t) \\ \boldsymbol{J}(t) & \boldsymbol{J}^*(t) \end{bmatrix} \tag{64}$$

$$\begin{bmatrix} \dot{\vec{x}}_1 \\ \dot{\vec{x}}_2 \end{bmatrix} = \begin{bmatrix} -\dfrac{\left(\boldsymbol{C}(t) + \boldsymbol{D}(t)\right)}{\boldsymbol{M}} & -\dfrac{\boldsymbol{G}(t)}{\boldsymbol{M}} \\ \boldsymbol{J}(t) & \boldsymbol{J}^*(t) \end{bmatrix} \begin{bmatrix} \vec{x}_1 \\ \vec{x}_2 \end{bmatrix} + \begin{bmatrix} \dfrac{\boldsymbol{B}}{\boldsymbol{M}} \\ 0 \end{bmatrix} \vec{\chi} \Leftrightarrow \dot{\vec{x}} = \boldsymbol{A}\vec{x} + \boldsymbol{B}'\vec{u} \tag{65}$$

The evaluation of the above mentioned matrixes can be processed in a simple way provided the following assumptions are made:

- the airship moves very slowly and if it is in a steady state, its velocity can be supposed to be zero,
- the angles of inclination ϕ and θ are approximately equal to zero because the propelling and other forces are not strong enough to get the airship into a tilted position,
- provided the airship's velocity is close to zero, the Coriolis force is supposed to be zero. Therefore:

$$\boldsymbol{C}(\varpi)\varpi = 0 \tag{66}$$

Under the assumptions described above, according to [46] the matrixes utilized in the above listed equations can be expressed as follows:

$$\boldsymbol{M} = \begin{bmatrix} m + a_{11} & 0 & 0 & 0 & mz_g & 0 \\ 0 & m + a_{22} & 0 & -mz_g & 0 & mx_g \\ 0 & 0 & m + a_{33} & 0 & -mx_g & 0 \\ 0 & -mz_g & 0 & I_{xx} + a_{44} & 0 & 0 \\ mz_g & 0 & -mx_g & 0 & I_{yy} + a_{55} & 0 \\ 0 & mx_g & 0 & 0 & 0 & I_{zz} + a_{66} \end{bmatrix} \quad (67)$$

Where:

a) x_g and z_g are members of the vector $\vec{\varepsilon}$ that represents the position of the centre of gravity according to the coordinate system **a**. As the airship is symmetrical and also the mass displacement in its gondola is supposed to be symmetrical, the y_g can be considered to be zero.

$$\vec{\varepsilon} = (x_g, y_g, z_g) \quad (68)$$

b) m is the mass weight at the centre of gravity,

c) I_{xx}, I_{yy} and I_{zz} are members of the matrix of inertial coefficients $\mathbf{I}_a$, relevant to the coordinate system **a** [46]:

$$I_a \approx \begin{bmatrix} I_{xx} & 0 & 0 \\ 0 & I_{yy} & 0 \\ 0 & 0 & I_{zz} \end{bmatrix} \quad (69)$$

d) a_{11} to a_{66} are the members of the matrix $\mathbf{M}_{A,}$ considering additional weight generated by friction forces, propulsion, gravity etc. As the airship is considered to move slowly and to be symmetrical according to axes of its coordinate system, it can be assumed that only those coefficients that lie on the diagonal of the matrix will affect the airship while the others can be neglected [50]. Therefore:

$$\boldsymbol{M}_A = diag(a_{11}, a_{22}, a_{33}, a_{44}, a_{55}, a_{66}) \quad (70)$$

The next matrix is marked **D** and describes the hydrodynamic damping forces. According to [46] the friction between the airship's coating and the air can be described accurately enough if the second order polynomial is utilized while the higher orders are neglected. When creating the simplified model, the coefficients listed in the matrix can further be reduced to constants, assuming the airship's velocity is close to zero [46]:

$$\boldsymbol{D} \approx \begin{bmatrix} D_{v_x} & 0 & 0 & 0 & 0 & 0 \\ 0 & D_{v_y} & 0 & 0 & 0 & 0 \\ 0 & 0 & D_{v_z} & 0 & 0 & 0 \\ 0 & 0 & 0 & D_{\omega_x} & 0 & 0 \\ 0 & 0 & 0 & 0 & D_{\omega_y} & 0 \\ 0 & 0 & 0 & 0 & 0 & D_{\omega_z} \end{bmatrix} \tag{71}$$

According to (61) the matrix **G** is created according to the vector of reaction forces and moments respecting the gravity and the lift force generated by helium $\vec{g}(\vec{\varsigma}_a)$. Provided the airship is well balanced and without additional external forces it does not increase or decrease its elevation and provided $y_g = 0$ (see (68)), according to [46], the $\vec{g}(\vec{\varsigma}_a)$ vector can be described as follows:

$$\vec{g}(\vec{\varsigma}_a) = \begin{bmatrix} 0 \\ 0 \\ 0 \\ -mg\cos(\theta)\sin(\phi)y_g + mg\cos(\theta)\sin(\phi)z_g \\ mg\sin(\theta)\,z_g + mg\cdot\cos(\theta)\cos(\phi)x_g \\ mg\cdot\cos(\theta)\sin(\phi)x_g - mg\cdot\sin(\theta)\,y_g \end{bmatrix}$$

$$= \begin{bmatrix} 0 \\ 0 \\ 0 \\ mg\cos(\theta)\sin(\phi)z_g \\ mg\sin(\theta)\,z_g + mg\cdot\cos(\theta)\cos(\phi)x_g \\ mg\cdot\cos(\theta)\sin(\phi)x_g \end{bmatrix} \tag{72}$$

According to (61) the **G** matrix can be evaluated as follows:

$$\boldsymbol{G} = \begin{bmatrix} 0 & 0 & 0 & 0 & 0 & 0 \\ 0 & 0 & 0 & 0 & 0 & 0 \\ 0 & 0 & 0 & 0 & 0 & 0 \\ 0 & 0 & 0 & z_g mg & 0 & 0 \\ 0 & 0 & 0 & 0 & z_g mg & 0 \\ 0 & 0 & 0 & -x_g mg & 0 & 0 \end{bmatrix} \tag{73}$$

Where:

m - the mass weight at the centre of gravity,

x_g, z_g - are members of the vector $\vec{\varepsilon}$ that represents the position of the centre of gravity according to the coordinate system **a,**

g - gravitational acceleration.

J is the transformation matrix obtained in (45). According to [50], it can be simplified and expressed as follows:

$$\boldsymbol{J} = \begin{bmatrix} \cos\psi_0 & -\sin\psi_0 & 0 & 0 & 0 & 0 \\ \sin\psi_0 & \cos\psi_0 & 0 & 0 & 0 & 0 \\ 0 & 0 & 1 & 1 & 1 & 1 \\ 0 & 0 & 1 & 1 & 1 & 1 \\ 0 & 0 & 1 & 1 & 1 & 1 \\ 0 & 0 & 1 & 1 & 1 & 1 \end{bmatrix} \tag{74}$$

The model description obtained above can be divided into two following cases that can be solved separately:

- motion in the xz plane (moving forward and elevation),
- rotation with respect to the z axis (yawn).

In fact, the separated solutions can only be obtained under simplifications and assumptions provided above. If the **C** matrix was not neglected, both motions would be non-linearly tied together.

4.4.1 Deployment of the forces in the airship's coordinate system

In Fig. 27 a diagram shows how the forces impacting the airship are deployed according to its coordinate system **a**. Because various forces are affecting the airship in various spots, moments that tend to tilt the airship are being generated.

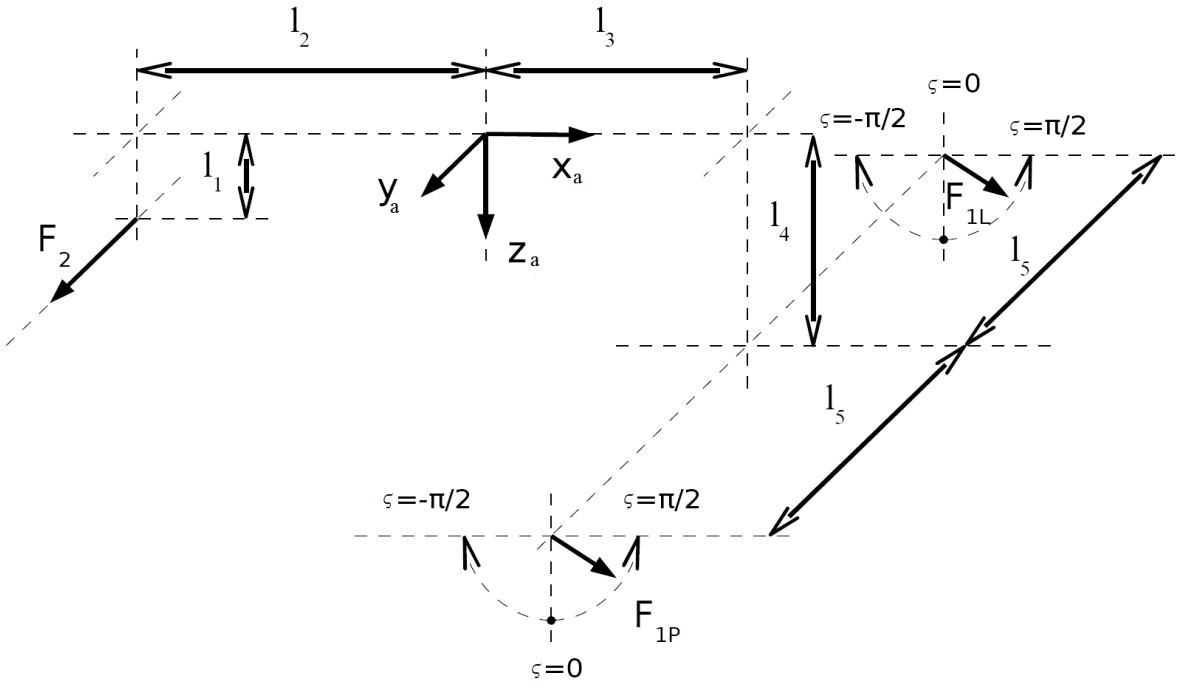

Fig. 27 – Forces deployment in the coordinate system of the airship [46]

The forces, angles and dimensions depicted in Fig. 27 are as follows:

l_1 - distance between the airship's centre of gravity (the x component) to the tail motor,

l_2 - distance between the airship's centre of gravity (the z component) to the tail motor,

l_3 - distance between the airship's centre of gravity (the x component) to the main motors,

l_4 - distance between the airship's centre of gravity (the z component) to the main motors,

l_5 - distance between the airship's centre of gravity (the y component) to the main motors,

F_{1P} - propelling force developed by the right motor,

F_{1L} - propelling force developed by the left motor,

F_2 - propelling force developed by the tail motor,

ς - angle of the motors swivelling.

The vector of forces and moments $\vec{\tau}_b$ utilized in (46) and the further equations consists of the following forces and moments in all axes:

$$\vec{\tau}_b = \left[F_x, F_y, F_z, M_x, M_y, M_z\right] \tag{75}$$

According to Fig. 27 and considering the symmetries of the airship, the following equations can be assumed to describe the members of the vector $\vec{\tau}_b$:

$$F_x = (F_{1P} + F_{1L}) \sin \varsigma \tag{76}$$

$$F_y = F_2 \tag{77}$$

$$F_z = (F_{1P} + F_{1L}) \cos \varsigma \tag{78}$$

$$M_x = -F_y l_1 \tag{79}$$

$$M_y = -F_z l_3 + F_x l_4 \tag{80}$$

$$M_z = F_y l_2 \tag{81}$$

4.4.2 Linearized and simplified model of the airship's rotation

When rotating, the airship makes a turn around its z_a axis. This situation is depicted in Fig. 28.

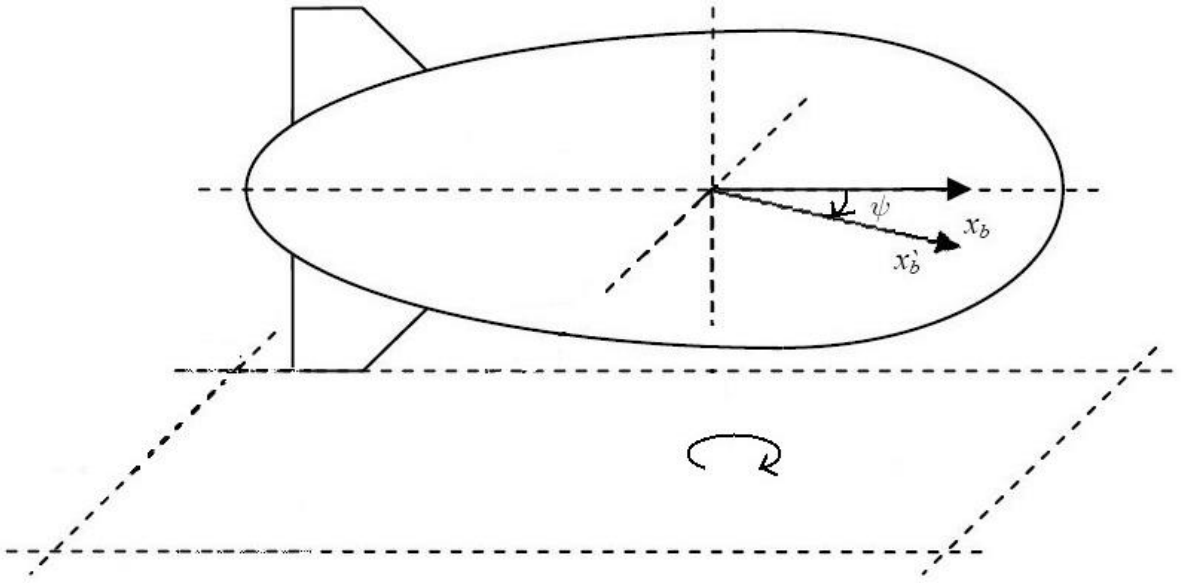

Fig. 28 – Representation of the rotational motion of the airship [50]

From the previously presented simplified model only those variables, which are relevant to this movement, are considered. In this case the state variables are as follows:

$$\vec{x}(t) = \left[v_y(t), \omega_x(t), \omega_z(t), y(t), \phi(t), \psi(t)\right]^T \tag{82}$$

The propulsion is obtained only by the force developed by the tail motor, therefore:

$$\vec{u} = F_2 \tag{83}$$

According to [50], [46], the following state equations are to be applied:

$$\frac{d\vec{x}}{dx} = \begin{bmatrix} -\boldsymbol{M^{-1}D} & -\boldsymbol{M^{-1}G} \\ J & \boldsymbol{[0]_{3x3}} \end{bmatrix} \vec{x} + \begin{bmatrix} \boldsymbol{M^{-1}B} \\ \boldsymbol{[0]_{3x1}} \end{bmatrix} u \tag{84}$$

In (84) the relevant matrixes $\mathbf{M}_{xy}$, $\mathbf{D}_{xy}$, $\mathbf{G}_{xy}$ and $\mathbf{J}_{xy}$ are to be applied. They are gained by picking the relevant members from the matrixes **M**, **D**, **G** and **J**. The matrix $\mathbf{B}_{xy}$ is given by the position of the tail motor according to the centre of the airship's coordinate system **a**. The appropriate matrixes are as follows:

$$\boldsymbol{M_{xy}} = \begin{bmatrix} m + a_{22} & -mz_g & mx_g \\ -mz_g & I_{xx} + a_{44} & 0 \\ mx_g & 0 & I_{zz} + a_{66} \end{bmatrix} \tag{85}$$

$$\boldsymbol{D_{xy}} = \begin{bmatrix} D_{v_y} & 0 & 0 \\ 0 & D_{\omega_y} & 0 \\ 0 & 0 & D_{\omega_y} \end{bmatrix} \tag{86}$$

$$\boldsymbol{G_{xy}} = \begin{bmatrix} 0 & 0 & 0 \\ 0 & z_g mg & 0 \\ 0 & -x_g mg & 0 \end{bmatrix} \tag{87}$$

$$\boldsymbol{J_{xy}} = \begin{bmatrix} \sin\psi_0 & \cos\psi_0 & 0 \\ 0 & 1 & 0 \\ 0 & 0 & 1 \end{bmatrix} \tag{88}$$

$$\boldsymbol{B_{xy}} = \begin{bmatrix} 1 \\ l_1 \\ -l_2 \end{bmatrix} \tag{89}$$

4.4.3 Linearized and simplified model of the airship propulsion in forward direction

This subchapter describes a simplified model and examines the effects of the main propellers on the airship's movement. The airship is in this case moved within the XZ plane and the propelling force is generated by two propellers (see (92)). In addition, propelling force can be split into two components, one acting in the x-direction and the other acting in the z-direction. The ratio of these two components depends on the swivel angle of the propellers. Therefore, there are two control variables and six state variables:

$$\vec{x}(t) = \left[v_x(t), v_z(t), \omega_y(t), x(t), z(t), \theta(t)\right]^T \tag{90}$$

$$u = [F_x, F_z]^T \tag{91}$$

$$F_1 = F_{1L} + F_{1P};\ F_{1L} \cong F_{1P} \tag{92}$$

$$F_x = F_1 \sin\alpha \tag{93}$$

$$F_z = F_1 \cos\alpha \tag{94}$$

Where:
F_1 - total propelling force [N],
F_{1L} - propelling force generated by the left propeller [N],
F_{1R} - propelling force generated by the right propeller [N],
F_x - total propelling force acting in x-dimension [N],
F_z - total propelling force acting in z-dimension [N],
α - swivelling angle of the propellers [°] relative to the x-dimension.

The state equations describing the system in this case are as follows:

$$\frac{d\vec{x}(t)}{dt} = \begin{bmatrix} -M^{-1}D & -M^{-1}G \\ J & [0]_{3x3} \end{bmatrix} \vec{x}(t) + \begin{bmatrix} M^{-1}B \\ [0]_{3x2} \end{bmatrix} \vec{u} \tag{95}$$

In (95) the relevant matrixes $\mathbf{M}_{rot}$, $\mathbf{D}_{rot}$, $\mathbf{G}_{rot}$ and $\mathbf{J}_{rot}$ are to be applied. They are gained by picking the relevant members from the matrixes **M**, **D**, **G** and **J**. The matrix $\mathbf{B}_{rot}$ is given by the position of the tail motor according to the centre of the airship's coordinate system **a**. The appropriate matrixes are as follows:

$$\boldsymbol{M}_{xz} = \begin{bmatrix} m + a_{11} & 0 & mz_y \\ 0 & m + a_{33} & -mx_g \\ mz_g & -mx_g & I_{yy} + a_{55} \end{bmatrix} \tag{96}$$

$$\boldsymbol{D}_{xz} = \begin{bmatrix} D_{v_x} & 0 & 0 \\ 0 & D_{v_y} & 0 \\ 0 & 0 & D_{\omega_y} \end{bmatrix} \tag{97}$$

$$\boldsymbol{G}_{xz} = \begin{bmatrix} 0 & 0 & 0 \\ 0 & 0 & 0 \\ 0 & 0 & z_g mg \end{bmatrix} \tag{98}$$

$$\boldsymbol{J}_{xz} = \begin{bmatrix} \cos\psi_0 & -\sin\psi_0 & 0 \\ 0 & 1 & 0 \\ 0 & 0 & 1 \end{bmatrix} \tag{99}$$

$$\boldsymbol{B}_{xz} = \begin{bmatrix} 1 & 0 \\ 0 & 1 \\ l_4 & l_3 \end{bmatrix} \tag{100}$$

Moreover, in this case the following effects are necessary to be considered:

- The centre of gravity is deflected in the x-direction of the **a** coordinate system.
- There is a slight rotation of the **a** coordinate system due to the **w** coordinate system.

These effects can be described in the matrix (99), which should be considered as follows:

$$\boldsymbol{J}_{rot_{xz}} = \begin{bmatrix} \cos\psi_0 & -\sin\psi_0 & 0 \\ \sin\Theta_0 & \cos\Theta_0 & 0 \\ 0 & 0 & 1 \end{bmatrix} \tag{101}$$

4.4.4 Airship's behaviour modelling

The dynamic behaviour of the airship has been modelled according to the procedure described in [46]. As the construction of the airship is similar to the one described in [46] and so are dimensions, the same procedure of creating the simple state-space model in Matlab Simulink was applied as in [47]. The set of equations and parameters is given below in this subchapter. Approximations described in [46] were applied.

In order to evaluate the airship's parameters, the following equations must be applied:

$$e = 1 - \left(\frac{b}{a}\right)^2 \tag{102}$$

$$\alpha_0 = \frac{2(1-e^2)}{e^3}\left(\frac{1}{2}ln\left(\frac{1+e}{1-e}\right) - e\right) \tag{103}$$

$$\beta_0 = \frac{1}{e^2} - \frac{1-e^2}{2e^3}ln\left(\frac{1+e}{1-e}\right) \tag{104}$$

$$m_{He} = \frac{4}{3}\pi\rho_{He}ab^2 \tag{105}$$

$$a_{11} = \frac{\alpha_0}{2-\alpha_0}m \tag{106}$$

$$a_{22} = a_{33} = \frac{\beta_0}{2-\beta_0}m \tag{107}$$

$$a_{44} = 0 \tag{108}$$

$$a_{55} = a_{66} = \frac{1}{5}\frac{(b^2-a^2)^2(\alpha_0-\beta_0)}{2(b^2-a^2)+(b^2-a^2)(\beta_0-\alpha_0)}m \tag{109}$$

$$I_{yy} = I_{zz} = \frac{4}{15}\pi\rho_{He}ab^2\,(a^2+b^2) \tag{110}$$

$$I_{xx} = \frac{8}{15}\,\pi\rho_{He}ab^4 \tag{111}$$

$$D_{v_x} \approx \frac{F_x}{v_x} \tag{112}$$

$$D_{v_y} \approx \frac{F_y}{v_y} \tag{113}$$

$$D_{v_z} \approx \frac{F_z}{v_z} \tag{114}$$

$$D_{\omega_x} \approx \frac{M_x}{v_x} \tag{115}$$

$$D_{\omega_y} \approx \frac{M_y}{v_y} \tag{116}$$

$$D_{\omega_z} \approx \frac{M_z}{v_z} \tag{117}$$

Where:

a - length of the major ellipsoid semi-axis [m],
b - length of the minor ellipsoid semi-axis [m],
m_{He} - helium gas weight [kg],
m - total bladder weight [kg],
ρ_{He} - helium density [kg/m^3].

The above mentioned parameters were applied to the dynamic behaviour modelling that is described in the Experimental part of this paper.

4.5 Electrical components

Several electrical components were used during the Autonomous monitoring system's electrical blocks development. Description of all the components exceeds the scope of this paper. Therefore, only a brief description of the most important components and solutions is described in this chapter.

4.5.1 Microcontroller

The final design of the Autonomous monitoring system is intended to be based on a central processing unit that ensures overall controlling of the system. Based on the previous experience, the microcontroller Freescale MC9S08SE8 encapsulated in 28-Pin PDIP case has been chosen for this purpose.

The microcontroller employs 8 bit Motorola HCS08 core operating at 20 MHz. The instruction set of HC08 is retained only with slight extensions. The microcontroller provides up to 8 kB of on-chip programmable flash memory with block protection and up to 512 B of on-chip RAM. Its block diagram as well as configuration of its peripherals are provided in Fig. 29.

A more detailed description of the microcontroller can be found in the pertinent datasheets provided by its manufacturer, e.g. [29].

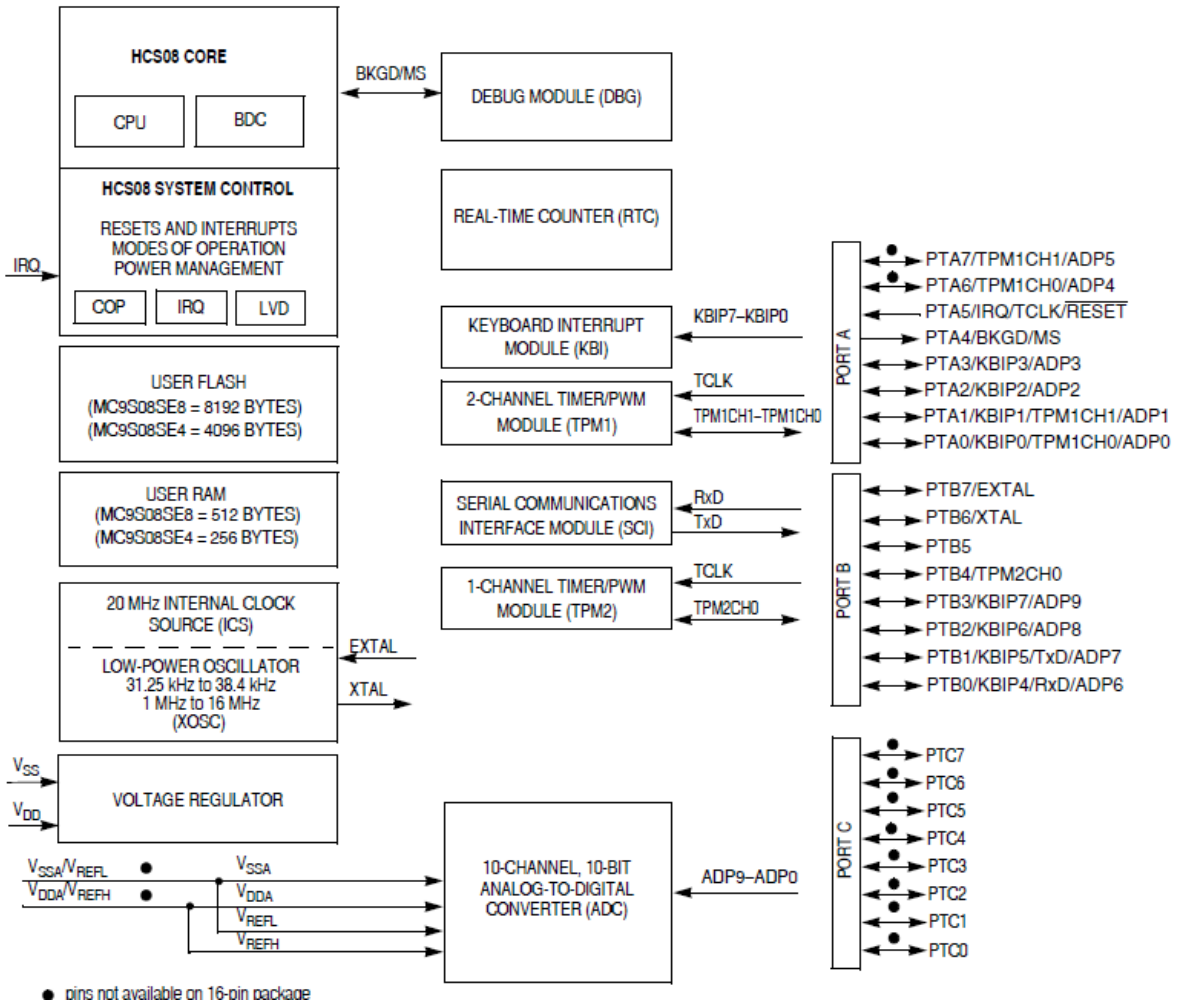

Fig. 29 – Block diagram of Freescale MC9S08SE8 microcontroller [29]

4.5.2 RFID reader

For the purposes of the RFID tags detection, AS3910 RFID reader is intended to be used. Out of all contacted manufacturers, only Austria Microsystems producing the AS3910, was capable of delivering several sample chips for testing purposes.

The AS3910 is a high performance 13.56MHz HF RFID Reader IC. It contains 2 differential low impedance antenna drivers. Without external booster it enables to drive the antenna with the power of up to 1 W that ensures the readability of the pertinent RFID tags from the distances of approximately 1 meter. The communication with the microcontroller is enabled by means of a standard SPI bus.

According to [40], the main features of this integrated circuit are as follows:

- Close loop adjustment of ASK modulation for accurate control of modulation depth in case of ISO-14443B protocol,
- Antenna trimming system providing correction range of LC,

- Low power operating mode reduces receiver consumption from 10mA to 5mA,
- Low power (3.5μA) NFC target mode,
- Integrated regulators to boost system PSRR,
- AM/PM demodulator to eliminate communication holes,
- RSSI measurement,
- Accurate RF envelope measurement (8 bit A/D),
- High output power at 3.3V power supply:
  - up to 1W in case regulator is externally shorted,
  - up to 500mW in case differential output and antenna trimming is used,
  - up to 125mW in case of single ended output and antenna trimming is used,
- Squelch feature which performs gain reduction to compensate the noise generated by transponder processing,
- User selectable and automatic gain control,
- Transparent mode to implement other standard and custom protocols (ISO-15693, Felica, ….),
- Quartz oscillator capable of operating with 13.56MHz or 27.12MHz crystal with fast start-up,
- Additional A/D converter input, Serial peripheral interface (SPI) with 32 byte FIFO,
- Supply voltage range from 2.4V to 3.6V,
- Wide temperature range: -40ºC to 85ºC,
- QFN 32 5x5 package.

The QFN package is the most definite disadvantage of the circuit because it makes the hand-made small batch production quite difficult. Unfortunately, in the time period in which the RFID reader design has been processed no other manufacturers capable of delivering small samples of integrated circuits were available.

The block diagram of the RFID reader chip is depicted in Fig. 30. The minimum configuration with differential antenna driving recommended by the manufacturer of the chip is depicted in Fig. 31.

A detailed description of the AS3910 RFID reader is provided in the pertinent datasheet [40].

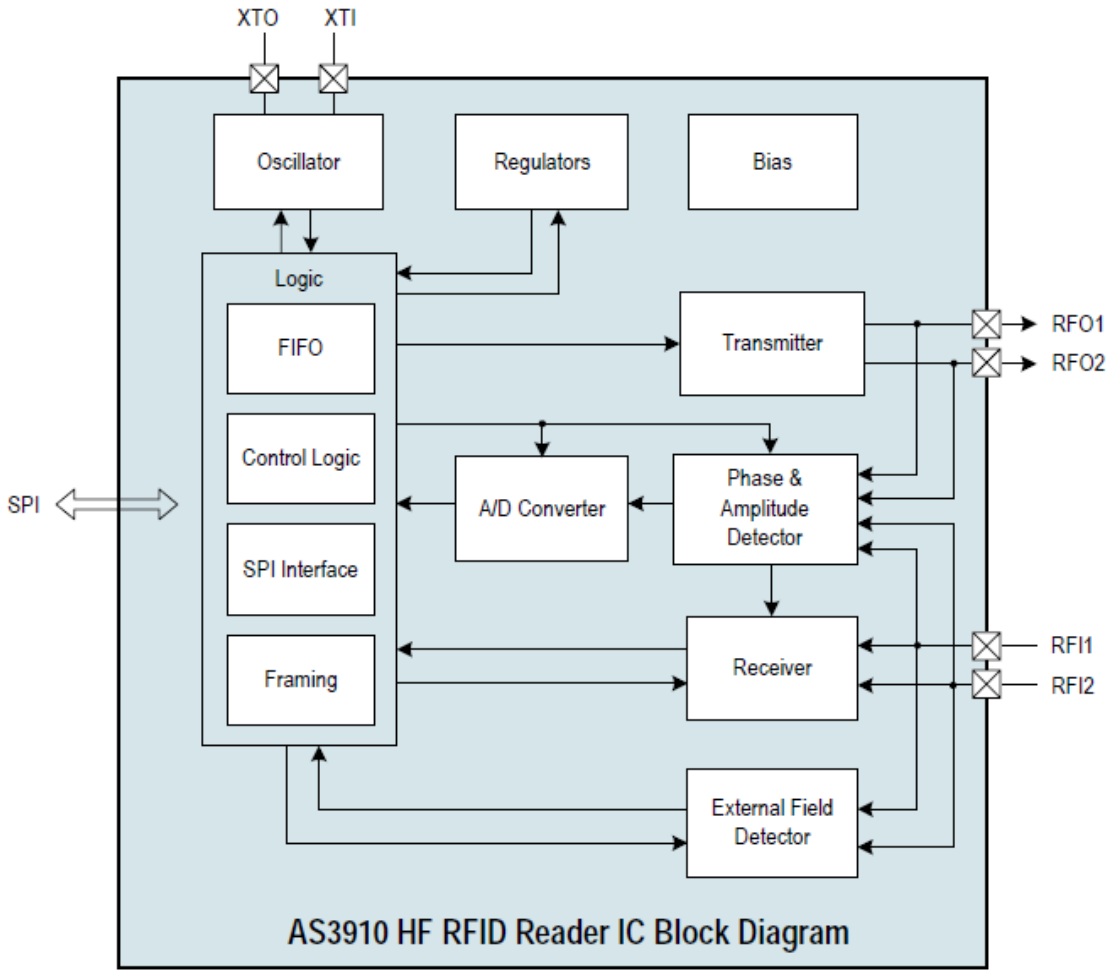

Fig. 30 – AS3910 internal components' block diagram [40]

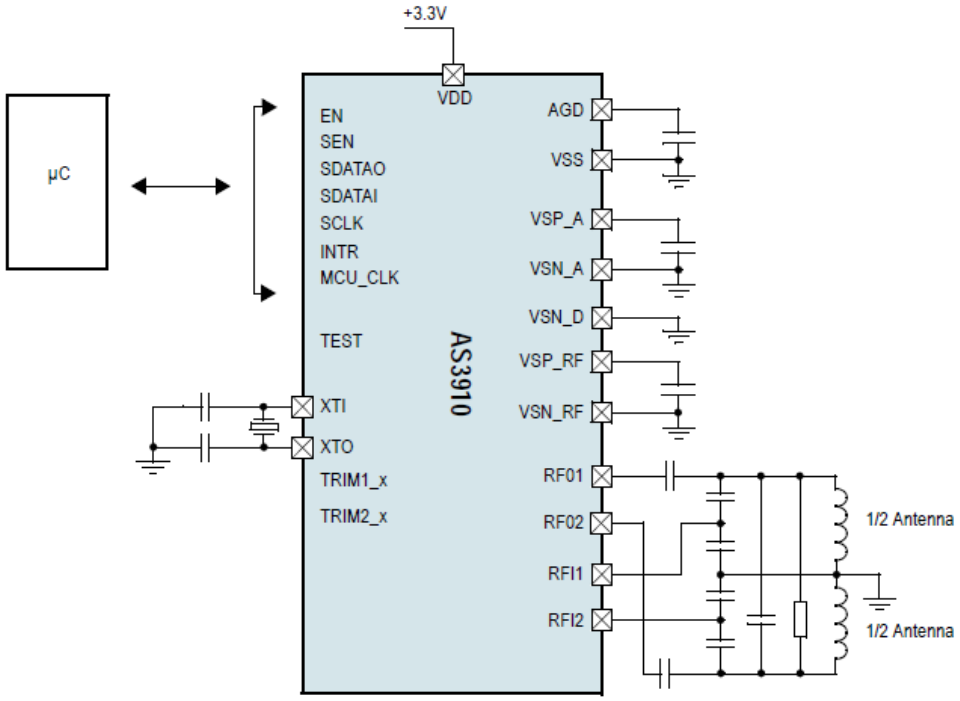

Fig. 31 – Minimum configuration of AS3910 with differential antenna driving [40]

4.5.3 Switching mode power supply source driver

As the components of the Autonomous monitoring system require different supply voltages, switching voltage converters are intended to be used, reflecting the effort to minimize the power losses in the circuitry.

From the available drivers LT1172 chips have been chosen for their parameters, especially for their possibility to be synchronized by an external clock source. All the voltage converters are intended to be used in SEPIC topology that enables easy shut down of their power outputs by simple hibernation of their oscillators.

Internal blocks of LT1172 are depicted in Fig. 32. A detailed description can be found in the appropriate datasheet [43].

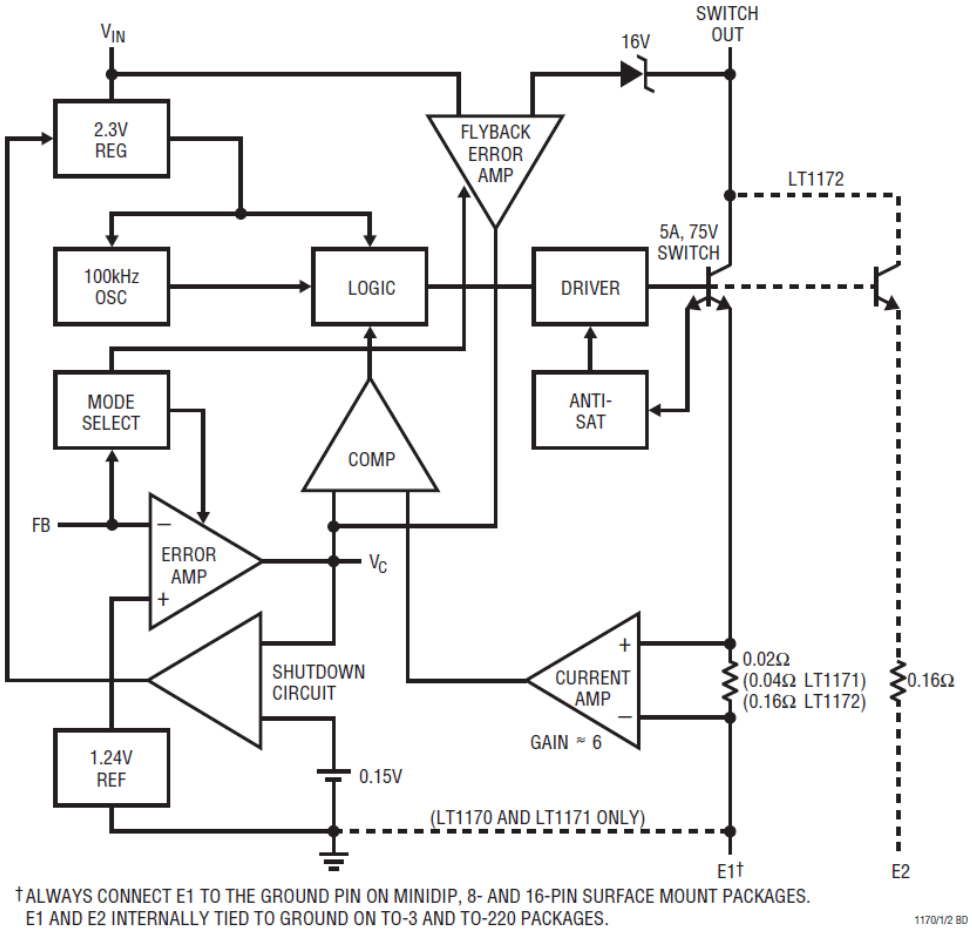

Fig. 32 – LT1172 internal blocks [43]

5 EXPERIMENTAL PART

When the design of the Autonomous monitoring system was processed, it was necessary to divide the project into two parts:

- hardware design,
- airship's motion modelling.

Both parts are described within the framework of this chapter. Design of controlling software was not processed within the framework of this thesis.

5.1 Minor hardware modules

The hardware design considers integration of all necessary functional blocks on one printed circuit board (PCB) that includes one microcontroller powerful enough to control the whole system. In order to simplify the development of the functional blocks, several independent hardware modules were developed so that their proper function could have been tested independently. There was an individual microcontroller employed for each of them. On the basis of the experience gained with these modules, the final hardware design of the Autonomous monitoring system circuitry was processed.

5.1.1 Module for communication with the ground station

The need for transferring data to the Autonomous monitoring system and back resulted in the development of the module that ensures connection with a ground station by means of the local data network. As the Autonomous monitoring system is supposed to be operated in enclosed areas and these areas are expected to be covered with wirelesses local LAN, it was decided to implement the whole communication on the WiFi basis. Therefore, the Autonomous monitoring system is expected to be equipped with a conventional WiFi router that allows its connection to the local data network in which the server of the ground station is expected to be implemented.

Owing to the complexity of the wireless router design, development of the individual router is not worth trying. Instead, standard WiFi router, IP camera and IP relay "Charon" were used to create this module. The IP camera provides image capture and its transmitting into the data network. The IP relay acts as a terminal IP device that is capable of identifying commands emitted by a web application running on the ground server. The output of the IP relay is represented by 8 bit TTL parallel signal output. This enables sending the controlling commands to the Autonomous monitoring system via the web interface running on the local server.

Due to the limited load capacity of the airship the weight of all components is crucial. Therefore, all components covers were removed and the total weight of the components was checked. All the components are designed as "All-on board", thus their PCBs can be used as separated parts. The weights of the components are listed in Tab. 1.

The block diagram of the Module for communication with the ground station is depicted in Fig. 33.

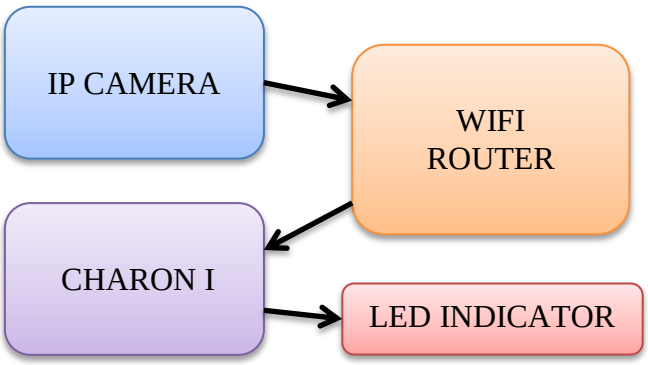

Fig. 33 - Module for communication with the ground station block diagram

Table 1 – Module for communication with the ground station components weight

Component	**Weight – covered**	**Weight - uncovered**
WiFi Router	317 g	146 g
IP Camera	237 g	54 g
Charon I	-	12 g
TOTAL	566 g	212 g

The IP Camera D-Link DCS 910 and the WiFi router Edimax BR-6304Wg were chosen for their low weight and the possibility of removing their plastic covers. According to Table 1 it is obvious that removal of plastic parts decreased the weight of the whole module significantly. The weight of the IP relay Charon I is negligible in comparison with them. The IP relay was chosen due to its functionalities and simple application.

5.1.1.1 IP Relay Charon I

The Charon I IP relay is an embeddable module employing a microcontroller and Ethernet controller. When connected to the motherboard of the Autonomous monitoring system controller, it can be utilized as an IP relay, which generates controlling signals according to the commands sent from the server by means of the IP communication protocol.

The proof of the module operation was processed in connection with Charon I Development Kit. The module uses its own MAC address and acts as a device that uses the IP communication protocol.

The Charon I module embedded to its development kit is depicted in Fig. 34. The red LEDs indicate receiving of the appropriate command. In the simple

communication mode 1-of-8 up to 8 different commands are distinguished. This number can be increased by pooling more commands together. Such commands must be sent sequentially. Considering the requirements on the communication speed based on how fast the Autonomous monitoring system moves, this can be done without any restrictions.

Fig. 34 – Charon I Development Kit with Charon I module embedded

5.1.1.2 IP Camera

As previously stated, D-Link DCS-910 IP camera is employed to scan and transmit the view of the Autonomous monitoring system. This device acts as a terminal IP device. Ethernet interface is embodied and the communication with the server is established via the IP communication protocol without any special requirements. As this camera is primarily intended for scanning the guarded spaces, the output data is in M-JPEG format.

The covering of the camera was removed so that its weight was decreased. Only its printed circuit board together with the lens are employed.

Fig. 35 – IP camera D-Link DCS-910

In the table below the main device parameters are listed.

Table 2: Main parameters of the D-Link DCS-910 camera

Sensor type	CMOS ¼”
Sensitivity	1 lx
Resolution	640 x 480 px
Frame speed	15 fps
Optical zoom	NO
Lens	4.57 mm, F1.9
Power consumption	4.5 W
Power supply	12 V

5.1.1.3 WiFi Router

The WiFi Router Edimax BR-6304Wg was chosen due to its low weight and easily removable coverings. It is operated in the Access Point mode and the radio communication is processed according to the 802.11b standard.

Fig. 36 – WiFi router uncovered

5.1.2 Module for obstacles detection

The obstacles detection module employs a set of ultrasonic detectors displaced around the airship’s bladder. Each detector communicates by means of I^2C bus which allows the constructer to change the number of the detectors as needed. The maximum number of the detectors is determined by the address space of the bus.

In order to prove the operation of the obstacles detector a hardware module has been created, utilizing the Atmel ATtiny2312 microcontroller. This module permanently communicates with 9 ultrasonic detectors placed on the canopy-shaped surface and displays distances of the prospective obstacles to each of the

ultrasonic detectors. Moreover, a set of LEDs is implemented to indicate that the pre-set "distance threshold" is trespassed. This feature can be utilized for a simple decision whether the obstacle is close enough or not.

The module for obstacles detection was also employed in measuring accuracy and reliability of the ultrasonic detectors; different obstacles in different distances and under different angles were detected and the measured distances were compared to the really measured ones.

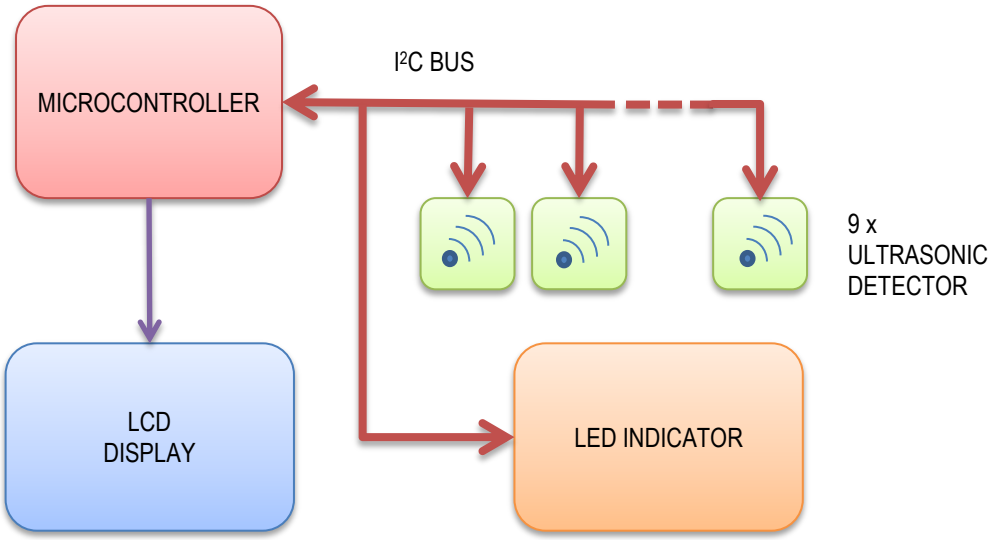

Fig. 37 – Module for obstacles detection block diagram

The physical construction of the module is realized on 3 different printed circuit boards. These boards are labelled as follows: AT-9, LED-9/1 and LED-9/2. The arrangement of the module is depicted in Fig. 38.

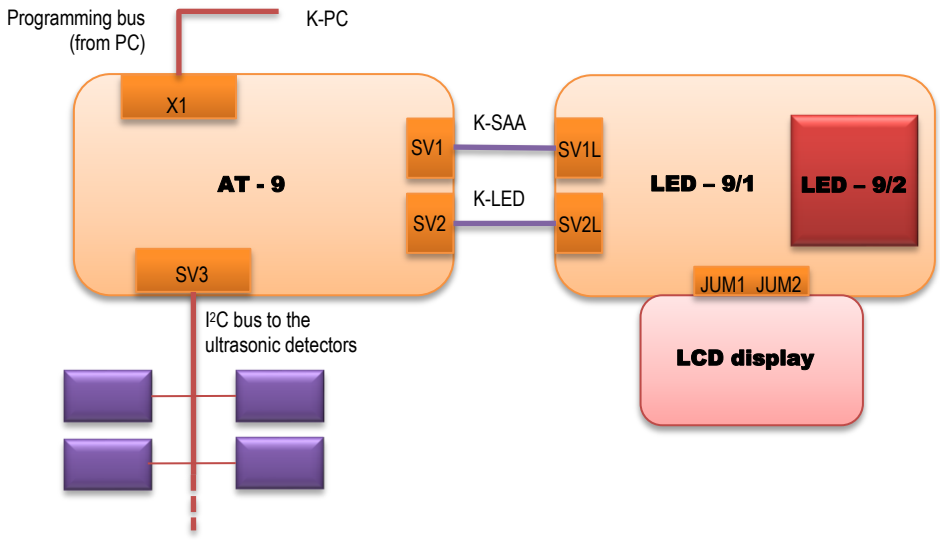

Fig. 38 – Physical arrangement of the module for obstacles detection

As obvious from Fig. 38, the boards AT-9 and LED-9/1 are interconnected by two flat multicore cables K-SAA and K-LED. The LED-9/2 board is connected firmly to the LED-9/1 board by means of a connector strip so that both boards are positioned concentrically one above the other and createa compact unit. The LCD display board, which was obtained separately as a completed module, is connected to the side of LED-9/1 board via the socket carriers JUM1 and JUM2.

5.1.2.1 AT-9 board electrical connection

The electrical connection of the AT-9 board is depicted in Fig. 39.

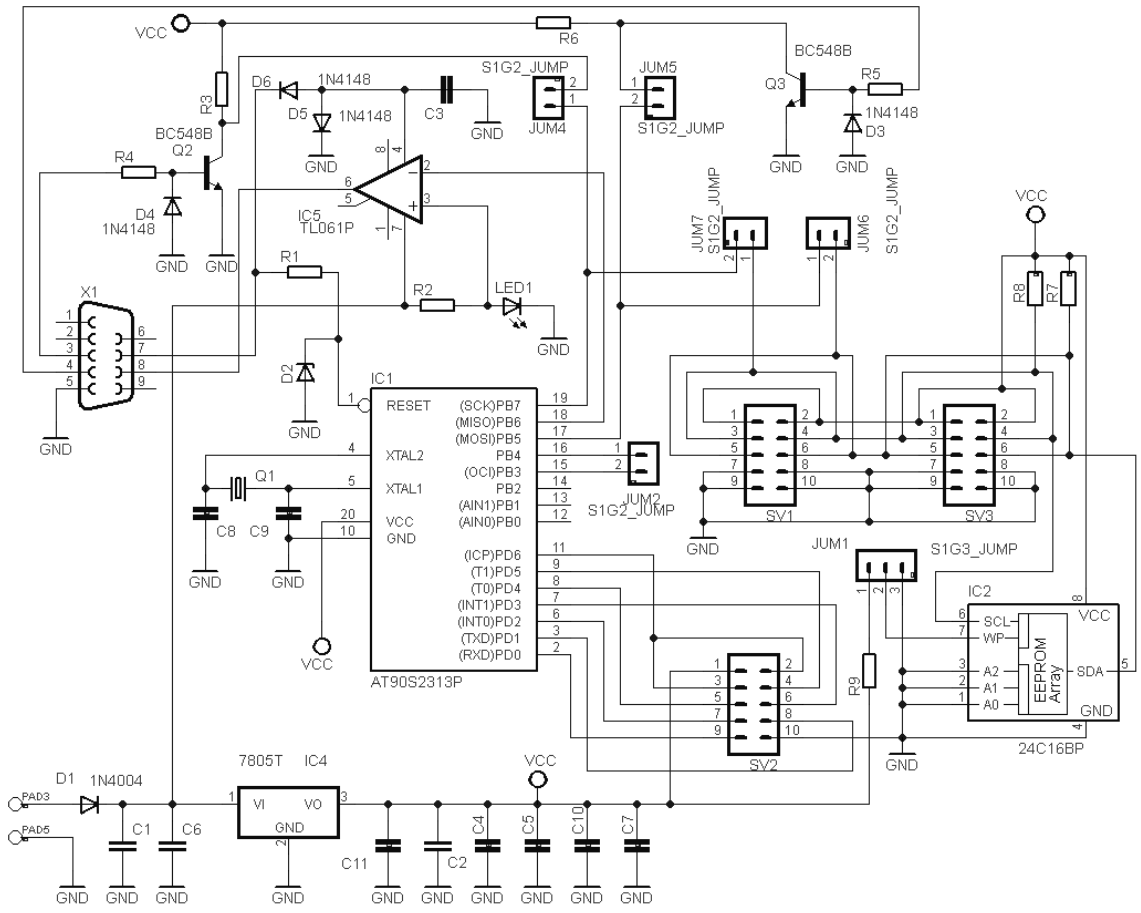

Fig. 39 – AT-9 board electrical connection

The power supply of the AT-9 board is delivered by means of a 9 V battery connected to the solder pads PAD3 and PAD5. The 1N4004 diode protects the circuitry from the reversed polarity. The monolithic voltage regulator IC4 stabilizes the power supply voltage to 5 V. The core of the board as well as of the whole module is the IC1 microcontroller (AT Tiny 2313) that controls the whole communication with the peripherals of the module, processes information gained from the ultrasonic detectors and evaluates and displays the appropriate distances.

In addition, there is an IC2 socket implemented on the board, which allows implementing an EEPROM memory in which the measured data can be stored.

In order the module was programmable directly via the serial interface of ordinary PCs, the board is equipped with the X1 connector and level converters. The RTS voltage level is affected by the D2 Zener diode, while the transistor Q2 affects the TxD signal voltage level and the transistor Q3 affects the DTR signal voltage level. The backward converter of TTL to RS-232 levels is created on the basis of the IC5 operational amplifier. Due to the low power consumption of this operational amplifier, its negative power supply is generated directly by the RTS line of the serial bus.

The board is also equipped with connectors the labelling of which corresponds to the Fig. 38.

5.1.2.2 LED-9/1 board electrical connection

The circuitry of the LED-9/1 board is depicted in Fig. 40.

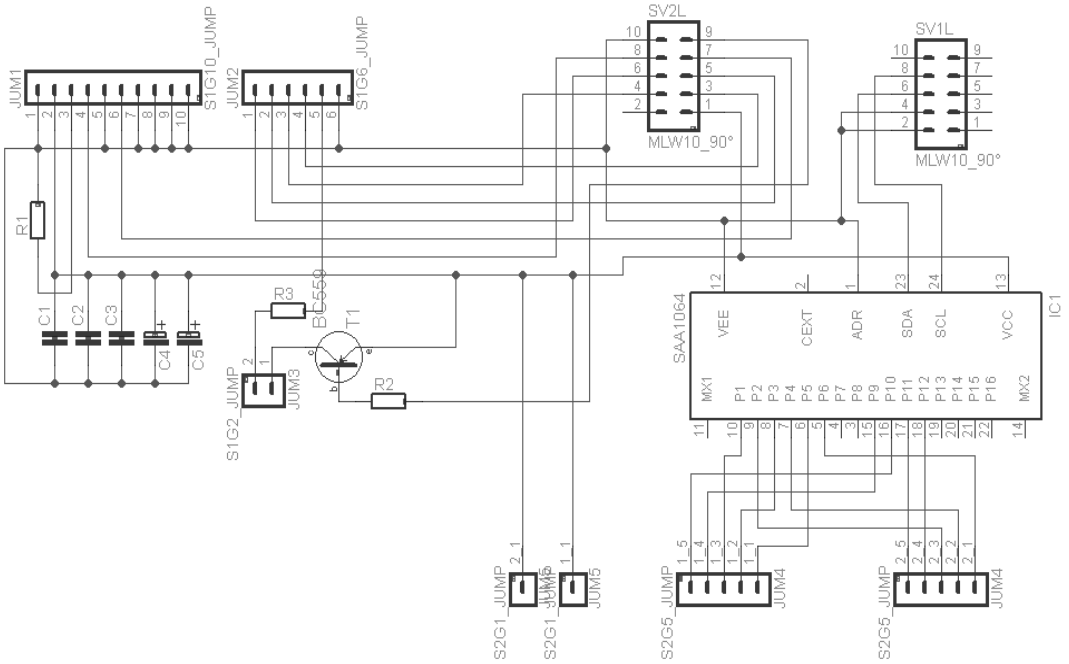

Fig. 40 – LED-9/1 board electrical connection

The LED-9/1 board holds the four-line LCD display as well as the LED-9/2 board. It is also equipped with SAA1064 decoder that drives the indication LEDs mounted on the LED-9/2 board.

5.1.2.3 LED-9/2 electrical connection

The circuitry of the LED-9/2 board is depicted in Fig. 41. Only the indication LEDs are mounted on this board, driven by the SAA1064 decoder mounted on the LED-9/1 board.

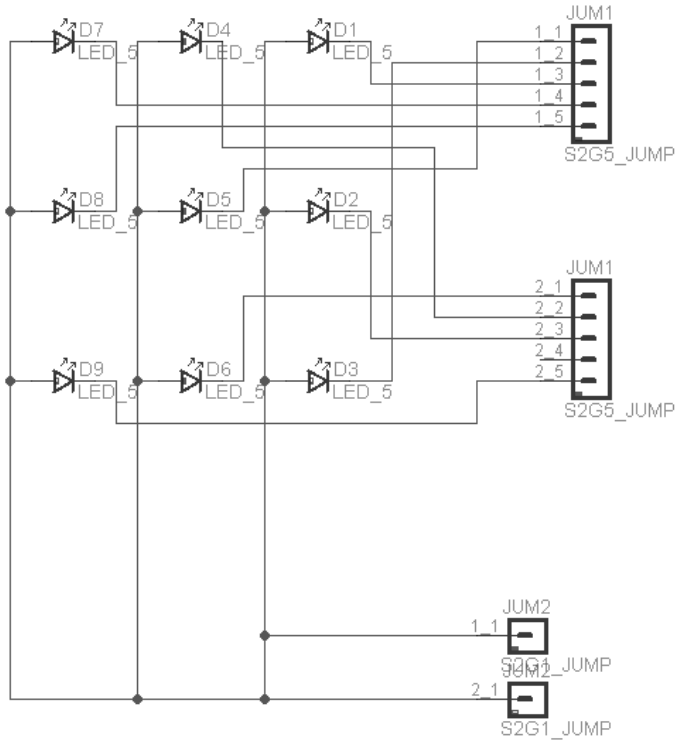

Fig. 41 – LED-9/2 boar electrical circuitry

5.1.2.4 Software of the module for obstacles detection

The software implemented in the Module for obstacles detection was created in ATMEL AVR Studio and integrated development environment with the aid of program libraries. It includes codes listed in the application notes AVR204 [60] and AVR300 [59] published by Atmel company. These codes are as follows:

a) BCD Arithmetics (AVR204): converts 8-bit and 16-bit values to the BCD code.
b) TWI (AVR300): describes controlling of the TWI bus.

In addition, the LCD display controlling code was implemented according to the information published in [63].

From the perspective of the user no adjustment of the module is required. The threshold of the obstacle proximity is set to 99 cm. The indication LEDs are bound to the addresses of the particular ultrasonic detectors. If some detector detects an obstacle that is closer than 99 cm, the indication LED appropriate to its address is lit. Because all detectors are connected to the same bus and distinguished by means of the unique address, their commutation does not influence the appropriate led to be lit. Also the values displayed on the LCD display are related to the specific detectors.

The program runs in a loop as follows: the ultrasonic detectors are addressed successively, being asked to return the information on the distance to the pertinent obstacle in front of them. In a period a set of numbers is collected. On

the basis of this set the displaying units are driven. If any detector indicates an obstacle being closer than 99 cm, the appropriate LED is lit and close to the measured distance a black rectangle is displayed on the display.

On the basis of the data gained and processed by the Module for obstacles detection the conclusions can be drawn in order to make a decision on the flight direction of the Autonomous monitoring system.

5.1.2.5 Mechanical construction of the Module for obstacles detection

The AT-9 and LED-9/1 boards are placed abreast, being interconnected by means of two flat multicore cables. The data for controlling of the LEDs are transmitted by means of SV1 connectors while the data for controlling the LCD display are transmitted by means of SV2 connectors. The SV3 connectors enable to connect the ten-core flat cable by means of which the set of 9 ultrasonic detectors is interconnected. The LED-9/2 board is fixed horizontally to the LED-9/1 board and next to it the LCD display is mounted. The mechanical arrangement is depicted in the following figures.

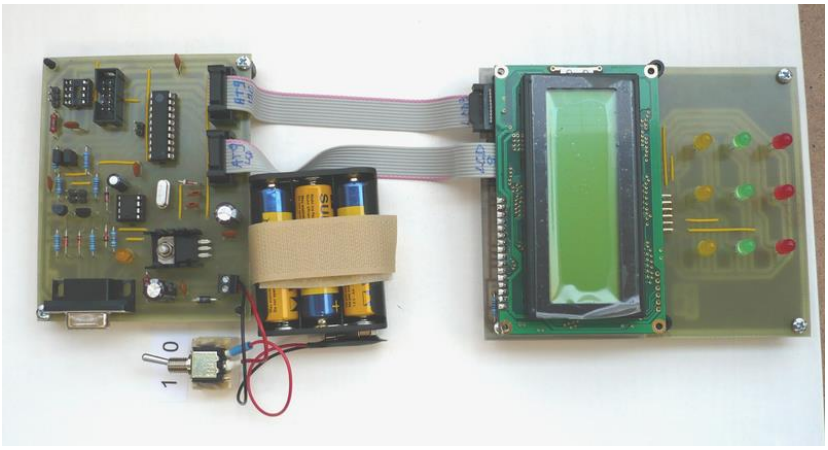

Fig. 42 – Mechanical arrangement of the Module for obstacles detection

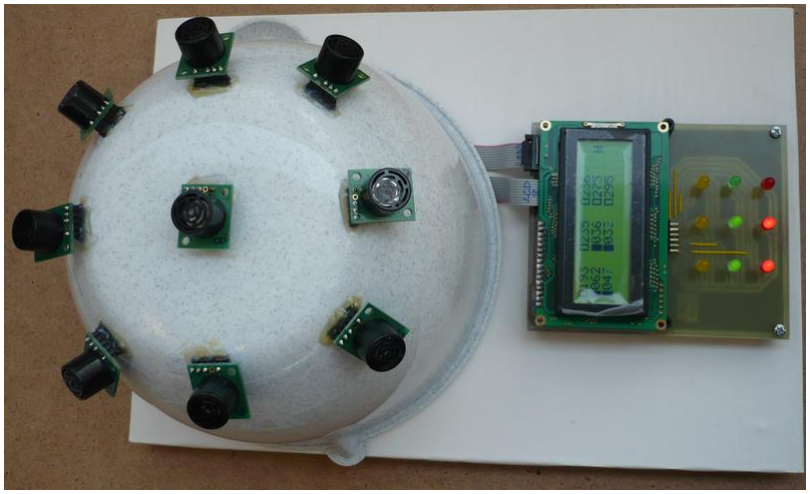

Fig. 43 – Module for obstacles detection together with the set of detectors

5.1.2.6 Results of the Module for obstacles detection testing

The Module for obstacles detection was utilized in several tasks arranged in order the accuracy and reliability of the ultrasonic detectors was proven. The purpose of these tasks was to claim the appropriateness of the ultrasonic detectors for obstacles detection the accuracy of which is, considering the utilization of this method by the Autonomous monitoring system, critical. By these tests it has been confirmed that in most cases the ultrasonic detectors are accurate and reliable enough to be employed for detecting the obstacles around the airship of the Autonomous monitoring system.

In accordance to the theory described in the theoretical part of this paper, the accuracy of the detection was affected by the ineligible width of the transmitted ultrasonic beam and the receiving characteristics of the ultrasonic detectors (see Fig. 1). However, when the inaccuracy of this type was observed, the measured distance was usually shorter than the real one, which does not affect the obstacles detection. The only consequence of such inaccuracies is that the obstacle is detected sooner or that spurious obstacle is detected. The above mentioned inaccuracies occur in the following cases:

a) the obstacle is not perpendicular to the axis of the ultrasonic beam,
b) there are other obstacles around the ultrasonic detector than the one to which the detector is directed being on the periphery of the ultrasonic beam, causing spurious reflections of the ultrasonic signal.

Whereas the above mentioned inaccuracies do not have a negative influence to the obstacles detection, unfortunately, there exist rare cases in which the detectors fail. The fail of the detectors occur when the surface of the obstacle attenuates the ultrasonic signal considerably or when the surface of the obstacle is too small in comparison with the transmitted ultrasonic beam width. Then the following problems can occur:

a) the range of the detector is decreased,
b) the detector does not detect the obstacle at all.

The results of the measurements obtained by the Module for obstacles detection are as follows:

a) metal column with a diameter of 75 mm was detected at a distance of 3.5 m,
b) paper box of dimensions 22 x 25 x 25 cm was detected at a distance up to 6 m,
c) aluminium foil coated target of dimensions 10 x 10 cm was detected at a distance of 5.16 m,
d) aluminium foil coated target of dimensions 20 x 20 cm was detected at a distance of 6.51 m,
e) wooden stick with a diameter of 12 mm was not detected at all, presumably due to scattering of the sound beam into the surroundings.

The inaccuracy of all the above mentioned measurements was lower than ± 2 cm.

Because in the area in which the operation of the Autonomous monitoring system is supposed there are several sound-absorbing sidings operating on the principle of Helmholtz resonators, the ultrasonic detectors were also tested on detecting these surfaces. The sound-absorbing sidings consist of performed plates, employing sound-absorbing material in the perforations. The sound absorption is efficient especially at high frequencies, making the ultrasonic detection difficult. The results obtained when detecting the sound-absorbing sidings were fluctuating according to the angle between the beam and the surface and the point on the surface at which the ultrasonic beam was aimed to. When aimed between the perforations, the ultrasonic detectors operated satisfactorily; only their maximum operating range decreased a little. When aimed directly to the perforation, the detectors failed. However, it is assumed that the detectors can detect the sound-absorbing surfaces with good reliability due to the fact that the Autonomous monitoring system is moving against their surface, resulting in the acoustic beam angle and position variation in time. Therefore, it is expected that some reflections from the surface will be detected properly.

In the text below the results of more systematic accuracy measurements are provided. The accuracy of the distance measurement was proven by measuring the distance from a flat wall and from a wooden column under various angles (60°, 90° and 120°).

The results obtained at measuring the distance from the flat wall are depicted in Fig. 44. The real distance measured manually is displayed on the x-axis while the distance measured by the ultrasonic detectors is depicted in the y-axis. The green line represents the ideally linear relationship between the results of both measurements. The blue line represents the results obtained when the acoustic beam was perpendicular to the wall while the red line represents the results when the acoustic beam clutched with the wall the angle of 120° or 60° respectively (the results for 60° and 120° were identical). It is obvious that for distances greater than 0.4 m and perpendicular acoustic beam to the measured surface the results delivered by the ultrasonic detectors are greatly close to the ideal characteristics while provided the acoustic beam is not perpendicular to the measured surface, the results show a considerable error. For a 30° difference from the right angle the error caused by the reflection of the lateral sections of the acoustic beam is approximately – 10 %. The consequence of this phenomenon results in the fact that large flat areas, such as walls, may be detected to be closer than they really are. However, this is not considered as a malfunction of the obstacle detection system.

Other measurements were processed with a wooden column with a rectangular cross-section of approximately 0.24 x 0.6 m. The results are depicted in Fig. 45. The same angles as in the previous measurement were applied. Also the graph elements are formatted in the same way as those depicted in Fig. 44. In this measurement the results were quite accurate for all applied angles

between the detectors and the measured object. This is a consequence of the fact that the area of the object's surface is limited and does not allow reflections of the lateral sections of the acoustic beam.

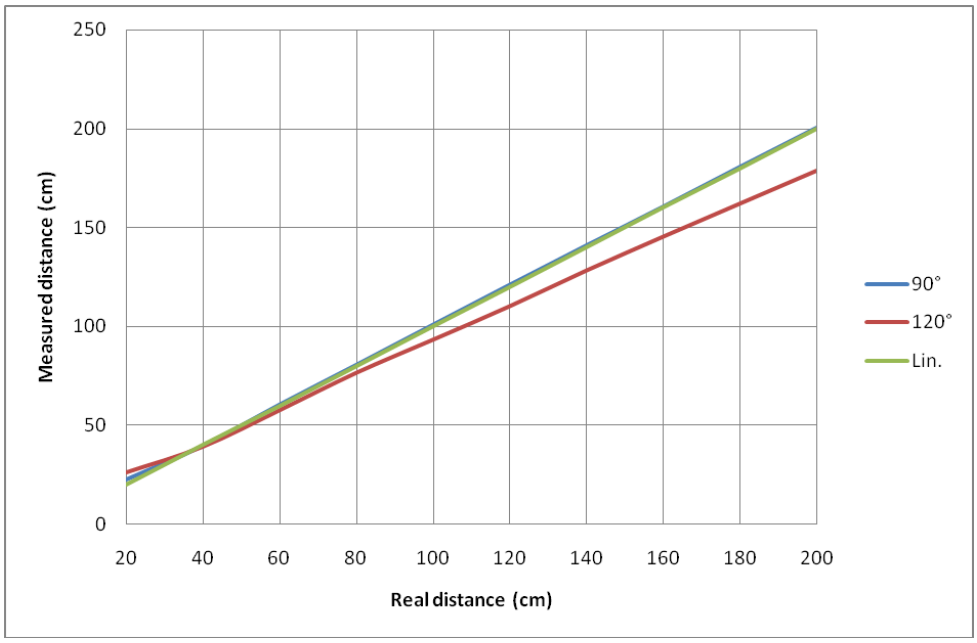

Fig. 44 – Distance from the flat wall measurement results (see text above)

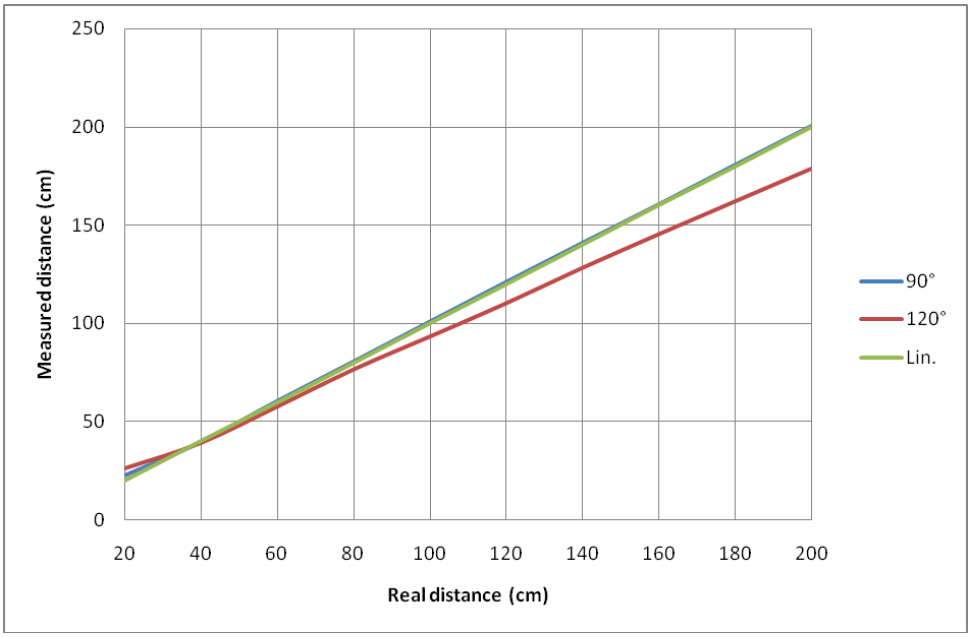

Fig. 45 – Distance from the wooden column measurement results (see text above)

On the basis of the above mentioned results it can be claimed that the ultrasonic detectors in the proven configuration are suitable for detecting the obstacles in the surroundings of the Autonomous monitoring system.

5.1.3 Module for driving of the motors

In order to study the behaviour of the power bridge driver L298, the Module for driving the motors of the Autonomous monitoring system was constructed. The module is controlled by the Freescale MC9S08SH4 microcontroller. This microcontroller belongs to the group of products which are to be implemented in the main controlling board. The Module for driving the motors ensures the controlled power delivery to the main motors as well as to the tail motor. Moreover, it enables to control the servo that swivels the main motors.

The L298 driver was selected because its parameters are best fitting to the requirements on the power circuitry of the Autonomous monitoring system. As it can be directly controlled by signals of TTL level, it can be connected directly to the microcontroller, which simplifies the design of the hardware significantly.

The Module for driving the motors is also equipped with two analogous inputs, enabling to connect optional accelerometers.

The motors of the Autonomous monitoring system driven by the module can be controlled by 6 on-board buttons or by outputs of the Module for obstacles detection. The Module for driving the motors together with the Module for obstacles detection create the most simple system of Autonomous monitoring system controlling. It is sufficient to let the Autonomous monitoring system operate independently on the supervision, flying incidentally inside the closed area. To more sophisticate controlling the more complex attitude must be applied as described below in this paper.

The block diagram of the Module for driving the motors is depicted in Fig. 46. It consists of three independent boards:

a) Main board – on this board the main circuitry of the module, capable of independent operation, is implemented.
b) Module for obstacles detection interface – this board enables to gain information on the obstacles detected by the ultrasonic detectors.
c) Multiplexer - enables the communication between the main board and the interface circuitry by means of a limited number of wires.

The information on the obstacles is gained by the LEDs controller present in the Module for obstacles detection (see text above).

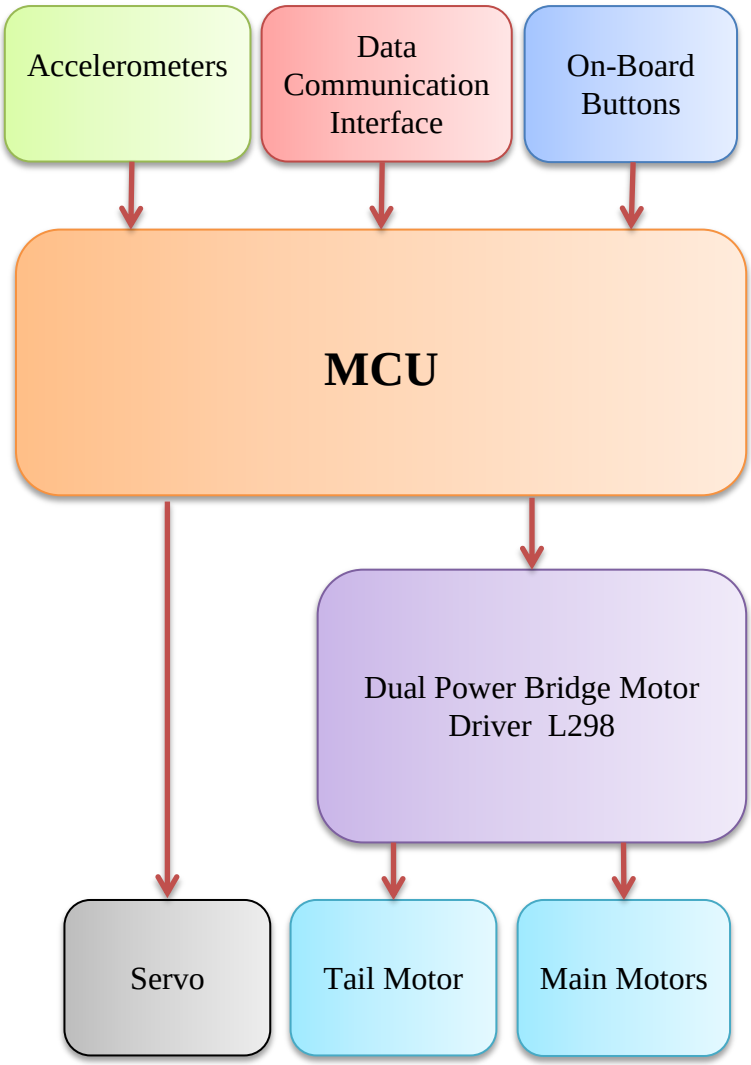

Fig. 46 – Block diagram of the Module for driving of the motors

5.1.3.1 Main board electrical circuitry

The schema of the electrical circuitry of the main board of the Module for driving the motors is depicted in Fig. 47.

The main device of the board is the IC101 microcontroller that belongs to the family of processors based on Motorola HC08 core. It utilizes peripherals and instruction set that are suitable for the complex main board of the Autonomous monitoring system construction. Another significant device on the main board is the dual bridge motor driver IC102 that is connected to the microcontroller via a 4 wire bus.

As obvious from the circuitry schema, the board is equipped with several connectors. Their purpose and characteristics are described in Table 3.

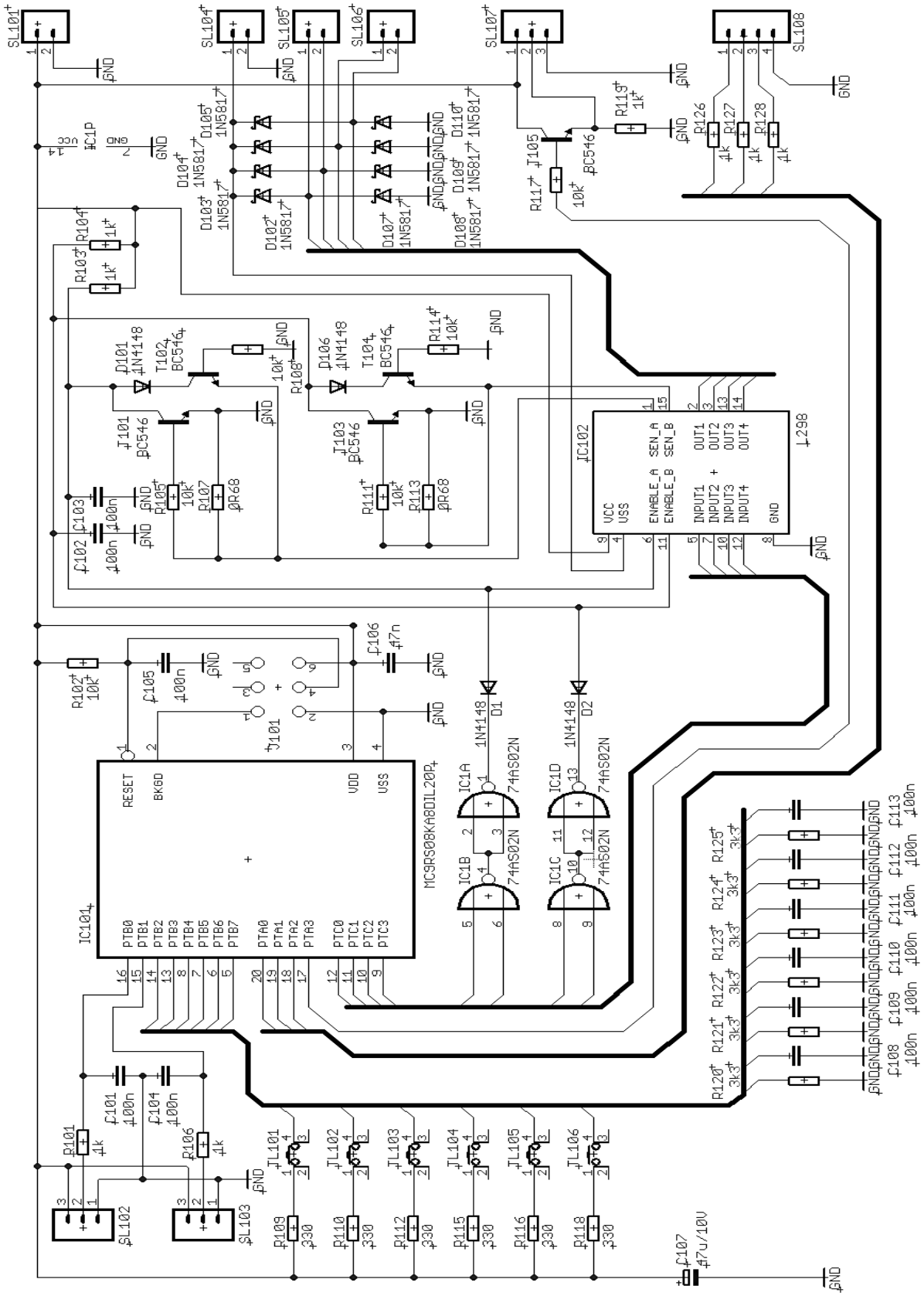

Fig. 47 – Connection diagram of the main board of the Module for driving of the motors

Table 3 – Main board connectors' description

Position	**No. of pins**	**Purpose and parameters**
SL101	2	Stabilised power supply delivery, + 5 V
SL102	3	Analogous accelerometers connection (optional)
SL103	3	
SL104	2	Power supply to the motors, + 7.2 V directly from accumulators
SL105	2	Main motors connection (parallel)
SL106	2	Tail motor connection
SL107	3	Power supply and controlling of the servo (50 Hz PWM controlling signal)
SL108	4	Data communication with other modules
J101	6	Programming interface

All ports of the microcontroller IC101 are utilized:

a) PTC port operates in the "output" mode and drives the bus controlling the bridge motor driver IC102.
b) PTB port operates in the "input" mode, uses the internal A/D converters for processing the signals from the external accelerometers and accepts the commands given by means of the on-board buttons. The buttons are equipped with RC circuits to eliminate their backswings.
c) PTA port operates in the "mixed" mode. Some of its pins operate as the input one and receive data from the data communication interface. The pin PTA3 is utilized as the output one and delivers the PWM signal to control the servo.

The power supply and the BDM programming interface was designed according to the application note provided by the manufacturer of the microcontroller [31].

There is also a set of NAND gates implemented in the circuitry. The integrated circuit is labelled as IC1 and was added during the module development in order to enable free running of the motors (the detailed description of the motors controlling is provided below in this paper).

The transistors T101, T102, T103 and T104 together with the appropriate devices around them are needed to establish the overcurrent protection. This overcurrent protection operates as follows: the pins SEN_A and SEN_B of the

IC102 driver deliver DC voltages whose level and polarity correspond to the current drawn by the motors and the direction of the motors' rotation. Once the U_{be} voltage of any transistor is trespassed, the prospective transistor starts to carry the current, causing a short circuit of the ENABLE_A or ENABLE_B pin of the driver. As a consequence all power transistors in the driver are closed and the current delivery to the prospective motor is discontinued. The threshold of the overcurrent protection is determined by the values of R107 and R113 resistors. In practice, when the overcurrent protection is in operation, the system oscillates around the maximum allowed current with the frequency given by the inductance of the motors' coils.

The Shottky diodes displayed in the circuit diagram protect the driver's transistors from overvoltage caused by voltage peak inductions that can occur when the motors are running and their power supply is disconnected.

The T105 transistor provides the output interface for controlling the servo.

5.1.3.2 Motor control logic

The principle of the bi-directional motors driving is depicted in Fig. 48. The truth table of the TTL controlling signals is listed in Tab. 4 on the next page.

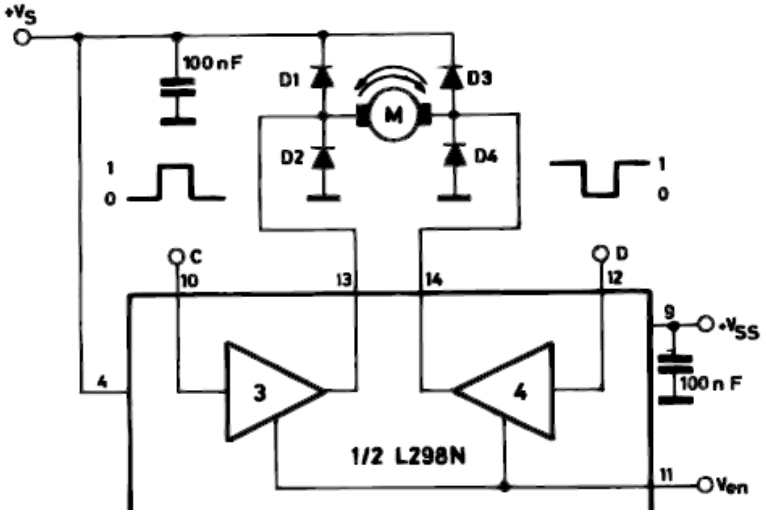

Fig. 48 – Bi-directional motor driving principle [33]

As shown in Tab. 4, in order to implement fluent controlling of motors by means of the pulse-width modulation, the ENABLE inputs must be utilized. For this reason the NOR gates IC1 were implemented, allowing to drive the ENABLE inputs low in case the logic signals C = D = low. The active deceleration of motors is then replaced by their free running, which enables their output power to be controlled by means of logic signals C and D. The active deceleration of the motors is still possible provided C = D = high.

Table 4 – Truth table of the controlling signals utilized by the motor driver

Inputs		**Operation**
ENABLE = H	C = H; D = L	Clockwise rotation
	C = L; D = H	Counterclockwise rotation
	C = D	Deceleration (the motor is short-circuited)
ENABLE = L	C = X; D = X	Free running (the motor is disconnected from the power supply)

Legend: H = high level, L = low level, X = has no effect

The following three cases can occur when driving the motors:

a) The inputs IN1 and IN2 (C and D signals) are driven by a combination of [0 1] or [1 0] according to the required direction of the rotation. If this condition is permanent, the motor operates with the full power (or with the power allowed by the overcurrent protection).
b) Both inputs IN1 and IN2 are fed by zeros [0 0]. Logic zero occurs at the output of the appropriate gate of the IC1 chip, pulling the proper ENABLE input to the low level. The motor is disconnected and if running, its angular speed is decreased with respect to its mass persistence. If this condition is alternately combined with the previous one, the output power of the driven motor can be controlled. One of the inputs is then kept low while the other is driven by the PWM signal; the choice of inputs to be driven depends on the required direction of rotation.
c) Both inputs IN1 and IN2 are fed by ones [1 1]. The appropriate logic gate remains in the high state and so does the proper ENABLE input. The winding of the motor is short circuited, which makes the motor decelerate intensively. This mode of operation is applicable when the immediate change of the rotation direction is required, which may happen in the tail motor when the stability of the airship’s course is somehow disrupted. In this case, a short overlapping of C and D signals high state is sufficient enough.

5.1.3.3 Circuitry for external commands receiving

External commands are generated by the Module for obstacles detection. To avoid remodelling of the module circuitry, that was constructed prior to the Module for driving the motors,, the circuitry presented in this chapter was

constructed to gather the information based on which the LEDs detecting obstacles are lit up. For this purpose the board LED-9/2 of the Module for obstacles detection is replaced by the board on which the LEDs are replaced by resistors, which enables the current to be sensed. The SAA1064 driver remains loaded properly with no effect on its operation. The principle of this replacement is depicted in Fig. 49.

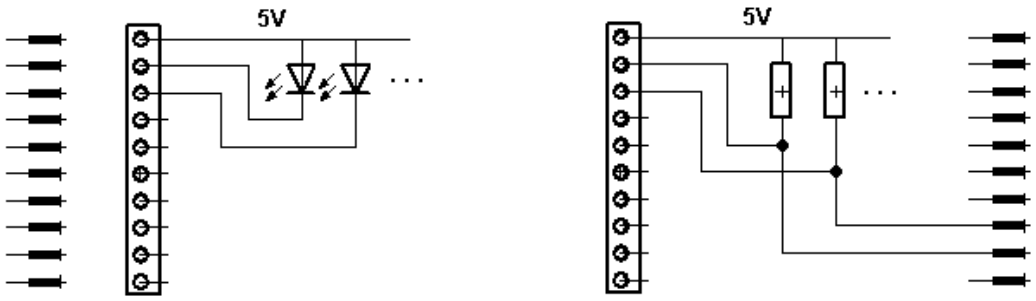

Fig. 49 – Replacing of LEDs at the LED-9/2 board with resistors

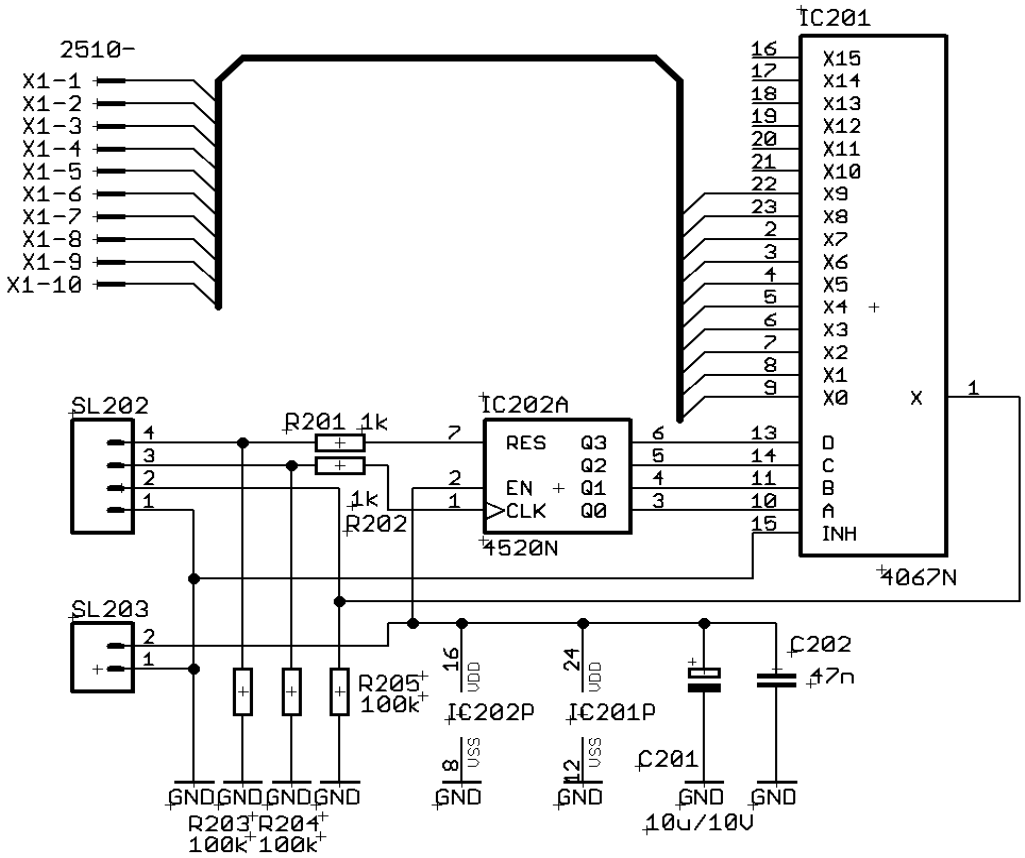

Fig. 50 – Time division multiplexer connection diagram

As the number of the IC101 microcontroller inputs is limited, time division multiplex must have been employed to connect the Module for driving the motors with the Module for obstacles detection. The circuitry of the multiplexer

is depicted in Fig. 50. The multiplexer board is equipped with a CMOS 1-of-16 multiplexer 4067, labelled as IC201 in the diagram. Its inputs are connected to the LED-9/2 replacement board by means of a ten core flat cable. This cable is connected to the X1 connector. The counter IC202 (4520) assures the addresses variations. The time multiplex is then connected with the Module for driving motors by means of a 4 core flat cable. On the side of the multiplexer this cable is connected to the connector SL202, while on the side of the main board it is connected to the connector SL108. The description of the SL202 connector's pins is provided in Tab. 5.

Table 5 – SL202 connector description

Pin	**Purpose**
1	Ground
2	Data
3	Counter clocking by the microcontroller (increases address)
4	Counter resetting by the microcontroller (address = 0)

5.1.3.4 Controlling algorithm

This chapter describes the control algorithm implemented in the IC101 microcontroller. When designed, time constants needed for the proper operation of the servo had to be considered. The servo shaft angle is determined by the length of the controlling pulses that must range within 1.0 and 2.0 ms. The basic (zero) position is obtained when the pulse length is 1.5 ms. The pulses must be repeated at the frequency of 50 Hz. The frequency of the PWM signals determining the output power of the motors is also 50 Hz, provided the shortest pulse can be 1 ms. As there are only two timers implemented in the MC9S08SH4 microcontroller and one of them is utilized for servo controlling pulses generation, the remaining timer generates a call for interruption every 1 ms. The 50 Hz frequencies are then obtained by dividing the "interrupting" frequency of 1 kHz by 20. This solution also allows to create proper PWM signals for motors output power controlling without the need for a timer; the length of the PWM pulses can be 1, 2, …, 20 ms, which makes it possible to control the power of motors in 20 steps.

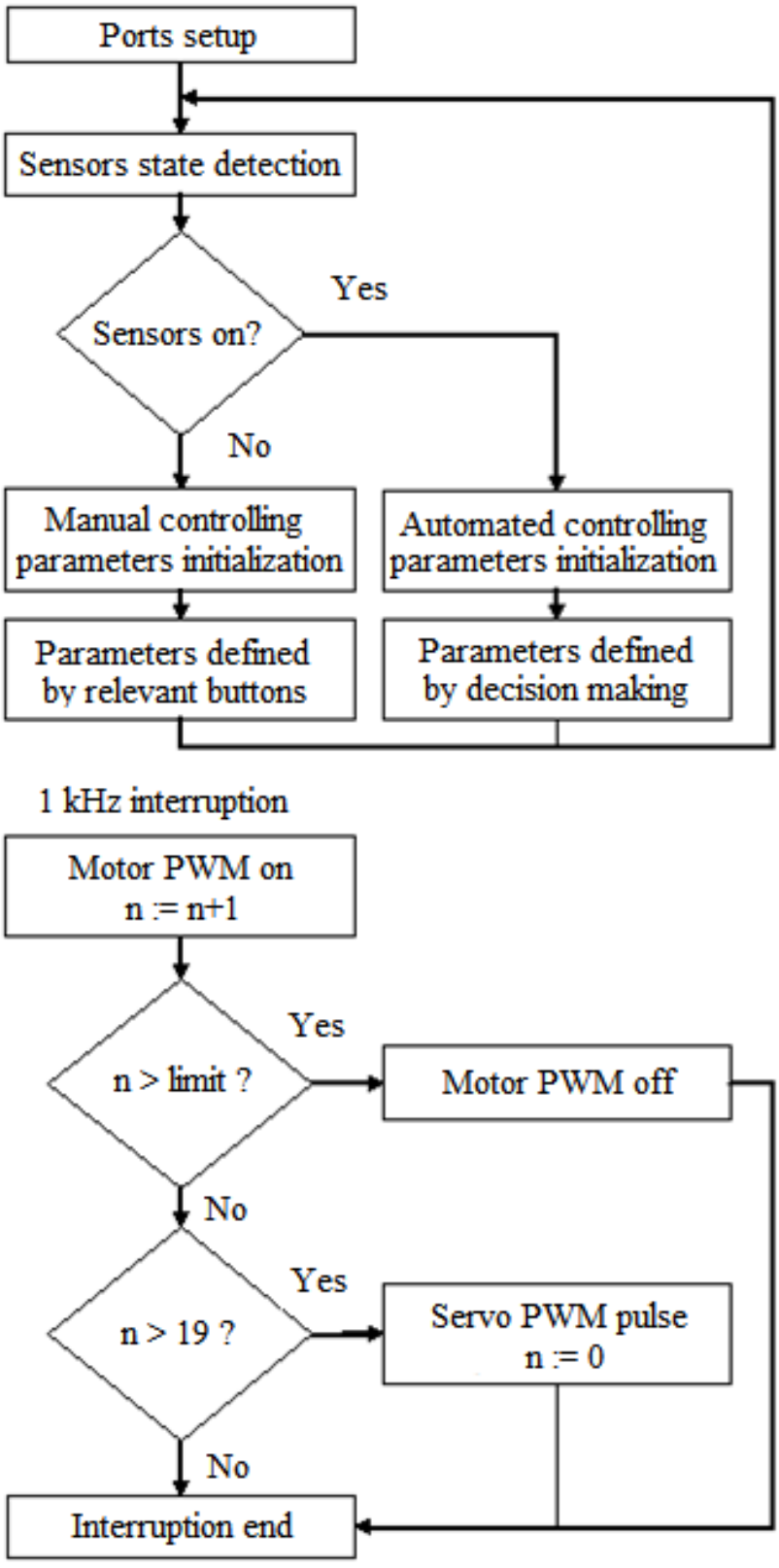

Fig. 51 – Controlling algorithm flowchart

In the rest of the computer time buttons state is observed and at the same time the data communication with the Module for obstacles detection is processed. Moreover, in the idle time there is enough capacity for a simple decision making process performed on the basis of the information gathered from the ultrasonic detectors. All these activities can be processed without accurate timing as this timing is not crucial.

The information from the ultrasonic detectors is written into a field of 9 elements. This field is cyclically updated as the state of each ultrasonic detector is scanned. When all of the relevant addresses are scanned, the counter of the multiplexer is reset. The connection of the Module for obstacles detection is monitored by the tenth wire of the interconnecting cable. This enables switching the manual operation, when the motors are driven according to commands given by the on-board buttons, to the autonomous operation with the ultrasonic detectors assistance and vice versa.

When accelerating from standstill, the motors are stimulated by short voltage peaks so that their starting torque overcomes the mechanical resistances.

5.1.3.5 Module for driving the motors control

The Module for driving the motors can operate in one of the following modes:

a) Manual – The module is controlled by the on-board buttons,
b) Automated – When the Module for obstacles detection is connected, the manual control is supressed and the motors are driven according to the information gained by the set of the ultrasonic detectors.

When in the manual mode of operation, six on-board buttons are available to command the module. Their purpose is described in the following table.

Table 6 – On-board buttons description

Button code	**Purpose**
TL101	Servo - descending
TL102	Servo - ascending
TL103	Main motors – start or more power
TL104	Main motors – stop or less power
TL105	Tail motor – turn to the left (operates only when the button is pressed)
TL106	Tail motor – turn to the right (operates only when the button is pressed)

The automated mode enables the simple autonomous operation; when an obstacle is detected, the motors are driven in such a way that the Autonomous monitoring system passes around it. This can serve as a protection of the airship

in case of a more serious failure of the controlling system. For this purpose the displacement of the ultrasonic detectors around the bladder of the airship is expected as depicted in Fig. 52. The sensors are numbered hexadecimally as follows: 0, 2, 4, 6, 8, A, C, E, F. Six zones are monitored: above the top of the bladder, under the bottom of the bladder, to the left from the bladder, to the right from the bladder, in front of the bladder and behind the bladder. The motors are driven based on the number of ultrasonic detectors warnings against obstacles. The number of ultrasonic detectors monitoring the appropriate zone is taken into account. Provided all ultrasonic detectors warn against obstacles in front of the airship, the main motors are reversed and the airship moves backwards.

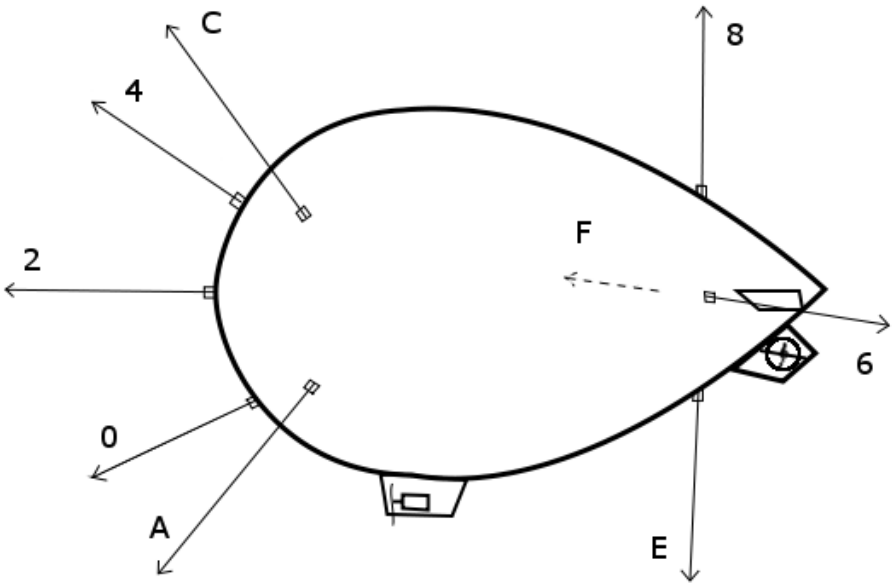

Fig. 52 – Suggested displacement of the ultrasonic detectors around the bladder of the airship

5.1.3.6 Practical implementation

All three boards of the Module for driving the motors were equipped with standard devices and the module was tested. It operates as expected. As the L298 driver can be purchased also in SMD case Power SO20, the construction can be considerably minimised by employing the SMD devices.

No special or expensive devices are needed to complete the construction. See the photography of the construction in Fig. 53.

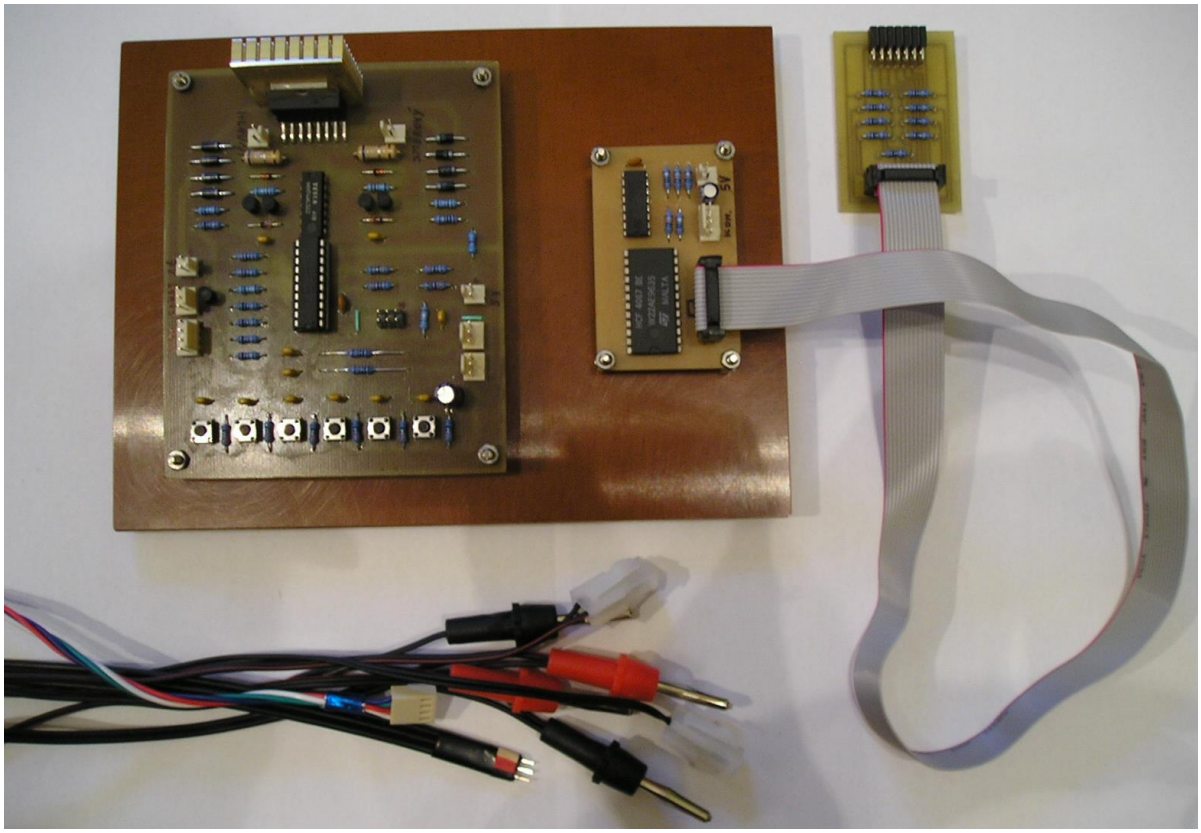

Fig. 53 – Practical implementation of the Module for driving the Motors

5.1.4 RFID tags detector

The RFID tags detector was created in order to extend the possibilities of the orientation of the Autonomous monitoring system in its operating space. The main idea consists in defining key points by means of RFID tags displaced in the space in which the Autonomous monitoring system operates. Provided the Autonomous monitoring system is operating in a defined trajectory and the inertial controlling is employed, the RFID tags can evaluate whether the current position is correct or not, suppressing the cumulative errors the inertial controlling systems usually suffer from.

Allowing reading tags from distances up to 1.5 m the RFID technology can replace the system of radio beacons. Unfortunately, purchasing the proper client chips is difficult. The RFID tags detector described herein is based on a chip AS3910 manufactured by Austria Microsystems. In terms of application in a prototype circuit this chip is rather objectionable as it is supplied only in a case suitable for automated surface mounting, sensitive to the soldering temperature, levels of power supply voltage and signal voltages.

The block diagram of this module is depicted in Fig. 54. The module is constructed on three separated boards that can be firmly connected each other. This allows the constructer to tune each board separately. The microcontroller and the RFID reader are mounted on the main board together with other necessary devices. The voltage regulator is separated in order to prove the function of the circuit and so are linear voltage regulator and switched-mode

operated voltage regulator. The antenna board is also separated from the main board.

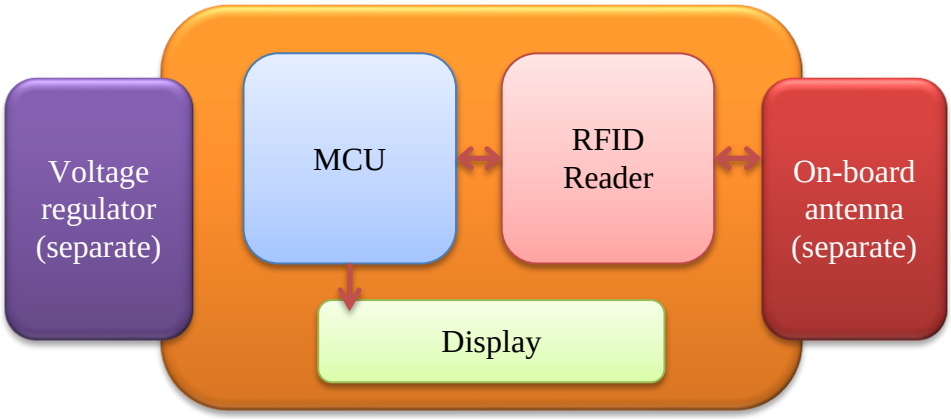

Fig. 54 – RFID tags detector block diagram

5.1.4.1 RFID tags detector main board circuitry

The main board circuitry of the RFID tags detector is depicted in Fig. 55. Linear or switched-mode operating voltage regulator can be used to deliver the power supply to the main board. This concept was chosen due to the possibility to study the influence of the voltage regulator interferences on the RFID detector operation that is expected mainly in the event of using the switched-mode operating voltage regulator. The reason for this is the fact that the switched-mode operating voltage regulators are supposed to be employed in the complex controller of the Autonomous monitoring system. The voltage regulators are fitted on the main board by means of the SV301 connector. The on-board antenna is fitted on the main board by means of the SV302 connector.

The heart of the module is the Freescale MC9S08SE8 microcontroller which is the same chip that is supposed to be employed as the MCU of the complex controller board. In the circuit diagram this microcontroller is labelled as IC301. The chip detecting the RFID tags is labelled as IC302 and it is connected to the microcontroller via four wire SPI bus. The programming interface BDM is connected in accordance with the application note of the microcontroller's manufacturer [33], including the JP301 jumper that allows the microcontroller to be supplied directly from the programming device (when being programmed) while the rest of the circuit is switched off.

Because the AS3910 chip can operate only with 3.3 V power supply, the power supply of the microcontroller was also decreased to this level. If utilized on the complex controller board this would increase the requirements on the power supply system would increase because there are also several devices that

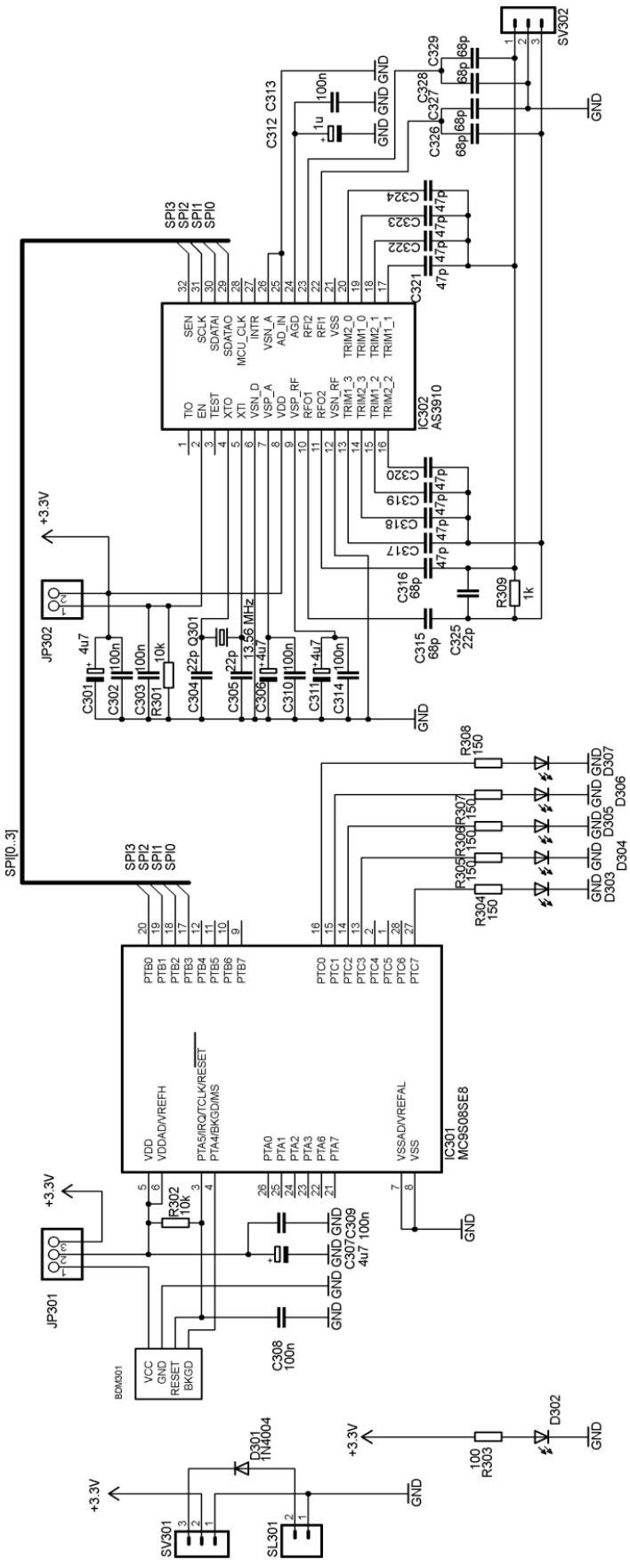

Fig. 55 – RFID detector main board circuit diagram

cannot be supplied with such low voltage and the need of having 3.3 V network together with 5 V network would arise.

On the main board there are 6 LEDs:

a) D302 is green and indicates that the power supply is on,
b) D303 is orange and indicates that the antenna circuit is being tuned up or that the tuning of the antenna circuit was not successful,
c) D304 to D307 are red and indicate that one of the four known tags was detected.

Although only 4 tags are recognized by the testing module of the RFID tags detector, this number can certainly be increased as required.

The IC302 chip is clocked by the crystal Q301 that oscillates at 13.56 MHz. The set of capacitors connected around the IC302 chip is designed according to its manufacturer's application note [40]. In case that a symmetrical antenna having a tap in the centre is employed, the output power of the radio signal can be up to 1 W. At this power the manufacturer of the chip ensures the minimum identification distance to be up to 1 m which is still sufficient for the purpose of the operation aboard the Autonomous monitoring system.

The IC302 chip can be disabled by disconnecting the JP302 jumper. This allows the constructer to tune the controlling algorithm without a risk of putting the chip to an undesirable state.

The IC302 chip is equipped with several outputs that can be internally enabled or disabled. The antenna is connected to these outputs via a set of capacitors. This allows the chip to fine-tune the resonant circuit even though the antenna inductance is not observed correctly.

The SPI bus between the microcontroller IC301 and the RFID reader chip IC302 consists of 4 wires. Two of them ensure duplex serial communication between these devices while the third one enables the microcontroller to provide time synchronization of the bus and the fourth one provides signalization and communication. The microcontroller always operate in the "master" mode while the IC302 reader always operate in the "slave" mode, waiting for commands from the microcontroller. More detailed information on the communication between the microcontroller and the RFID reader is provided in the following chapter.

5.1.4.2 Communication with the RFID reader

As stated above, the communication between the microcontroller and the RFID reader is operated by means of the 4 wire SPI bus. The RFID reader waits for commands from the microcontroller that must be timed and generated according to the manufacturer's application note [40].

The RFID reader distinguishes among several commands that are defined by bit sequences generated by the microcontroller. Some of the commands are initializing the reader to the required state or setting the required parameters while other commands are interrogative, requiring the feedback from the reader.

The feedback can consist in confirming the parameters that were currently set or in sending the numbers of the detected RFID tags. The processing of the tag numbers is then operated by the microcontroller.

The communication between the microcontroller and the reader is described by Fig. 56. The microcontroller sets the request for communication by setting the SEN wire to high level and starts clocking the bus via the SCLK wire. Consequently, it sends the set of bits corresponding to the relevant command and waits for the answer from the RFID reader. The first sequence of bits generated by the microcontroller sets the RFID reader to one of the following modes: WRITE, READ, FIFO Load, FIFO Read and COMMAND. The set of commands supported by the RFID reader can be found in the appropriate application note [40].

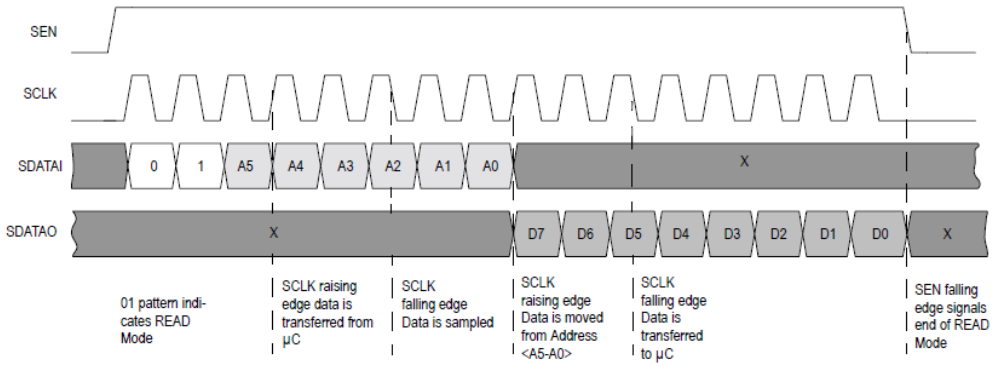

Fig. 56 – Example on reading 1 B of data from the reader [40]

When the power supply is turned on, the microcontroller generates the initializing sequence as described in Tab. 7.

Table 7 – RFID reader initializing sequence

Instruction	Instruction name	Comment
000001	SET DEFAULT	Initialization
000010	CLEAR	All processes are discontinued and the output register is cleared
010110	ADJUST REGULATORS	Automatic internal voltage references calibration
011000	CALIBRATE ANTENNA	Antenna calibration by means of the set of the capacitors connected to the TRIMx pins
011001	CHECK ANTENNA RESONANCE	The state register 0E is loaded with the information on the antenna calibration

5.1.4.3 Controlling algorithm

This chapter describes the controlling algorithm implemented in the IC301 microcontroller. This algorithm ensures the communication of the microcontroller with the RFID reader and periodical detection of the RFID tags in the surroundings of the RFID reader's antenna.

The flowchart of the controlling algorithm is depicted in Fig. 58.

Firstly, the RFID reader initialization is processed. Consequently, the antenna calibration process is run and when finished, the infinite loop of periodical interrogation on the RFID tags starts. If there is any tag in the reach of the RFID reader, its ID is interpreted to the microcontroller. The microcontroller checks whether this ID is stored in a lookup table and if it does, the appropriate LED is lit up for a few seconds.

The program is written in the C language. Code Warrior Development Studio by Freescale was utilized when writing the code.

5.1.4.4 Linear voltage regulator circuitry

The linear voltage regulator utilizes the LM317T monolithic voltage regulator. In the circuit diagram depicted in Fig. 57 this voltage regulator is labelled as IC101. The connection diagram is simple, designed according to the application note provided by the voltage regulator's manufacturer [64].

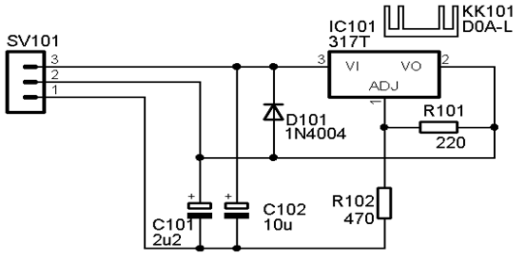

Fig. 57 – Linear voltage regulator circuit diagram

The output voltage of the regulator is defined by the ratio of values of resistors R101 and R102. Their effect is described by formula (118).

$$U_{OUT} = 1.25 \cdot \left(1 + \frac{R102}{R101}\right) + I_{ADJ} \cdot R102 \quad [V] \tag{118}$$

Where:

U_{OUT} - nominal output voltage [V],

I_{ADJ} - current escaping the voltage regulator from the ADJ pin [A],

R_{101}, R_{102} - resistances of the appropriate resistors [Ω]

The linear voltage regulator can be directly fitted on the main board of the RFID tags detector by means of the SV101 connector.

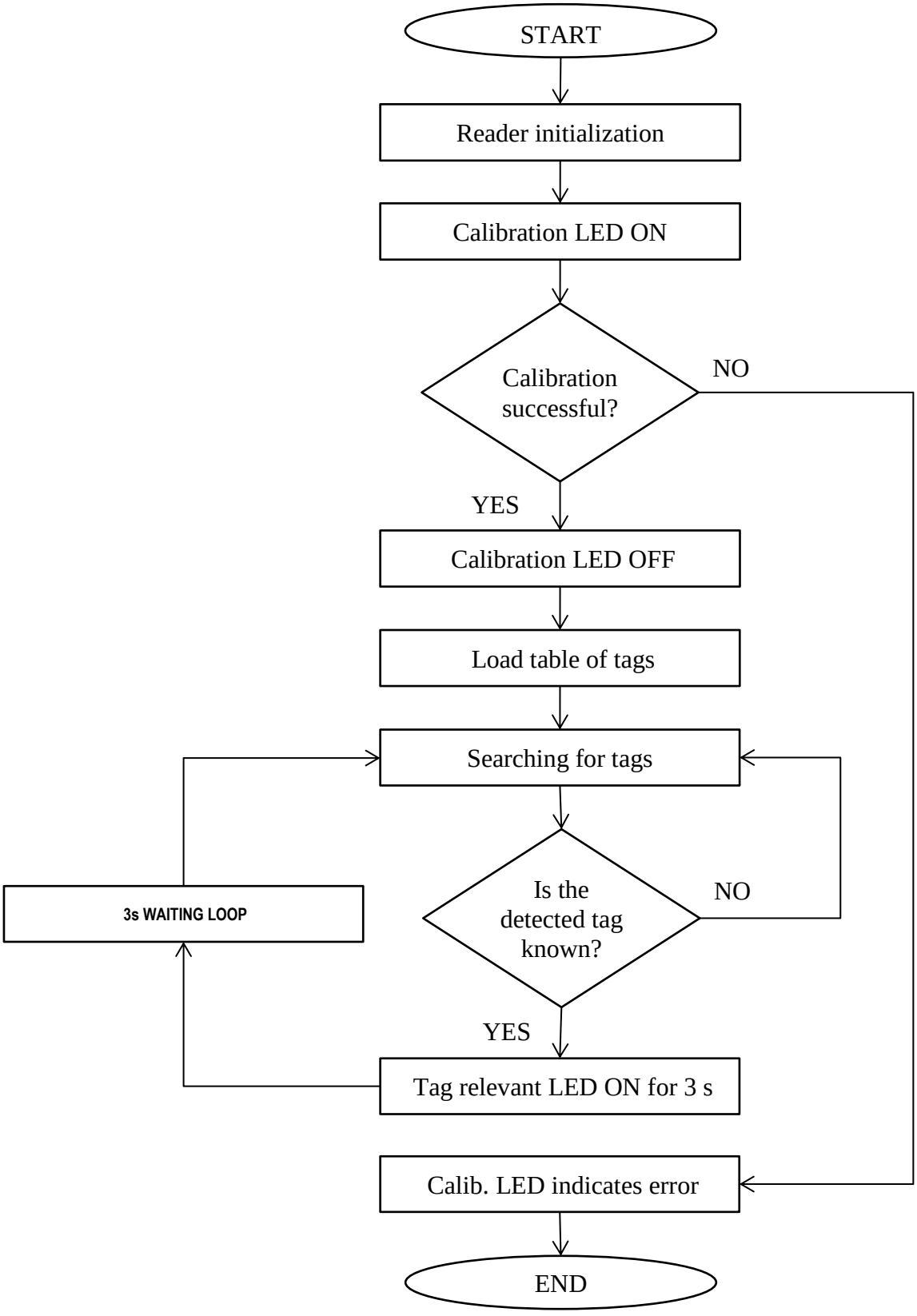

Fig. 58 – RFID tag detector controlling algorithm flowchart

5.1.4.5 Switched-mode operating voltage regulator

The switched-mode operating voltage regulator was constructed in order to observe its influence on the quality of RFID tags detection. The MC34063 controller was used owing to its nonsynchronous mode of operation, which results in a wide spectrum of generated interfering signals. Similar to the above mentioned linear voltage regulator, also this voltage regulator can be fitted directly on the main board of the RFID tag detector. Its nominal output voltage is 3.3 V and the nominal operating frequency is 30 kHz.

The circuit diagram of the switched-mode operating voltage regulator is depicted in Fig. 59. The controller is labelled as IC201 and its connection was designed according to the application note provided by its manufacturer [40].

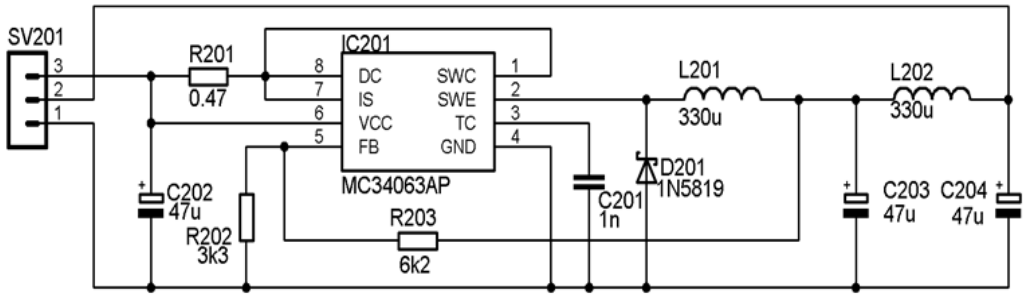

Fig. 59 – Switched-mode operating voltage regulator

The SV201 connector serves for fitting the board of the voltage regulator on the main board of the RFID tags detector. The R201 resistor adjusts the sensitivity of the overcurrent protection as follows. The overcurrent protection is activated provided the difference of voltage levels between the IC201 pins complies with the following condition:

$$U_{VCC} - U_{IS} \geq 0.3 \pm 0.05\ [V] \tag{119}$$

The voltage difference is reached when the maximum allowed peak current through the SWC pin is reached. The maximum switched current is defined by the following equation:

$$I_{PK_{switch}} = 2 \cdot I_{OUT_{max}}\ [A] \tag{120}$$

The variables employed in (119) and (200) are as follows:

U_{VCC} - voltage at the VCC pin of the MC34063 controller [V],
U_{IS} - voltage at the IS pin of the MC34063 controller [V],
$I_{PKswitch}$ - maximum peak current flowing through the SW pin of the MC34063 controller [A],
I_{OUTmax} - maximum required output current delivered by the voltage regulator [A].

Provided the nominal threshold voltage of the overcurrent protection is 0.3 V, the following formula can be utilized to compute the value of the R201 resistor:

$$R_{201} = \frac{0.3}{2 \cdot I_{OUT_{max}}} = \frac{0.3}{2 \cdot 0.3} \cong 0.47\ [\Omega] \tag{121}$$

Provided the overcurrent protection is not in duty, the output voltage of the voltage regulator is defined by the ratio of R203 and R202 resistors as follows:

$$U_{OUT} = 1.25 \cdot \left(1 + \frac{R203}{R202}\right) = 1.25 \cdot \left(1 + \frac{6200}{3300}\right) \cong 3.6\ [V] \tag{122}$$

The inductance of the accumulation inductor L201 is determined by the required output current, operating frequency and ripple current through the inductor. Generally speaking, the higher inductance of the inductor, the better for decreasing the ripple current but the worse for losses in the inductor's wiring. Therefore, a compromise is usually applied, by determining the sufficient inductance so that the ripple current is acceptably low. The following formula can be applied in order to determine the smallest inductor needed to keep the voltage regulator operating in the continuous mode:

$$L_{min} = \left(\frac{U_{IN_{min}} - U_{SAT} - U_{OUT}}{2 \cdot I_{OUT_{max}}}\right) \cdot t_{ON_{max}} \quad [H] \tag{123}$$

Where:

L_{min} - minimum inductance [H],
U_{INmin} - minimum voltage at the input of the circuit [V],
U_{SAT} - saturation voltage between collector and emitter of the switching device (transistor) [V],
U_{OUT} - output voltage [V],
I_{OUTmax} - maximum required output current delivered by the voltage regulator [A],
t_{ONmax} - maximum time in which the switching device (transistor) is on [s].

The time t_{ONmax} is determined by the C201 capacitor according to the following equation:

$$C_T = 4 \cdot 10^{-5} \cdot t_{on} \Longrightarrow t_{on} = \frac{C_T}{4 \cdot 10^{-5}} = \frac{10^{-9}}{4 \cdot 10^{-5}} = 2.5 \cdot 10^{-5}[s] \tag{124}$$

Once the time t_{ON} and the minimum input voltage are known, the L201 inductance can be computed, taking into account that it should be considerably

higher than the minimum inductance L_{min} in order to limit the current ripple. The following formula was applied:

$$L_{201} \geq 10 \cdot L_{min} = \left(\frac{4.8 - 0.8 - 3.6}{2 \cdot 0.3}\right) \cdot 2.5 \cdot 10^{-5} \geq 10 \cdot 1.7 \cdot 10^{-5} \approx 330\ [\mu H] \quad (125)$$

5.1.4.6 Antenna

The RF antenna design exceeds the scope of this paper. Therefore, for the purposes of this unit, the copy of an antenna operating successfully in other RFID system was utilized.

It is expected to have the same parameters, provided the dimensions, shape and materials are as similar as possible.

The antenna is placed on a separated board the dimensions of which are 100 x 100 mm. It can be connected perpendicularly to the main board by means of the SV302 connector.

5.2 Software application

In the framework of the minor software blocks, an application that allows communication between the Module for communication with the ground station and the ground station was created. This application allows the authorised user to establish the communication with the Autonomous monitoring system, which includes receiving the camera pictures and sending commands by means of which the Autonomous monitoring system can be manually controlled.

The application is run on the local server that can access the WiFi network in the range of which the Autonomous monitoring system operates. The user interface is based on the website of this server that uses PHP5, HTML4, CSS and JavaScript.

If the user is unauthorised, only the picture from the web camera can be viewed. In order to get the full access, the operator must be authorised. After authorisation the controlling functions are available, as depicted in Fig. 60. Through the web interface, the camera view can be zoomed to the centre of the picture in the following steps: 1x, 2x, 3x, 4x. Moreover, the controlling commands can be generated by pressing the buttons that are displaced around the camera view. The user can use a total of 7 buttons:

- Ascension (Nahoru),
- Descension (Dolů),
- Counter-clockwise rotation (Vlevo),
- Clockwise rotation (Vpravo),
- Move forward (Vpřed),

- Move backward (Zpět),
- Light (Světlo).

The number of buttons as well as their functions can be revised in the future. In the current mode up to 8 commands can be sent to the Autonomous monitoring system but after minor revisions this number can be increased by improving the communication protocol. Moreover, the backward data transmission can be established to gain information from the Autonomous monitoring system, for example on the pressure, temperature, RF fields strength etc., depending on the monitoring device mounted on the Autonomous monitoring system.

In the Configuration section, the following settings can be made:

- IP address of the camera,
- port of the IP camera,
- mode of the buttons' operation.

Fig. 60 – Autonomous monitoring system web interface – manual control mode

As listed above, the buttons' operating mode can be switched to one of the following options:

- Timer – once the button is clicked on, it remains active for a period set in the Configuration menu. The appropriate output of the IP relay is active for this period.
- On/Off – once the button is clicked on, it remains active until it is clicked on again (toggle button).

Fig. 61 – Autonomous monitoring system web interface – camera view

5.3 Final hardware design

The final hardware design consists of creating a complex circuitry that integrates all the modules introduced in the chapter "Minor hardware modules". One central microcontroller is intended to be employed, covering all the above mentioned functionalities.

As the load capacity of the airship is limited, it seems to be convenient to design the printed circuit boards of the controlling circuitry in such a way to make it work as the self-supporting construction and the main bearing element of the camera and the connected sensors. Even in this case the hardware can consist of more separated boards connected together by means of solid connectors. The following set of boards is expected to be utilized:

- Switched-mode operating power supply,
- Central controller board,
- IP relay Charon I (described above),
- Separately mounted IP camera and WiFi router.

5.3.1 Power supply source

The power for the Autonomous monitoring system is supplied by a lightweight Li-Ion accumulator. Its nominal values are:

- Nominal voltage: 7.2 V,
- Nominal capacity: 2.4 Ah.

If the load is lower than the maximum load capacity, more accumulators of this type can be used, provided they are connected in parallel.

Unfortunately, different hardware parts require different supply voltages, which must be reflected in the power source design. In order to reach the required efficiency, the stabilized supply branches are fed by switched-mode operating voltage regulators, while the motors are fed directly by the accumulators.

The requirements on the power supply source are as follows:

- Direct power supply to the motors so that high efficiency was achieved,
- 3.3 V / 1 A output for RFID tags detectors and other optional modules,
- 5.0 V / 1 A output for the central microcontroller, ultrasonic detectors, WiFi router, IP relay Charon I, motor controller and other optional modules,
- 12.0 V / 0.5 A output for the IP camera.
- The accumulator must be protected from the deep discharge.

As the accumulator consists of two 3.6 V cells, the deep discharge protection must check the condition of both of them. The deep discharge protection is expected to generate two types of signals:

- Warning – if the voltage of any of the cells drops below 3.0 V, the warning signal is generated. This signal is then processed by the controller of the Autonomous monitoring system. For example, on the basis of this signal the controlling algorithm can be switched to the mode that ensures that the Autonomous monitoring system returns to the starting point at which the accumulator can be charged or replaced.
- Emergency – if the voltage of any of the cells drops below 2.85 V, the emergency signal is generated, causing the disconnection of all circuits from the accumulator. In this case, the Autonomous monitoring system is in an “emergency off” state, and being uncontrolled, it descends to the ground by its own weight. This is because the cells of the accumulator can be irreversibly damaged in case their voltage drops below 2.75 V.

Based on the analysis of fluctuation of voltage at the accumulator terminals, the range of input voltage of the power supply source is determined; the power supply source must feed the appropriate power supply branches by the nominal voltages within the range of the input voltage from 5.0 to 9.0 V. For this reason, the more complex SEPIC (single-ended primary-inductor converter) topology was chosen for the power source design instead of simple buck and boost converters. The advantages of this solution are as follows:

- The same voltage converter can increase or decrease the voltage level. This is very useful in case of the 5.0V branch that cannot be fed by the buck converter as if the accumulator was almost discharged, its voltage would not be sufficient enough to cover the voltage drop on the voltage regulator.
- As the energy is transferred via a capacitor, when not oscillating, the circuit feeds the connected devices by no voltage. This is very useful in case of 12 V branch, because if the simple boost converter was used, when stopped at its output, there would still remain the accumulator's voltage. The power source based on this structure can be switched off by simple halting of the oscillator. This enables an easy implementation of the "Emergency off" function.

In order to minimize interferences produced by the power supply source it is required to operate all three power supply branches synchronously. When operated at a single frequency, the voltage regulation is maintained by changing the duty cycles of the appropriate switches. For this purpose monolithic SMPS controllers LT1171 were selected as they can be synchronized externally.

The block diagram of the power supply unit of the Autonomous monitoring system is depicted in Fig. 62. The accumulator is connected to the power supply board by means of cables – the power one and the voltage measurement supporting one. The power cable delivers the power to motors as well as well as to three switched-mode operating power supply voltage regulators. The voltage measurement cable supplies the low-power comparators that have the capability of generating the warning and emergency shutdown signals. While the warning signal is delivered to the output connector, the emergency shutdown signal turns the voltage regulators off immediately. Once it occurs, the emergency shutdown signal can only be discontinued by disconnecting the accumulator. The synchronization of the SMPS controllers is provided by the synchronization block that ensures that the individual controllers are triggered at the defined moments, as described in the following chapter. On the power supply board there is also the motor driver implemented to make the power lead from the accumulator to the motors was as short as possible.

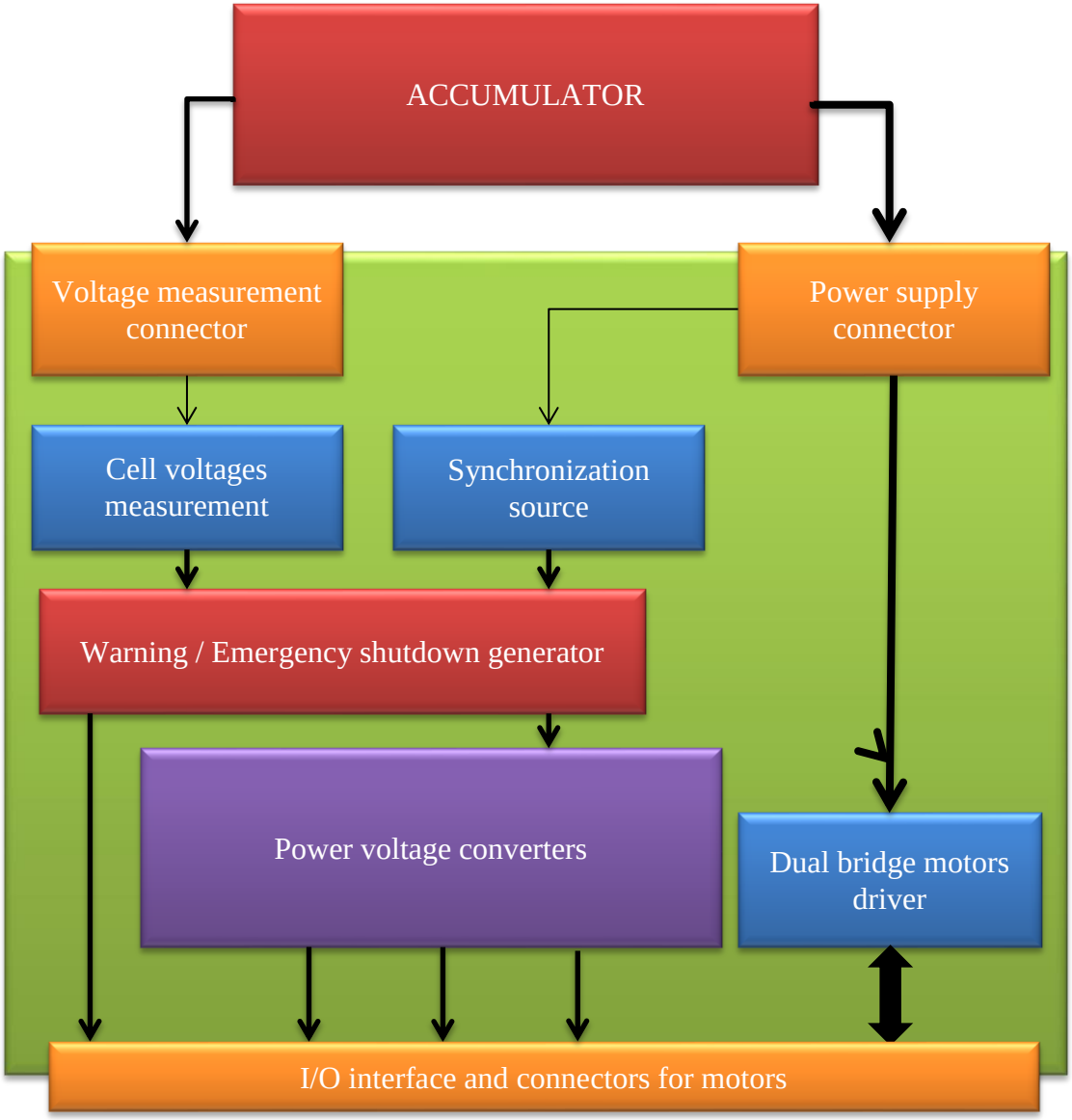

Fig. 62 – Power supply board block diagram

The Power supply source board must be equipped with the following interfaces:

- Power supply connector (2 pins),
- Voltage measurement connector (3 pins),
- I/O interface pin stripe connecting the board to the main board (for description of pins see Tab. 8),
- Servo connector (3 pins),
- Tail motor connector (2 pins),
- Main motors connector (2 pins).

The I/O interface pin stripe consists of many pins whose purpose is described in the following table.

Table 8 – Power supply board I/O interface pins description

Pin	Description
1	GND
2	3.3 V power supply
3	5.0 V power supply
4	12.0 V power supply
5	Low-accumulator warning signal (TTL level H) Total accumulator voltage (0.6 – 0.9 V)[1]
6	Motors controlling bus (1) (TTL level)
7	Motors controlling bus (2) (TTL level)
8	Motors controlling bus (3) (TTL level)
9	Motors controlling bus (4) (TTL level)
10	Motors controlling bus (5) (TTL level)
11	Motors controlling bus (6) (TTL level)
12	Servo controlling signal (TTL level)

5.3.1.1 Voltage regulators time synchronisation principle

There are three different switched-mode operating voltage converters intended to be employed on the power supply board. It is convenient to make them operate synchronously in defined time shifts among their triggering pulses. All three voltage regulators are based on LT1172 voltage controllers. When triggered at different time periods, a sum of current ripples at the output of the accumulator can be obtained that shows a considerable DC component. In this chapter the synchronisation principle is described together with advantages it brings.

There is a set of equations below according to which the duty cycles of all three voltage regulators can be estimated. The considerations are as follows:

- The duty cycles are estimated for minimum (5 V) and maximum (9 V) input voltage,
- The load of the voltage converters is "nominal", which means 1.0 A for 3.3 V and 5.0 V branch and 0.5 A for 12 V branch.

[1] As the motors are fed directly by the accumulator, their output power depends not only on the duty cycle of the controlling signals but also on their supply voltage. The dynamic model of the Autonomous monitoring system, which is described in the theoretical part of this paper and according to which the trajectory is predicted, requires the accurate information on the output power of the propellers. Unfortunately, this information can be gained only indirectly from the information on the duty cycle of the controlling signals driving the bridge motor driver. For this reason, the information on the supply voltage is required as well. In order to minimize the number of pins and to make the I/O interface more universal, one pin is used for giving the information on the accumulator's voltage as well as for generating the signal that warns that the accumulator is discharging. Provided the accumulator is not close to the state of deep discharge, the voltage at the pin 4 of the I/O interface refers to the voltage on the accumulator. From the view of TTL signals the level is always LOW. If one of the accumulator cells gets close to the state of deep discharge, the warning signal is generated by overdriving this output and pulling it to the TTL HIGH state.

- The voltage drop on the Schottky diodes is U_D = 0.4 V.

$$D_{3.3V_{min}} = \frac{U_{OUT} + U_D}{U_{IN_{max}} + U_{OUT} + U_D} = \frac{3{,}3 + 0{,}4}{9 + 3{,}3 + 0{,}4} = 0{,}291 \approx 29\ \% \quad (126)$$

$$D_{3.3V_{max}} = \frac{U_{OUT} + U_D}{U_{IN_{min}} + U_{OUT} + U_D} = \frac{3{,}3 + 0{,}4}{5 + 3{,}3 + 0{,}4} = 0{,}425 \approx 43\ \% \quad (127)$$

$$D_{5V_{min}} = \frac{U_{OUT} + U_D}{U_{IN_{max}} + U_{OUT} + U_D} = \frac{5 + 0{,}4}{9 + 5 + 0{,}4} = 0{,}375 \approx 38\ \% \quad (128)$$

$$D_{5V_{max}} = \frac{U_{OUT} + U_D}{U_{IN_{min}} + U_{OUT} + U_D} = \frac{5 + 0{,}4}{5 + 5 + 0{,}4} = 0{,}519 \approx 52\ \% \quad (129)$$

$$D_{12V_{min}} = \frac{U_{OUT} + U_D}{U_{IN_{max}} + U_{OUT} + U_D} = \frac{12 + 0{,}4}{9 + 12 + 0{,}4} = 0{,}579 \approx 58\ \% \quad (130)$$

$$D_{12V_{max}} = \frac{U_{OUT} + U_D}{U_{IN_{min}} + U_{OUT} + U_D} = \frac{12 + 0{,}4}{5 + 12 + 0{,}4} = 0{,}713 \approx 73\ \% \quad (131)$$

The maximum current consumptions of the voltage regulators are estimated under the following conditions:

- The efficiency of the voltage converter is 85 %,
- The input voltage is 5 V (as low as possible according to specifications),
- The voltage regulators have to deliver nominal output currents.

$$I_{IN_{3,3V}} = I_{OUT} \cdot \frac{1}{\eta} \cdot \frac{U_{OUT}}{U_{IN}} = 1 \cdot \frac{1}{0{,}85} \cdot \frac{3{,}3}{5} \cong 0{,}78\ [A] \quad (132)$$

$$I_{IN_{5V}} = I_{OUT} \cdot \frac{1}{\eta} \cdot \frac{U_{OUT}}{U_{IN}} = 1 \cdot \frac{1}{0{,}85} \cdot \frac{5}{5} \cong 1{,}18\ [A] \quad (133)$$

$$I_{IN_{12V}} = I_{OUT} \cdot \frac{1}{\eta} \cdot \frac{U_{OUT}}{U_{IN}} = 0{,}5 \cdot \frac{1}{0{,}85} \cdot \frac{12}{5} \cong 1{,}41\ [A] \quad (134)$$

Furthermore, if the operating frequency of the voltage regulators is estimated to be up to 125 kHz (the period T = 8 μs) and the current ripple is estimated to be up to ± 40 %, the currents flowing into the appropriate voltage converters can be described according to the following equations:

$$i_{IN_{3,3V}} = H\left(D_{3,3V}\cdot nT-(t+nT)\right)\cdot\left(0{,}6\cdot I_{nom_{3,3V}}+\left(\frac{0{,}8\cdot I_{nom_{3,3V}}}{D_{3,3V}\cdot T}\cdot(t+nT)\right)\right)+H\left((t+nT)-D_{3,3V}\cdot nT\right)\cdot\left(1{,}4\cdot I_{nom_{3,3V}}-\left(\frac{0{,}8\cdot I_{nom_{3,3V}}}{\left(1-D_{3,3V}\right)\cdot nT}\right)\cdot\left((t+nT)-D_{3,3V}\cdot nT\right)\right)\ [A],\qquad t\in\langle 0;T),n\subset\mathbb{Z}\qquad(135)$$

$$i_{IN_{5V}} = H\left(D_{5V}\cdot nT-(t+nT)\right)\cdot\left(0{,}6\cdot I_{nom_{5V}}+\left(\frac{0{,}8\cdot I_{nom_{5V}}}{D_{5V}\cdot T}\cdot(t+nT)\right)\right)+H\left((t+nT)-D_{5V}\cdot nT\right)\cdot\left(1{,}4\cdot I_{nom_{5V}}-\left(\frac{0{,}8\cdot I_{nom_{5V}}}{(1-D_{5V})\cdot nT}\right)\cdot\left((t+nT)-D_{5V}\cdot nT\right)\right)\ [A],\quad t\in\langle 0;T),n\subset\mathbb{Z}\qquad(136)$$

$$i_{IN_{12V}} = H\left(D_{12V}\cdot nT-(t+nT)\right)\cdot\left(0{,}6\cdot I_{nom_{12V}}+\left(\frac{0{,}8\cdot I_{nom_{12V}}}{D_{12V}\cdot T}\cdot(t+nT)\right)\right)+H\left((t+nT)-D_{12V}\cdot nT\right)\cdot\left(1{,}4\cdot I_{nom_{12V}}-\left(\frac{0{,}8\cdot I_{nom_{12V}}}{(1-D_{12V})\cdot nT}\right)\cdot\left((t+nT)-D_{12V}\cdot nT\right)\right)\ [A],\qquad t\in\langle 0;T),n\subset\mathbb{Z}\qquad(137)$$

The current waveforms described by the above mentioned equations were analysed in the Maple software. In the figures below the currents flowing into the particular voltage converters are depicted as well as their sum for two cases. The first case shows how these currents look like if all the converters are triggered at once while the second case shows the situation that occurs when the converters are triggered in mutually shifted periods.

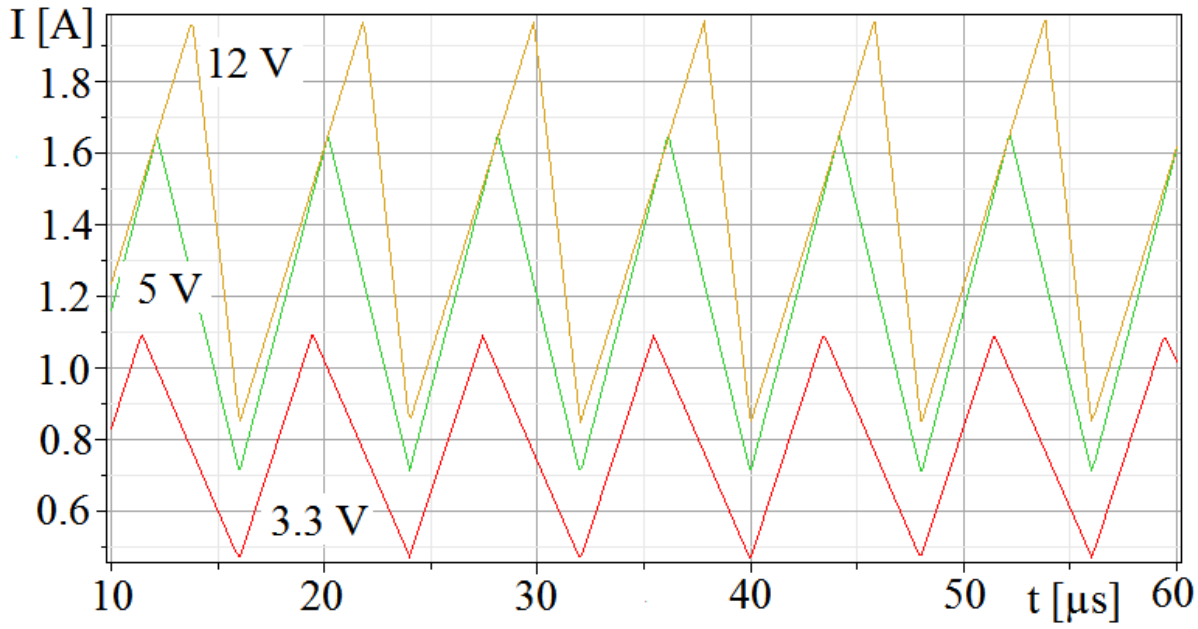

Fig. 63 – Currents drawn by voltage converters when triggered at the same time

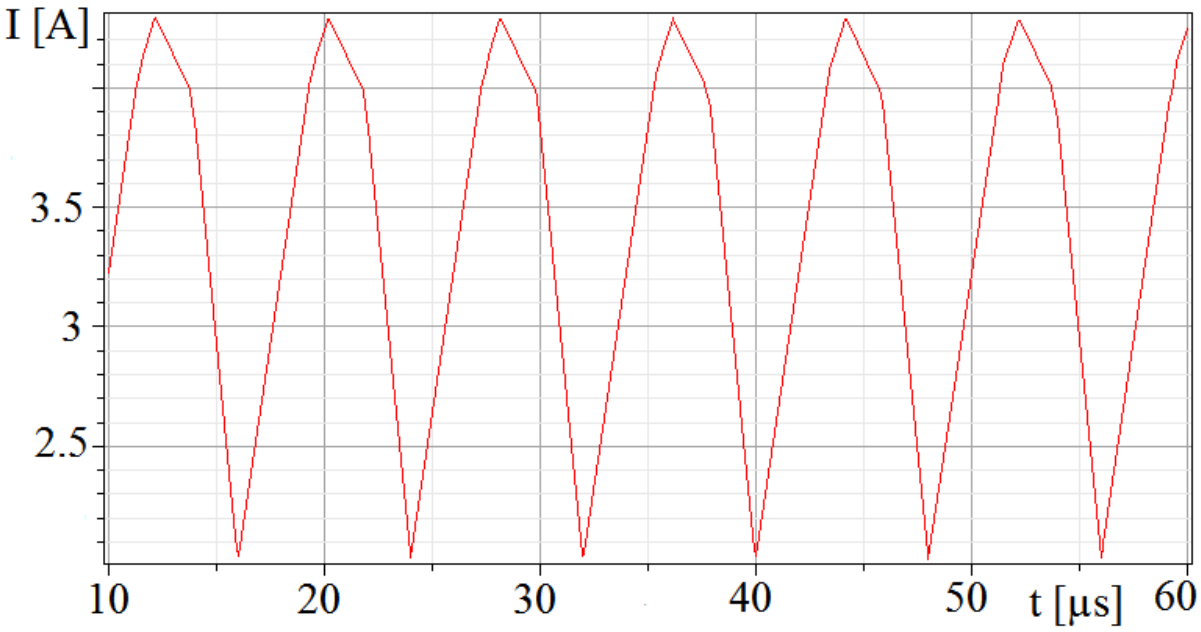

Fig. 64 – Sum of the currents drawn by the converters when triggered at same time

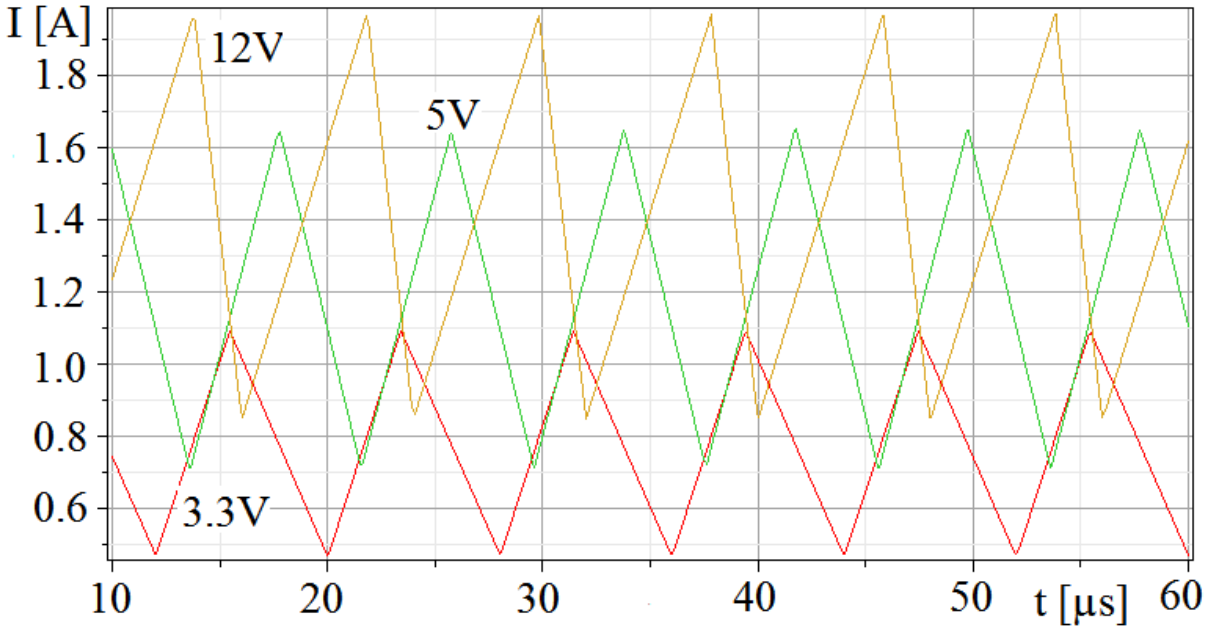

Fig. 65 - Currents drawn by voltage converters when the shifted triggering is applied

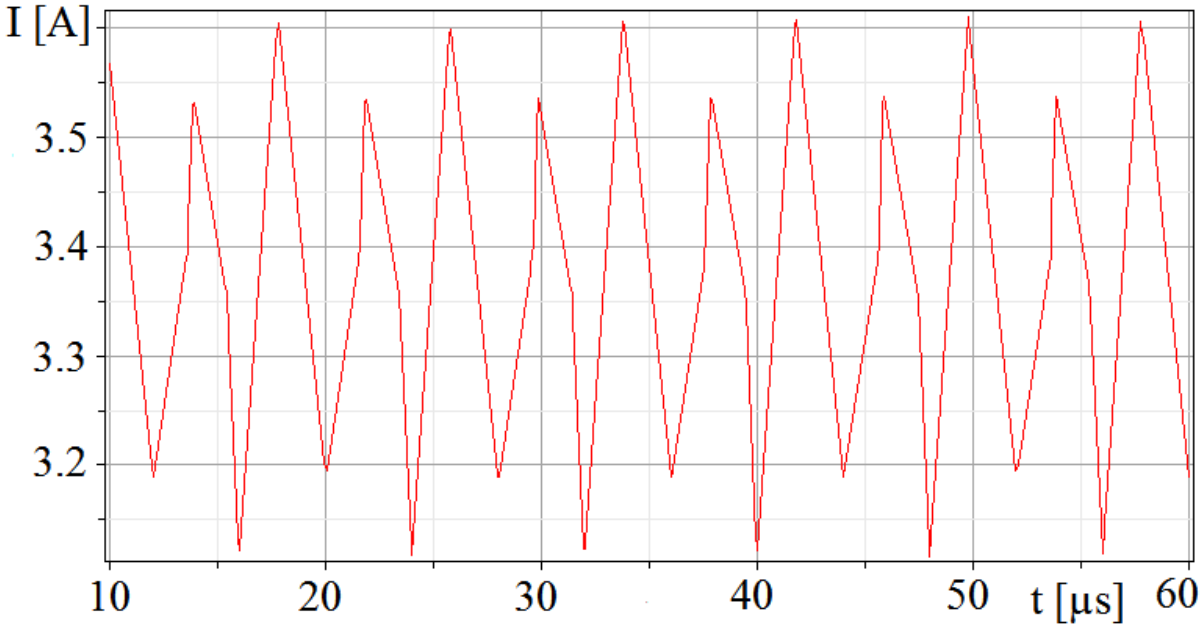

Fig. 66 - Sum of the currents drawn by the converters when shifted triggering is applied

Based on the above pictures the following conclusions can be made: If the triggering of the voltage converters is not optimized, the pulse component of the current drawn from the accumulator can be up to $\Delta I = 2.3$ A. Moreover, it is obvious that the current ripple is mostly caused by the 12 V and 5 V branches. Therefore, it is convenient to shift the triggering time of the 5 V branch in such a way so that the maximum peak in the 5 V branch meets the minimum peak in

the 12 V branch. Obviously, there is a need to find a compromise that allows simple construction of the triggering circuit. For the purpose of this paper dividing the period of the converters operation by ten was chosen. The tenths of the basic clock signal can be generated simply by the Johnson's counter. The following time shifts were defined[2] by modelling:

- 12 V branch voltage converter is triggered in t = (nT + 0) μs,
- 5 V branch voltage converter is triggered in t = (nT + 2.4) μs,
- 3.3 V branch voltage converter is triggered in t = (nT + 4.0) μs.

The resulting waveforms are depicted in Fig. 65. In Fig. 66 the waveform of the current drawn from the accumulator is depicted. It is obvious that the pulse component is lowered from $\Delta I = 2.3$ A to $\Delta I' = 0.5$ A, thus by 78 %. In practice, the effective decrease of the pulse component will be lower because the timing of the voltage converters is fixed and does not reflect the load or input voltage variability. This is a compromise between simple construction and ideal conditions. Nevertheless, every decrease of the pulse component in the current drawn by the voltage converters brings the following positive effects:

- The pulse load on the accumulator is declined, resulting in its higher lifetime,
- The pulse component of the drawn current flowing through the cable between the accumulator and the power supply board is decreased, which results in lower emitting of interfering electromagnetic field.
- The pulse current through the decoupling capacitor on the power supply board is decreased, which has several positive effects:
    - The capacity of the decoupling capacitor can be lower,
    - The capacitor is subjected to a smaller ripple current, which results in its higher lifetime.

Furthermore, the amount of the pulse component was modelled for the above mentioned triggering for the cases in which the loads of the voltage converters are still nominal, but the accumulator voltage varies in the following steps: 5, 6, 7, 8 and 9 V. Fig. 67 depicts the level of the pulse component at these voltages for the case of triggering at the same time and for the case of shifted triggering. The calculated points are interleaved with a curve base on the 4^{th} order polynomial. It can be observed that the pulse component of the current drawn from the accumulator is decreased at any supply voltage.

The modelling was done for the nominal loads of the voltage regulators, because it was expected that under less loads the supply current would also be lesser, resulting in the smaller pulse component.

[2] The nominal operating frequency is expected to be up to 125 kHz, resulting in 8 μs period. The oscillator frequency then must be up to 1.25 MHz, resulting in the time shift steps of 0.8 μs.

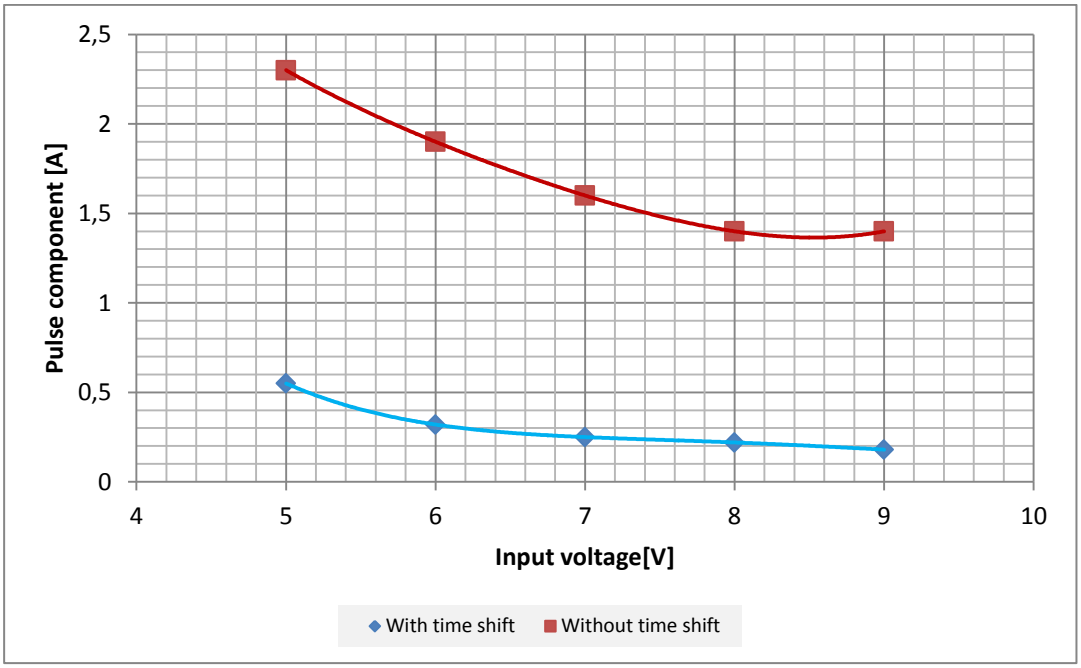

Fig. 67 – Comparison of the pulse components in the accumulator current

As the triggering circuit is a part of the set of voltage converters, its simulation is described together with the simulation of the voltage converters in one of the chapters below.

5.3.1.2 Accumulator disconnector

While the power part of the Power supply board can be switched off by stopping the oscillations of the voltage converters, the accumulator management circuits must be connected to the accumulator to enable this. In order to protect the accumulator from the deep discharge risk, the controlling circuits must be fed via a disconnector that disconnects the accumulator when its voltage is dangerously low.

A simple low-current voltage dependent switch is depicted in Fig. 68a. Its expected behaviour was simulated. The result is depicted in Fig. 68b. At voltages lower than approximately 5.7 V (2 x 2.85) the power supply to the cells measurement circuit is rapidly limited, protecting the accumulator from deep discharge that might occur if the cell measurement circuit was connected to the measured cells for a long period of time. The threshold voltage of the LED1, depicted in Fig. 68a, must be 3 V. Otherwise the resistors R3 and R4 must be of different values in order to ensure the proper function of the circuit. Also, the LED1 must be of a low-current type, operating at approximately 2 mA. By simulation it was verified that the current drawn from the accumulator approaches zero provided the accumulator voltage is below 5.5 V. The estimated maximum current drawn by the controlling circuits is 10 mA and should be as low as possible.

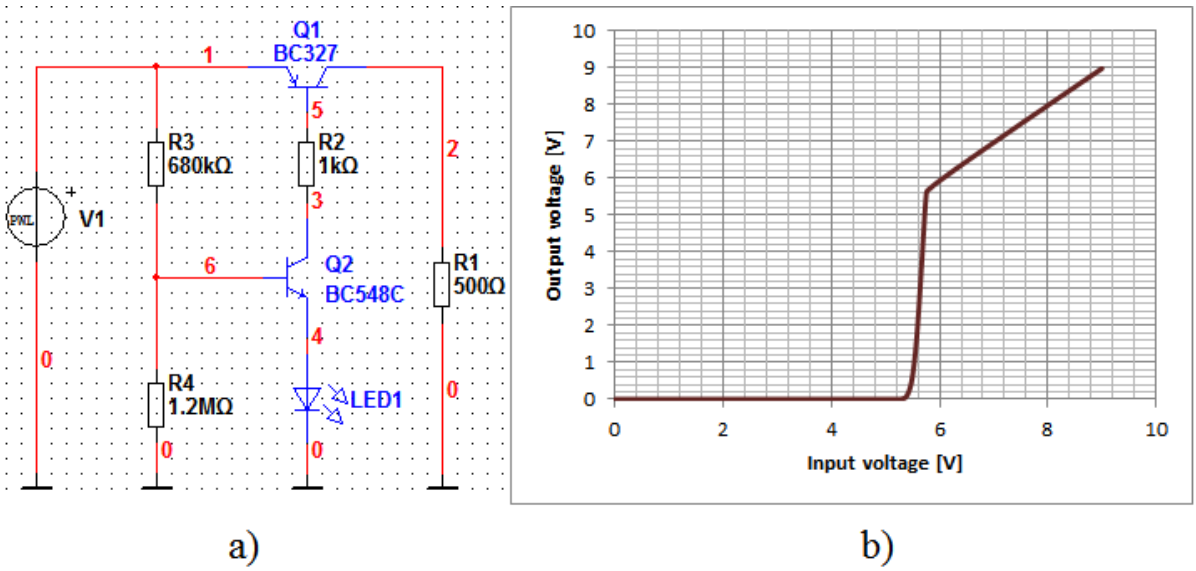

Fig. 68 – Cells measurement power supply disconnector (a) and its typical behaviour (b)

5.3.1.3 Measuring of the lower cell voltage

As the voltage of the worse cell must be measured, the worse cell selector was designed. At the output of this circuit the voltage of the worse of the cells is always present. The simulation schema of this circuit is depicted in Fig. 69.

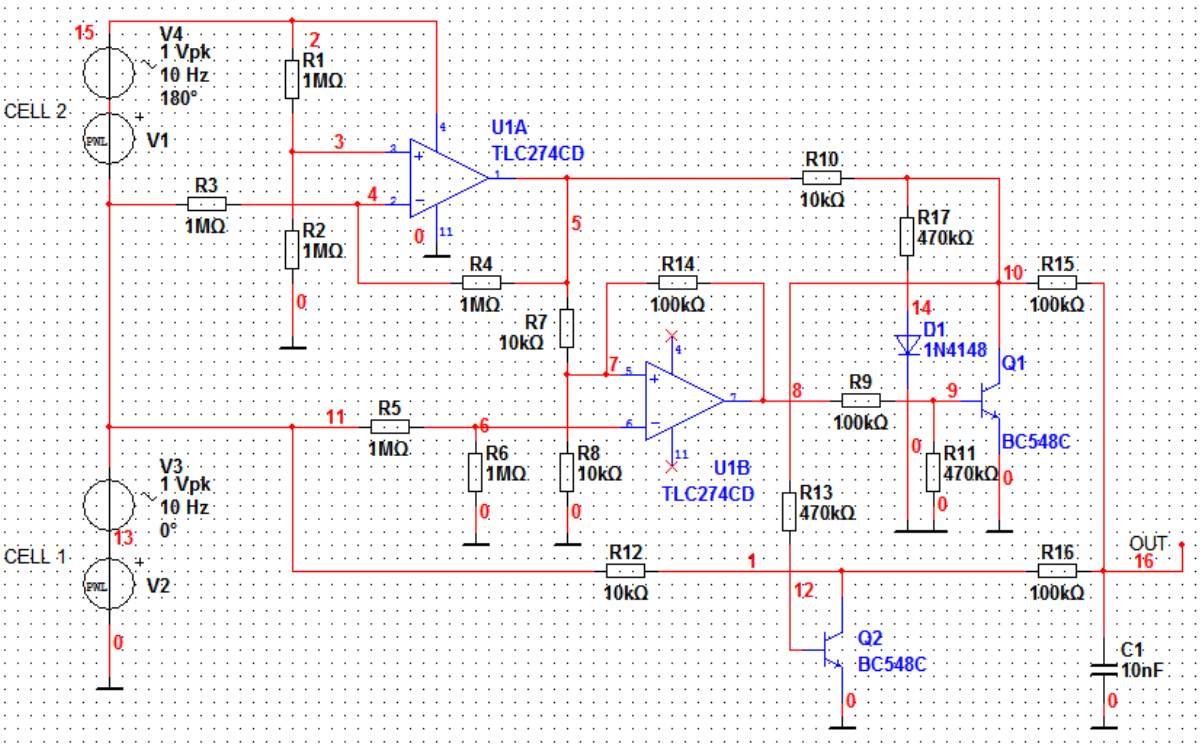

Fig. 69 – Worse cell selector simulation circuit diagram

The principle of the worse cell selector is as follows. Both cells are represented by the voltage sources V1 and V2. Additive sinusoidal voltage sources operating in antiphase are also added to simulate the differences between the cells. During the simulation, the DC voltage of both cells is simultaneously increased from 2.5 to 5.0 V, being wobbled by the sinusoidal voltage generated by the V3 and V4 voltage sources. The CELL1 voltage is measured directly to the ground while the CELL2 voltage is measured by the differential amplifier, implemented on the basis of U1A operational amplifier. The comparison of the cell voltages is processed by the U1B comparator, utilizing a slight hysteresis defined by a R14 resistor. According to the state of the comparator's output, either transistor Q1 or transistor Q2 is driven. These transistors create short-circuits of the voltage measured on the better cell to the ground via the resistors R10 or R12 respectively. The voltage at the output of the summation circuit created by resistors R15 and R16 is then always proportional only to the voltage of the worse cell. As the node 10, when not shorted to the ground, is loaded with the R13 resistor and the base of the Q2 transistor, a compensation for the second branch must be introduced. This compensation is created by the R17 resistor and D1 diode.

In order to prove the behaviour of the circuit, transient simulation was processed, considering the voltage at the cells is changing in time. The simulation results are depicted in Fig. 70. Obviously, the voltages at the cells are varying and the voltage of the worse cell is always present at the output of the circuit.[3]

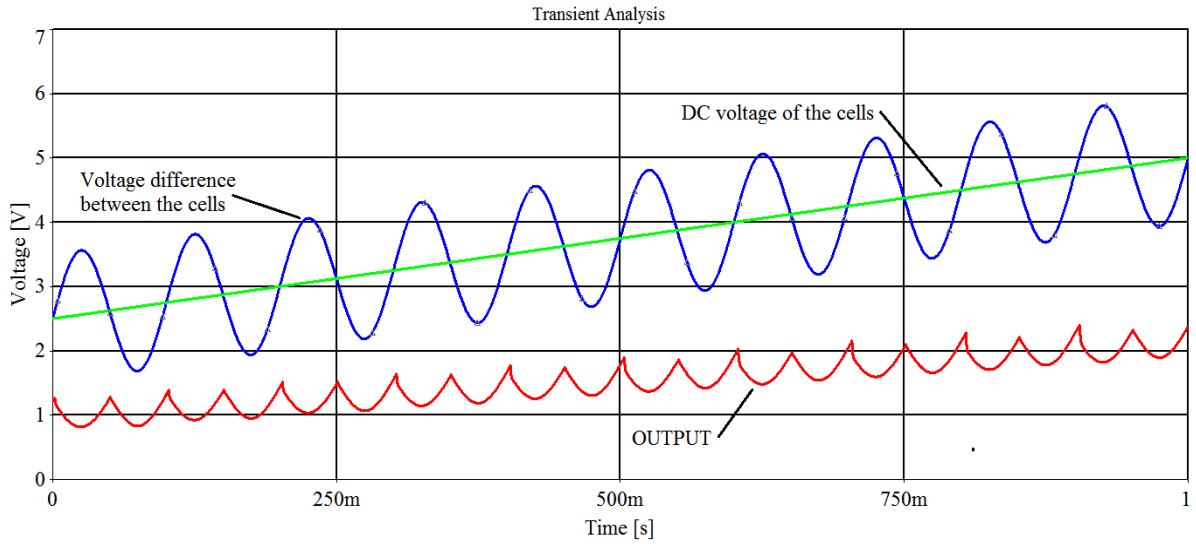

Fig. 70 – Worse cell selector simulation results

[3] The „worse cell" refers to that cell of the accumulator whose voltage is lower.

5.3.1.4 Generator of Warning and Emergency shutdown signals

This circuit utilizes the output of the worse cell selector and by comparing it to the accurate voltage reference it generates the Warning and Emergency shutdown signals. While the Warning signal is present at the output of the Power supply board, the Emergency signal is used only internally to block the voltage regulators.

Both signals are generated by comparators that are supplied from the accumulator disconnector and fed by accurate reference voltages. The required specification of the Warning and Emergency signals is described in Tab. 9.

Table 9 – Accumulator management output specifications

Signal	**Specification**
Warning	TTL-H if voltage of any cell is lower than 3.0 V
Emergency shutdown	TTL-L if voltage of any cell is lower than 2.85 V
Total voltage	0.6 to 0.9 V signal referring to the accumulator voltage between 6 and 9 V. This signal is overridden with the Warning signal if the voltage of any cell drops below 3.0 V.

Whereas the Warning signal is represented by the TTL-H value, the Emergency shutdown signal is represented by the TTL-L value. This simplifies the construction of the voltage converters that can simply be connected directly to the accumulator and to be switched off when there is not enough voltage to pull them into active state. The TTL-L level can be achieved by two ways:

- The voltage is low enough to drive the output of the comparator to the L state.
- The voltage is too low and the accumulator management circuits are turned off by the accumulator disconnector.

The simulation schema of the Warning and Emergency shutdown generator is depicted in Fig. 71. The output of the Worse cell selector is simulated for the following devices: R6, R3, R4, R7, D1, Q1 and R5. This respects the behaviour of the worse cell switch. The measured cell is simulated by the V3 voltage source the voltage of which varies in time within 5.0 to 2.0 V and back.

The simulation revealed that the simulator does not respect the collector-to-emitter voltage of the Q1 transistor. Owing to that the simulation may not be accurate enough. This inaccuracy is intended to be compensated by utilizing the programmable voltage reference that is represented by the voltage source V2. Adjusting the reference voltage modifies the threshold of both comparators.

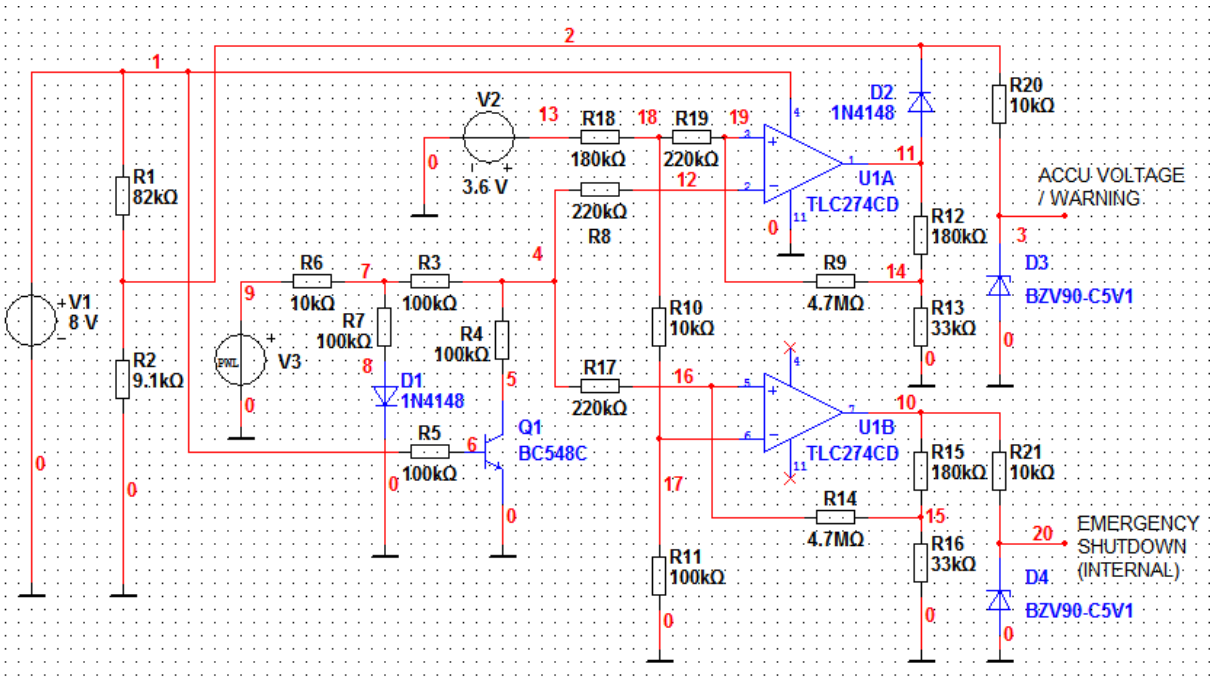

Fig. 71 – Warning and Emergency shutdown signals generator simulation schema

The U1A operational amplifier is connected as a comparator that generates the Warning signal. The warning signal is carried to the output via the D2 diode. If the comparator is in the L state, only the voltage referring to the state of the accumulator is present at the appropriate output. This voltage is defined by the 9:1 division ratio of the voltage divider created by the resistors R1 and R2. If the comparator output is in the H state, it forces the output to the TTL-H level via the D2 diode. As the output voltage of the comparator is dependent on its supply voltage, the output voltage is limited by the D3 Zener diode.

The U1B operational amplifier is also connected as a comparator generating the Emergency shutdown signal. This signal is then distributed to the voltage converters placed on the Power supply board. Its level is also limited to the maximum of 5 V by means of the D4 Zener diode.

Both comparators utilize weak positive feedbacks preventing them from oscillating if the input voltage is close to the comparison threshold. These feedbacks are damped with 6.5:1 voltage dividers placed at the outputs of the comparators.

The performance of the generator is depicted in Fig. 72. It is obvious, that when the weaker cell voltage lowers below 3.0 V, the Warning signal is generated. For the voltages below 2.85 V also the Emergency shutdown signal is generated. The emergency shutdown signal is represented by the negated value, making it similar to the state in which the controlling circuits are disconnected by the accumulator disconnector due to very low voltage on the accumulator.

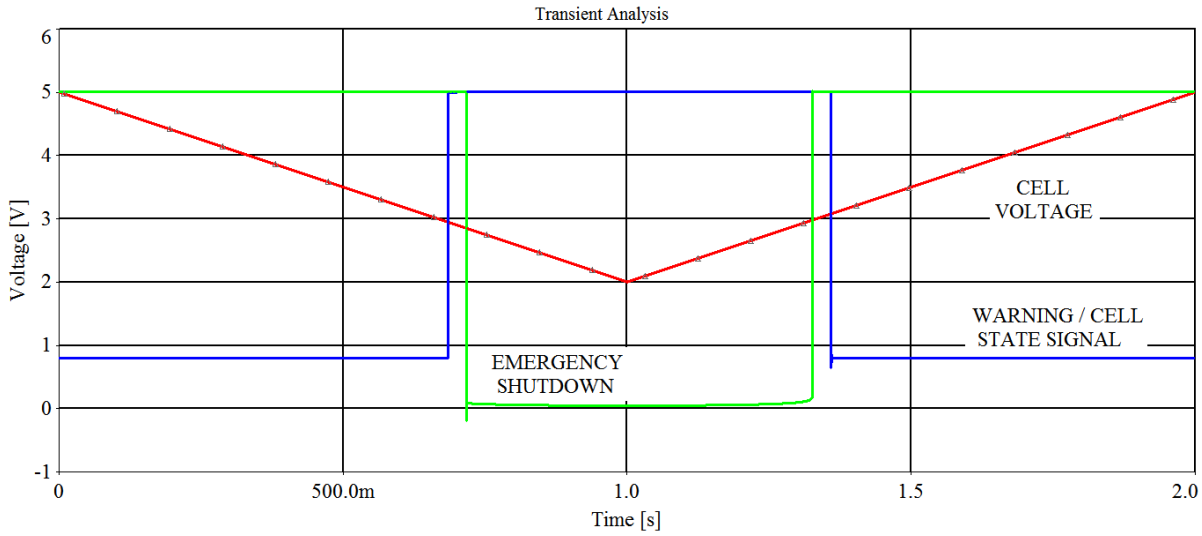

Fig. 72 – Warning and Emergency shutdown signals generator simulation results

5.3.1.5 Voltage regulators design

As previously stated, there are three different voltage regulators operating in the switched mode. The regulators are all based on the LT1172 controllers and their topology is also identical. They differ only in the device values. Therefore, in the text below only a design of the 5V branch voltage regulator is described in details. For two other regulators only additional notes are provided.

The design is based on the SEPIC topology, utilizing the information given by the manufacturer of the LT1172 chips in the appropriate datasheet [43]. Although in comparison with other topologies the efficiency of the SEPIC voltage converters is lower, they were chosen for their following advantages:

- The output of the voltage regulator is always disconnected for DC currents when the regulator is not clocked.
- The output voltage can be lower or higher than the input voltage in the same topology.
- The output polarity is not inverted.

The basic circuit diagram of the voltage regulator was simulated in LT Spice IV software. This is a freeware circuit simulator based on SPICE libraries, modified by the LT1172 manufacturer. Unfortunately, the external synchronization cannot be simulated here. Only the 100 kHz internal oscillator embedded in the chip is utilized. Moreover, there are some features of the controller that are simultaneously controlled via its VC pin and not all of them can be simulated at once. These functions are as follows:

- Soft start
- Overcurrent protection
- Synchronization

The overcurrent protection and soft start functionality are tied together as the maximum current through the accumulating inductor is limited by the voltage at

the VC pin. Unfortunately, the peak values of the current through the inductor depend not only on the output current of the converter but it is inversely proportional to the supply voltage as well.

The basic simulation diagram of the 5V converter is depicted in Fig. 73. The device values were determined according to the following computations and assumptions.

The Schottky diode D1 is MBRS340. Its reverse breakdown voltage is up to 40 V and its forward voltage is expected to be at least 0.4 V. According to (127) and (130), the duty cycle at the maximum load can vary from approximately 38 % to approximately 52 %. The maximum allowed current ripple at the inductors was considered to be no higher than ±15 %, thus 30 %. The ripple current can be expressed as follows:

$$\Delta I_L = I_{OUT} \cdot \frac{U_{OUT}}{U_{IN(min)}} \cdot 30\% = 1 \cdot \frac{5}{5} \cdot 0.3 = 0.3\ [A] \qquad (138)$$

According to this knowledge the minimum inductance of the inductors can be calculated:

$$L_{min} = \frac{U_{IN(min)}}{\Delta I_L \cdot f_{sw}} \cdot D_{(max)} = \frac{5}{0.3 \cdot 10^5} \cdot 0{,}52 = 3.25 \cdot 10^{-5} = 86.7\ [\mu H] \qquad (139)$$

Unfortunately, the simulator does not support the simulation of the externally synchronized circuit operating at the frequency of 125 kHz. Instead, only 100 kHz operating frequency is expected. Therefore, the f_{SW} parameter was considered to be 100 kHz. However, it is reasonable to choose one of the standardized inductor values. Moreover, according to (139) the minimum required inductance is inversely proportional to the operating frequency f_{SW}. Let us therefore consider the application of 100 µH inductors in the real application that are replaced by 125 µH inductors for the purpose of the simulations. Then the peak currents in the simulation will be equal to the peak currents obtained in the real circuits. The calculation of the peak currents is as follows:

$$I_{L1(peak)} = I_{OUT} \cdot \frac{V_{OUT} + V_D}{V_{IN(min)}} \cdot \left(1 + \frac{30\%}{2}\right) = 1 \cdot \frac{5 + 0.4}{5} \cdot 1.15 = 1.24\ [A] \qquad (140)$$

$$I_{L2(peak)} = I_{OUT} \cdot \left(1 + \frac{30\%}{2}\right) = 1 \cdot 1.15 = 1.15\ [A] \qquad (141)$$

In practical realization both inductors can be made on one core because their magnetic fluxes are synchronous and approximately of the same value. Moreover, their value can be decreased to 2 x 50 µH, resulting in better

efficiency due to their lower serial resistance. The serial resistance of the inductors in the simulation diagram was considered to be up to 0.1 Ω.

The coupling capacitors C1 and C5 shall be of a good quality and low-ESR type. These capacitors are loaded with current as follows:

$$I_{C(rms)} = I_{OUT} \cdot \sqrt{\frac{U_{OUT} + U_D}{U_{IN(min)}}} = 1 \cdot \sqrt{\frac{5.4}{5}} = 1.04\ [A] \tag{142}$$

Tantal capacitors with the voltage rating of 16 V will be sufficient for this application. Their capacity can be determined as follows:

$$C_s = \frac{I_{OUT} \cdot D_{max}}{\Delta U_{Cs} \cdot f_{sw}} = \frac{1 \cdot 0.52}{2.5 \cdot 10^5} = 2.08\ [\mu F] \tag{143}$$

The ΔU_{Cs} parameter refers to the voltage ripple at the capacitors and for the purposes of this design it was expected that:

$$\Delta U_{Cs} \leq 0.5\ U_{IN(min)} \tag{144}$$

In order increase the efficiency of the converter, two 2.2 µF capacitors connected in parallel are considered.

The maximum voltage ripple at the output of the converter is expected to be at least 50 mV. Mainly the serial resistance of the filtering capacitors is critical. It can be determined as follows:

$$ESR \leq \frac{U_{ripple} \cdot 0{,}5}{I_{L1(peak)} + I_{L2(peak)}} = \frac{0.05 \cdot 0.5}{2{,}39} \cong 0.01\ [\Omega] \tag{145}$$

This implies that more filtering capacitors connected in parallel must be used. However, such a small ESR cannot be achieved in practice because of the finite conductivity of the printed circuit board copper clad.

The capacity of the filtering capacitor(s) can be calculated as follows[4]:

$$C_{OUT} \geq \frac{I_{OUT} \cdot D_{max}}{0.5 \cdot U_{ripple} \cdot f_{sw}} = \frac{0.52}{0.5 \cdot 0.05 \cdot 10^5} = 207.6\ [\mu F] \tag{146}$$

[4] Again, f_{SW} = 100 kHz instead of f_{SW} = 125 kHz is considered as explained in the text above. In this case the effect of this change will probably be negligible due to the fact that the ESR practically cannot be as small as possible and the error caused by the real ESR value will be much higher than the error caused by the change of the f_{SW} parameter.

In practical realization, four 47 μF capacitors will be employed being amended with 4.7 μF tantal capacitor and 100 nF ceramic capacitor, all connected in parallel.

The internal voltage reference is stabilized to 1.25 V. Therefore, in order to limit the output voltage to 5 V, the voltage dividers R1 and R2 ensuring the voltage feedback must divide the output voltage by 4. The values R1 = 100 kΩ and R2 = 33 kΩ are perfect for this purpose.

In the following paragraphs a design of indirect current limitation feedback is described. As stated in the description of the LT1172 chip, the current limitation is set internally to the peak current of 2 A and can be adjusted by decreasing the voltage at the Vc pin of the chip. In order to avoid affecting the efficiency of the converter it was decided to measure the output current indirectly from the peak current flowing through the inductors. However, not only is this current proportional to the output current but it also is inversely proportional to the input voltage, being additionally affected by the change of the ripple current due to the change of the duty cycle of the converter. Therefore, at least two peak currents at different input voltages must be known.

Let us choose the maximum and the minimum input voltage and calculate the peak currents obtained by the circuit devices described in the text above. Because the inductors are expected to be of higher inductance than calculated, new calculations of the ripple current are needed[5]:

$$L = \frac{U_{IN}}{\Delta I_L \cdot f_{sw}} \cdot D \;\Rightarrow \Delta I_L = \frac{U_{IN}}{L \cdot f_{sw}} \cdot D \tag{147}$$

$$\Delta I_L(9V) = \frac{9}{1.25 \cdot 10^{-4} \cdot 10^5} . 0.38 = 0.27\ [A] \tag{148}$$

$$\Delta I_L(5V) = \frac{5}{1.25 \cdot 10^{-4} \cdot 10^5} . 0.52 = 0.15\ [A] \tag{149}$$

The percentage value of the ripple R can then be determined as follows:

$$\Delta I_L = I_{OUT} \cdot \frac{U_{OUT}}{U_{IN}} \cdot \frac{R}{100} \;\Rightarrow\; R = 100 \cdot \frac{\Delta I_L . U_{IN}}{I_{OUT} \cdot U_{OUT}} \tag{150}$$

$$R\ (9V) = 100 \cdot \frac{0.27 \cdot 9}{1 \cdot 5} = 48.6\ \% \tag{151}$$

$$R\ (5V) = 100 \cdot \frac{0.15 \cdot 5}{1 \cdot 5} = 15\ \% \tag{152}$$

[5] Assuming the duty cycles are D = 38 % @ 9 V and D = 52 % @ 5 V

It must be noted that the above mentioned calculations are only approximate, not considering the influence of the Schottky diode, coupling capacitors, serial resistances, switch saturation voltage etc.

Subsequently, the peak currents can be estimated as follows:

$$I_{L1(peak)} = I_{OUT} \cdot \frac{U_{OUT} + U_D}{U_{IN}} \cdot \left(1 + \frac{R}{200}\right) \tag{153}$$

$$I_{L1(peak)}(9V) = 1 \cdot \frac{5 + 0.4}{9} \cdot \left(1 + \frac{48.6}{200}\right) = 0.75\ [A] \tag{154}$$

$$I_{L1(peak)}(5V) = 1 \cdot \frac{5 + 0.4}{5} \cdot \left(1 + \frac{15}{200}\right) = 1.16\ [A] \tag{155}$$

According to the datasheet [43], the control voltage to switch current transconductance of the LT1172 is 2 A/V. The simulation shown that if the switched current is 0.9 A, the relevant Vc voltage is 1.8 V. This implies that in an "idle" state when no current is drawn the bias at the Vc pin is approximately 1.3 V and this voltage is increased proportionally to the output current. The maximum Vc pin voltage is 2.0 V, referring to the maximum switched current of approximately 1.4 A[6]. This can be expressed as follows:

$$U_{Vc} \cong 1.3 + 0.5\ I_{L1(peak)}\ \ [V] \tag{156}$$

This implies that the input voltage compensating circuit must ensure that the voltage at the Vc pin is limited to approximately 1.68 V if the input voltage is 9 V and to 1.88 V if the input voltage is 5 V. Beside the necessary bias, the gain of this circuit must be as follows:

$$A = \frac{U_{OUT\ high} - U_{OUT\ low}}{U_{IN\ high} - U_{IN\ low}} = \frac{-0.2}{4} = -0.05 \tag{157}$$

The bias must take into account the forward voltage of the coupling diode and the bias of the Vc pin. Utilizing the 1N4148 small-signal diode, at low currents that are sufficient to activate the Vc pin, its forward voltage can be considered at least 0.5 V. The total bias must then be set to approximately U_{BIAS} = 0.8 V. It is worth noting that by changing the bias voltage the current limit is being adjusted. Therefore, the inaccuracies in the calculations can be compensated by employing one trimmer adjusting the bias voltage.

[6] The LT1172 manufacturer guarantees the maximum switched current between 1.25 and 3.5 A provided the duty cycle is 50 %.

The compensating circuit is based on the U2 operational amplifier and its behaviour can be described as follows. The superposition principle makes it possible to analyse the circuit separately for the inverting and the non-inverting input of the operational amplifier. Then the output voltage of the operational amplifier can be described as follows:

$$U_{OUT} = U_{OUT}^{+} + U_{OUT}^{-} \tag{158}$$

The + and – signs refer to the contributions of the non-inverting (+) and the inverting (-) input. The circuit can then be described separately, assuming the following conditions:

- The U^{+} voltage is expressed as the contribution to the output of the circuit in case the non-inverting input is driven while the source connected to the inverting input is of zero voltage.
- The U^{-} voltage is expressed as the contribution to the output of the circuit in case the inverting input is driven while the source connected to the non-inverting input is of zero voltage.

Then the behaviour of the circuit can be described by the following equations:

$$U_{OUT}^{-} = -U_{IN} \cdot \frac{\frac{R7 \cdot R8}{R7 + R8}}{R4 + \frac{R7 \cdot R8}{R7 + R8}} \cdot \frac{R5}{R8} \tag{159}$$

$$U_{OUT}^{+} = U_{BIAS} \cdot \left(1 + \frac{R5}{R8 + \frac{R7 \cdot R4}{R7 + R4}}\right) \tag{160}$$

$$U_{OUT} = U_{BIAS} \cdot \left(1 + \frac{R5}{R8 + \frac{R7 \cdot R4}{R7 + R4}}\right) - U_{IN} \cdot \frac{\frac{R7 \cdot R8}{R7 + R8}}{R4 + \frac{R7 \cdot R8}{R7 + R8}} \cdot \frac{R5}{R8} \tag{161}$$

The voltage divider R4, R7 decreases the input voltage that can occur at the inverting input of the operational amplifier. As the FET based operational amplifier is expected to be employed, the current flowing through the divider can be very small. In order to simplify the calculations it is reasonable to choose the resistors R4, R7 and R8 of the same value. The following values can be chosen: R4 = R7 =R8 = 680 kΩ. This will simplify the (161) expression to the following state:

$$U_{OUT} = U_{BIAS} \cdot \left(1 + \frac{R5}{1.02 \cdot 10^{6}}\right) - U_{IN} \cdot 0.33 \cdot \frac{R5}{3.4 \cdot 10^{5}} \tag{162}$$

Beside the bias, the R5 resistor must be set according to the requirement resulting from the equation (163):

$$\Delta U_{OUT} = -0.05 \cdot \Delta U_{IN}$$

$$\Rightarrow \frac{\Delta U_{OUT}}{\Delta U_{IN}} = 0.33 \cdot \frac{R5}{3.4 \cdot 10^5} = 0.05 \Rightarrow R5 \cong 51\ [k\Omega] \qquad (163)$$

Now the bias voltage can be determined as well under the assumption that when the input voltage is 5 V, the required output voltage of the circuit is 1.88 - 0.5 = 1.38 V[7]:

$$U_{OUT} = 1.05 \cdot U_{BIAS} - 0.05 \cdot U_{IN}$$

$$\Rightarrow U_{BIAS} = \frac{U_{OUT} + 0.05 \cdot U_{IN}}{1.05} = \frac{1.38 + 0.05 \cdot 5}{1.05} = 1.55\ [V] \qquad (164)$$

On completion the above mentioned calculations, the circuit was simulated. According to results of simulations only the value of the resistor R5 was increased from 51 to 82 kΩ and consequently the bias voltage was decreased from 1.55 to 1.45 V. This modification covered the inaccuracies that occurred in the calculations as a result of neglecting a greater amount of minor or parasitic parameters of the utilized devices.

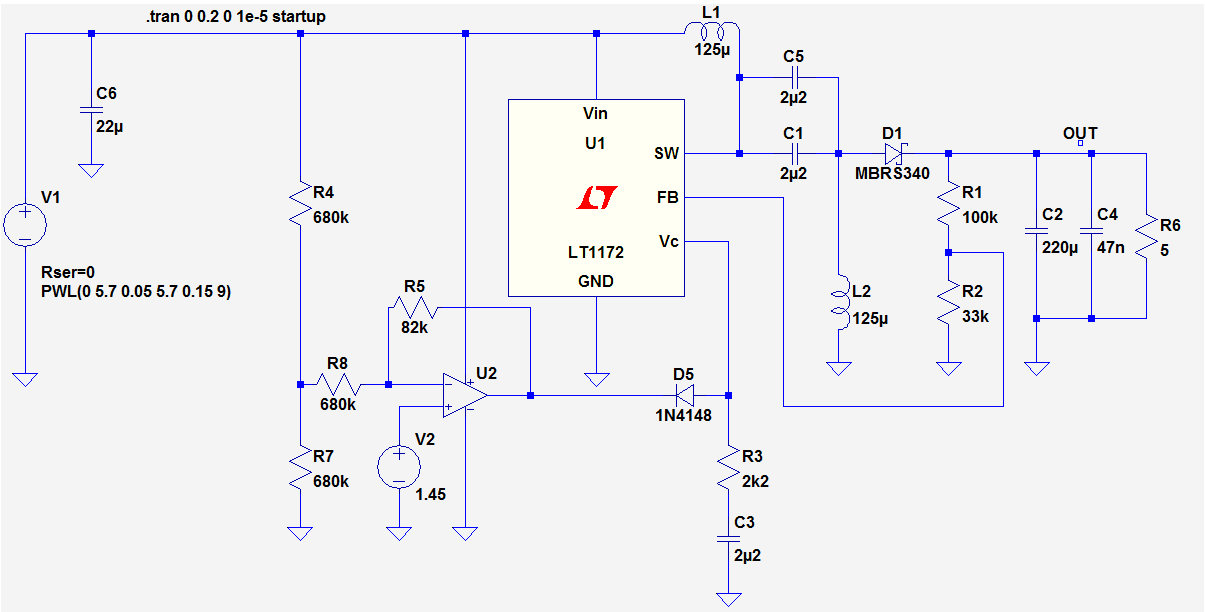

Fig. 73 – Basic circuit diagram for 5 V voltage regulator simulation (LT Spice)

[7] It is necessary to calculate the voltage drop at the coupling diode.

The final simulations of the 5V regulator were processed for the input voltage varying from 5.7 V to 9 V. The minimum value is given by the theoretical minimum input operating voltage at which the Emergency shutdown circuit should suspend the operation of the power supply source. The maximum value is expected not to exceed 9 V for the 7.2V accumulator that is assumed to be employed. As the nominal output voltage is 5 V, the 5 Ω load resistor refers to the load that consumes 1 A.

The behaviour of the circuit including the load realized by the 5Ω resistor is depicted in Fig. 74.

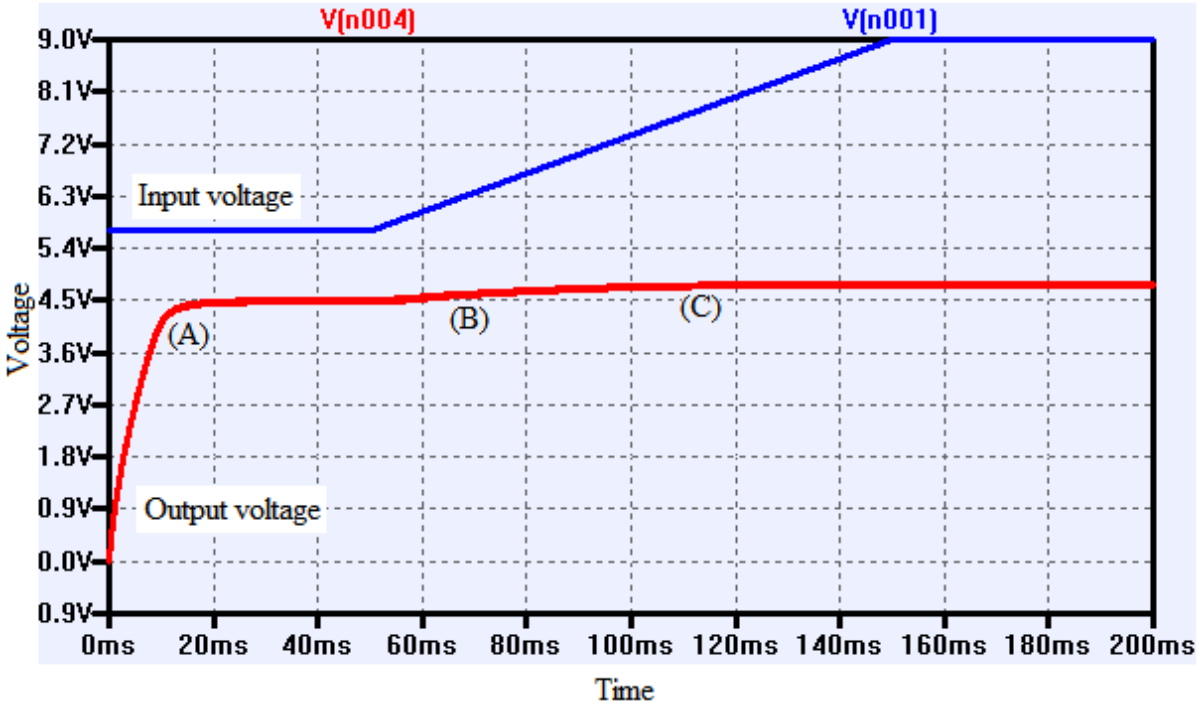

Fig. 74 – Simulation results of the circuit from Fig. 73 for different input voltage and 5Ω load

Unfortunately, at the maximum expected load the circuit is not capable of delivering sufficient power. This is caused by the fact that the internal overcurrent protection of the chip is active at low voltages. In the Fig. 74 the following phenomena can be observed: the input voltage is fixed at the lowest level in the first 50 ms. Then it is raised to the maximum value at which it stays until the end of the simulation. The Output voltage curve refers to the output voltage of the voltage converter. There are three interesting points of this curve, marked by the letters (A), (B) and (C). From the end to the point (A) the soft start ramp is active. The time in which the converter starts to deliver the maximum output power is determined by the serial combination of R3 and C3 devices. Their values were set according to the recommendation of the manufacturer of the chip. When the soft start period finishes, the output voltage is stabilized to approximately 4.5 V, referring to the output current of 0.9 A. The nominal output voltage is not achieved due to the overcurrent protection

implemented in the chip that does not allow to exceed the switching current of 1.25 A[8]. Even though, this may seem to be too strict in the simulation, but in practice the manufacturer guarantees the switching current to lie within 1.25 and 3.5 A. From the point (C) the output voltage is stabilized to approximately 4.8 V. From this point the external current limiting is active, setting the current limit to 0.96 A. Unfortunately, for this kind of chip and the indirect current sensing the overcurrent protection characteristics are quite weak, resulting in the fact that the threshold of the overcurrent protection migrates according to the load resistance.

Additional simulations were processed assuming the same configuration except the load resistance. The load resistance was set to 10 and 2.5 Ω. The results are depicted in Fig. 75 and Fig. 76. From the results of these it is obvious that the voltage converter operates properly. With the output current of 0.5 A the output voltage is precisely stabilized to 5.0 V and with the overloaded output the output voltage is approximately 2.9 V, referring to the output current of 1.16 A.

The Fig. 77 shows how the output voltage depends on the current drawn by the load provided the input voltage is of some nominal value, e.g. 7.2 V. For the nominal output current of 1 A the drop of the output voltage is approximately 10 %. This value can be adjusted by tuning the U_{BIAS} voltage.

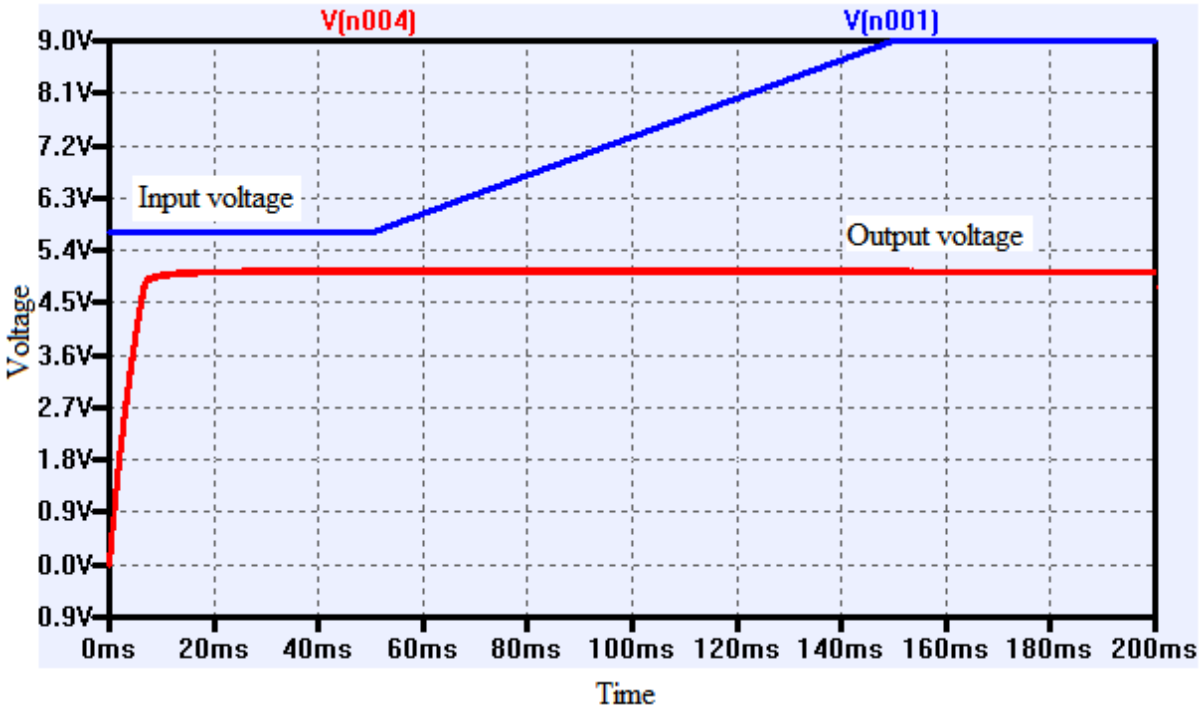

Fig. 75 – Simulation results of the circuit from Fig. 73 for different input voltage and 10Ω load

[8] According to the calculations, the current of 1.25 A would never be exceeded. However, many factors are neglected in the calculations, for example the serial resistances of the devices, the saturation voltage of the power switch etc.

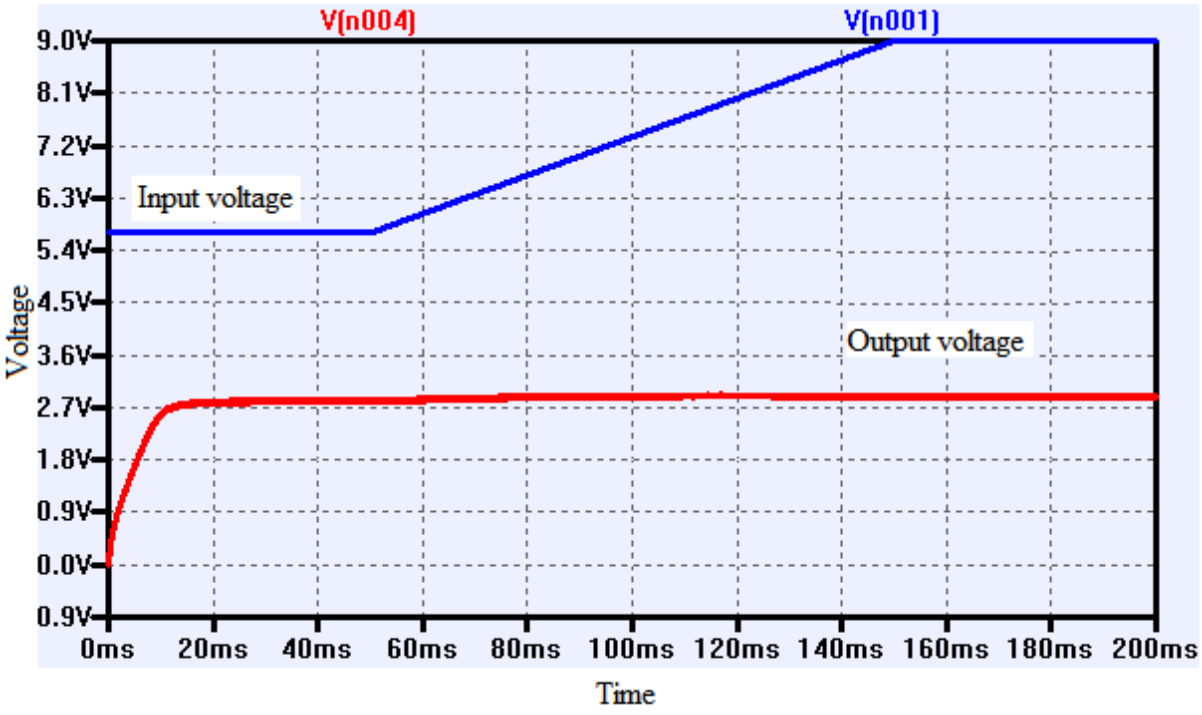

Fig. 76 – Simulation results of the circuit from Fig. 73 for different input voltage and 2.5Ω load

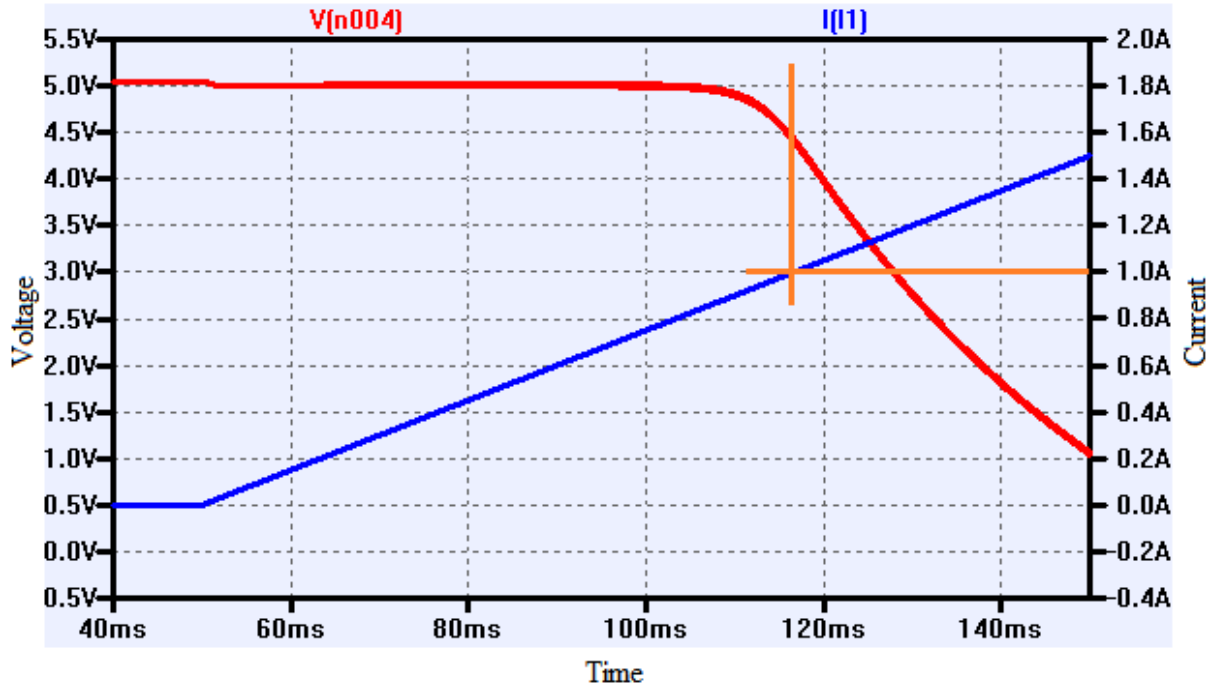

Fig. 77 – Simulation results of the circuit from Fig. 73 for different output current I(1).

However, it is obvious that the current limiting is quite soft and such adjustment will increase the shorted circuit current limit. Provided the values of

the devices are as described in this paper, the short circuit current will not exceed 1.75 A.

In Fig. 78 the current through the L1 inductor is depicted provided the input voltage is 7.2 V and the output current is 1 A. The peak current is 0.87 A.

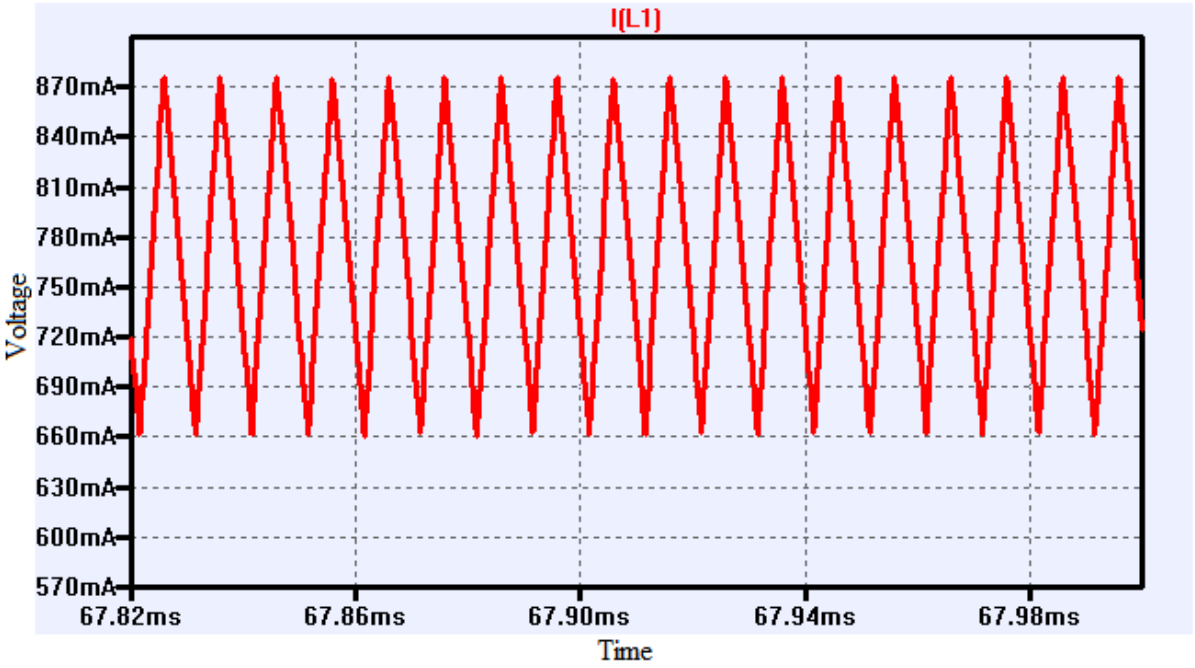

Fig. 78 – Simulation results of the circuit from Fig. 73 - waveform of the current passing through L1 inductor at the output current of 1 A and input voltage of 7.2 V

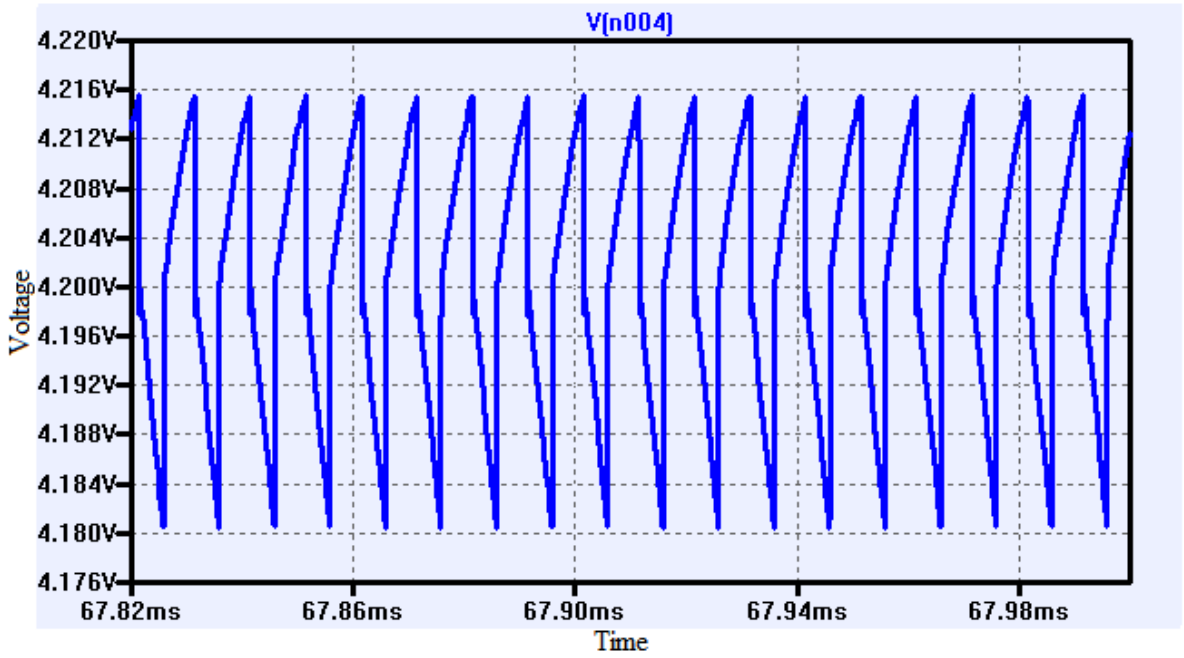

Fig. 79 – Simulation results of the circuit from Fig. 73 – voltage ripple at the output of the converter at the output current of 1 A and input voltage of 7.2 V

In Fig. 79 the ripple voltage at the output of the voltage converter is depicted provided the output is loaded with the current of 1 A and the input is fed by the nominal voltage of 7.2 V. The ripple voltage is 36 mV provided the ESR of the filtering capacitor is at least 0.01 Ω. This refers to the relative ripple of 0.85 %. The spectrum analysis of the output voltage under the above mentioned circumstances is depicted in Fig. 80.

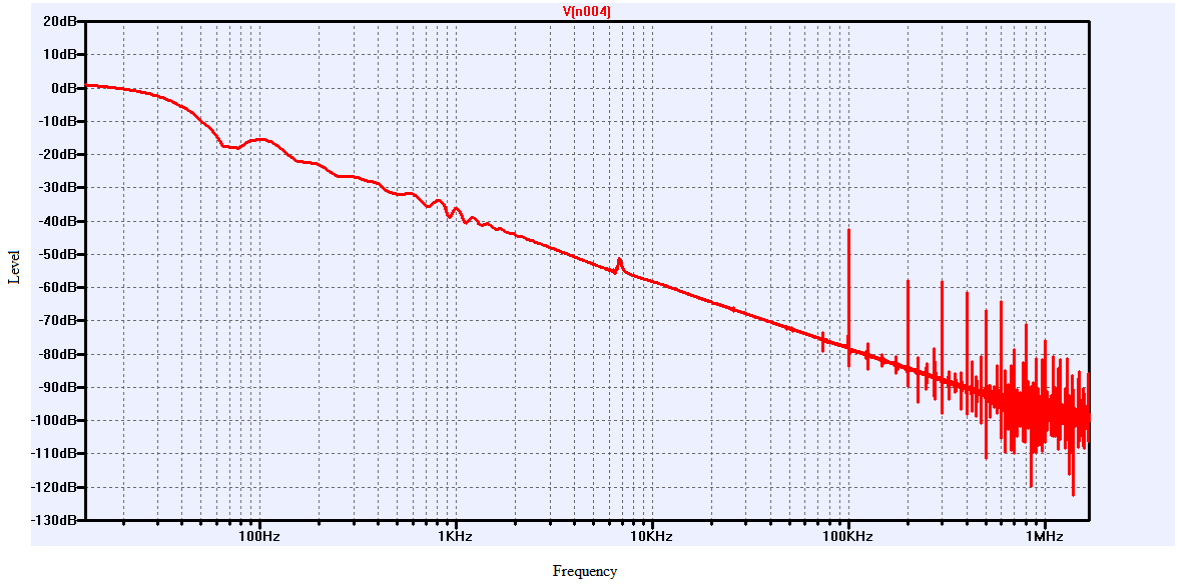

Fig. 80 – Simulation results of the circuit from Fig. 73 – spectrum analysis of the output voltage when the output current is at least 1 A

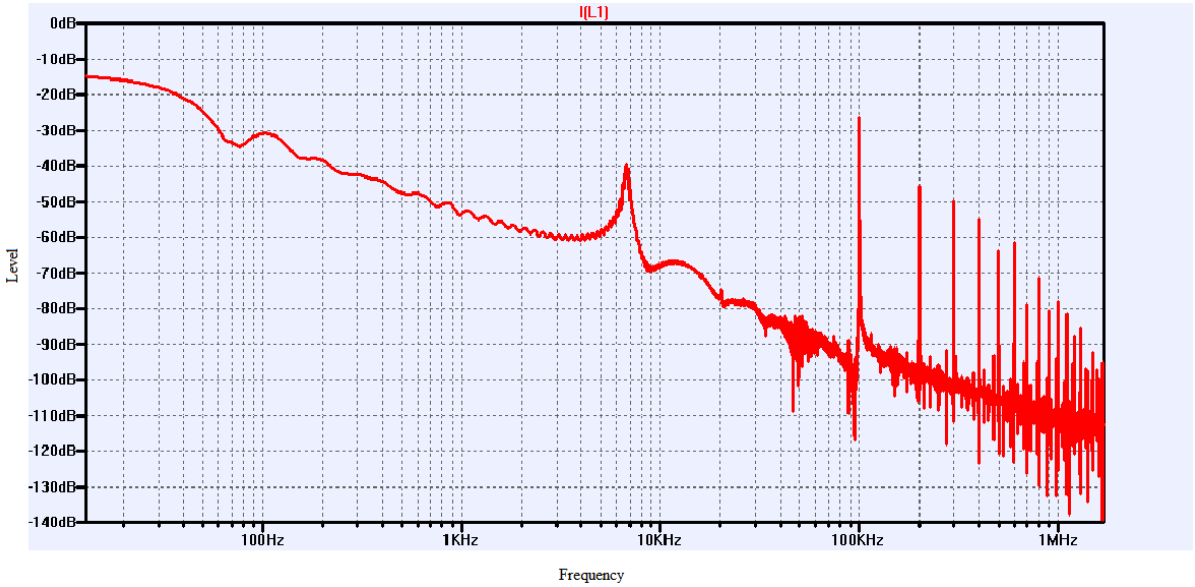

Fig. 81 – Simulation results of the circuit from Fig. 73 – spectrum analysis of the current passing through the L1 inductor when the output current is at least 1 A

As stated above, the 3.3V and 12V voltage converters are connected in the same way and differ from the 5V converter only by the device values. The

calculations of these converters can be processed in the same way as shown in this chapter for the 5V converter. In order to avoid exceeding the scope of this paper the calculations for the 3.3V and 12V converters are not included explicitly, but the appropriate device values referring to the schema depicted in Fig. 73 are provided as the results of the calculations. These values are listed in the following table.

Table 10 – Summary of calculated devices for all three voltage regulators

	Regulator		
Nominal output voltage [V]	**3.3**	**5.0**	**12.0**
Nominal output current [A]	1.0	1.0	0.5[9]
L1 [µH][10]	50	125	300
L2 [µH][10]	50	125	300
C1 [µF]	4.7	2.2	1.5
C2 [µF]	220	220	220
C3 [µF]	2.2	2.2	2.2
C4 [nF]	47	47	47
C5 [µF]	4.7	2.2	1.5
R1 [kΩ]	82	100	150
R2 [kΩ]	51	33	18
R3 [kΩ]	2.2	2.2	2.2
R4 [kΩ]	680	680	680
R5 [kΩ]	68	82	150
R7 [kΩ]	680	680	680
R8 [kΩ]	680	680	680
U_{BIAS} [V]	1.55		

5.3.1.6 Time synchronization

The time synchronization circuit ensures that the Vc pins of the appropriate voltage regulators are synchronously tied to the ground for very short periods. This allows establishing the synchronized operation of all three voltage converters as described in the text above.

The circuit diagram of the synchronization block is depicted in Fig. 82. The oscillator runs at the frequency of 1.25 MHz which is then divided by ten. In each period of 8 µs ten different pulses are available. These pulses are then utilized to feed the Vc pins of the appropriate voltage converters. According to the chip's manufacturer's notes the synchronization pulses should be at least 0.2

[9] Due to the internal overcurrent protection of the chip the nominal output voltage can be achieved only for $U_{IN} > 7$ V.

[10] This value is valid only for the simulation schema. In practice the value should be lowered by 20 %. See text for details

µs. This is ensured by the connection of the pulling transistors according to the application notes of the chip.

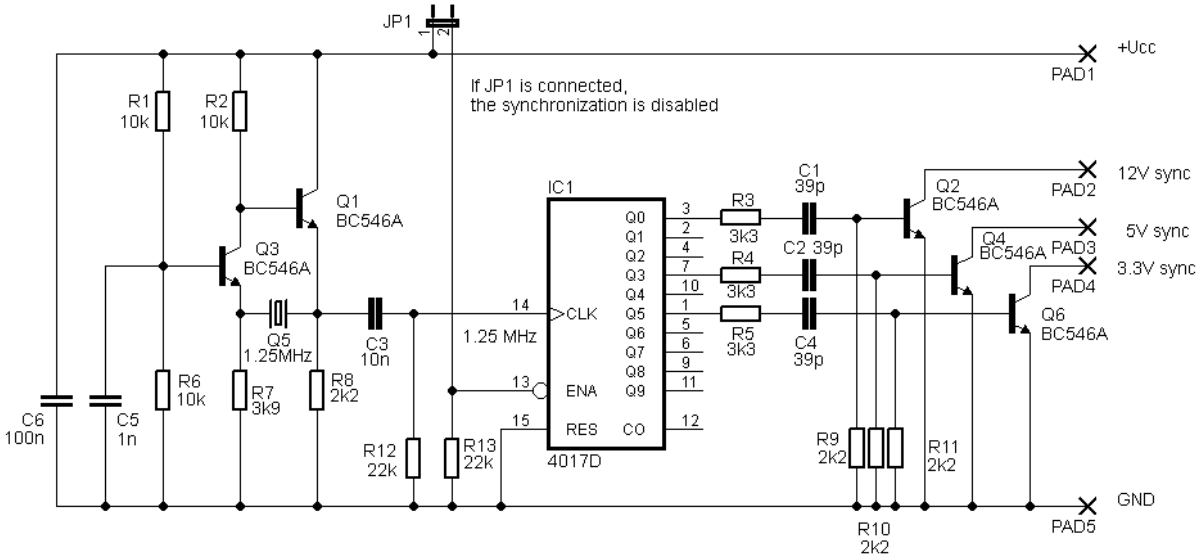

Fig. 82 – Time synchronization circuit

5.3.1.7 Complex power source circuitry

In this subchapter all the aspects mentioned in the previous sections are merged, resulting in a design of the power supply module for the Autonomous monitoring system. All the hardware blocks are connected according to the block diagram depicted in Fig. 62. The full circuit diagram of the power supply source unit is depicted in Fig. 83. Moreover, it can be found in better resolution in Appendix A enclosed to this paper.

The wires carrying higher currents are marked by thicker lines. These wires must be optimized in length and potential current-turn area as they may tend to radiate the electromagnetic field as a consequence of the switched-mode operation of the voltage converters and the motors driver. The numbering of the devices begins with the number 1000. This numbering is introduced as it is necessary to differentiate the final power supply circuitry design from the previously introduced circuit diagrams.

The accumulator is connected to the connectors numbered as SL1001 and SL1005. The first of the inputs serves for the accumulator state measurement and power supply delivery to the auxiliary circuits while the second serves for delivering the power to the voltage converters and the motors driver.

The circuit consisting of the transistors T1001 and T1002 switches off the power supply delivery to the auxiliary circuits in case the accumulator is close to the deep discharge state. This circuit was above described as the Cells measurement power supply disconnector (see Fig. 68). The LED1 depicted in Fig. 68 has been replaced with the more accurate voltage reference based on the parametric voltage regulator TL431, numbered as VR1002 in Fig. 83.

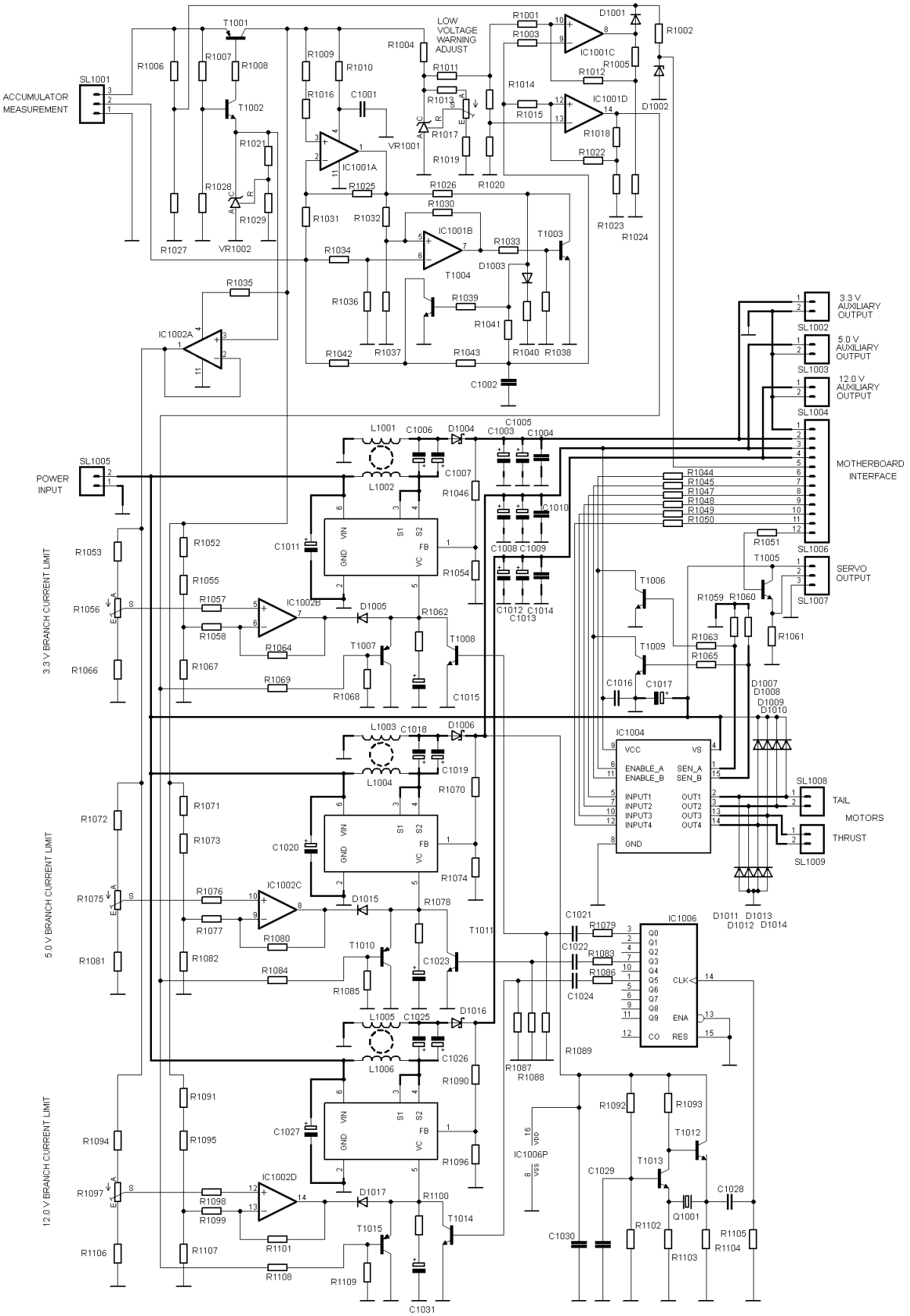

Fig. 83 – Power supply source complex circuit diagram

However, the reference voltage of 3 V is still considered. This reference voltage is also buffered by the IC1002A operational amplifier and serves as the bias of the voltage regulators' current limiting circuitry.[11] In total, two low-voltage low-power quad operational amplifiers (IC1001 and IC1002) are employed. The operational amplifiers IC1001A and IC1001B serve to recognize which cell of the accumulator is discharged deeper. Their connection is the same as described in the chapter "Measuring of the lower cell voltage". Instead of 1 resistor in the non-inverting input of the IC1001A operational amplifier two resistors (R1009 and R1016) are intended to be used. This is because the need for additional balancing of the circuit is expected as the voltage drop at the transistor R1001 was not expressed accurately. However, it must be taken into account.

The operational amplifiers IC1001C and IC1001D are connected as comparators according to the simulated circuit being described in the chapter "Generator of Warning and Emergency shutdown signals". The adjustable voltage reference is based on the TL431 voltage regulator labelled as VR1001. The output of IC1001C is connected to the pin 5 of the motherboard interface connector (SL1006). As described in the given chapter, there is a voltage relevant to the total accumulator voltage at this output, provided no low voltage warning is generated. If the low voltage warning signal is generated, the output is tied to the TTL H level (see Table 9).

The internal emergency shutdown signal is generated by the operational amplifier labelled as IC1001D. As this signal is negated, in standard operation state the output of the operational amplifier is in positive saturation, making the transistors T1007, T1010 and T1015 closed. If the emergency signal is active, the transistors are not blocked and get opened through the resistors R1068, R1085 and R1109. This turns the voltage converters to the stand-by state and disables their operation. Due to their construction employing capacitors in series with the accumulator and the load, the outputs of the voltage converters are turned off. Also if the accumulator voltage drops so low that the accumulator management circuitry is disconnected by the disconnector consisting of the transistors T1001 and T1002, the transistors T1007, T1010 and T1015 remain opened, keeping the power supply unit in the shutdown mode.

The topology of the voltage converters responds to the simulated circuit diagram described in the chapter "Voltage regulators design". The operational amplifiers IC1002B, IC1002C and IC1002D ensure the proper bias of the VC pins according to the accumulator voltage in order to ensure the proper operation of the current limiting without any need of sensing the output current by means of the sensing resistor. This enables to improve the efficiency of the circuit.

The synchronization pulses are generated by transistors T1008, T1011 and T1014. These transistors are driven by the Johnson's counter 4017 as described

[11] For more details please see chapter „Voltage regulators design".

in the chapter “Synchronization”. The counter is labelled as IC1006 and is driven by the crystal oscillator whose frequency is set to 1.25 MHz by means of the Q1001 crystal. The connection of the oscillator is described in [38].

As it is convenient to shorten the length of the power wires, the motors driver L298 is implemented directly in the power supply source module, while connected to the power input SL1005. The connection of this bridge motors driver comply with the circuit diagram depicted in Fig. 47. The transistor T1006 and T1009 are intended to short circuit the ENABLE signals when the current through the motors is higher than allowed by resistors R1059 and R1060.

5.3.2 Motherboard

The motherboard is intended to bear the central microcontroller and all peripheral interfaces. Moreover, it should be designed in order to mount the IP relay, IP camera and WiFi router on it.

The supported peripherals are as follows:

- thrust and tail motors controlling bus (6 wires),
- IP relay interface (8 wires[12]),
- ultrasonic detectors I^2C bus (2 wires),
- ultrasonic detectors power supply (2 wires),
- accumulator monitoring (1 wire),
- extension optional analogous / digital input (1 wire),
- RFID detector (implemented on the motherboard).

The 22 pin interface microcontroller Freescale MC9S08SE8 is intended to be used. This microcontroller was chosen because of the need to maintain the continuity with previous designs and experiences. As it does not support I^2C, standard SPI bus is implemented as the basic motherboard bus. The I^2C peripherals are realized by means of external driver CP2120. The simplified block diagram of the motherboard is depicted in Fig. 84. All the controlling algorithms are intended to be run in the central microcontroller. The microcontroller communicates with the ultrasonic detectors and the RFID reader by means of the internal SPI bus. For the purposes of further hardware extensions, SPI interface for an external device is also implemented. The microcontroller communicates also with the Power board, IP relay and enables direct connection of other optional devices. The final circuit diagram is depicted in Fig. 85.

[12] From the total number of 8 wires, 4 of them can be configured either as the input or the output. One of them is reserved to assist LED light controlling.

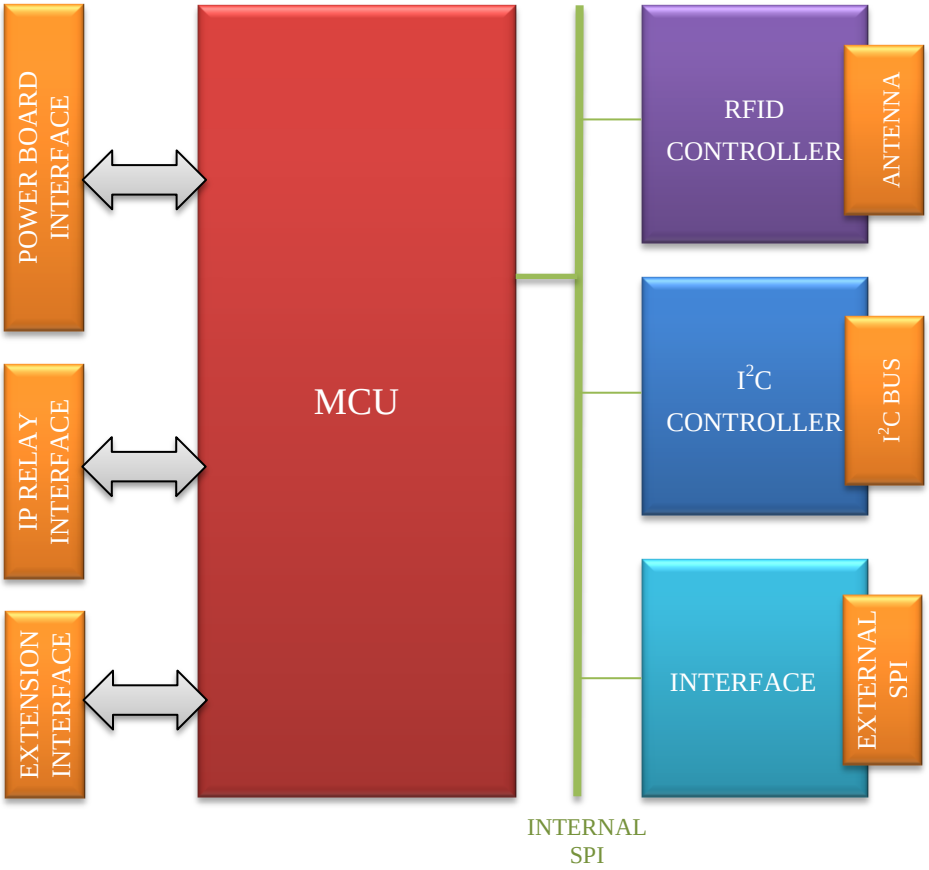

Fig. 84 –Motherboard block diagram

5.3.2.1 Motherboard circuit diagram

The numbering of the motherboard devices starts at 2,000 in order to avoid confusion when more circuit diagrams (power board etc.) are read simultaneously. Five chips are implemented on the motherboard. The microcontroller is marked as IC2001. As it utilizes almost all I/O pins, the programming interface is not implemented on the board. The microcontroller is intended to be loaded with the firmware by a separated programming device and then to be inserted into the appropriate socket. The microcontroller is clocked by its internal clock generator and provides several possibilities of the I/O communication. The IP Relay Interface (SL2001) and Power Board Interface (SL2003) are connected directly to the appropriate I/O pins of the microcontroller, using a set of protective resistors. Via the SL2003 the power delivery from the Power board is also realized, resulting in 3V3, 5V and 12V nets on the motherboard. These nets are primarily decoupled by the capacitors C2013, C2014 and C2015.

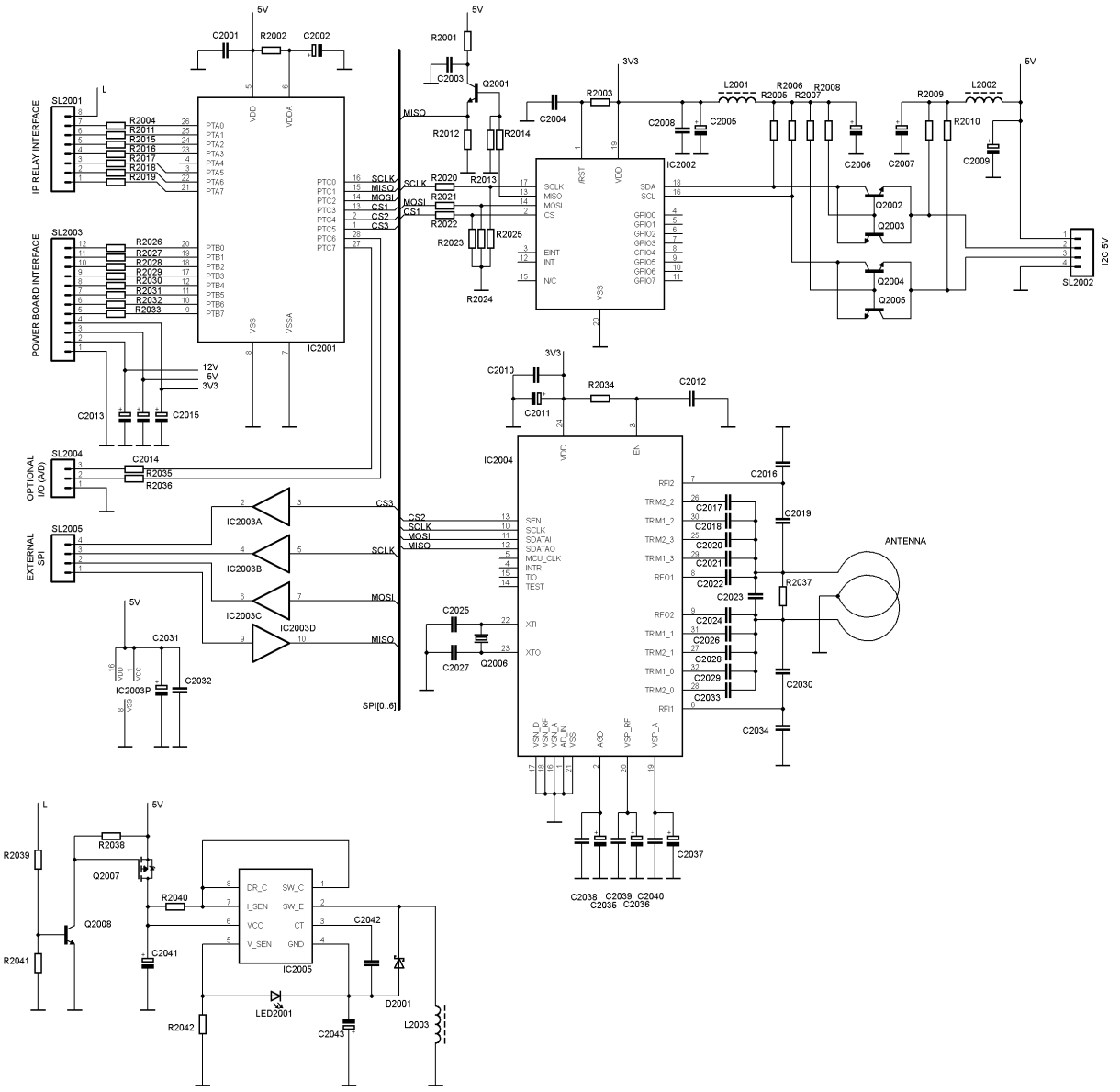

Fig. 85 – Motherboard circuitry proposal

Another optional I/O connector is SL2004 that is also connected directly to the PTC6 and PTC7 pins of the microcontroller by means of protective resistors. These two I/O pins can be set in several ways by appropriate setting in the system's firmware. While the output is considered to be digital, the input can either be digital or analogous, depending on the immediate needs. Typically, these pins can be used as the interface for accelerometers mounted on the airship.

As the microcontroller IC2001 does not directly support the I^2C bus, the central SPI bus is intended to be implemented on the motherboard, allowing the connection of up to three slave devices. The first slave device is IC2002, the CP2120 SPI to I^2C bridge, that is necessary for connection the set of ultrasonic detectors to the motherboard. The communication with this chip is enabled by means of the CS1 selector wire. When enabled, the communication on the SPI

bus is shifted to the I^2C bus levels. As the CP2120 bridge can be supplied only by the voltage of 3.3 V, voltage levels shift must be realized by means of appropriate voltage dividers and the transistor Q2001 that increases the level of the H signal. The power supply of the IC2002 chip is decoupled by the capacitors C2008 and C2005. Its RESET pin is permanently tied up by the R2003 resistor, being decoupled by the C2004 capacitor. As the SDA and SCL levels are of 3.3V logic, the logical level shifter using transistors Q2002 – Q2005 is implemented. At the connector SL2002 the I^2C bus is used, enabling to connect a chain of ultrasonic detectors. Apart from the 5 V logic levels it also provides 5 V power supply to the connected devices. The inductors L2001 and L2002 together with the capacitors C2006 and C2007 are intended to decrease the noise in the power supply nets caused by the communication on the I^2C bus.

The second device to be connected to the internal SPI bus is IC2004, the AS3910 RFID reader. The communication with this chip is enabled by CS2 selector wire. The connection of the chip is the same as described in the chapter "5.1.4.1. RFID Tags reader main board circuitry". The chip is supplied from 3V3 supply net. Its power supply is decoupled by C2010 and C2011 capacitors. The ENABLE pin is permanently tied on by means of R2034 resistor. The antenna is intended to be created directly on the printed circuit board. As it is necessary to tune the antenna's resonant frequency (see the appropriate datasheet [40] for more details), trimming capacitors C2017, C2018, C2020, C2021, C2022, C2024, C2026, C2028 and C2033 are used. The antenna calibration is processed automatically by the chip on request of the microcontroller.

The third device connected to the internal SPI bus is a set of buffers IC2003. These buffers provide I/O interface for optional external device that is also capable of communication on the SPI bus. This communication is enabled by CS3 selector wire.

The ancillary LED light is also intended to be mounted directly on the PCB, being fed by the current source. The current source is realized with IC2005 switching voltage regulator that is connected as a voltage invertor. This allows different threshold voltages of the appropriate LED (LED2001) while the supply voltage of 5 V is always the same. The circuit is turned on when the signal "L" delivered from the IP Relay through the SL2001 connector is active. The power consumption of the LED should not exceed 1 W.

5.3.2.2 Motherboard connectors

In this subchapter detailed information on the connectors used at the motherboard is provided in the form of a table below.

Table 11 – Motherboard connectors' description

SL2001	**IP Relay Interface**
1	5V TTL input "L". Turns the assist LED on/off by means of the web interface
2	5V TTL input. Receives commands from the web interface.
3	5V TTL input. Receives commands from the web interface.
4	5V TTL input. Receives commands from the web interface.
5	5V TTL input/output. Receives commands from the web interface or transmits bits back to the web interface.
6	5V TTL input/output. Receives commands from the web interface or transmits bits back to the web interface.
7	5V TTL input/output. Receives commands from the web interface or transmits bits back to the web interface.
8	5V TTL input/output. Receives commands from the web interface or transmits bits back to the web interface.
SL2002	**I^2C bus for connecting of external devices**
1	+ 5 V power supply for external devices
2	SDA (5V level)
3	SCL (5V level)
4	GND for external devices
SL2003	**Power board interface**
1	GND
2	+ 3.3 V power supply input
3	+ 5 V power supply input
4	+ 12 V power supply input (not used in this version of the motherboard)
5	Low-accumulator warning signal (> 3.5 V) or total accumulator voltage (0.6 – 0.9 V)
6	Motors control 1 (5V TTL level)
7	Motors control 1 (5V TTL level)
8	Motors control 1 (5V TTL level)
9	Motors control 1 (5V TTL level)
10	Motors control 1 (5V TTL level)
11	Motors control 1 (5V TTL level)
12	Servo control (5V TTL level)
SL2004	**Optional I/O extension**
1	5 V TTL level output / analog or digital input (according to firmware)
2	5 V TTL level output / analog or digital input (according to firmware)
3	GND

SL2005	External SPI
1	MISO 5V TTL (serial line slave to master)
2	MOSI 5V TTL (serial line master to slave)
3	SCLK 5V TTL (clock)
4	CS 5V TTL (enables communication when high)

5.3.2.3 List of motherboard devices

In this subchapter the list of motherboard devices is provided, specifying their basic parameters and other descriptive information.

Table 12 – Motherboard devices

Position	Value	Description
C2001	100 nF	Ceramics. Microcontroller power supply decoupling
C2002	1 µF	Tantal. Internal microcontroller's A/D converter reference power supply decoupling
C2003	100 nF	Ceramics.
C2004	100 nF	Ceramics.
C2005	1 µF	Tantal. IC2002 power supply decoupling.
C2006	1 µF	Tantal. 3V3 SDA / SCL line decoupling.
C2007	1 µF	Tantal. 5V SDA / SCL line decoupling.
C2008	47 nF	Ceramics. IC2002 power supply decoupling.
C2009	4.7 µF	Tantal. External 5V devices power supply decoupling.
C2010	47 nF	Ceramics. IC2004 power supply decoupling.
C2011	1 µF	Tantal. IC2004 power supply decoupling.
C2012	100 nF	Ceramics.
C2013	100 µF	Electrolytic. 3.3 V power supply bulk capacitor.
C2014	100 µF	Electrolytic. 5 V power supply bulk capacitor.
C2015	22 µF	Electrolytic. 12 V power supply bulk capacitor.
C2016	68 pF	Ceramics, according to [40].
C2017	47 pF	Ceramics for antenna tuning.
C2018	47 pF	Ceramics for antenna tuning.
C2019	68 pF	Ceramics, according to [40].
C2020	47 pF	Ceramics for antenna tuning.
C2021	47 pF	Ceramics for antenna tuning.
C2022	68 pF	Ceramics, according to [40].
C2023	22 pF	Ceramics, according to [40].
C2024	68 pF	Ceramics, according to [40].
C2025	22 pF	Ceramics, according to [40].
C2026	47 pF	Ceramics for antenna tuning.
C2027	22 pF	Ceramics, according to [40].
C2028	47 pF	Ceramics for antenna tuning.

C2029	47 pF	Ceramics for antenna tuning.
C2030	68 pF	Ceramics, according to [40].
C2031	1 μF	Tantal. IC2003 power supply decoupling.
C2032	47 pF	Ceramics. IC2003 power supply decoupling.
C2033	47 pF	Ceramics for antenna tuning.
C2034	68 pF	Ceramics, according to [40].
C2035	1 μF	Tantal. Decoupling according to [40].
C2036	4.7 μF	Tantal. Decoupling according to [40].
C2037	4.7 μF	Tantal. Decoupling according to [40].
C2038	100 nF	Ceramics. Decoupling according to [40].
C2039	100 nF	Ceramics. Decoupling according to [40].
C2040	100 nF	Ceramics. Decoupling according to [40].
C2041	10 μF	Electrolytic.
C2042	470 pF	Ceramics. Timing of IC2005. Operating frequency approximately 50 kHz.
C2043	47 μF	Electrolytic.
D2001		Fast Schottky (according to availability of suitable types)
R2001	47 Ω	
R2002	1 kΩ	VDDA of IC2001 decoupling
R2003	1 kΩ	/RST of IC2002 decoupling
R2004	470 Ω	PTA0 of IC2001 protection
R2005	10 kΩ	3V3 I^2C pull up
R2006	10 kΩ	3V3 I^2C pull up
R2007	47 kΩ	3V3 I^2C transistor's base pull up
R2008	47 kΩ	3V3 I^2C transistor's base pull up
R2009	4.7 kΩ	5V I^2C pull up (the current is increased because higher line capacity is expected)
R2010	4.7 kΩ	5V I^2C pull up (the current is increased because higher line capacity is expected)
R2011	470 Ω	PTA1 of IC2001 protection
R2012	1.5 kΩ	SPI bus MISO driver
R2013	10 kΩ	Q2001 base switching bias
R2014	10 kΩ	
R2015	470 Ω	PTA2 of IC2001 protection
R2016	470 Ω	PTA3 of IC2001 protection
R2017	470 Ω	PTA5 of IC2001 protection
R2018	470 Ω	PTA6 of IC2001 protection
R2019	470 Ω	PTA7 of IC2001 protection
R2020	2.2 kΩ	SPI bus 5 to 3.3 V divider
R2021	2.2 kΩ	SPI bus 5 to 3.3 V divider
R2022	2.2 kΩ	SPI bus 5 to 3.3 V divider

R2023	4.7 kΩ	SPI bus 5 to 3.3 V divider
R2024	4.7 kΩ	SPI bus 5 to 3.3 V divider
R2025	4.7 kΩ	SPI bus 5 to 3.3 V divider
R2026	470 Ω	PTB0 of IC2001 protection
R2027	470 Ω	PTB1 of IC2001 protection
R2028	470 Ω	PTB2 of IC2001 protection
R2029	470 Ω	PTB3 of IC2001 protection
R2030	470 Ω	PTB4 of IC2001 protection
R2031	470 Ω	PTB5 of IC2001 protection
R2032	470 Ω	PTB6 of IC2001 protection
R2033	470 Ω	PTB7 of IC2001 protection
R2034	1 kΩ	EN pin of IC2004 decoupling
R2035	470 Ω	PTC7 of IC2001 protection
R2036	470 Ω	PTC6 of IC2001 protection
R2037		Antenna damping, see [40]
R2038	100 kΩ	Q2007 gate pull up
R2039	10 kΩ	
R2040	0.51 Ω	According to MC34063 universal calculator
R2041	4.7 kΩ	
R2042	6.8 Ω	Sets LED2001 current to 200 mA
IC2001	MC9S08SE8	Central MCU
IC2002	CP2120	SPI/I^2C bridge
IC2003	4010	set of buffers
IC2004	AS3910	RFID reader
IC2005	MC34063A	SMPS driver
L2001		Spike suppressor, according to experience
L2002		Spike suppressor, according to experience
L2003	> 100 μH	
D2001		Fast Schottky
Q2001	BC817	
Q2002	BC817	
Q2003	BC817	
Q2004	BC817	
Q2005	BC817	
Q2007		Any suitable MOSFET
Q2008	BC817	

5.4 Airship's behaviour modelling

In order to develop the controlling algorithm, there is a need for at least rough knowledge of the way the airship reacts to the propelling force generated by the propellers. For these purposes a simple state-space model was created in Matlab

Simulink, using theory described in [50], [46], [47]. The necessary sets of equations and approximations are provided in chapter "4.4 Airship's model".

The dimensions of the Autonomous monitoring system's airship have been measured together with the positions of the propellers. The airship's shape has been replaced by a rotary ellipsoid. The centre of gravity is estimated to be 15 % to the front from the centre of the ellipsoid and 20 % lower according to its central axis. According to the equation (68), the position of the centre of gravity with respect to the coordinate system a can be expressed as follows.

$$\vec{\varepsilon} = \left(x_g, y_g, z_g\right) = (0.2, 0, 0.13)\ [m] \tag{165}$$

The length of the ellipsoid is 2.7 m and its width is 1.3 m. Then the lengths of the relevant semi-axes are a = 1.35 m and b = 0.65 m. The position of the centre of the gravity is then lies in the XZ plane of the bladder, being placed 1.55 m far from the tail and 0.13 m below the XY plane of the bladder. According to Fig. 27, the relevant lengths for calculation of the force moments are provided in the following Table.

Table 13 – Force arms according to Fig. 27

Parameter	**Value**	**Note**
l_1	0.07 m	Tail propelling source distance from the axis of the centre of gravity with respect to the z-axis
l_2	1.23 m	Tail propelling source distance from the axis of the centre of gravity with respect to the z-axis
l_3	0.1 m	Distance between main propellers and the centre of gravity with respect to the x-axis
l_4	0.6 m	Distance between main propellers and the centre of gravity with respect to the z-axis
l_5	0.28 m	Distance of the main propellers from the central XZ plane of the bladder

The estimated propelling force was considered to lie within 0.2 and 1.5 N (see Fig. 23 and chapter y) per one propeller. The measured weight of the unloaded airship is approximately 1.25 kg. With the balancing load, the operating weight is expected to be approximately 1.75 kg (according to the amount of helium inserted into the bladder).

The next calculations may be processed according to the theory presented in chapter "4.4 Airship's model". The power consumed by one motor is considered to be as high as 5 W, resulting in the propelling force of approximately 0.9N @

4,000 rpm per one propeller[13]. The airship of the Autonomous monitoring system is represented by the following parameters:

$$e = 1 - \left(\frac{b}{a}\right)^2 = 1 - \left(\frac{0.65}{1.35}\right)^2 = 0.77\ [-] \tag{166}$$

$$\alpha_0 = \frac{2(1-e^2)}{e^3}\left(\frac{1}{2}ln\left(\frac{1+e}{1-e}\right) - e\right)$$
$$= \frac{2(1-0.768^2)}{0.768^3}\left(\frac{1}{2}ln\left(\frac{1+0.768}{1-0.768}\right) - 0.768\right) = 0.49 \tag{167}$$

$$\beta_0 = \frac{1}{e^2} - \frac{1-e^2}{2e^3}ln\left(\frac{1+e}{1-e}\right) = \frac{1}{0.768^2} - \frac{1-0.768^2}{2\cdot 0.768^3}ln\left(\frac{1+0.768}{1-0.768}\right) = 0.92 \tag{168}$$

$$m_{He} = \frac{4}{3}\pi\rho_{He}ab^2 = \frac{4}{3}\pi\cdot 0.179\cdot 1.35\cdot 0.65^2 = 0.43\ [kg] \tag{169}$$

$$a_{11} = \frac{\alpha_0}{2-\alpha_0}m = \frac{0.49}{2-0.49}\cdot 1.75 = 0.58\ [kg] \tag{170}$$

$$a_{22} = a_{33} = \frac{\beta_0}{2-\beta_0}m = \frac{0.92}{2-0.92}\cdot 1.75 = 1.49\ [kg] \tag{171}$$

$$a_{44} = 0 \tag{172}$$

$$a_{55} = a_{66} = \frac{1}{5}\frac{(b^2-a^2)^2(\alpha_0-\beta_0)}{2(b^2-a^2)+(b^2-a^2)(\beta_0-\alpha_0)}m$$
$$= \frac{1}{5}\frac{(0.65^2-1.35^2)^2(0.49-0.92)}{2(0.65^2-1.35^2)+(0.65^2-1.35^2)(0.92-0.49)}\cdot 1.75$$
$$= 0.087\ [kg] \tag{173}$$

[13] This estimation is based on the consideration that the airship was previously in a steady state. According to Fig. 24 the propelling force will decrease with respect to the increasing velocity down to 0.6 N @ 2 m/s.

$$I_{yy} = I_{zz} = \frac{4}{15}\pi\rho_{He}ab^2\,(a^2 + b^2)$$

$$= \frac{4}{15}\pi \cdot 0.179 \cdot 1.35 \cdot 0.65^2 \cdot (1.35^2 + 0.65^2)$$

$$= 0.19\ [kg \cdot m^2] \tag{174}$$

$$I_{xx} = \frac{8}{15}\,\pi\rho_{He}ab^4 = \frac{8}{15}\pi \cdot 0.179 \cdot 1.35 \cdot 0.65^4 = 0.072\ [kg \cdot m^2] \tag{175}$$

Unfortunately, the damping forces according to equations from (112) to (117) cannot be determined on a theoretical basis. Because the complex measurements in laboratory were not processed, the parameters measured at a similar airship described in [46] were applied.

$$D_{v_x} \approx 0.2\ \left[\frac{N}{m \cdot s^{-1}}\right] \tag{176}$$

$$D_{v_y} \approx 0.78\ \left[\frac{N}{m \cdot s^{-1}}\right] \tag{177}$$

$$D_{v_z} \approx 0.78\ \left[\frac{N}{m \cdot s^{-1}}\right] \tag{178}$$

$$D_{\omega_x} \approx 0.01\ \left[\frac{N \cdot m}{s^{-1}}\right] \tag{179}$$

$$D_{\omega_y} \approx 0.3\ \left[\frac{N \cdot m}{s^{-1}}\right] \tag{180}$$

$$D_{\omega_z} \approx 0.09\ \left[\frac{N \cdot m}{s^{-1}}\right] \tag{181}$$

5.4.1 Operation with no elevation

This model represents the situation in which the airship is moved according to the x-axis by the force of the main propellers. The calculations have been made with respect to the theory presented in chapter “4.4 Airship’s model”. The tail motor is off while the main motors are fed with 5 W of power each, unless otherwise indicated.

$$F_x = (F_{1P} + F_{1L}) \sin \varsigma = (0.9 + 0.9) \sin\left(\frac{\pi}{2}\right) = 1.8\ [N] \tag{182}$$

$$F_y = F_2 = 0\ [N] \tag{183}$$

$$F_z = (F_{1P} + F_{1L}) \cos \varsigma = (0.9 + 0.9) \cos\left(\frac{\pi}{2}\right) = 0\ [N] \tag{184}$$

$$M_x = -F_y l_1 = -0 \cdot 0.07 = 0\ [N \cdot m] \tag{185}$$

$$M_y = -F_z l_3 + F_x l_4 = -0 \cdot 0.13 + 1.8 \cdot 1.25 = 2.25\ [N \cdot m] \tag{186}$$

$$M_z = F_y l_2 = 0 \cdot 1.23 = 0\ [N \cdot m] \tag{187}$$

At this point, the relevant matrixes needed to fulfil the equation (95) can be constructed from the above calculated and estimated parameters. The matrix operations have been processed by means of Maple software and the results are as follows:

$$\boldsymbol{M}_{xz} = \begin{bmatrix} m + a_{11} & 0 & mz_y \\ 0 & m + a_{33} & -mx_g \\ mz_g & -mx_g & I_{yy} + a_{55} \end{bmatrix} = \begin{bmatrix} 2.33 & 0 & 0.23 \\ 0 & 3.24 & -0.35 \\ 0.23 & -0.35 & 0.28 \end{bmatrix} \tag{188}$$

$$\boldsymbol{D}_{xz} = \begin{bmatrix} D_{v_x} & 0 & 0 \\ 0 & D_{v_y} & 0 \\ 0 & 0 & D_{\omega_y} \end{bmatrix} = \begin{bmatrix} 0.2 & 0 & 0 \\ 0 & 0.78 & 0 \\ 0 & 0 & 0.3 \end{bmatrix} \tag{189}$$

$$\boldsymbol{G}_{xz} = \begin{bmatrix} 0 & 0 & 0 \\ 0 & 0 & 0 \\ 0 & 0 & z_g mg \end{bmatrix} = \begin{bmatrix} 0 & 0 & 0 \\ 0 & 0 & 0 \\ 0 & 0 & 2.23 \end{bmatrix} \tag{190}$$

Because the motion according to the x-axis is considered (with no height change), the pitch angle (see Fig. 26) is expected to be $\Theta = 0$. Therefore a simplified matrix (99) can be used instead of (101). The rotation degree $\Psi_0 = 0$ because straight flight direction is expected (Ψ_0 refers to the rotation of the airship with respect to the z-axis).

$$\boldsymbol{J}_{xz} = \begin{bmatrix} \cos\psi_0 & -\sin\psi_0 & 0 \\ 0 & 1 & 0 \\ 0 & 0 & 1 \end{bmatrix} = \begin{bmatrix} 1 & 0 & 0 \\ 0 & 1 & 0 \\ 0 & 0 & 1 \end{bmatrix} \tag{191}$$

$$\boldsymbol{B}_{xz} = \begin{bmatrix} 1 & 0 \\ 0 & 1 \\ l_4 & l_3 \end{bmatrix} = \begin{bmatrix} 1 & 0 \\ 0 & 1 \\ 0.6 & 0.1 \end{bmatrix} \tag{192}$$

Now the state-space model description can be applied, utilizing the equation (95). The appropriate matrixes $\mathbf{A_{ss}}$, $\mathbf{B_{ss}}$, $\mathbf{C_{ss}}$, $\mathbf{D_{ss}}$ of the state-space model are, according to [46], as follows:

$$\boldsymbol{A_{ss}} = \begin{bmatrix} -\boldsymbol{M_{xz}}^{-1}\boldsymbol{D_{xz}} & -\boldsymbol{M_{xz}^{-1}G} \\ \boldsymbol{J_{xz}} & [\mathbf{0}]_{3x3} \end{bmatrix}$$

$$= \begin{bmatrix} -0.095 & 0.038 & 0.14 & 0 & 0 & -1.00 \\ 0.0097 & -0.28 & -0.15 & 0 & 0 & 1.11 \\ 0.090 & -0.39 & -1.38 & 0 & 0 & 10.29 \\ 1 & 0 & 0 & 0 & 0 & 0 \\ 0 & 1 & 0 & 0 & 0 & 0 \\ 0 & 0 & 1 & 0 & 0 & 0 \end{bmatrix} \tag{193}$$

$$\boldsymbol{B_{ss}} = \begin{bmatrix} \boldsymbol{M_{xz}^{-1}B_{xz}} \\ [\mathbf{0}]_{3x2} \end{bmatrix} = \begin{bmatrix} 0.20 & -0.094 \\ 0.25 & 0.41 \\ 2.32 & 0.96 \\ 0 & 0 \\ 0 & 0 \\ 0 & 0 \end{bmatrix} \tag{194}$$

Now there is a need to describe the output vector y(t) of the continuous time-invariant system. Generally, the following equation can be applied:

$$\vec{y}(t) = \boldsymbol{C_{ss}}\vec{x}(t) + \boldsymbol{D_{ss}}\vec{u} \tag{195}$$

According to [46] the matrixes $\mathbf{C_{ss}}$ and $\mathbf{D_{ss}}$ were defined as follows:

$$\boldsymbol{C_{ss}} = \begin{bmatrix} 1 & 0 & 0 & 0 & 0 & 0 \\ 0 & 1 & 0 & 0 & 0 & 0 \\ 0 & 0 & 1 & 0 & 0 & 0 \\ 0 & 0 & 0 & 1 & 0 & 0 \\ 0 & 0 & 0 & 0 & 1 & 0 \\ 0 & 0 & 0 & 0 & 0 & 1 \end{bmatrix} \tag{196}$$

$$\boldsymbol{D_{ss}} = \begin{bmatrix} 0 & 0 \\ 0 & 0 \\ 0 & 0 \\ 0 & 0 \\ 0 & 0 \\ 0 & 0 \end{bmatrix} \tag{197}$$

Now the state-space model can be implemented in Matlab Simulink. The state-space block uses the matrixes $\mathbf{A_{ss}}$, $\mathbf{B_{ss}}$, $\mathbf{C_{ss}}$ and $\mathbf{D_{ss}}$. The input vector u(t) consists of two functions that represent the forces F_x and F_z (see (166) and (168)). In case of the straight flight only the force F_x applies. Three simulations have been processed. One simulation considers the propelling force to be constant (1.8 N according to (166)), the second one considers the propelling force to be time-dependent and decrease from 1.8 to 1.2 N in 10 seconds. This is to respect the effect of the decreasing propelling force with respect to the increasing velocity of the airship (see Fig. 24). After the next 10 seconds the propelling forces are inhibited in order to show the airship's inertia and damping of its movement. The third simulation shows the effect of active deceleration by the propellers spinning in opposite direction.

The Matlab Simulink simulation diagram is depicted in the following figure.

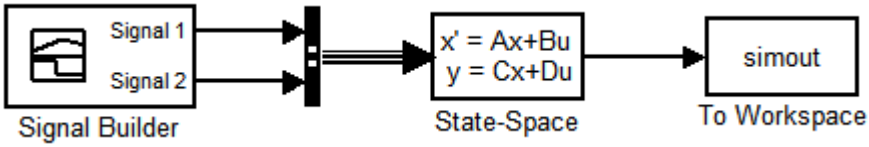

Fig. 86 – State-space model of the airship's flight and elevation processed in Matlab Simulink

In Fig. 86 the Signal Builder produces two signals. Signal 1 refers to the force F_x according to (182) and Signal 2 refers to the force F_z according to (184). The output vector of the State-Space model consists of the following functions:

1. Speed with respect to the x-axis $v_x(t)$,
2. Speed with respect to the z-axis $v_z(t)$,
3. Angular velocity with respect to the y-axis $\omega_y(t)$,
4. Position with respect to the x-axis x(t),
5. Position with respect to the z-axis z(t),
6. Angle of rotation with respect to the y-axis $\Theta(t)$.

5.4.1.1 Simulation 1: short force pulse

In simulation 1 the 1.8N force impulse with the length of 10 s is applied to the airship. The waveform of the forces is depicted in Fig. 87. Signal 1 refers to the force F_x according to (182) and Signal 2 refers to the force F_z according to (184). The behaviour of the airship in this case is described by figures below.

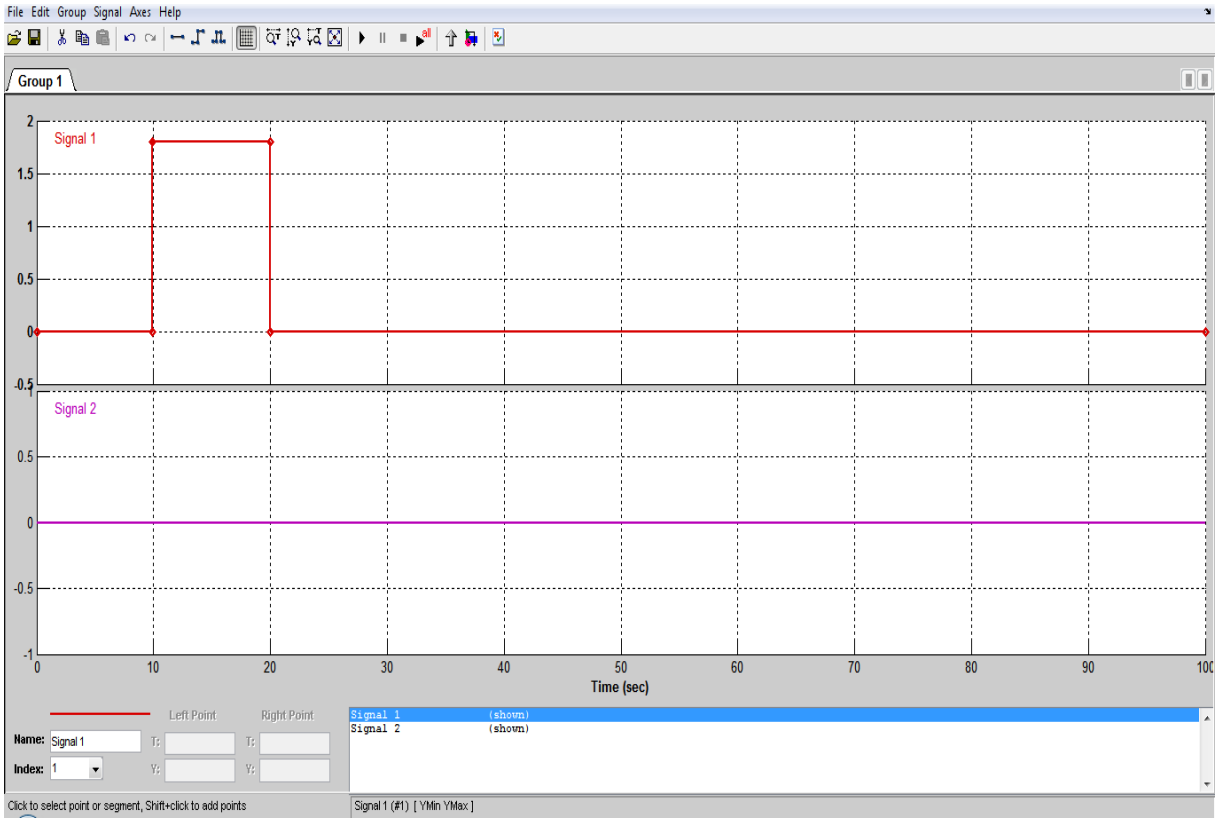

Fig. 87 – Signal generator setting for Simulation 1 (force impulse of 1.8 N in time from 10 to 20 s)

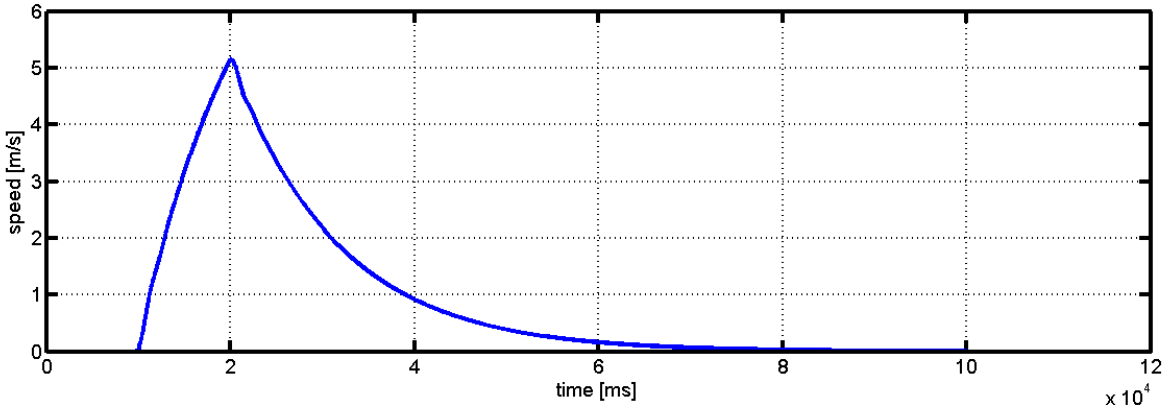

Fig. 88 – Simulation 1: Speed with respect to the x-axis

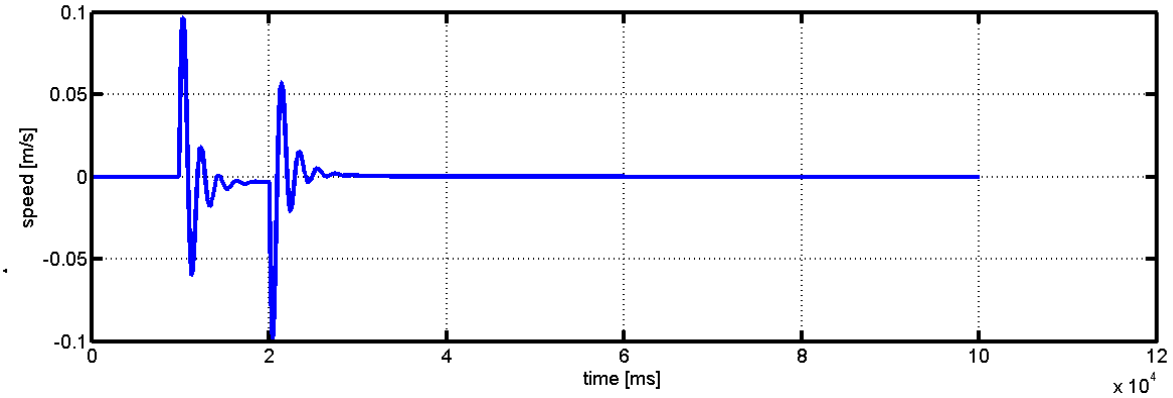

Fig. 89 – Simulation 1: Speed with respect to the z-axis

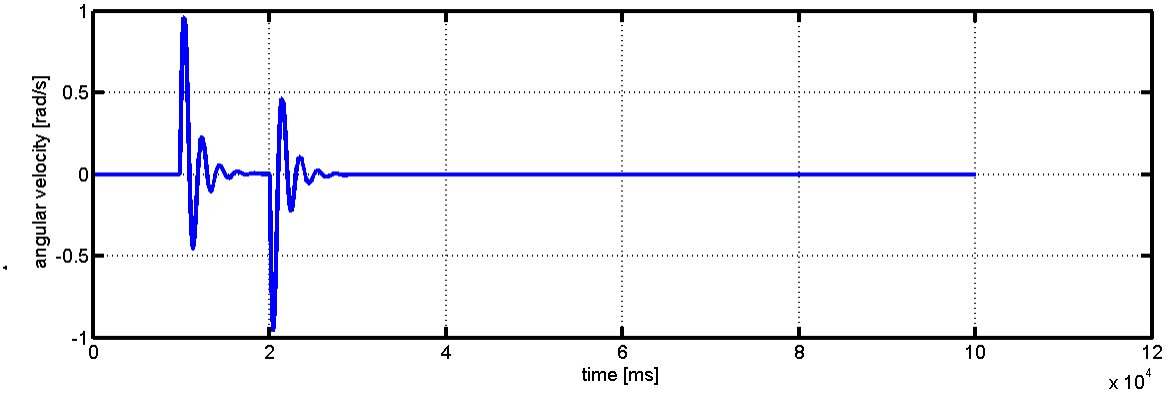

Fig. 90 – Simulation 1: Angular velocity with respect to the y-axis

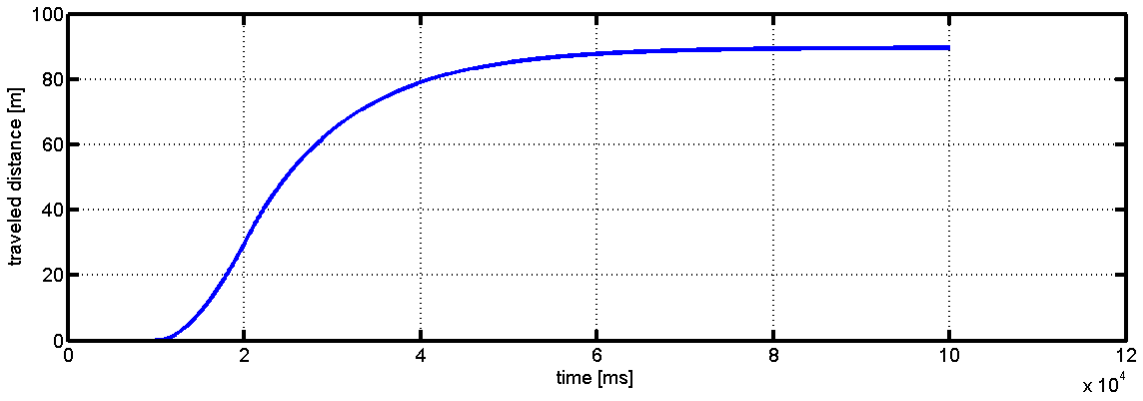

Fig. 91 – Simulation 1: Travelled distance

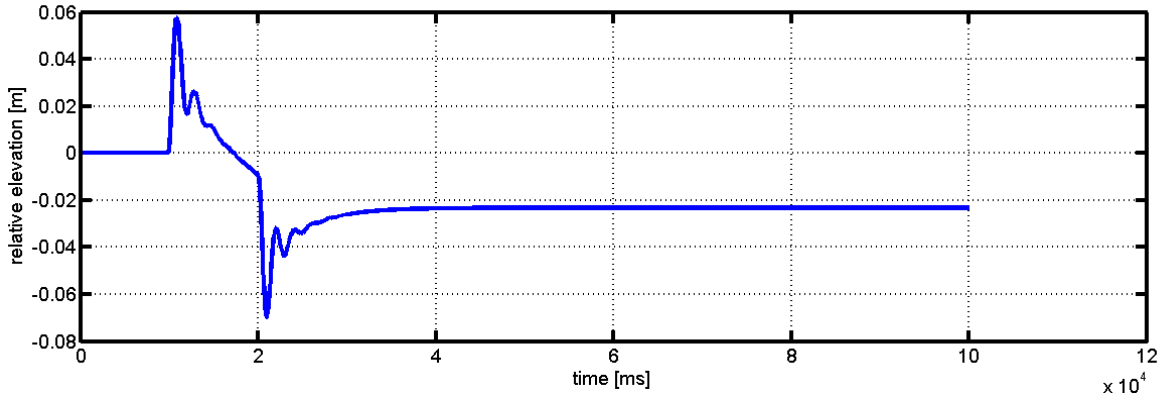

Fig. 92 – Simulation 1: Relative elevation

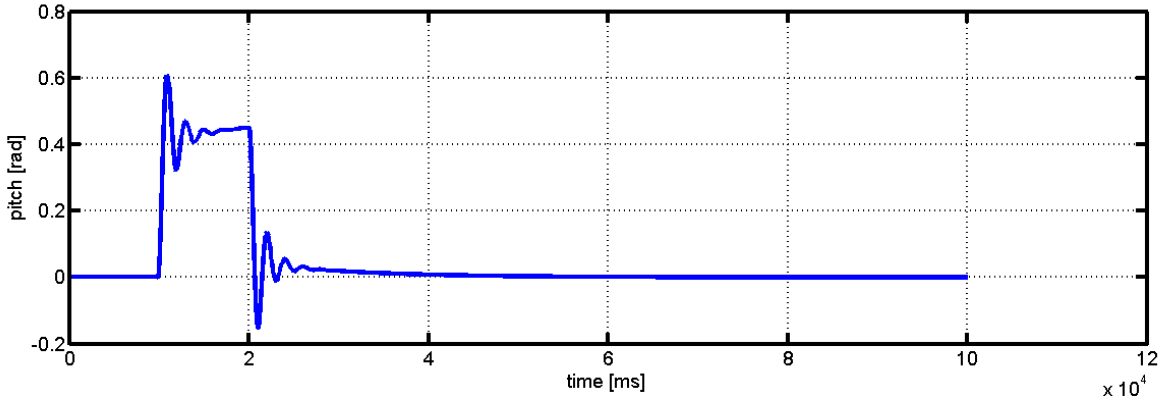

Fig. 93 – Simulation 1: Pitch angle

This simulation shows that the power of 10 W together with the propellers APC Slow Flyer (8x3.8)" can drive the airship at high speeds or that the damping coefficients for the simulation are too low. According to this simulation the airship would in 10 seconds after application of the propelling force reach the speed of approximately 5 m/s. On the other hand the force impulse is so high that it causes enormous pitch of up to 35° from the stable horizontal position of the airship. This finding raises the requirement of moderate power dosing to the main motors.

5.4.1.2 Simulation 2: propelling differences for various speeds are respected

This simulation respects the decrease of the propelling force which occurs when the speed of the airship is increasing. It also simulates the persistence of the propellers resulting in reaching of their nominal speed in the time of 100 ms after applying of the power. The waveform of the expected force, better representing the reality, is depicted in Fig. 94. In the time of 10 s the propelling force starts to rise up to the value of 1.8 N in 10.1 s. According to the previous

simulation, in 10 s after the propelling application the speed should be approximately 5 m/s. According to Fig. 24 the propelling force per one propeller should drop from 0.9 N to approximately 0.5 N at this speed. Therefore in 20 s the propelling force is decreased from 1.8 N to 1.0 N and the power is delivered for another 20 s in order to reach the steady-state. Then the force of the propellers is decreased to zero in a time period of 100 ms.

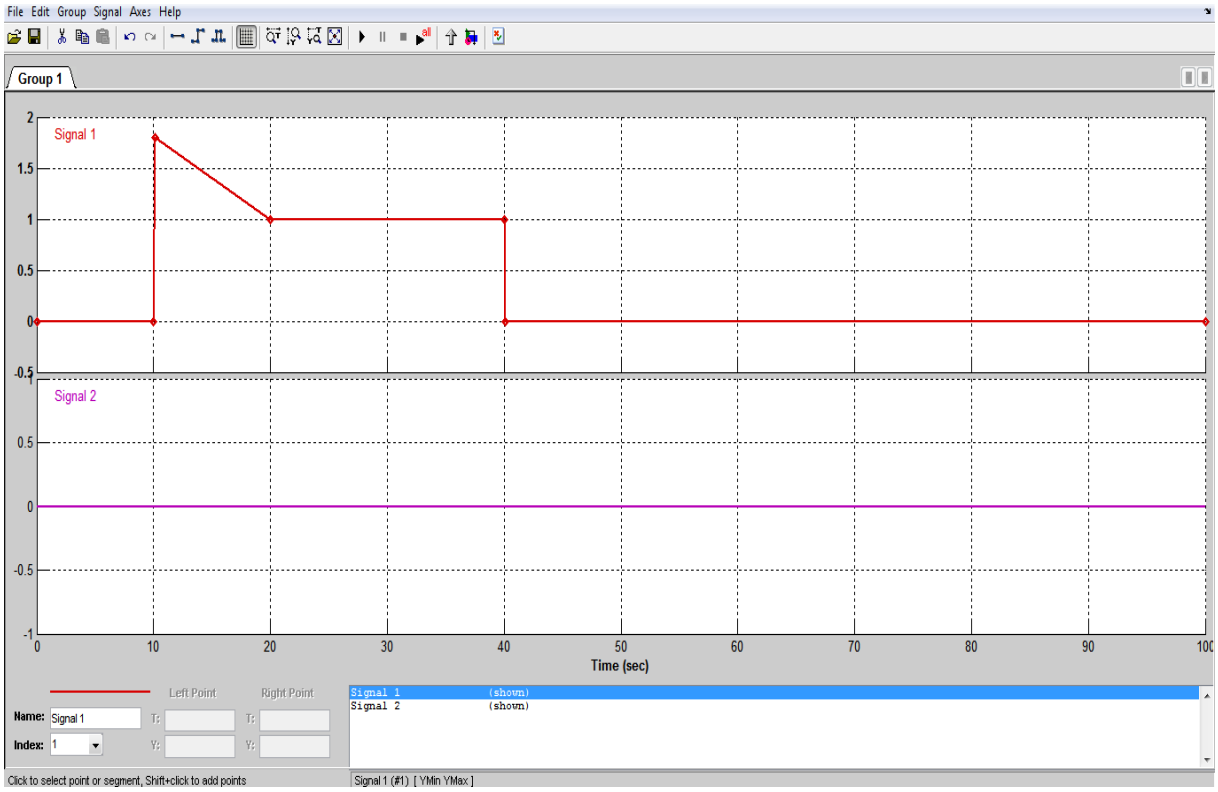

Fig. 94 – Simulation 2: Signal generator setting

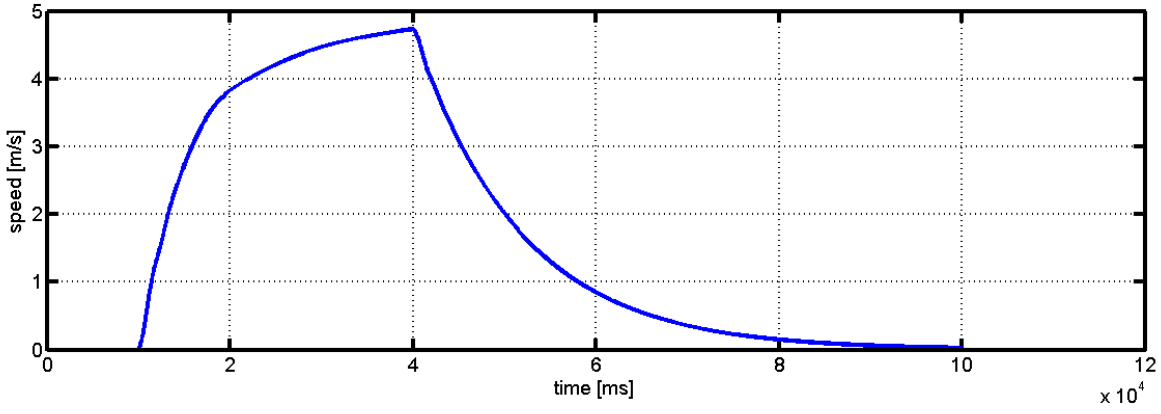

Fig. 95 – Simulation 2: Speed with respect to the x-axis

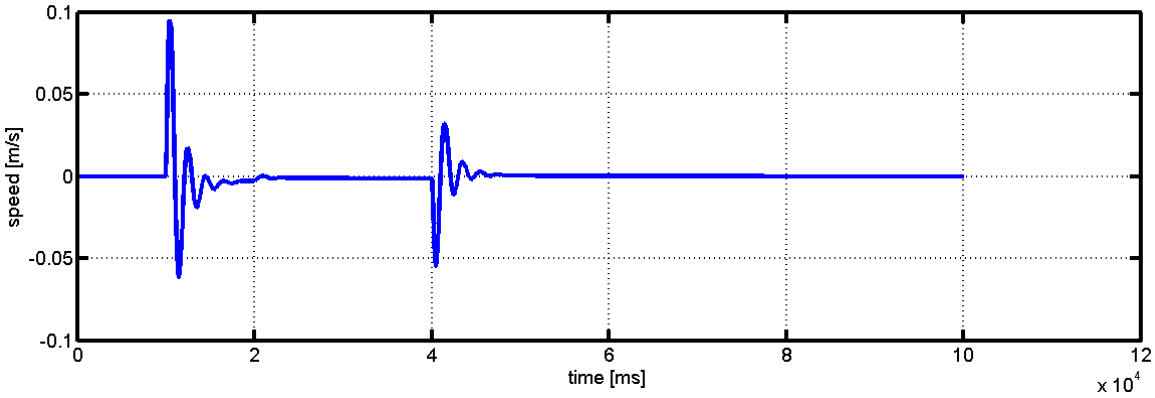

Fig. 96 – Simulation 2: Speed with respect to the z-axis

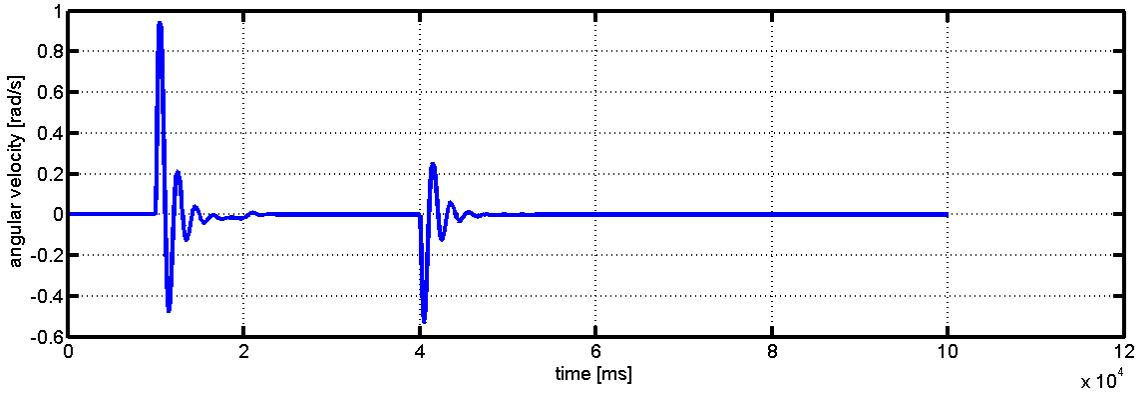

Fig. 97 – Simulation 2: Angular velocity with respect to the y-axis

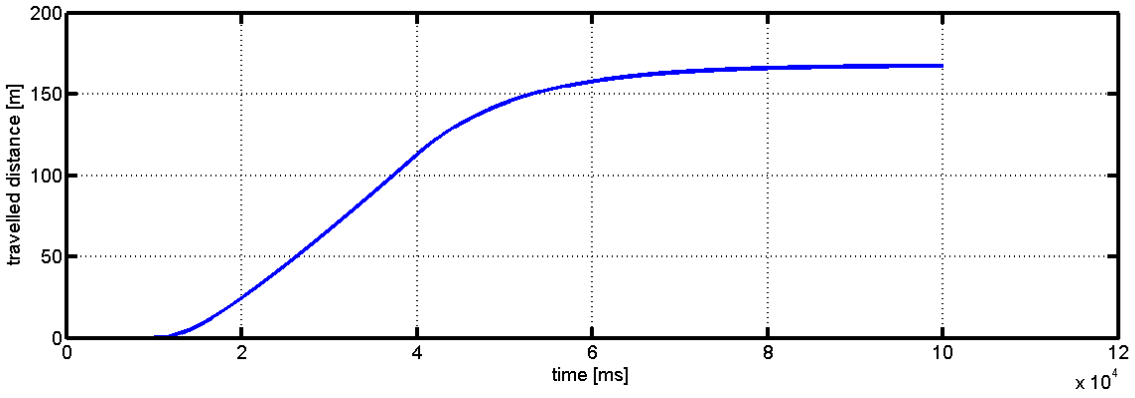

Fig. 98 – Simulation 2: Travelled distance

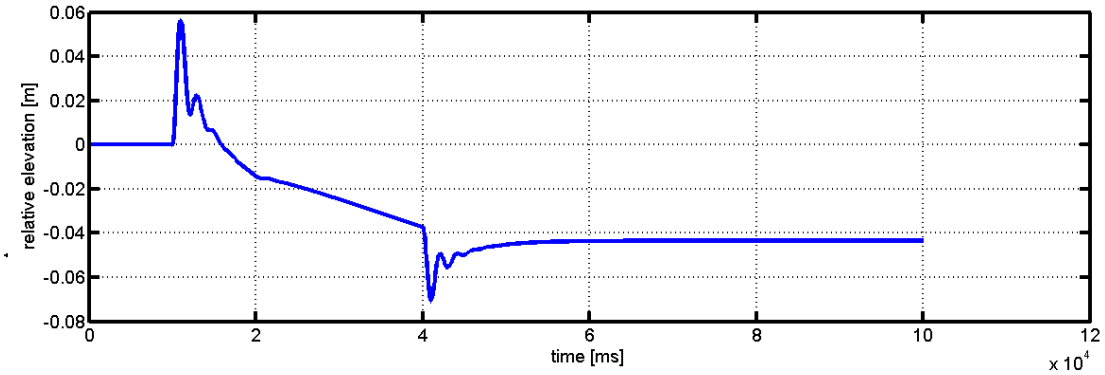

Fig. 99 – Simulation 2: Relative elevation

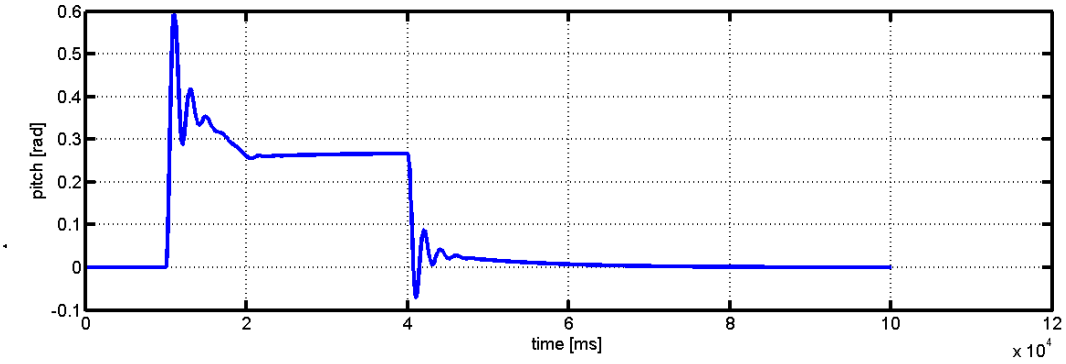

Fig. 100 – Simulation 2: Pitch relative to the y-axis

Although this simulation respects the real parameters of the propellers better, for the damping parameters (see equations from (182) to (187) and the pertinent text) the propelling force is quite high. The horizontal speed of the airship reaches the value of approximately 5 m/s which is quite high. As a side effect there is a constant pitch of approximately 15° that causes a slight misbalance of the model resulting in loosing of its height. For such high operating speeds the equation (101) should be used instead of (99). However, once the indoor operation is expected, operating the airship at such speeds makes no sense. For example, from the steady-state speed it decelerates to zero in 40 seconds and in this period it travels a distance of approximately 50 m (see Fig. 99).

5.4.1.3 Simulation 3: lowered power and fast braking

This simulation was processed with more moderate power dosing. The power delivered to the main motors is increased fluently and the maximum power is 1 W per one motor. This will result into starting propelling force of approximately 0.25 N @ 2,200 rpm per one propeller that decreases to approximately 0.15 N after 10 seconds. To stop the airship immediately, a short pulse of a counterforce

is generated consequently, by generating a propelling force of 1.5 N per one propeller at 5,200 rpm (the total braking power of approximately 22 W) for a short period of time (1 s).

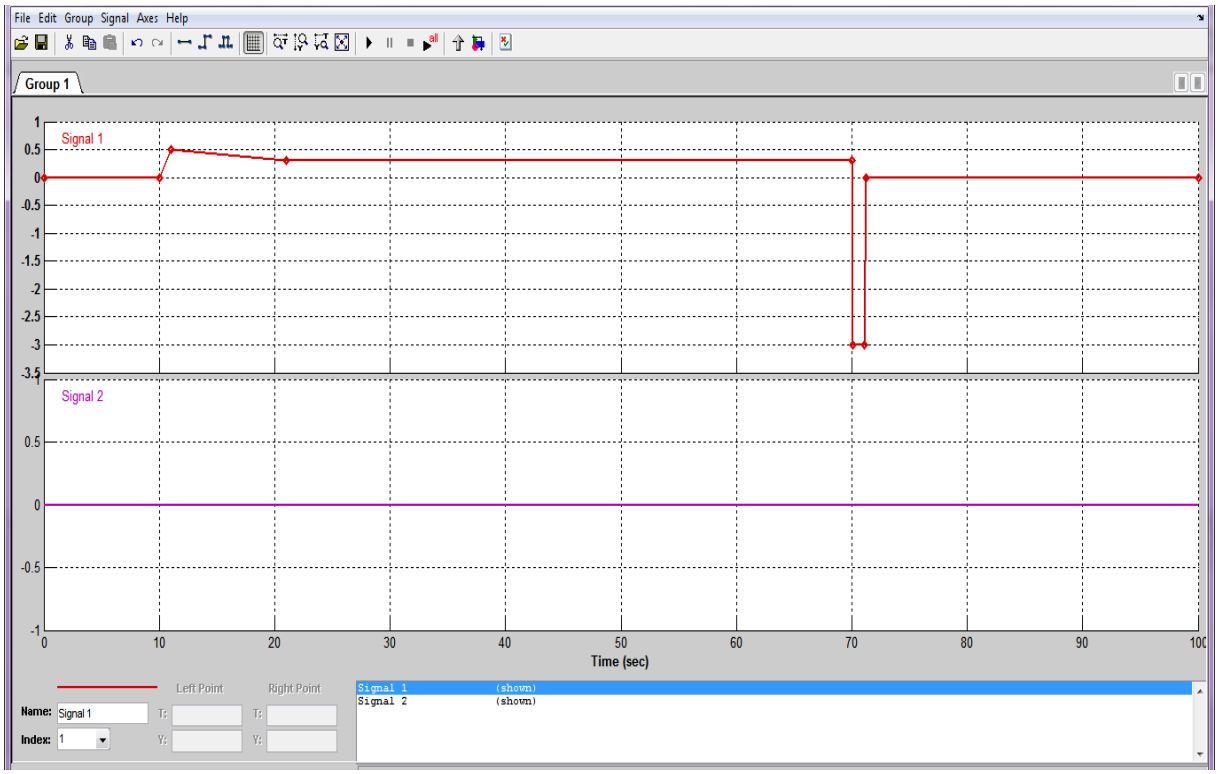

Fig. 101 – Simulation 3: Signal generator setting

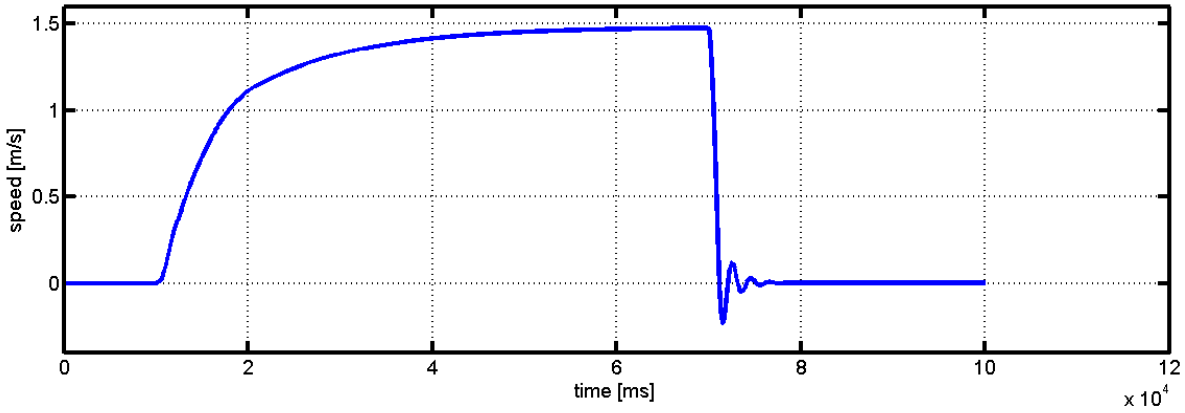

Fig. 102 – Simulation 3: Speed with respect to the x-axis

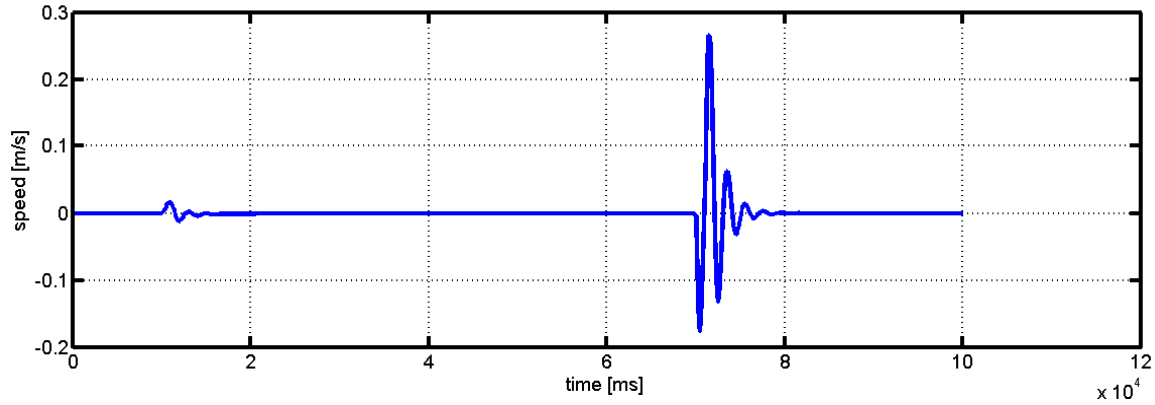

Fig. 103 – Simulation 3: Speed with respect to the z-axis

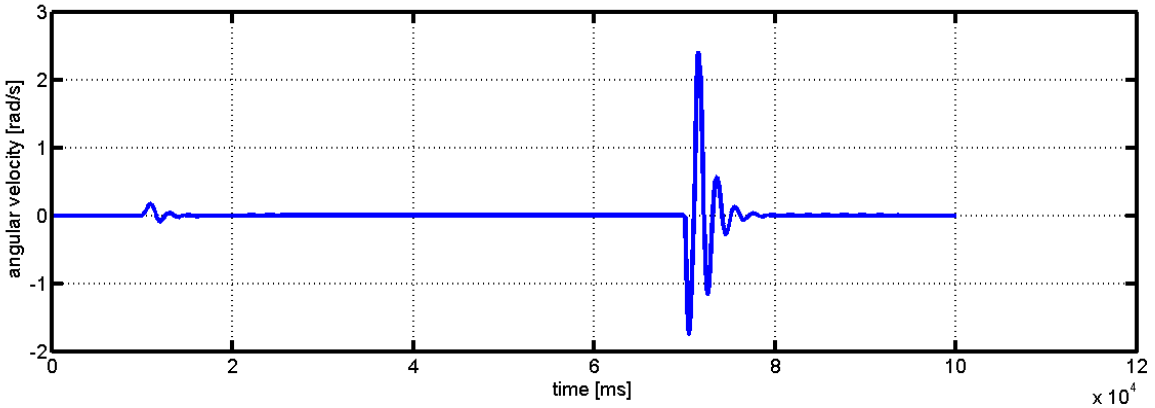

Fig. 104 – Simulation 3: Angular velocity with respect to the y-axis

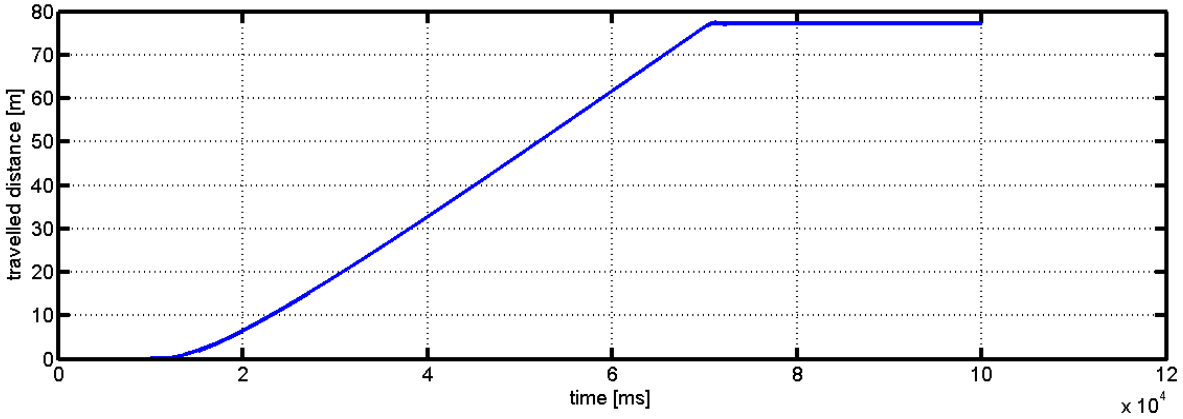

Fig. 105 – Simulation 3: Travelled distance

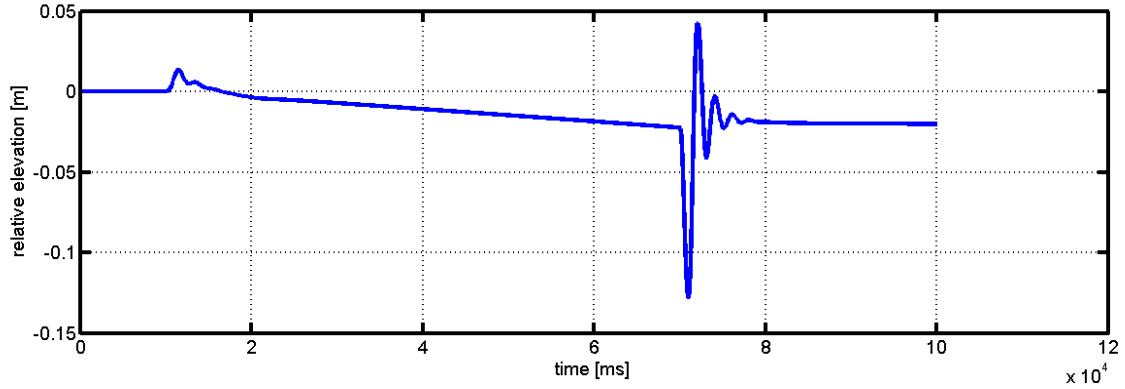

Fig. 106 – Simulation 3: Relative elevation

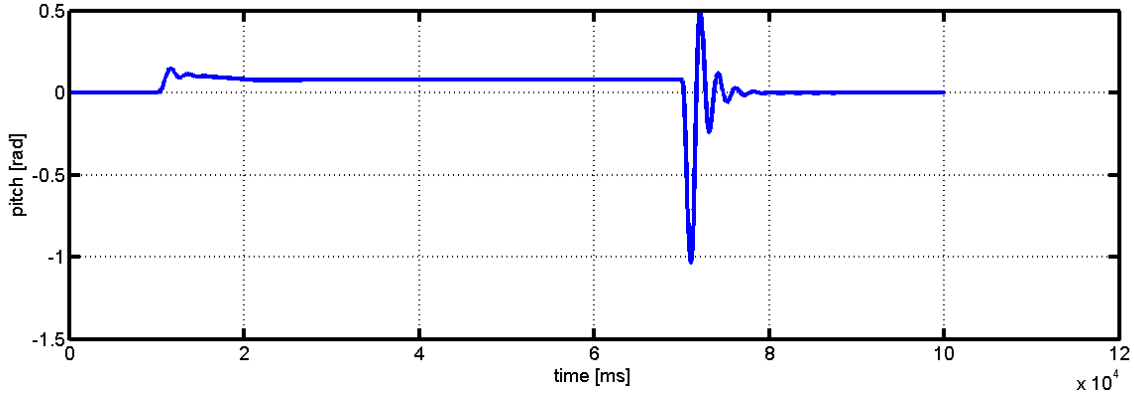

Fig. 107 – Simulation 3: Pitch relative to the y-axis

This simulation shows that the airship can be propelled by quite low force. With the power consumption of 2 W the estimated forward speed is approximately 1.5 m/s. According to Fig. 25 almost the maximum propellers' efficiency is achieved[14]. Its value is approximately 40 %. By driving the motors with the total power of 22 W the airship can be stopped in approximately 1 s. As a result, great swing with the amplitude of up to 60° may occur. This is caused by the position of the propellers which are mounted approximately 0.6 m below the centre of the gravity. Unfortunately, the height maintenance does not work properly in this model even if the propelling forces are low. Instead of (99) the equation (101) concerning the pitch caused by the moment of force caused by the propelling force and the arm between the centre of gravity and the propellers should be applied. A pitch of 5° is expected when the airship is driven by the

[14] At the speed of 1.5 m/s the best efficiency according to Fig. 25 and the relevant calculations is 43 % @ 1,900 rpm.

force of approximately 0.3 N. The expected operating time at the approximate speeds 1.5 m/s is expected to be approximately 5 hours.[15]

5.4.2 Operation with Fast Elevation

In this simulation the propelling forces of 2 x 0.9 N are expected. After 10 s the forces are decreased to 2 x 0.6 N in order the model respected the propelling forces decrease with respect to the increasing velocity. The swivelling angle of the motors is 75°, ensuring that more power is spend to change the elevation of the airship. In this simulation the equations from (188) to (197) can be applied as well as the simulation diagram depicted in Fig. 86.

The forces and moments are as follows:

$$F_x = (F_{1P} + F_{1L}) \sin \varsigma = (0.9 + 0.9) \sin(15°) = 0.47\ [N] \tag{198}$$

$$F_y = F_2 = 0\ [N] \tag{199}$$

$$F_z = (F_{1P} + F_{1L}) \cos \varsigma = (0.9 + 0.9) \cos(15°) = 1.73\ [N] \tag{200}$$

$$M_x = -F_y l_1 = -0 \cdot 0.07 = 0\ [N \cdot m] \tag{201}$$

$$M_y = -F_z l_3 + F_x l_4 = -0 \cdot 0.1 + 0.47 \cdot 0.6 = 0.28\ [N \cdot m] \tag{202}$$

$$M_z = F_y l_2 = 0 \cdot 1.23 = 0\ [N \cdot m] \tag{203}$$

The simulation details are described by the figures below.

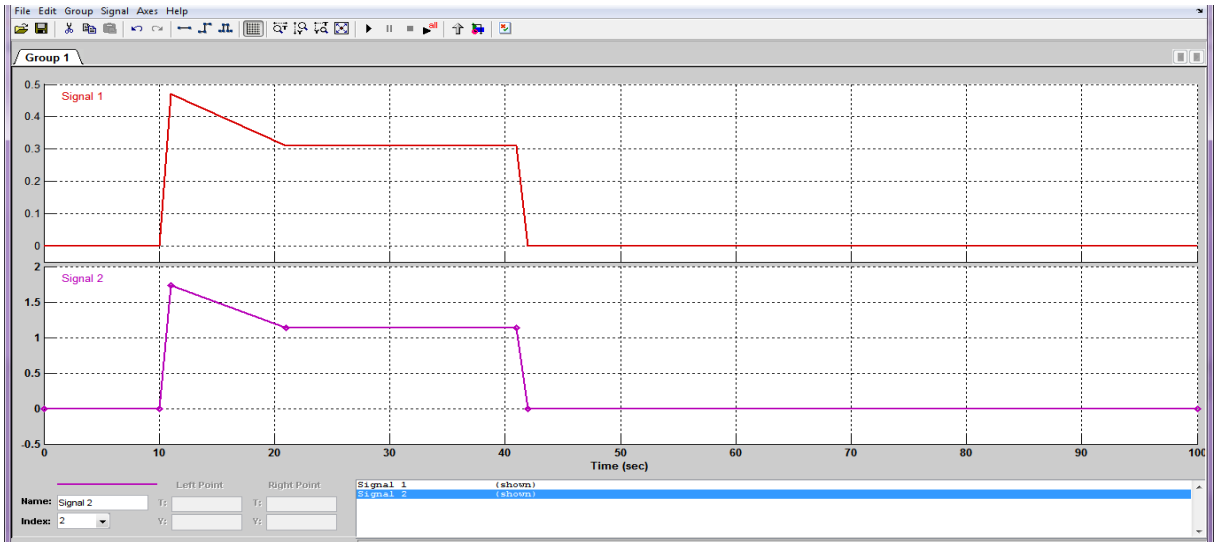

Fig. 108 – Propelling forces setting (operation with elevation)

[15] Concerning the accumulator 7.4 V / 2.2 Ah and minor power consumption of other electrical components.

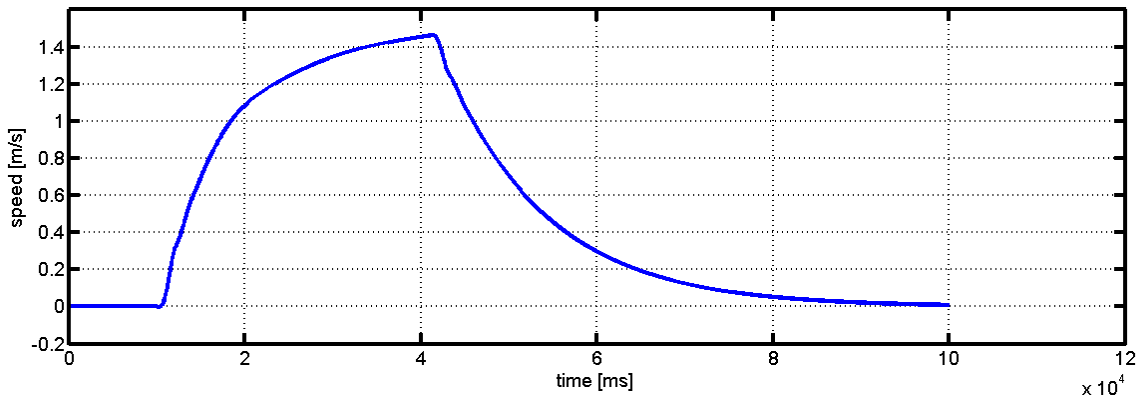

Fig. 109 – Simulation 4: Operation with elevation – speed with respect to the x-axis

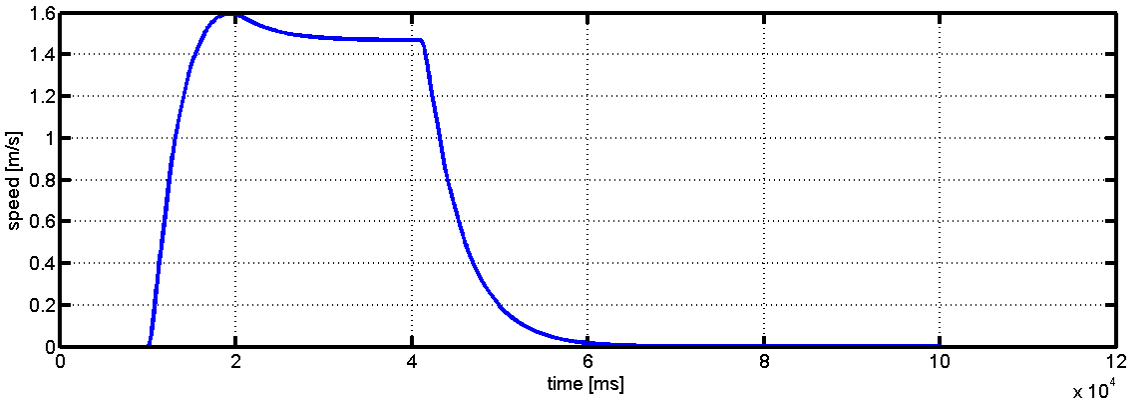

Fig. 110 – Simulation 4: Operation with elevation – speed with respect to the z-axis

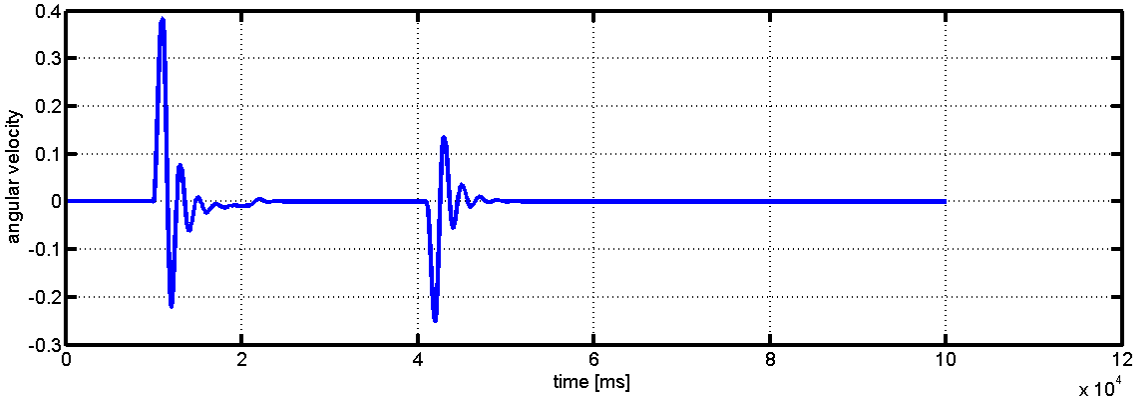

Fig. 111 – Simulation 4: Operation with elevation – angular velocity with respect to the y-axis

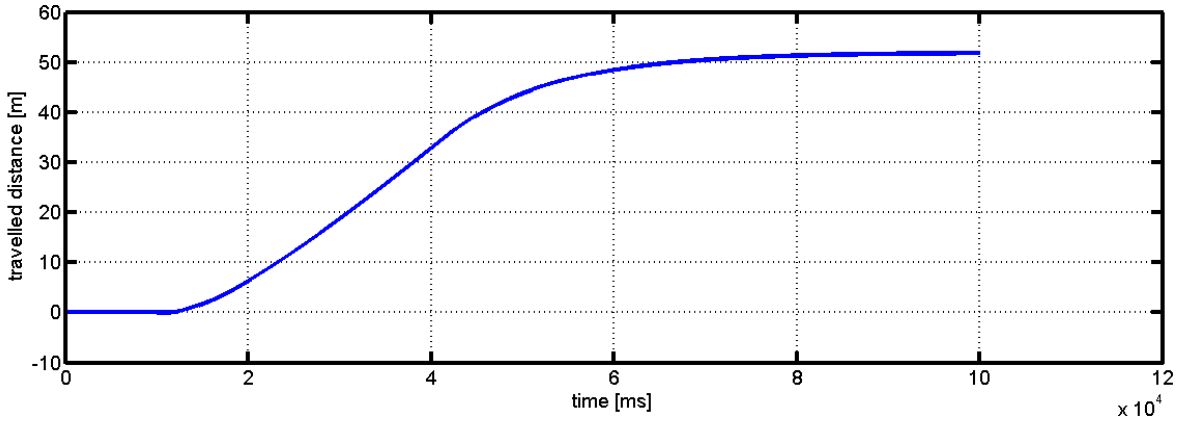

Fig. 112 – Simulation 4: Operation with elevation – travelled distance

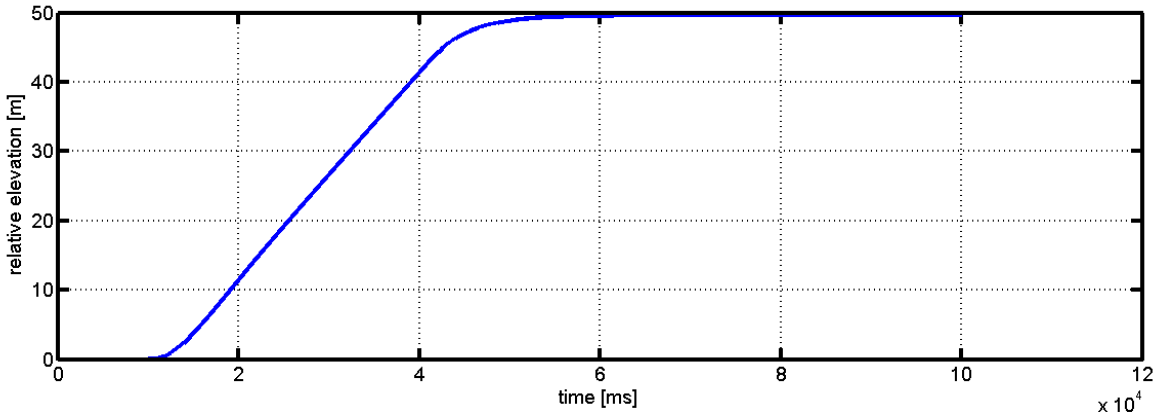

Fig. 113 – Simulation 4: Operation with elevation – relative elevation

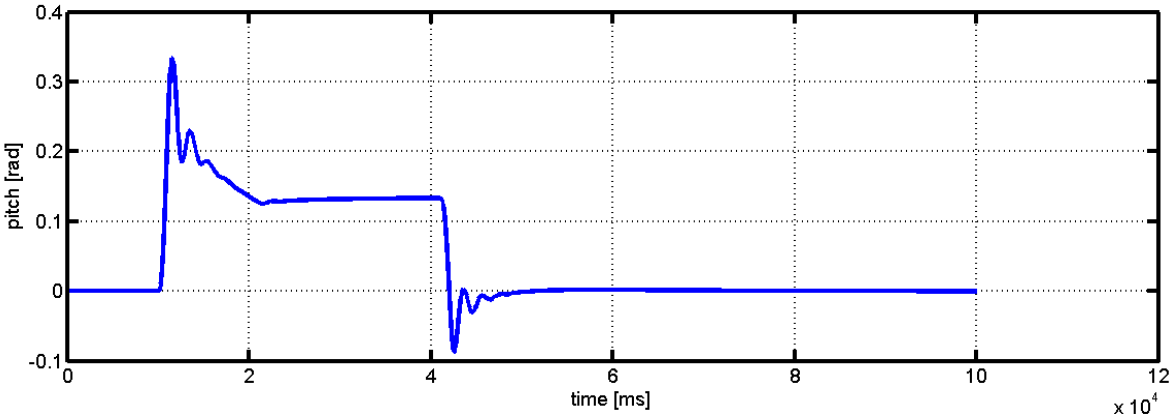

Fig. 114 – Simulation 4: Operation with elevation – pith with respect to the x-axis

According to this simulation it seems reasonable to use powerful propellers because with respect to the z-axis the aerodynamic damping is higher than the damping with respect to the x-axis. Therefore higher force is needed to develop the approximate speed of elevation 1.5 m/s. The ratio between the forces F_x and F_z depends on the angle ς which is dependent on the motors swivelling. The power of the motors must be adjusted in accordance to this angle.

5.4.3 Change of flight direction

The change of flight direction is processed by means of the propeller mounted at the tail of the bladder.

The simulation of this manoeuvre is based on the following consideration: The tail motor is driven by the power of 5 W for 1 second. This will generate the force pulse of 0.9 N that is 1 s long. The main motors are off and the airship does not move with respect to the x and the z-axis.

The relevant matrixes for this model are based on equations from (82) to (89). By using of the measured parameters of the airship, the following equations were obtained:

$$\boldsymbol{M}_{xy} = \begin{bmatrix} m + a_{22} & -mz_g & mx_g \\ -mz_g & I_{xx} + a_{44} & 0 \\ mx_g & 0 & I_{zz} + a_{66} \end{bmatrix} = \begin{bmatrix} 3.24 & -0.23 & 0.35 \\ -0.23 & 0.072 & 0 \\ 0.35 & 0 & 0.28 \end{bmatrix} \quad (204)$$

$$\boldsymbol{D}_{xy} = \begin{bmatrix} D_{v_y} & 0 & 0 \\ 0 & D_{\omega_y} & 0 \\ 0 & 0 & D_{\omega_y} \end{bmatrix} = \begin{bmatrix} 0.78 & 0 & 0 \\ 0 & 0.3 & 0 \\ 0 & 0 & 0.3 \end{bmatrix} \quad (205)$$

$$\boldsymbol{G}_{xy} = \begin{bmatrix} 0 & 0 & 0 \\ 0 & z_g mg & 0 \\ 0 & -x_g mg & 0 \end{bmatrix} = \begin{bmatrix} 0 & 0 & 0 \\ 0 & 2.23 & 0 \\ 0 & -3.43 & 0 \end{bmatrix} \quad (206)$$

$$\boldsymbol{J}_{xy} = \begin{bmatrix} \sin\psi_0 & \cos\psi_0 & 0 \\ 0 & 1 & 0 \\ 0 & 0 & 1 \end{bmatrix} = \begin{bmatrix} 0 & 1 & 0 \\ 0 & 1 & 0 \\ 0 & 0 & 1 \end{bmatrix} \quad (207)$$

$$\boldsymbol{B}_{\boldsymbol{xy}} = \begin{bmatrix} 1 \\ l_1 \\ -l_2 \end{bmatrix} = \begin{bmatrix} 1 \\ 0.07 \\ -1.23 \end{bmatrix} \quad (208)$$

As indicated by (207), the initial yaw angle of the airship is $\Psi_0 = 0$. For the state space description, the equation (84) is applicable. After processing by Maple software, the following equations describing the state-space model were obtained:

$$\boldsymbol{A_{ss}} = \begin{bmatrix} -\boldsymbol{M_{xy}^{-1}D_{xy}} & -\boldsymbol{M_{xy}^{-1}G_{xy}} \\ \boldsymbol{J_{xy}} & [\boldsymbol{0}]_{\boldsymbol{3x3}} \end{bmatrix}$$

$$= \begin{bmatrix} -0.38 & -0.46 & 0.18 & 0 & 5.48 & 0 \\ -1.18 & -5.61 & 0.58 & 0 & -48.3 & 0 \\ 0.47 & 0.58 & -1.31 & 0 & 19.3 & 0 \\ 0 & 1 & 0 & 0 & 0 & 0 \\ 0 & 1 & 0 & 0 & 0 & 0 \\ 0 & 0 & 0 & 1 & 0 & 0 \end{bmatrix} \tag{209}$$

$$\boldsymbol{B_{ss}} = \begin{bmatrix} -\boldsymbol{M_{xy}^{-1}B_{xy}} \\ [\boldsymbol{0}]_{\boldsymbol{3x1}} \end{bmatrix} = \begin{bmatrix} 1.33 \\ 5.19 \\ -6.13 \\ 0 \\ 0 \\ 0 \end{bmatrix} \tag{210}$$

$$\boldsymbol{C_{ss}} = \begin{bmatrix} 1 & 0 & 0 & 0 & 0 & 0 \\ 0 & 1 & 0 & 0 & 0 & 0 \\ 0 & 0 & 1 & 0 & 0 & 0 \\ 0 & 0 & 0 & 1 & 0 & 0 \\ 0 & 0 & 0 & 0 & 1 & 0 \\ 0 & 0 & 0 & 0 & 0 & 1 \end{bmatrix} \tag{211}$$

$$\boldsymbol{D_{ss}} = \begin{bmatrix} 0 \\ 0 \\ 0 \\ 0 \\ 0 \\ 0 \end{bmatrix} \tag{212}$$

At this point, according to the input vector $\vec{x}$ (82), the following State-Space model can be simulated in Matlab Simulink:

$$\frac{d\vec{x}}{dt} = \boldsymbol{A_{ss}}\vec{x} + \boldsymbol{B_{ss}}\,\vec{F}_2 \tag{213}$$

$$\vec{y}(t) = \boldsymbol{C_{ss}}\vec{x}(t) + \boldsymbol{D_{ss}}\vec{u} \tag{214}$$

The output vector $\vec{y}(t)$ consists of the following functions:

1. Circumferential velocity with respect to the y-axis,
2. Angular velocity with respect to the x-axis,
3. Angular velocity with respect to the z-axis,
4. Position according to the y-axis,
5. Rolling angle of the airship with respect to the x-axis,
6. Yawing angle of the airship with respect to the y-axis.

5.4.3.1 Simulation 5: yawig without braking

In this simulation only a 1 second long force pulse is generated without any attempt to stop the rotation of the airship. As stated above, the motor expected power generated by the propeller is 5 W, resulting in the propelling force of approximately 0.9 N.

The graphical representation of the pertinent Matlab Simulink model is depicted in the following figure.

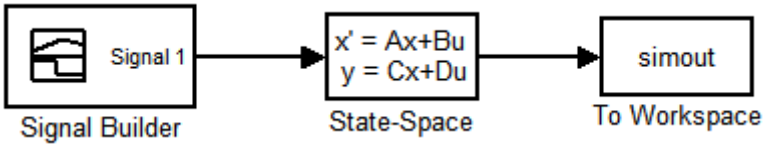

Fig. 115 – State-space model of the airship's yawing processed in Matlab Simulink

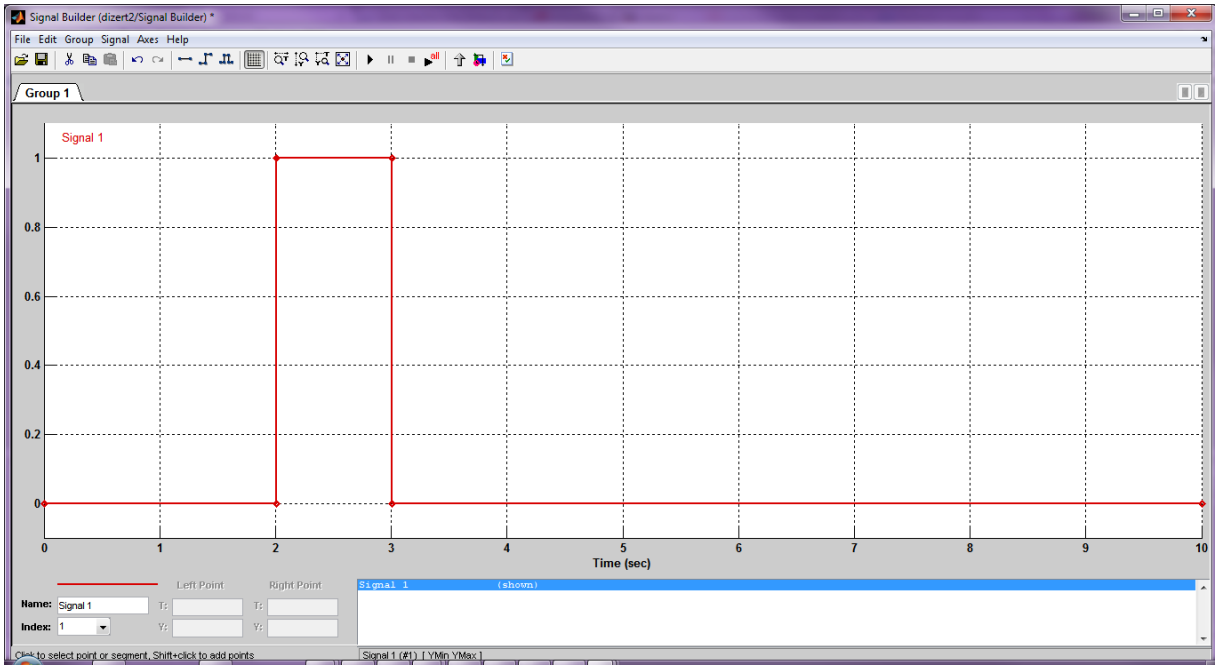

Fig. 116 – Simulation 5: Propelling force setting in Signal Builder

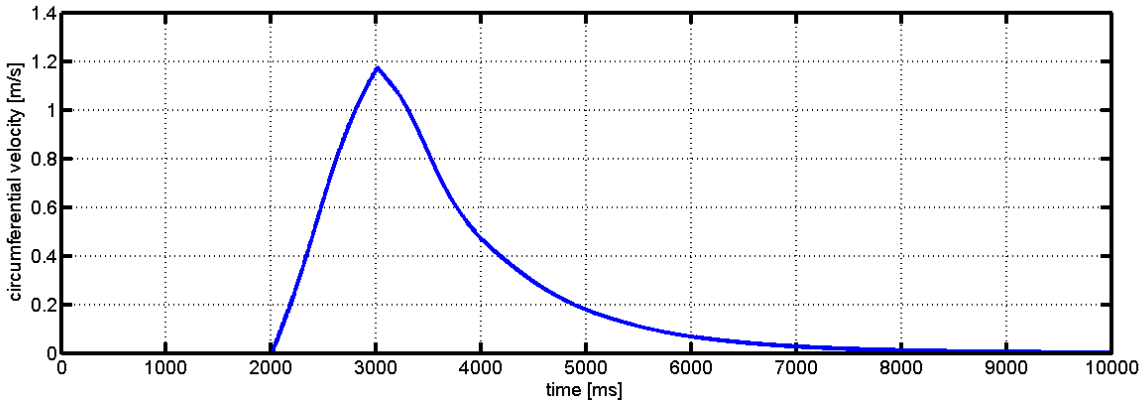

Fig. 117 – Simulation 5: Circumferential velocity with respect to the y-axis

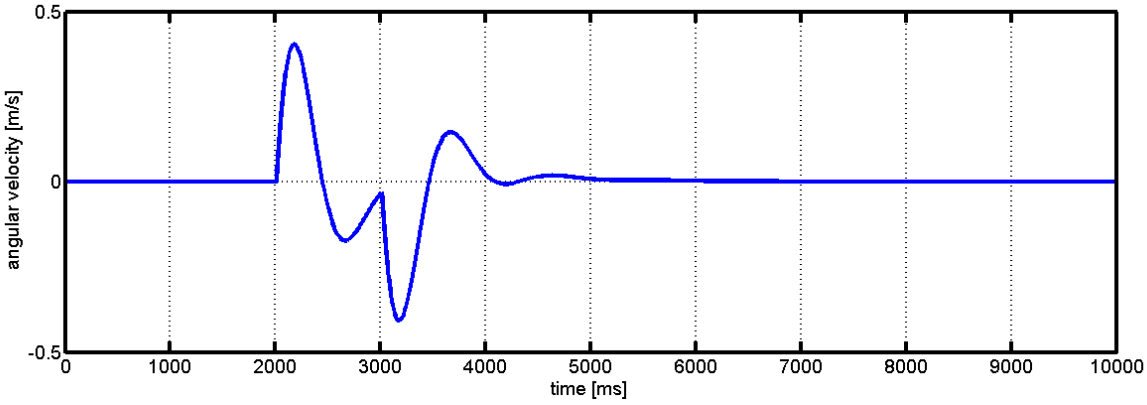

Fig. 118 – Simulation 5: Angular velocity with respect to the x-axis

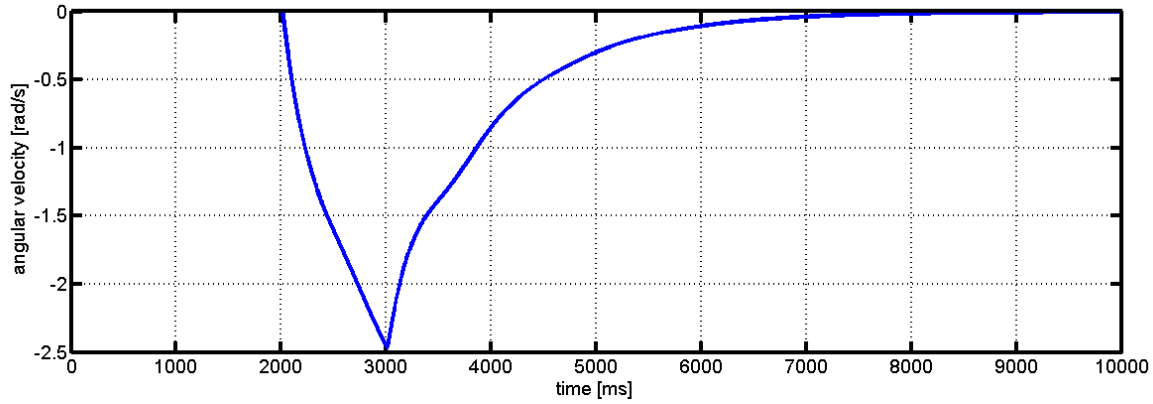

Fig. 119 – Simulation 5: Angular velocity with respect to the z-axis

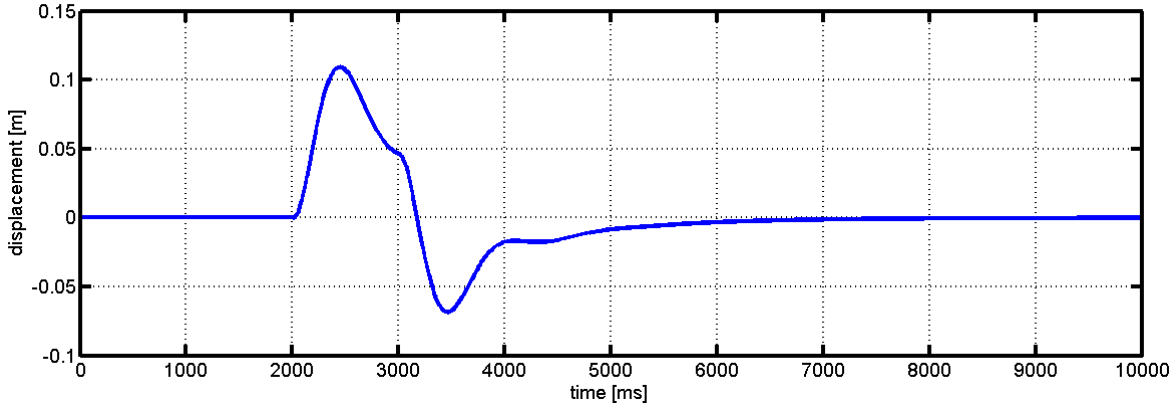

Fig. 120 – Simulation 5: Displacement according to the y-axis

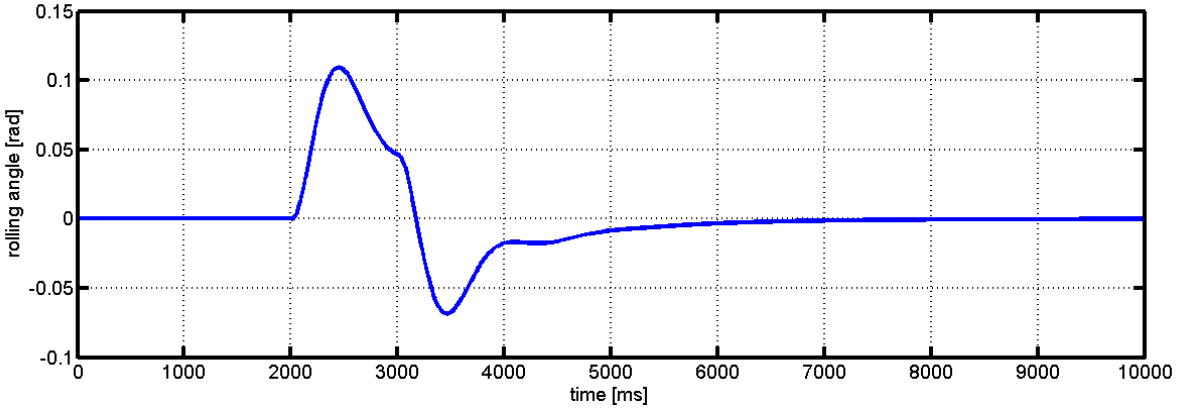

Fig. 121 – Simulation 5: Rolling angle with respect to the y-axis

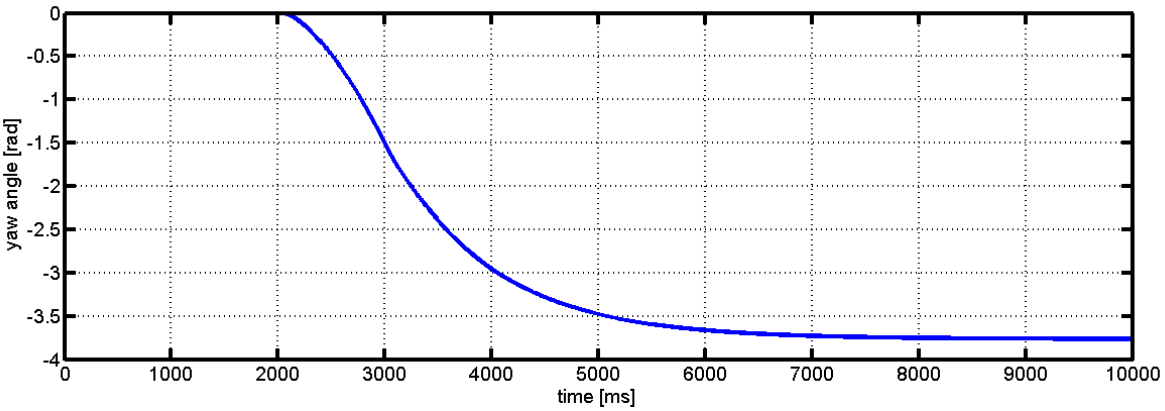

Fig. 122 – Simulation 5: Yawing angle

This simulation shows that there is a need for stabilization of the airship's yawing. Although the force pulse is only 1 s long, the yawing time of the airship is approximately 5 s due to its mass persistence. Therefore, instead of the approximate 90° yaw angle change that is reached while the force is acting (in 1 s), the total yaw angle is almost 220°.

5.4.3.2 Simulation 6: yawing with braking

This simulation uses the same force pulse as the previous one. After this pulse a short counter pulse is generated. The braking force is expected to be 1.5 N, which corresponds to the propeller's power of approximately 11 W. The length of the yawing force pulse is 1 s while the length of the braking pulse is 0.31 s. By this approach the yaw angle is stabilized to approximately 90°.

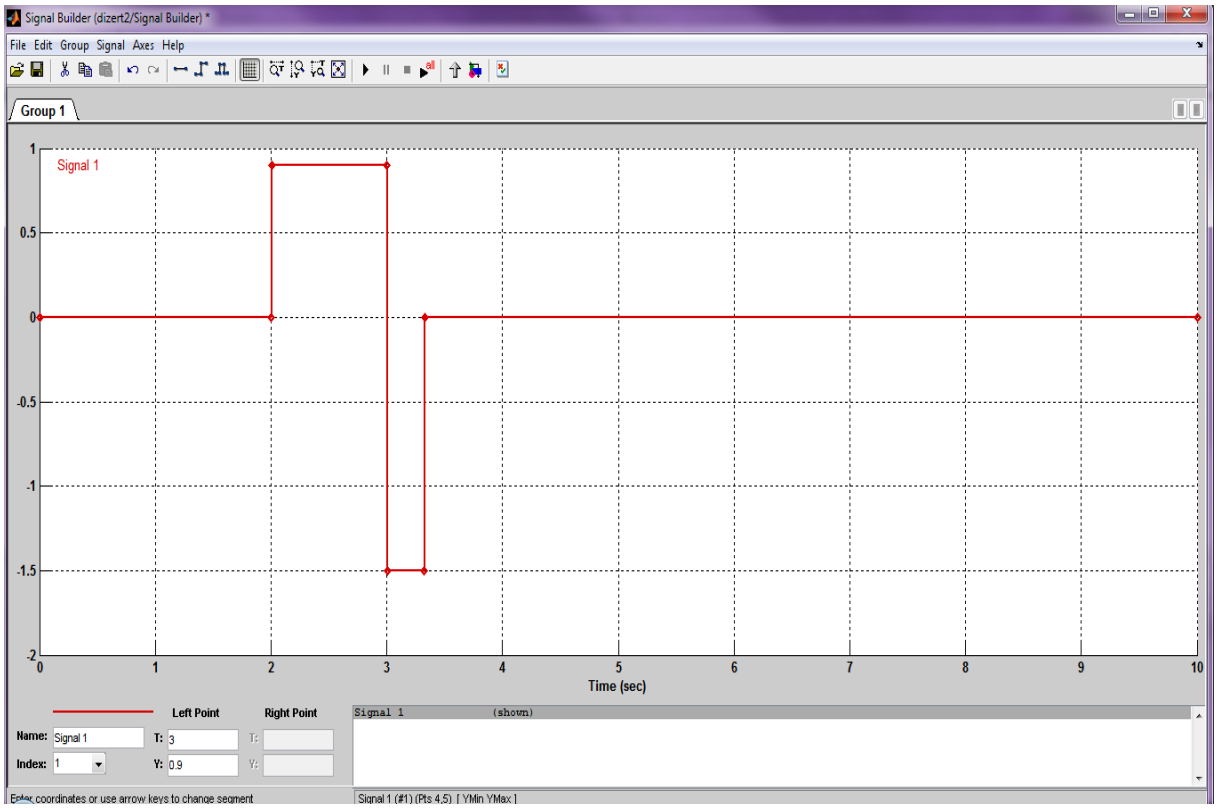

Fig. 123 – Simulation 6: Propelling force setting in Signal Builder

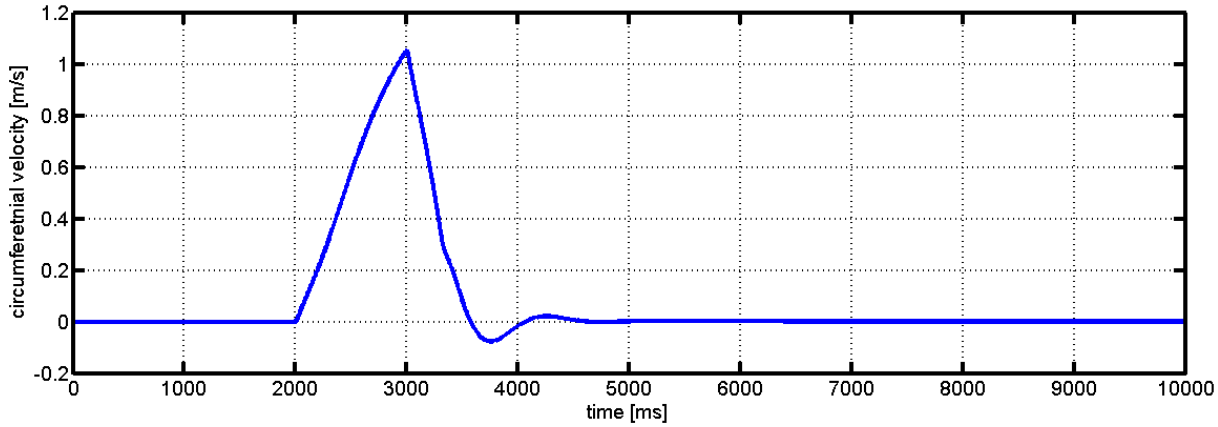

Fig. 124 – Simulation 6: Circumferential velocity with respect to the y-axis

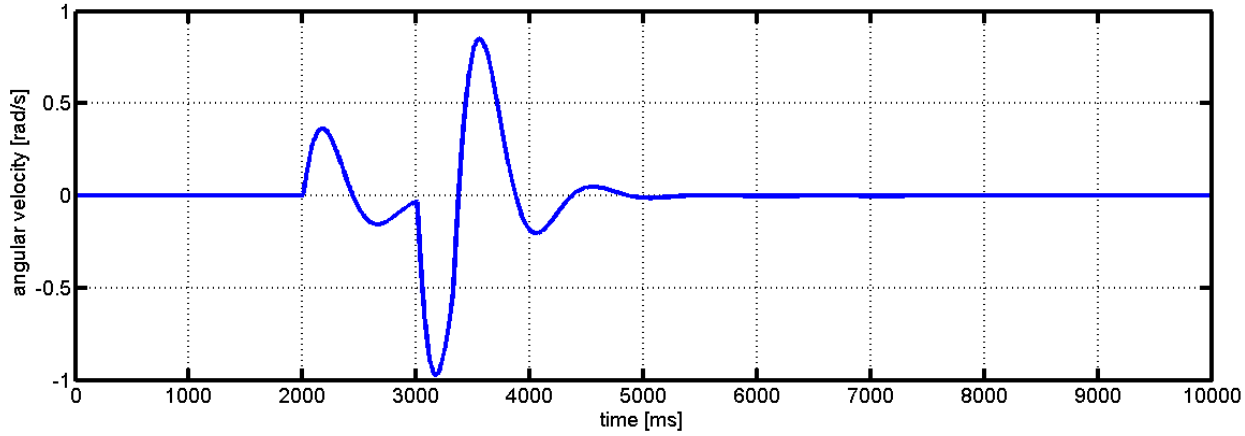

Fig. 125 – Simulation 6: Angular velocity with respect to the x-axis

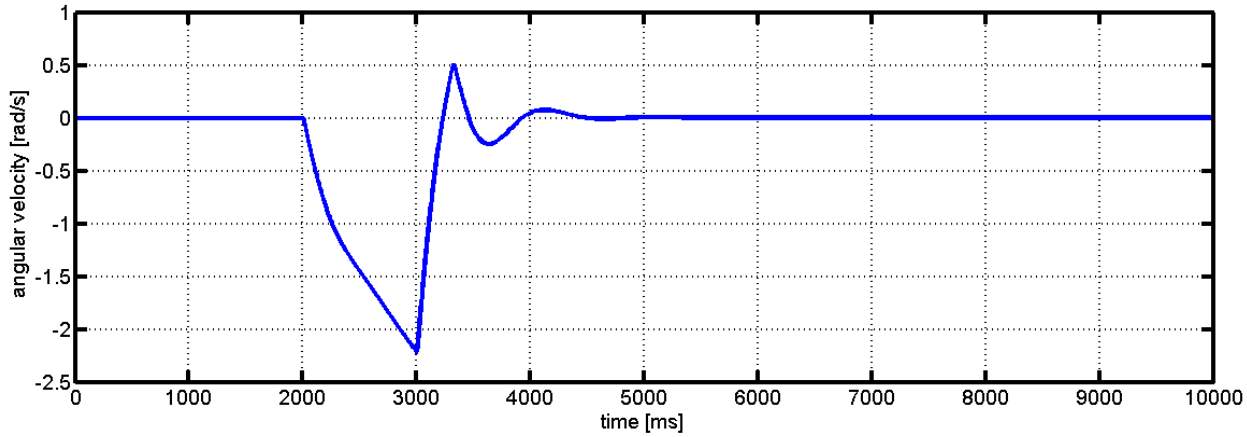

Fig. 126 – Simulation 6: Angular velocity with respect to the z-axis

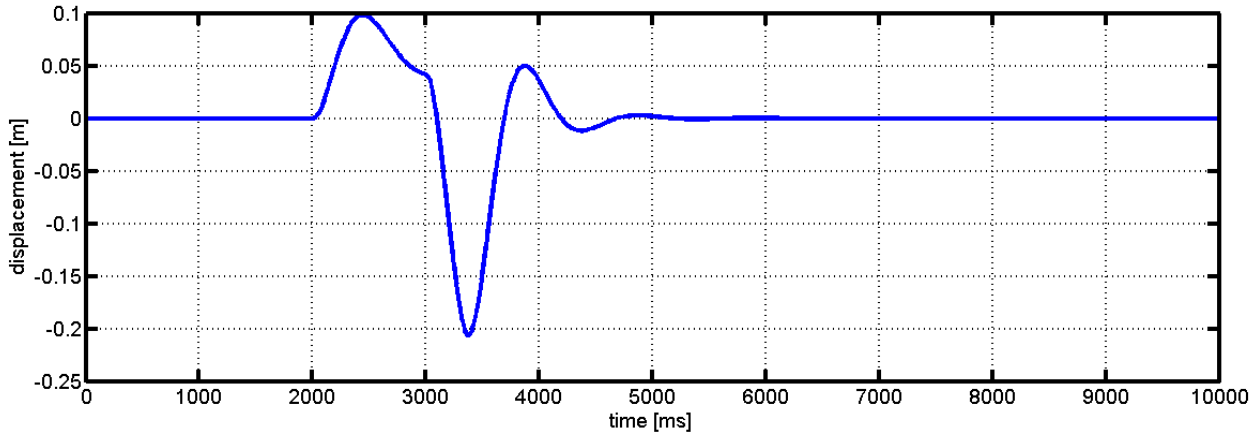

Fig. 127 – Simulation 6: Displacement according to the y-axis

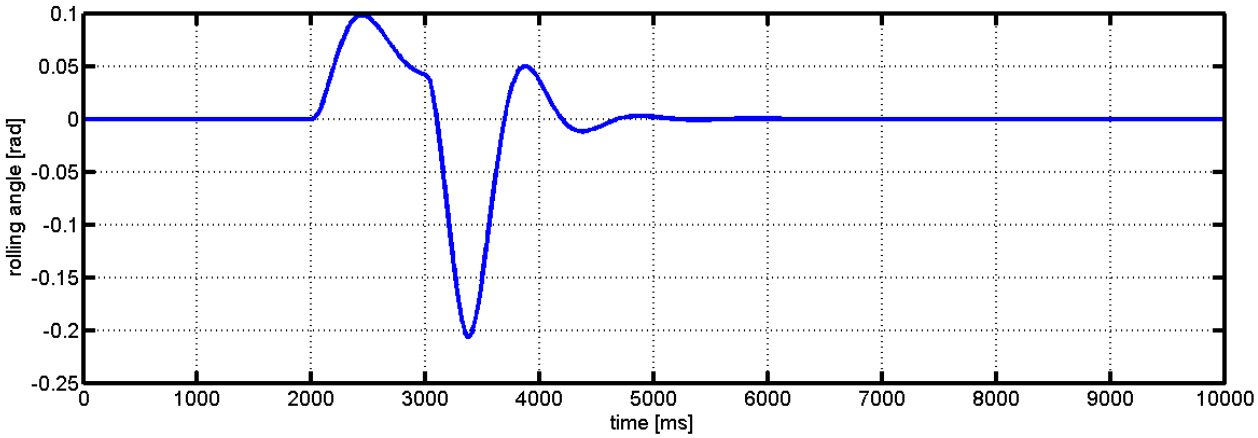

Fig. 128 – Simulation 6: Rolling angle of the airship with respect to the x-axis

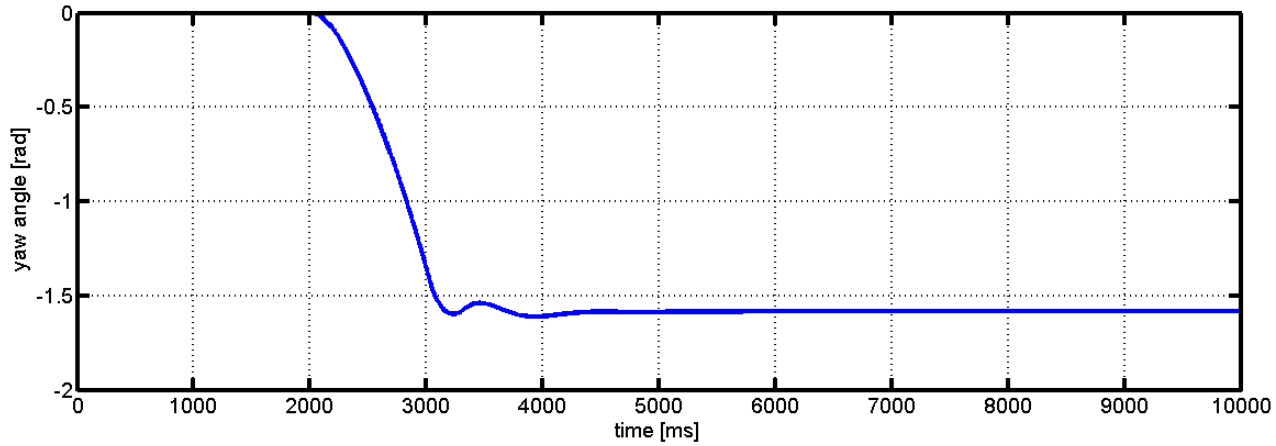

Fig. 129 – Simulation 5: Yawing angle

According to this simulation it is theoretically possible to stabilize the yaw position of the airship by means of creating a counter force pulse by the tail motor. As depicted at Fig. 129 it takes 1 second to turn the airship by 90° and other 2 seconds to stabilize its position.

6 CONCLUSION

This thesis is focused on a design of a small Autonomous monitoring system that consists of a small airship filled with helium, its propelling and controlling systems and several monitoring devices such as a camera etc. As the amount of issues connected with this topic is quite large, only several issues are discussed within the framework of the thesis.

The primary idea consisted in development of a small airship that is capable of operating inside an enclosed hall and of bearing several monitoring devices, such as the camera, RF signal gauges, thermometers etc. During the work on this project a lot of problems appeared, such as detection of obstacles, autonomous orientation in space etc. Soon it became apparent that the complex design exceeded the framework of one Ph.D. thesis. Therefore, only the following topics were discussed in the thesis: detection of obstacles, hardware design, effective power supply, propelling and basic dynamical model of the system. These topics are sufficient to help a designer to construct the Autonomous monitoring system in minimum configuration, in which it is capable of autonomous operating and avoiding obstacles when operating on a random trajectory. The controlling unit of the airship also enables reading of RFID tags that can be used for position checking in case the inertial trajectory control is implemented; once the starting point is defined and the dynamic model of the airship is accurate enough, the trajectory can be defined by driving the pertinent propellers in time according to a preprogramed table. The cumulative position error is intended to be minimized by means of RFID tags displaced around the trajectory, according to which the information on the current position can be corrected.

The main findings and topics of this thesis are described below:

Obstacles detection

The obstacles detection is based on measurements of the distance between the airship and the given obstacle. According to the study provided in the theoretical part of this thesis, ultrasonic detectors are quite sufficient for this application, despite their disadvantages. To prove their reliability, special ultrasonic detectors testing kit has been constructed and a set of measurements was processed. The detailed description of this kit can be found in chapter “5.1.2 Module for obstacles detection”. This module is capable of detecting up to 9 obstacles at once and it is able to provide information on overpassing the pre-set distance threshold. Information on the reliability of the obstacles detection is also included in the above mentioned chapter.

Motors driving

The airship is propelled by three motors. Two main motors are mounted on the gondola below the airship’s bladder while the third motor is mounted on the tail of the bladder. The main motors provide the forward thrust force. Being

mounted on a rod that is swivelled by a servo, they also allow controlling the airship's elevation. The motor at the tail controls the airship's rotation according to the z axis (yaw). The power of the PMDC motors is regulated by PWM modulation. This enables quite good estimation of their output power when the PWM ratio and the power supply voltage are known. This topic is discussed in chapter "4.2 Motors and swivelling mechanisms". In order to prove the possibilities of the motors' power controlling, a standalone Module for driving of the motors was developed. It employs a dual bridge controller L298. Moreover, it is capable of driving the swivelling servo directly by means of a PWM signal. The detailed description of this module is provided in chapter "5.1.3 Module for driving of the motors". This module cooperates with the Module for obstacles detection. A simple algorithm for driving the motors according to the obstacles detected by the detectors was also created.

RFID tags detecting

As stated above, one of the possible applications is to let the airship operate according to a preprogramed trajectory with the aid of inertial controlling. As in case of operation in this mode the cumulative error increases in time, there is a need for correction of the detection of the current position. For this purpose the RFID tags detecting system was intended to be applied. The module of RFID tags detector was created. The detailed description is provided in chapter "5.1.4. RFID tags detector".

Communication with the ground station

As the Autonomous monitoring system needs a connection with the ground station, a module for this communication was created together with the necessary software support. The description of the hardware components of this module is provided in "5.1.1 Module for communication with the ground station", while the description of the server software application is provided in chapter "5.2 Software application". The communication is based on conventional devices, employing local WiFi inside the object in which the airship operates. The software application is run on a local server and enables communication with the airship via the IP relay. The module also includes a web-camera the picture of which is transmitted to the server. After the proper authorization, the airship can be driven manually via the web interface, with the help of the video stream.

Power supply

The whole system is supplied from a Li-Pol battery with the nominal voltage of 7.4 V. As the components of the Autonomous monitoring system require different voltages (3.3 V, 5 V, 12 V and direct feed through to the motors), a three branch SMPS is required. Special interest was given to its design in order to ensure good operability and high efficiency. The design of the appropriate

SMPS is described in chapter “5.3.1 Power supply source” in details. The main idea consists in employing SEPIC voltage converters that can be simply turned off by disabling their oscillators. These voltage converters are triggered in defined times so that the sum of the ripple currents drawn from the battery includes considerable DC component. As proved by simulations, this method allows to decrease the interference radiation from the cables between the SMPS and the battery significantly as well as to make the appropriate capacitors and inductors, involved in the SMPS, smaller. The power supply unit is equipped with a circuit measuring the voltage at separated battery cells. If any of the cells is deeply discharged, first a warning signal is provided and consequently the whole power supply unit is switched off in emergency. This protects the battery from the damage by deep discharging.

Motherboard

Within the framework of this paper, a single board circuit was designed to integrate the functions of all the tested modules. The whole system is considered to be controlled by means of a single MCU. The detailed description of the motherboard is provided in chapter “5.3.2 Motherboard”. The motherboard communicates with the power supply unit, so the power electronics driving the motors can be mounted close to the power supply input on the PCB of the power supply unit.

Dynamic model of the airship

The idea of inertial trajectory controlling the airship requires accurate dynamic model of the system as well as an accurate description of the propeller’s behaviour. According to chapter “4.3 Propellers” the thrust of the propellers depends on their geometry, angular velocity and the flight velocity of the airship. Also the efficiency of the propellers is affected by the flight velocity of the airship. Knowing the propeller’s parameters, a connection between the power supplied to the motors and the thrust forces can be established, enabling to implement the inertial position controlling. The dynamic model of the airship is described in chapter “4.4 Airship’s model”. It is a simplified model that enables calculations of the airship’s velocities and position according to the forces the airship is driven with. The simulation of the airship’s behaviour using the data measured on the real model of the airship is provided in chapter “5.4 Airship’s behaviour modelling”. These simulations show how the airship reacts on throttle forces that make it fly straight, turn or ascend to higher position. At low velocities the model respects the damping of the motion by the surrounding air as well as the mass persistence that cause cumulative errors in position controlling (the airship moves a small period of time after all motors have been turned off). It can be considered as a good basis for development of the controlling software that will enable the inertial controlling of this model. The

controlling software was not developed within this thesis as it exceeds its framework.

During the work on the project of Autonomous monitoring system the following features were observed:

- Very little energy is consumed when the airship is required to stay at one position. However, high power consumption is observed when there is a need to move the airship at higher speeds.
- The bearing capacity of the airship is limited. The airship used in the project was 2.7 m long, 1.3 m high and was capable of bearing approximately 500 g of load. The hardware to be mounted on the airship must be lightweight and embody low power consumption as the weight of the battery is limited as well.
- The force needed to change the airship's direction or velocity is quite low. However, the mass persistence is high so when immediate change of flight direction or velocity is needed, a high braking force pulse must be generated.
- The propellers should be mounted as close to the mass of gravity as possible. If not, the thrust forces cause considerable swinging of the airship. According to the model, when forced to stop immediately, the pitch angle can shortly reach up to ± 60°. This would make the video stream unusable.
- The costs of operation are considerably high. The airship used in the project had the bladder volume of approximately 2.7 m^3. The cost of one filling is approximately 3,000 CZK. After the filling, the airship can be in operation for several days. After this period the filling gas must be replenished. With each filling and replenishing a small amount of air also gets into the bladder. This causes losing of the load capacity.
- The operational possibilities are limited because the small airship cannot be operated outdoors but it needs considerably large indoor areas.
- In past, the Autonomous monitoring system was intended to be utilized by the CEBIA-Tech research team as a firemen supporting radio translation system in the vicinity of large areas engulfed by fire. At this time the concurrently developed quadrocopter seems more suitable for these purposes.
- The airship is a great system for practical teaching of issues on automation.

7 REFERENCES

[1] JINJUN, Rao, et al, *A Flight Control and Navigation System of a Small Size Unmanned Airship*. In Proceedings of the IEEE International Conference on Mechatronics & Automation. Canada : [s.n.], 2005. s. 1491 - 1496. ISBN 0-7803-9044-X/05/$20.00.

[2] ALBERTO, Elfes, et al, *A Semi-Autonomous Robotic Airship for Environmental Monitoring Missions*. In Proceedings of the IEEE International Conference on Mechatronics & Automation. Belgium : [s.n.], 1998. s. 3449 - 3455.

[3] SUAY, Halit Bener; YAIRI, Takehisa; MACHIDA, Kazuo. *A Self-modeling Autonomous Airship*. In . ICROS-SICE International Joint Conference. Japan : [s.n.], 2009. s. 61 - 66.

[4] HYOCHOONG, Bang; SANGJONG, Lee; HAECHANG, Lee. *Nonlinear Trajectory Tracking using Vectorial Backstepping Approach*. In International Conference on Control, Automation and Systems. Korea : [s.n.], 2008. s. 169-174.

[5] GASPAR, José; WINTERS, Niall; SANTOS-VICTOR, José. *Vision-Based Navigation and Environmental Representations with an Omnidirectional Camera*. In IEEE Transactions On Robotics And Automation. [s.l.] : [s.n.], 2000. s. 890 - 898.

[6] AZOUZ, Naoufel; BESTAOUI, Yasmina; LEMAITRE, Olivier. *Dynamic Analysis of Airship with Small Deformations*. In Third International Workshop on Robot Motion and Control. [s.l.] : [s.n.], 2002. s. 209 - 215

[7] NOVÁK, P., *Mobilní roboty*, 1. díl, Praha: BEN – technická literatura, 2007, 248s., ISBN 80-7300-140-1.

[8] ĎAĎO, S., KREIDL, M., *Senzory a měřicí obvody*, Praha: Vydavatelství ČVUT, 1999, 315s., ISBN 80-01-02057-6.

[9] CHUDÝ, V., PALENČÁR, R., KUREKOVÁ, E., HALAJ, M., *Meranie technických veličín*, Bratislava: Vydavateľstvo STU, 1999, 672s., ISBN 80-227-1275-2

[10] FRADEN, J., *Handbook of modern sensors*, New York: Springer-Verlag, Inc., 2004, 589s., ISBN 0-387-00750-4.

[11] SKALICKÝ, P., *Mikroprocesory řady 8051*, Praha: BEN – technická literatura, 2001, 159s., ISBN 80-86056-39-2.

[12] ZÁHLAVA, V., *Metodika návrhu plošných spojů*, skripta ČVUT, Praha 2000

[13] ZÁHLAVA, Vít, VOBECKÝ, Jan. Elektronika : *Součástky a obvody, principy a příklady*. Praha : Grada Publishing, 2001. 192 s. ISBN 80-7169-844-9.

[14] SÝKORA, J., *Teorie digitální komunikace*, Praha: Vydavatelství ČVUT, 2003, 330 stran, ISBN 80-01-02478-4

[15] HRDINA, Z., VEJRAŽKA, F., *Digitální radiová komunikace*, Praha: Vydavatelství ČVUT, 1994, 257 stran, ISBN 80-01-01059-7

[16] KOCOUREK, P., *Přenos informace*, Praha: Vydavatelství ČVUT, 1994, 242 stran, ISBN 80-01-01169-0

[17] HANUS, S., *Bezdrátové a mobilní komunikace*, Brno: Ústav radioelektroniky FEKT VUT, 134 stran, ISBN 80 – 214 – 1833 – 8

[18] HORÁK, M. *IP kamery a jejich využití v průmyslu komerční bezpečnosti*. Zlín, 2007. 123 s. Bakalářská práce. Univerzita Tomáše Bati ve Zlíně.

[19] KOMÍNEK, A. *Robotický systém na zaměření cíle*. Zlín, 2006. 53 s. Bakalářská práce. Univerzita Tomáše Bati ve Zlíně.

[20] BABIUCH, M. 2002. *Implementation of User-friendly Programming Environment for Standalone Micro-controllers*. In Proceedings of 3rd International Carpathian Control Conference. Ostrava : VŠB-TU Ostrava, 27. - 30. 5. 2002, p. 471-475. ISBN 80-248-0089-6.

[21] MAHDAL, M. 2008. *Wireless Technologies and Their Applications*. In 9th International Carpathian Control Conference ICCC´2008. Sinaia, Romania, May 25 - 28, 2008, pp. 388 – 391. ISBN 978-973-746-897-0.

[22] FORMÁNEK, I. *Základy automatizace. Logické řízení*. 1. vyd. Ostrava : VŠB-TU Ostrava, 2006. 86 s. ISBN 80-248-1012-3.

[23] SAX, H. SGS THOMSON. *Stepper Motor Driving: Application Note*. 1995.

[24] KUCHAŘ, M., *Stejnosměrné stroje*.

[25] FALIN, J. TEXAS INSTRUMENTS INC. *Designing DC/DC converters based on SEPIC topology*. Texas, USA, 2008.

[26] WAITZ, I. *Unified Propulsion*. 2001.

[27] *Performance of Propellers* [online]. Massachusetts, USA [cit. 2012-08-07]. Dostupné z: mit.edu/16.unified/www/FALL/thermodynamics/notes/node86.html. Educative Material. Massachusetts Institute of Technology.

[28] WILLIAMSON, T. INTEL CORPORATION. *Oscillators for Microcontrollers*. Illinois, USA, 1983.

[29] FREESCALE SEMICONDUCTOR. *MC9S09SE8: Data Sheet: Technical Data*. 3. vyd. Denver, USA, 2009.

[30] LINEAR TECHNOLOGY. *LTC1751/LTC1751-3.3/LTC1751-5: Micropower, Regulated Charge Pump DC/DC Converters*. USA.

[31] ON SEMICONDUCTOR. *LM285, LM385B Micropower Voltage Reference Diodes: Data Sheet*. 8. vyd. USA, 2008.

[32] MARRO, G. a D. PRATTCHIZZO. *Summer School of Time Delay Equations and Control Theory: Linear Control Theory* [online]. Italy: University of Bologna & University of Siena, 2001 [cit. 2012-08-02]. Dostupné z: http://www.deis.unibo.it/Staff/FullProf/GiovanniMarro/geometric.htm

[33] ST MICROELECTRONICS. *L298: Dual Full-Bridge Driver*. Italy, 2000.

[34] HUBÍK, V., I. SZABÓ a M. ŠVÉDA. UNIS, spol s r.o. *Analýza bezsenzorového řízení BLDC motorů v leteckých aplikacích*.

[35] VAS, P. *Electrical Machines and Drivers*. Department of Engineering at the University of Aberdeen, UK. Oxford University Press: UK, 1992. ISBN 0-19-659397-X.

[36] KAMM, L. J. *Understanding Electro-Mechanical Engineering: An Introduction to Mechatronics*, IEEE Press Understanding Science & Technology Series. Wiley-IEEE Press: New York, August 1995. ISBN 0-78-031031-4

[37] SKALICKÝ, J. *Elektrické servopohony*. Ústav výkonové elektrotechniky a elektroniky, FEKT VUT. Brno, 2008.

[38] NEUBIG, B. *Design of Crystal Oscillator Circuits*.

[39] BRANDT, J. B. a M. S. SELIG. Propeller Performance Data at Low Reynolds Numbers. In: *Proceedings of 49th AIAA Aerospace Sciences Meeting*. Orlando, Florida, USA: American Institute of Aeronautics and Astronautics, 2011.

[40] AUSTRIAMICROSYSTEMS. *AS3910: Data Sheet*. Austria, 2009.

[41] WEI, G. a Z. DONGBING. NATIONAL SEMICONDUCTOR. *Designing a SEPIC Converter*. 2008.

[42] NELSON, C. LINEAR TECHNOLOGY. *LT1070 Design Manual: Application Note*. USA, 1986.

[43] LINEAR TECHNOLOGY. *LT1170/LT1171/LT1172: High Efficiency Switching Regulators*. California, USA, 1991.

[44] METELO, F. M. S., CAMPOS, L. R. G. *Vision based control of an autonomous blimp* [online]. 2007, [cit. 2007-6-12] Available at WWW: http://vislab.isr.ist.utl.pt/thesis/03-videoblimp-tfc.pdf

[45] Google Loon. http://www.google.com/loon

[46] MÜLLER, M. *Vzducholoď - orientace v prostoru*. ČVUT v Praze, 2008. Diploma Thesis. Supervisor: J. Bayer.

[47] VONDRA, M., *Vzducholoď – dynamický model.* ČVUT v Praze, 2009. Diploma Thesis. Supervisor: J. Bayer.

[48] KOTEK,Z., *Nelineární regulace a servomechanismy*, SNP Praha, 1966

[49] ETKIN, B., REID, L. D. *Dynamics of Flight Stability and Control* , 1996. John Wiley & Sons. Inc., ISBN 0-471-03418-5

[50] CASTILLO, P., LOZANO, R., DZUL, A. E. *Modelling and Control of Mini – Flying Machines*, 2005. Springer - Verlag London Limited, ISBN 1-85233-957-8

[51] CHEN, H. H., GUZIANI, M., *Next Generation Wireless Systems and Networks*, 2006, John Wiley & Sons. Inc., ISBN 0-470-02434-8

[52] HAMILL, D. C., JEFFERIES, D. J., *Subharmonics and chaos in a controlled switched-mode power converter*, IEEE Trans. on Circuits and Systems, vol. 35, no. 8, Aug. 1988, pp. 1059-1061.

[53] IVAN, C.M., *Contributions regarding the analysis and modelling of power switching converters*, Ph.D. Thesis, "Politehnica" University of Timisoara, 2008.

[54] ZHANG, Y. Ch., WEI, L., SHEN, X., LIANG, H., *Study of Supercapacitor in the Application of Power Electronics*, In WSEAS Transactions on Circuits and Systems, Issue 6, Vol. 8, 2009, ISSN: 1109-2734

[55] ZHANG, H. Y, WEI, T. Z., *Study on Ultracapacitor Energy Storage. Power system technology*, Vol.30, 2006, pp.92-95

[56] CHEN R. Ch., HUANG, S. L., *A New Method for Indoor Location Base on Radio Frequency Identification*, In WSEAS Transactions on Communications, Issue 7, Volume 8, 2009, ISSN: 1109-2742

[57] DOSTÁLEK, P., VAŠEK, V., DOLINAY, J., *Direction of Sound Wave Arrival Determination Using Time Estimation and Beamforming Methods*, In WSEAS Transactions on Circuits and Systems, Issue 12, Volume 8, 2009, ISSN: 1109-2734

[58] *Atmel AVR 8-Bit RISC* [online].[cit. 2009-01-25]. Available at WWW: http://www.atmel.com/dyn/product/datasheets.asp?family_id=607#791

[59] *AVR300* [online].[cit. 2009-01-18]. Available at WWW: http://www.atmel.com/dyn/resources/prod_documents/AVR300.pdf

[60] *AVR204* [online].[cit. 2009-01-18]. Available at WWW: http://www.atmel.com/dyn/resources/prod_documents/doc2543.pdf

[61] MATOUŠEK, D.: *Programování a aplikace ATtiny2313*. Vydavatelství AMARO, Praha 2006, 40 s., ISSN 1211-3557

[62] *SAA1064* [online].[cit. 2009-04-25]. Available at WWW: http://www.datasheetcatalog.com/datasheets_pdf/SAA1064.shtml

[63] *HD44780* [online].[cit. 2009-04-25]. Available at WWW: http://www.datasheetarchive.com/pdf-datasheets/Datasheets-13/DSA-247674.pdf

[64] TEXAS INSTRUMENTS. *LM117/LM317A/LM317-N: Three-Terminal Adjustable Regulator*. 2013.

[65] VOŘÍŠEK, J., *Ultrazvukové měření vzdálenosti od překážky*. Zlín, 2009. 73 s. Diploma thesis. Univerzita Tomáše Bati ve Zlíně.

[66] PUCHAR, J., *Přenos signálu z videokamery prostřednictvím WiFi*. Zlín, 2009. 68 s. Diploma thesis. Univerzita Tomáše Bati ve Zlíně.

[67] MARCANÍK, L., *Řízení motorů pomocí procesoru*, Zlín, 2009. 59 s. Diploma thesis. Univerzita Tomáše Bati ve Zlíně.

[68] *SRF02 datasheet*

8 LIST OF FIGURES

Figure	Description	Page
1	Typical ultrasonic transmitter radiation diagram	14
2	Measurement error caused by non-perpendicular reflection	14
3	Error caused by the mutual geometry of the measured object and the surface of the obstacle (computed in mathematical software, see text)	15
4	Ultrasonic detector example	16
5	Continuous mode reflexive distance meter principle [9]	17
6	Optical distance meter utilizing a semitransparent mirror principle [9]	17
7	Coincidence distance meter operating principle [9]	18
8	Triangular optical distance meter principle [9]	19
9	Permanent magnet DC motor construction (Internet)	20
10	PMDC motor operating principle [7]	21
11	Current-based (a) versus voltage-based (b) PMDC motor controlling [24]	23
12	BLDC motor: a) cross-section, b) induction in the air gap, c) currents through the coils according to the rotor position, d) stator coils connection [34]	24
13	Typical static characteristics of the stepper motor [23]	25
14	Reluctance stepper motors: a) three phase reluctance stepper motor, b) four phase reluctance stepper motor with increased number of steps per one turn. [23]	26
15	Stepper motor employing permanent magnet, cross-section [23]	27
16	Bipolar versus unipolar stepper motor driving [23]	29
17	Example of internal stepper motors drivers – unipolar (L6222) and bipolar (L293D) [23]	30
18	Switching mode current regulation of the motor coil [23]	31
19	Switching mode current regulator reference voltage modulation example for different modes of the motor's operation [23]	33
20	Internal organization of a conventional low-power servo [7]	34
21	Typical propeller efficiency curves for different blade angles as functions of the advance ratio [27]	37
22	Static efficiency characteristics of the propeller APC Slow Flyer (8x3.8)" [39]	38

23	Estimated propelling force and consumed power of the propeller APC Slow Flyer (8x3.8)”	39
24	Propelling force at different airship velocities (propeller APC Slow Flyer (8x3.8)”	39
25	Propeller efficiency at different airship velocities and different motor shaft revolutions (propeller APC Slow Flyer (8x3.8)”)	40
26	Schematic description of the coordinate systems used for the airship’s trajectory description	41
27	Forces deployment in the coordinate system of the airship [46]	49
28	Representation of the rotational motion of the airship [50]	50
29	Block diagram of Freescale MC9S08SE8 microcontroller [29]	56
30	AS3910 internal components’ block diagram [40]	58
31	Minimum configuration of AS3910 with differential antenna driving [40]	58
32	LT1172 internal blocks [43]	59
33	Module for communication with the ground station block diagram	61
34	Charon I Development Kit with Charon I module embedded	62
35	IP camera D-Link DCS-910	62
36	WiFi router uncovered	63
37	Module for obstacles detection block diagram	64
38	Physical arrangement of the module for obstacles detection	64
39	AT-9 board electrical connection	65
40	LED-9/1 board electrical connection	66
41	LED-9/2 boar electrical circuitry	67
42	Mechanical arrangement of the Module for obstacles detection	68
43	Module for obstacles detection together with the set of detectors	68
44	Distance from the flat wall measurement results	71
45	Distance from the wooden column measurement results	71
46	Block diagram of the Module for driving of the motors	73
47	Connection diagram of the main board of the Module for driving of the motors	74
48	Bi-directional motor driving principle [33]	76

49	Replacing of LEDs at the LED-9/2 board with resistors	78
50	Time division multiplexer connection diagram	78
51	Controlling algorithm flowchart	80
52	Suggested displacement of the ultrasonic detectors around the bladder of the airship	82
53	Practical implementation of the Module for driving the Motors	83
54	RFID tags detector block diagram	84
55	RFID detector main board circuit diagram	85
56	Example on reading 1 B of data from the reader [40]	87
57	Linear voltage regulator circuit diagram	88
58	RFID tag detector controlling algorithm flowchart	89
59	Switched-mode operating voltage regulator	90
60	Autonomous monitoring system web interface – manual control mode	93
61	Autonomous monitoring system web interface – camera view	94
62	Power supply board block diagram	97
63	Currents drawn by voltage converters when triggered at the same time	101
64	Sum of the currents drawn by the converters when triggered at same time	101
65	Currents drawn by voltage converters when the shifted triggering is applied	102
66	Sum of the currents drawn by the converters when shifted triggering is applied	102
67	Comparison of the pulse components in the accumulator current	104
68	Cells measurement power supply disconnector (a) and its typical behaviour (b)	105
69	Worse cell selector simulation circuit diagram	105
70	Worse cell selector simulation results	106
71	Warning and Emergency shutdown signals generator simulation schema	108
72	Warning and Emergency shutdown signals generator simulation results	109
73	Basic circuit diagram for 5 V voltage regulator simulation (LT Spice)	115
74	Simulation results of the circuit from Fig. 73 for different input voltage and 5Ω load	116

75	Simulation results of the circuit from Fig. 73 for different input voltage and 10Ω load	117
76	Simulation results of the circuit from Fig. 73 for different input voltage and 2.5Ω load	118
77	Simulation results of the circuit from Fig. 73 for different output current I(1).	118
78	Simulation results of the circuit from Fig. 73 - waveform of the current passing through L1 inductor at the output current of 1 A and input voltage of 7.2 V	119
79	Simulation results of the circuit from Fig. 73 – voltage ripple at the output of the converter at the output current of 1 A and input voltage of 7.2 V	119
80	Simulation results of the circuit from Fig. 73 – spectrum analysis of the output voltage when the output current is at least 1 A	120
81	Simulation results of the circuit from Fig. 73 – spectrum analysis of the current passing through the L1 inductor when the output current is at least 1 A	120
82	Time synchronization circuit	122
83	Power supply source complex circuit diagram	123
84	Motherboard block diagram	126
85	Motherboard circuitry proposal	127
86	State-space model of the airship’s flight and elevation processed in Matlab Simulink	138
87	Signal generator setting for Simulation 1 (force impulse of 1.8 N in time from 10 to 20 s)	139
88	Simulation 1: Speed with respect to the x-axis	139
89	Simulation 1: Speed with respect to the z-axis	140
90	Simulation 1: Angular velocity with respect to the y-axis	140
91	Simulation 1: Travelled distance	140
92	Simulation 1: Relative elevation	141
93	Simulation 1: Pitch angle	141
94	Simulation 2: Signal generator setting	142
95	Simulation 2: Speed with respect to the x-axis	142
96	Simulation 2: Speed with respect to the z-axis	143
97	Simulation 2: Angular velocity with respect to the y-axis	143
98	Simulation 2: Travelled distance	143
99	Simulation 2: Relative elevation	144
100	Simulation 2: Pitch relative to the y-axis	144

101	Simulation 3: Signal generator setting	145
102	Simulation 3: Speed with respect to the x-axis	145
103	Simulation 3: Speed with respect to the z-axis	146
104	Simulation 3: Angular velocity with respect to the y-axis	146
105	Simulation 3: Travelled distance	146
106	Simulation 3: Relative elevation	147
107	Simulation 3: Pitch relative to the y-axis	147
108	Propelling forces setting (operation with elevation)	148
109	Simulation 4: Operation with elevation – speed with respect to the x-axis	149
110	Simulation 4: Operation with elevation – speed with respect to the z-axis	149
111	Simulation 4: Operation with elevation – angular velocity with respect to the y-axis	149
112	Simulation 4: Operation with elevation – travelled distance	150
113	Simulation 4: Operation with elevation – relative elevation	150
114	Simulation 4: Operation with elevation – pith with respect to the x-axis	150
115	State-space model of the airship's yawing processed in Matlab Simulink	153
116	Simulation 5: Propelling force setting in Signal Builder	153
117	Simulation 5: Circumferential velocity with respect to the y-axis	154
118	Simulation 5: Angular velocity with respect to the x-axis	154
119	Simulation 5: Angular velocity with respect to the z-axis	154
120	Simulation 5: Displacement according to the y-axis	155
121	Simulation 5: Rolling angle with respect to the y-axis	155
122	Simulation 5: Yawing angle	155
123	Simulation 6: Propelling force setting in Signal Builder	156
124	Simulation 6: Circumferential velocity with respect to the y-axis	157
125	Simulation 6: Angular velocity with respect to the x-axis	157
126	Simulation 6: Angular velocity with respect to the z-axis	157
127	Simulation 6: Displacement according to the y-axis	158
128	Simulation 6: Rolling angle of the airship with respect to the x-axis	158
129	Simulation 5: Yawing angle	158

9 LIST OF TABLES

Table	Description	Page
1	Module for communication with the ground station components weight	61
2	Main parameters of the D-Link DCS-910 camera	63
3	Main board connectors' description	75
4	Truth table of the controlling signals utilized by the motor driver	77
5	SL202 connector description	79
6	On-board buttons description	81
7	RFID reader initializing sequence	87
8	Power supply board I/O interface pins description	98
9	Accumulator management output specifications	107
10	Summary of calculated devices for all three voltage regulators	121
11	Motherboard connectors' description	129
12	Motherboard devices	130
13	Force arms according to Fig. 27	133

LIST OF AUTHOR'S ACTIVITIES

Papers in reviewed journals

1. Pospisilik, M., Adamek, M., Software checking of Audio Transformers Manufacturability, International Journal of Circuits, Systems and Signal Processing, Issue 6, Volume 6, pp. 419-429, 2012, ISSN: 1998-4464, online: http://www.naun.org/multimedia/NAUN/circuitssystemssignal/16-638.pdf

2. Pospisilik, M., Varacha, P., An Approach to the Optimization of the Ackerberg-Mossberg's Biquad Circuitry, International Journal of Circuits, Systems and Signal Processing, Issue 6, Volume 6, pp. 410-418, 2012, ISSN: 1998-4464, online: http://www.naun.org/multimedia/NAUN/circuitssystemssignal/16-636.pdf

3. Pospisilik, M., Adamek, M., Audio Signal Dynamics Expansion, International Journal of Circuits, Systems and Signal Processing, Issue 6, Volume 6, pp. 402-409, 2012, ISSN: 1998-4464, online: http://www.naun.org/multimedia/NAUN/circuitssystemssignal/16-634.pdf

4. Pospisilik, M., Varacha, P., Adamek, M., Low-Cost Rectifier for Measuring of AC Voltage or Current Frequency Compensation Proposal, International Journal of Systems and Signal Processing, Issue 6, Volume 6, pp. 394-401, 2012, ISSN: 1998-4464, online: http://www.naun.org/multimedia/NAUN/circuitssystemssignal/16-632.pdf

5. Kouril, L., Pospisilik, M., Adamek, M., Jasek, R., Application of Differential Evolution for Audio Transformers Optimization, International Journal of Circuits, Systems and Signal Processing, Issue 4, Volume 6, pp. 231-240, 2012, ISSN: 1998-4464, online: http://naun.org/multimedia/NAUN/circuitssystemssignal/16-391.pdf

6. Kouril, L., Pospisilik, M., Adamek, M., Jasek, R., Flat Coil Optimizer in the Meaning to Coil Optimization, International Journal of Circuits, Systems and Signal Processing, Issue 4, Volume 6, pp. 241-248, 2012, ISSN: 1998-4464, online: http://naun.org/multimedia/NAUN/circuitssystemssignal/16-392.pdf

7. Pospisilik, Martin, Adamek, Milan. Logarithmic VU Meter Driver, International Journal of Mathematics and Computers in Simulation [online], 2011, Vol. 5, Issue 5 [cit. 2011-29-11], s. 454-461, available at WWW < http://www.naun.org/journals/mcs/17-130.pdf>, ISSSN 19980159

8. Pospisilik Martin, Adamek, Milan. Simulation and Design of Voltage Controlled Amplifier for Dynamic Expanders, International Journal of Mathematics and Computers in Simulation [online], 2011, Vol. 5, Issue 5 [cit. 2011-29-11], s. 446-453, available at WWW < http://www.naun.org/journals/mcs/17-129.pdf>, ISSSN 19980159

9. Brazda, Michal, Pospisilik, Martin, Adamek, Milan. Ultraviolet Radiation Device for Prototype Production of Printed Circuit Boards. International Journal of Mechanics [online], 2011, Vol. 5., Issue 4 [cit. 2011-29-11], s. 302 – 309, available at WWW < http://www.naun.org/journals/mechanics/17-132.pdf>, ISSN 19984448

10. Pospisilik, M., Adamek, M., Autonomous Airship, In Transactions of the VŠB – Technical University of Ostrava, Mechanical Series No. 2, 2009, vol. LV, article No. 1698, 2009, Ostrava, pp 109 - 114

Papers in conference proceedings

1. Pospisilik, M., Adamek, M., Optimised Power Supply Design, In Proceedings of 15th IEEE Symposium on Design and Diagnostics of Electronic Circuits and Systems, ISBN 978-1-4673-1185-4

2. Kouril, L., Pospisilik, M., Adamek, M., Jasek, R., Coil Optimization with Aid od Flat Coil Optimizer, In Proceedings of 5th WSEAS World Congress on Applied Computing Conference, ISBN 978-1-61804-089-3

3. Kouril, L., Pospisilik, M., Adamek, M., Jasek, R., Audio Transformers Optimization By Means of Evolutionary Algorithms, In Proceedings of 5th WSEAS World Congress on Applied Computing Conference, ISBN 978-1-61804-089-3

4. Pospisilik, M., Varacha, P., Evolutionary Algorithm Aided Biquad Design, In Proceedings of 16th WSEAS Conference on Circuits And Systems, ISBN 978-1-61804-108-1

5. Pospisilik, M., Varacha, P., Adamek, M., A Method of Improvement of the Low-Cost Rectifiers Performance in Wideband AC Voltmeters and Amperemeters, In Proceedings of 16th WSEAS Conference on Circuits And Systems, ISBN 978-1-61804-108-1

6. Pospisilik, M., Adamek, M., Software-Based Audio Signal Dynamics Expander, In Proceedings of 16th WSEAS Conference on Circuits And Systems, ISBN 978-1-61804-108-1

7. Pospisilik, M., Kouril, L., Otahal, J., Adamek, M., Proposal on Intelligent Wearable Sensor Suit, In Proceedings of 16th WSEAS Conference on Circuits And Systems, ISBN 978-1-61804-108-1

8. Pospisilik, M., Adamek, M., Determining the Audio Transformer Manufacturability, In Proceedings of 16th WSEAS Conference on Circuits And Systems, ISBN 978-1-61804-108-1

9. Pospisilik, M., Adamek, M., Audio Transformers Simulation, In Proceedings of 16th WSEAS Conference on Circuits And Systems, ISBN 978-1-61804-108-1

10. Pospisilik, M., Kouril, L., Adamek, M., Zelinka, I., Jasek, R., SOMA Based Audio Transformers Optimization, In Proceedings of 18th International Conference on Soft Computing, June 27-29, Brno, Czech Republic, ISBN 978-80-214-4540-6

11. Pospisilik, M., Kouril, L., Adamek, M., Contactless ECG Scanning Device Hardware Design Proposal, In Proceedings of XX IMEKO World Congress, Busan, Korea, 2012, ISBN 978-89-950000-5-2

12. Pospisilik, M., Lapkova, D., Adamek, M., Malanik, Z., The Utilization of an Impulse Force in Self-Defence, In Proceedings of XX IMEKO World Congress, Busan, Korea, 2012, ISBN 978-89-950000-5-2

13. Pospisilik, M., Sulovska, K., Adamek, M., Comparing Manually Measured Anthropometrical Points of Human Faces With Fully Computerized Ones, In Proceedings of XX IMEKO World Congress,

Busan, Korea, 2012, ISBN 978-89-950000-5-2

14. Pospisilik, M., Adamek, M. RFID Reader Testing Kit for Autonomous Airship. In: Proceedings of the 23rd International DAAAM Symposium, Zadar, Croatia. DAAAM International, Vienna, Austria, 2012 , p 667-670. ISBN 978-3-901509-91-9.

15. Pospisilik, M., Adamek, M., Intercom for a Fire Brigade Truck. In: Proceedings of the 23rd International DAAAM Symposium, Zadar, Croatia. DAAAM International, Vienna, Austria, 2012 , p 667- 670. ISBN 978-3-901509-91-9.

16. Pospisilik, M., Adamek, M., LED Based Universal Lighting System. In: Proceedings of the 23rd International DAAAM Symposium, Zadar, Croatia. DAAAM International, Vienna, Austria, 2012 , p 667- 670. ISBN 978-3-901509-91-9.

17. Vařacha Pavel ; Pospíšilík Martin ; Motýl Ivo ; Bližňák Michal ; Slovák Dalibor ; Kolek Jan ., Comparison of Evolutionary Algorithms SOMA, DE, PSO, In Proceedings of 16th WSEAS Conference on Circuits And Systems, ISBN 978-1-61804-108-1

18. Pospisilik, Martin, Adamek, Milan. Advanced Rectifier and Driver for Analog VU Meter, In VIERHAUS. T. Heinrich et al. Proceedings of the 14th IEEE International Symposium od Design and Diagnostics of Electronic Circuits and Systems, 1. Vyd., Cottbus: Institute of Electrical and Electronic Engineers, 2011, Poster Session III, s. 413 – 414, ISBN-978-1-4244-9753-9

19. Pospisilik, Martin, Adamek, Milan. Advanced Voltage Controlled Amplifier for Volume Expanders, In VASEK, V. et al. Proceedings of the 13th WSEAS International Conference on Automatic Control, Modelling & Simulation, 1. Vyd., Lanzarote: WSEAS Press, 2011, Recent Researches in Automatic Control, s. 325 – 330. ISBN 978-1-61804-004-6

20. Pospisilik, Martin, Adamek, Milan. Logarithmic VU Meter Driver, In VASEK, V. et al. Proceedings of the 13th WSEAS International

Conference on Automatic Control, Modelling & Simulation, 1. Vyd., Lanzarote: WSEAS Press, 2011, Recent Researches in Automatic Control, s. 331 – 336. ISBN 978-1-61804-004-6

21. Brazda, Michal, Pospisilik, Martin, Adamek, Milan. LED Based Ultraviolet Light Source, In VASEK, V. et al. Proceedings of the 13th WSEAS International Conference on Automatic Control, Modelling & Simulation, 1. Vyd., Lanzarote: WSEAS Press, 2011, Recent Researches in Automatic Control, s. 421 – 425. ISBN 978-1-61804-004-6

22. Pospisilik, Martin, Kouril, Lukas, Motyl, Ivo, Adamek, Milan. Single and Double Layer Spiral Planar Inductors Optimisation with the Aid of Self-Organising Migrating Algorithm, In [n.a.]. Proceedings of the 11th WSEAS International Conference on Signal Processing, Computational Geometry and Artificial Vision & the 11th WSEAS International Conference on Systems Theory and Scientific Computation, 1. Vyd., Florence: WSEAS Press, 2011, Recent Advantages in Signal Processing, Computational Geometry and Systems Theory, s. 272 – 277. ISBN 978-1-61804-027-5

23. Pospisilik, Martin, Kouril, Lukas, Adamek, Milan. Planar Inductor Optimised by Evolutionary Algorithm. In MATOUSEK, Radek. Proceedings of the 17th International Conference on Soft Computing Mendel 2011, 1. Vyd., Brno: Faculty of Mechanical Engineering, Institue od Automation and Computer Science, 2011, s. 38 – 42. ISBN 978-80-214-4302-0

24. Pospisilik, M., Puchar, J., Adamek, M., WiFi Module for Autonomous Monitoring System, In The 20th INTERNATIONAL DAAAM SYMPOSIUM ""Intelligent Manufacturing & Automation: Theory, Practice & Education"", Vienna, Austria, 2009

25. Pospisilik, M., Plsek, S., Adamek, M., Autonomous Airship as a Surroundings Monitor, In XXXV. Seminar ASR 2010 "Instruments and Control, VSB - TUO Ostrava, Czech Republic, 2010

26. Pospisilik, M., Adamek, M., Autonomous Airship, In 9th International Conference PROCESS CONTROL 2010, Kouty nad Desnou, Czech Republic

27. Pospisilik, M., Kouril, L., Adamek, M., Employing the Artificial Intelligence at Electrical Circuitry Designing, In 16th International Conference on Soft Computing Mendel 2010, 2010, Brno, Czech Republic, pp. 319 – 324

28. Pospisilik, M., Adamek, M., Switching Power Supply for an Autonomous Monitoring System, In. WSEAS Transactions on Circuits and Systems, 2010

29. Pospisilik, M., Plesek, S., Adamek, M. 2010. Autonomous Airship As An Surroundings Monitor. In XXXV. Seminar ASR 2010. Ostrava, Czech Republic

30. Pospisilik, M., Adamek, M. 2009. Autonomous Monitoring System. In 13th International Research/Expert Conference TMT2009. Hammamet, Tunisia, pp 777 – 780, ISSN 1840494.

31. Pospisilik, M., Adamek, M. 2009. Autonomous Airship As A Surrounding Monitor. In XXXIV. Seminar ASR 2009. Ostrava, Czech Republic, pp 277 - 284, ISBN 978 - 80 - 248 - 1953 - 2

32. Pospisilik M., Adamek, M. 2009. Autonomous Monitoring System. In Int. Carpathian Control Conferece 2009. Zakopane, Poland, 2009, ISBN 83-89772-51-5

33. Nemcik, Martin, Levak, Michal, Pospisilik, Martin. Hardware module based on FPGA for the testing of speech quality. In Digital Technologies 2007 : Book of Abstracts. Žilina : [s.n.], 2007. Image, Video and Signal Processing I. s. 27.

34. Pospisilik, M., Adamek, M. 2009. Autonomous Airship. In Transactions of the VŠB – Technical University of Ostrava, Mechanical Series, No. 2, 2009, vol. LV, Ostrava, Czech Republic, pp 109 – 114, ISBN 978-80-248-2144-3.

Other publications

1. Pospisilik, Martin; Brazda, Michal; Adamek, Milan. LED Based Exposing Unit. Trilobit [online]. 2010, n. 2, [cit. 2010-06-13]. Available at WWW: <www.trilobit.fai.utb.cz>. ISSN 1804-1795

2. Pospíšilík, M., Kouřil, L., Adámek, M., Approach to Electrical Circuitry Designing By Employing Differential Evolution, In Proceedings on Internet, Competitiveness and Organizational Security, March 2011, Tomas Bata University in Zlin, ISBN: 978-80-7454-012-7

3. Pospíšilík, M., Kouřil, L., Adámek, M., Comparison Of Differential Evolution and Self-Organising Migrating Algorithm at Flat Spiral Inductor Optimisation, In Proceedings on Internet, Competitiveness and Organizational Security, March 2011, Tomas Bata University in Zlin, ISBN: 978-80-7454-012-7

4. Pospisilik, M., Proximity Distance Measurement By Means of Proximity Detectors, Trilobit, 2012, Vol. 2, ISSN 1804-1795

5. Pospisilik, M., Buttonless Keyboard, Trilobit, 2012, Vol. 1, ISSN 1804-1795

Intership abroad

1. ESTIG Beja, Portugal, 2010, 3 months, Ph.D. Erasmus programme

2. METU Ankara, Turkey, 2011, 1 week, Teacher's Exchange Eramsus programme

3. ESTIG Beja, Portugal, 2013, 1 week, Tecaher's Exchange Erasmus programme

Functional samples / constructions

1. Pospíšilík, M., Adámek, M. : Pokročilý usměrňovač a logaritmizátor pro buzení analogového indikátoru vybuzení

2. Pospíšilík, M., Marcaník, M., Adámek, M.: Jednotka pro řízení motorů vzducholodi

3. Pospíšilík, M., Voříšek, M., Adámek, M.: Soustava ultrazvukových dálkoměrů

4. Pospíšilík, M., Adámek, M.: Duplexní interkom pro vozidlo hasičského záchranného sboru

5. Pospíšilík, M., Adámek, M.: Detektor kovových armatur ve zdivu

6. Pospíšilík, M.: Thereminův syntetizér využívající oscilátory sestavené z hradel CMOS

7. Pospíšilík, M.: Modul zesilovače, jehož zisk je přímo úměrný řídicímu napětí, využívající linearizaci pomocí vložení identického zesilovače do zpětnovazební smyčky

8. Pospíšilík, M.: Analogová zpožďovací linka pracující na principu spínaných kapacitorů

9. Pospíšilík, M.: FM modulátor pro přenos více EKG signálů jedním vedením

10. Pospíšilík, M.: FM modulátor pro přenos více EKG signálů jedním vedením

11. Pospíšilík, M., Brázda, M.: Výkonový modul UPS systému s elektronickým připojováním akumulátoru

Software

1. Pospíšilík, M. : Audio Transformer Optimizer

2. Neckář, P., Pospíšilík, M. , Designer pokročilých návrhů odporových děličů (Advanced Designer for Resistors Dividers)

3. Pospíšilík, M., Kouřil, L., Flat Coil Optimiser

4. Pospíšilík, M., Adámek, M., Expandér dynamiky audiosignálu (Audio Signal Dynamics Expander)

AUTHOR'S CV

Education:

Since 2008	Tomas Bata University in Zlin, Faculty of Applied Informatics, Ph.D. Student
2002 - 2008	Czech Technical University in Prague, Faculty of Electrical Engineering, Specialization: Electronics, Achieved degree: MSc.

Professional career:

Since 2011	Tomas Bata University in Zlin, Faculty of Applied Informatics - Lecturer - Assistant
2008	Airship Club Prague - External researcher
2006 - 2007	Sitronics Telecom Solutions Czech Rep. - Junior technical writer - Junior researcher

Teaching:

- Hardware of communication systems
- Digital communications
- Programming in ANSI C

Research Activities:

Since 2012	CEBIA-Tech - Member of "Security research" team

LIST OF VARIABLES

$\vec{\varsigma}_0(t)$	vector of parameters determining the initial position of the airship
$\vec{\varsigma}_a$	position vector recalculated to the **a** coordinate system
$\vec{\tau}_b$	vector of propelling force and moment generated by the motors
$\vec{\omega}_0(t)$	vector of parameters determining the initial velocities of the airship
$\vec{\omega}_a$	velocity vector recalculated to the **a** coordinate system
C_T	capacity to determine clock frequency [F]
$D_{3.3V_{max}}$	maximum duty cycle in 3.3V branch [-]
$D_{3.3V_{min}}$	minimum duty cycle in 3.3V branch [-]
$I_{IN_{3,3V}}$	average input current of the voltage converter – 3.3V branch [A]
L_{min}	minimum inductance [H]
P_p'	output power of a propeller [W]
U_{BIAS}	bias voltage [V]
f_{sw}	switching frequency [Hz]
$\vec{g}(\vec{\varsigma}_a)$	vector of reaction forces and moments respecting the gravity and the lift force generated by helium
$\vec{g}(\vec{\varsigma}_a)$	vector of reaction forces and moments respecting the gravity and the lift force generated by helium
m_{He}	height of the helium [kg]
$\vec{u}$	vector of the propelling forces (used for State-space model)
$v_{x0}(t)$	initial velocity of the airship with respect to the x-axis
$v_{y0}(t)$	initial velocity of the airship with respect to the y-axis
$v_{z0}(t)$	initial velocity of the airship with respect to the z-axis
$\vec{x}(t)$	vector describing the state of the airship
$x_0(t)$	initial position of the airship with respect to the x-axis of the a coordinate system
$\vec{y}(t)$	vector of output states (in State-space model simulation)
$y_0(t)$	initial position of the airship with respect to the y-axis of the a coordinate system
$z_0(t)$	initial position of the airship with respect to the z-axis of the a coordinate system
$\boldsymbol{B_{xy}}$	simplified matrix of force arms for Simulation of the airship's movement within the xy plane
$\boldsymbol{D}_{xy}$	simplified matrix of hydrodynamic damping for Simulation of the airship's movement within the xy plane
$\boldsymbol{G}_{xy}$	simplified matrix of gravitational forces for Simulation of the airship's movement within the xy plane
$\boldsymbol{J}_{xy}$	simplified transformation matrix for Simulation of the airship's

	movement within the xy plane
$\boldsymbol{M}_{xy}$	simplified matrix of masses for Simulation of the airship's movement within the xy plane
$\vec{\varepsilon}$	vector determining the centre of gravity misalignment
$\theta_0(t)$	initial pitch angle of the airship
$\vec{\iota}$	vector of the airship's coordinates according to the **w** coordinate system
$\vec{\xi}$	vector of angular velocities ω_x, ω_y and ω_z, representing the angular velocity of the airship's rotation according to the x, y and z axes of the **w** coordinate system
$\vec{\varsigma}$	vector of position and rotation of the airship according to the **w** coordinate system
$\vec{\upsilon}$	vector of sliding velocities v_x, v_y and v_z, representing the velocity according to the x, y and z axes of the **w** coordinate system
$\psi_0(t)$	initial yaw angle of the airship
$\omega_{x0}(t)$	initial angular velocity of the airship with respect to the x-axis
$\omega_{y0}(t)$	initial angular velocity of the airship with respect to the y-axis
$\omega_{z0}(t)$	initial angular velocity of the airship with respect to the z-axis
$\vec{\vartheta}$	vector of the airship's angles of rotation according to the **w** coordinate system
$\phi_0(t)$	initial roll angle of the airship
ϕ_m	magnetic flux in a motor [Wb],
$\vec{\varpi}$	total velocities vector according to the w coordinate system
ΔI_L	ripple current flowing through the appropriate inductor [A]
$\Delta\omega_m$	change of the angular velocity of the shaft rotation when loaded by the moment M_L $[rad \cdot s^{-1}]$.
μ_g	gas (air, fluid) viscosity $[m^2 \cdot s^{-1}]$,
a	airship's coordinate system
a	length of the major ellipsoid semi-axis [m]
A	gain
$\mathbf{A_{ss}}$	State-space system description matrix A
b	length of the minor ellipsoid semi-axis [m]
B_{pm}	magnetic induction induced by permanent magnets [T],
$\mathbf{B_{ss}}$	State-space system description matrix B
B_v	viscous friction coefficient $[kg \cdot s^{-1}]$,
$\mathbf{C}_A$	centripetal and Corliss's forces relative to the additional weights
c_m	constant of the machine / motor (determined by its construction etc.),
C_{pow}	power coefficient of a propeller

$\mathbf{C}_{RB}$	centripetal and Corliss's forces relative to the fixed point of a rigid body of the airship
c_s	sound velocity $[m \cdot s^{-1}]$
$\mathbf{C_{ss}}$	State-space system description matrix C
d	distance (general, see text for context) [m]
D_p	propeller diameter [m],
$\mathbf{D_{ss}}$	State-space system description matrix D
f	general coefficient, see text for context
F_{1L}	propelling force developed by the left motor [N]
F_{1P}	propelling force developed by the right motor [N]
F_2	propelling force developed by the tail motor [N]
F_T	thrust generated by the propeller [N],
g	general coefficient, see text for context
h	general coefficient, see text for context
i	immediate electric current [A] (general, see text for context)
I_a	current through the active winding of the motor [I],
I_{ADJ}	current escaping the ADJ pin of LM317 voltage regulator [A]
I_{OUTmax}	maximum output current [A]
$I_{PKswitch}$	peak switching current [A]
$\mathbf{J_2}$	angular speed transformation matrix
J_m	total persistence moment on the shaft $[kg \cdot m^2]$,
J_p	advance ratio of a propeller
K_g	gas (air, fluid) bulk elascitcity modulus $[N \cdot m^2]$,
k_Q	torque coefficient of a propeller
k_T	thrust coefficient of a propeller
L_0	inceptive inductance, constant [H]
l_1	distance between the airship's centre of gravity (the x component) to the tail motor [m]
l_2	distance between the airship's centre of gravity (the z component) to the tail motor [m]
l_3	distance between the airship's centre of gravity (the x component) to the main motors [m]
l_4	distance between the airship's centre of gravity (the z component) to the main motors [m]
l_5	distance between the airship's centre of gravity (the y component) to the main motors [m]
L_a	motor coil inductance [H]

l_m	measured distance [m],
$L_m(\phi_m)$	motor coil inductance as a function of rotor to stator angle [H]
L_{mn}	nominal inductance of a motor coil [H]
l_{real}	real distance (if different from the measured one) [m]
l_w	rotor winding length [m],
m	total height of the airship [kg]
$\mathbf{M}_A$	additional weight matrix, caused by friction, propulsion, gravity etc.
M_L	load torque moment at the shaft of the motor $[N \cdot m]$.
M_m	electromagnetic torque moment of the motor $[N \cdot m]$.
M_p	propeller torque moment $[N \cdot m]$,
$\mathbf{M}_{RB}$	mass weight matrix
M_{tip}	Mach number of the propeller's tip
n_m	motor shaft revolutions [rpm]
N_n	number of notches on the stepper motor's rotor
n_p	propeller rotation velocity [rpm],
n_{ph}	number of the motor phases
p_{g0}	gas (air) pressure at 0°C (273.15 K) [Pa],
p_p	number of stepper motor poles
P_p	power consumed by a propeller [W]
$\mathbf{R}$	matrix of the airship rotation according to the world's coordinate system
R_a	resistance of the active winding in the motor [Ω]
Re	Reynold's number
$\mathbf{R_x}$	matrix of the airship rotation according to the x-axis of the world's coordinate system
$\mathbf{R_y}$	matrix of the airship rotation according to the y-axis of the world's coordinate system
$\mathbf{R_z}$	matrix of the airship rotation according to the z-axis of the world's coordinate system
T	time period (general) [s],
t	time [s]
T	time period [s]
t_g	gas (air) temperature [K],
t_{ONmax}	maximum time period of the "on" state [s]
U_a	total voltage across the motor winding [V]
U_D	threshold voltage of a diode [V]

u_e	immediate voltage across the active stator phase of a stepper motor [V]
U_{INmin}	minimum input voltage [V]
U_O	output voltage [V]
U_{OUT}	output voltage [V]
U_{SAT}	saturation voltage [V]
U_{VCC}	voltage (supply net) [V]
v_f	flight velocity $[m \cdot s^{-1}]$
$v_x(t)$	current sliding velocity in the x-direction $[m \cdot s^{-1}]$
$v_z(t)$	current sliding velocity in the z-direction $[m \cdot s^{-1}]$
w	world's coordinate system
w_w	rotor winding diameter [m],
x	x-axis of a coordinate system
y	y-axis of a coordinate system
z	z-axis of a coordinate system
α	angle (general, see text for context)
β	angle (general, see text for context)
γ	angle (general, see text for context)
γ_g	coefficient of the gas (air) thermal expansiveness $[m \cdot K^{-1}]$,
η_p	propeller efficiency
θ	airship's pitch angle
κ	Poisson's constant,
ρ_g	gas (air, fluid) density $[m^2 \cdot s^{-1}]$,
ρ_{g0}	gas (air) density at 0°C (273.15 K) $[kg \cdot m^{-3}]$,
ρ_{He}	helium density [kg/m^3]
τ	timc constant [s]
ϕ	airship's roll angle
ϕ_m	rotor to stator displacement angle [rad]
ψ	airship's yaw angle
ω_m	angular velocity of a motor shaft $[rad \cdot s^{-1}]$
ω_{m0}	angular velocity of a motor shaft rotation under no load $[rad \cdot s^{-1}]$
ς	angle of the motors swivelling
ESR	equivalent series resistance [Ω]
$\boldsymbol{D}$	matrix of coefficients of hydrodynamic damping
$\boldsymbol{D}(\vec{\varpi}_a)$	hydrodynamic damping force

LIST OF ABBREVIATIONS

AC	Alternating Current
BCD	Binary-Coded Decimal
BDM	Backgroud Debugger Mode (interface by Freescale)
BLDC	BrushLess Direct Current (Motor)
CCD	Charge-Coupled Device
CMOS	Complementary Metal-Oxide-Semiconductor
DC	Direct Current
DTR	Data Terminal Ready (RS232 Bus signal)
EEPROM	Electrically Erasable Programmable Read-Only Memory
ESR	Equivalent Serial Resistance
FET	Field Effect Transistor
FIFO	First In First Out
GND	GrouND
GPS	Global Positioning System
HTML	HyperText Markup Language
I^2C	Inter-Integrated Circuit
IP	Internet Protocol
LAN	Local Area Network
LCD	Liquid Crystal Display
LED	Light Emitting Diode
MAC	Media Access Control (Address)
MCU	MicroController Unit
M-JPEG	Motion-JPEG (Joint Photographic Experts Group)
MOSFET	Metal Oxide Semiconductor Field Effect Transistor
PCB	Printed Circuit Board
PHP	Hypertext PreProcessor (recursive)
PMDC	Permanent Magnet Direct Current (Motor)
PSD	Position Sensitive Detector
PWM	Pulse-Width Modulation
RF	Radio Frequency
RFID	Radio-Frequency IDentification
RTS	Ready-To-Send (RS232 Bus signal)
SCL	Serial CLock
SDA	Serial DAta
SEPIC	Single-Ended Primary-Inductor Converter
SMD	Surface Mount Device
SMPS	Switched-Mode Power Supply
SPI	Serial Peripheral Interface
TTL	Transistor-Transistor-Logic
TWI	Two Wire Interface

APPENDIX A

Maple codes for generation of matrixes needed for airship's movement simulation.

1. Matrixes for the movement in the xz plane

```
restart;

m := 1.75;
a11 := 0.58;
zg := 0.13;
a33 := 1.49;
xg := 0.2;
Iyy := 0.19;
a55 := 0.087;
g := 9.81;
l4 := 0.6;
l3 := 0.1;
M := Matrix([[m + a11, 0, m·zg], [0, m + a33, -m·xg], [m·zg, -m·xg, Iyy + a55]]);
DD := Matrix([[0.2, 0, 0], [0, 0.78, 0], [0, 0, 0.3]]);
J := Matrix([[1, 0, 0], [0, 1, 0], [0, 0, 1]]);
G := Matrix([[0, 0, 0], [0, 0, 0], [0, 0, zg·m·g]]);
ZERO := Matrix([[0, 0, 0], [0, 0, 0], [0, 0, 0]]);
ZERO2 := Matrix([[0, 0], [0, 0], [0, 0]]);
A := Matrix([[evalm(-M^(-1)&*DD), evalm(-M^(-1)&*G)], [J, ZERO]]);
B := Matrix([[1, 0], [0, 1], [l4, l3]]);
C := Matrix([[evalm(M^(-1)&*B)], [ZERO2]]);
v1 := t→1;
v2 := t→1;
v3 := t→1;
v4 := t→1;
v5 := t→1;
v6 := t→1;
x := t→Vector_column([1, 1, 1, 1, 1, 1]);
u := t→1.8;
```

$$m := 1.75$$

$$a11 := 0.58$$

$$zg := 0.13$$

$$a33 := 1.49$$

$$xg := 0.2$$

$$Iyy := 0.19$$

$$a55 := 0.087$$

$$g := 9.81$$

$$l4 := 0.6$$

$$l3 := 0.1$$

$$M := \begin{bmatrix} 2.33 & 0 & 0.2275 \\ 0 & 3.24 & -0.350 \\ 0.2275 & -0.350 & 0.277 \end{bmatrix}$$

$$DD := \begin{bmatrix} 0.2 & 0 & 0 \\ 0 & 0.78 & 0 \\ 0 & 0 & 0.3 \end{bmatrix}$$

$$J := \begin{bmatrix} 1 & 0 & 0 \\ 0 & 1 & 0 \\ 0 & 0 & 1 \end{bmatrix}$$

$$G := \begin{bmatrix} 0 & 0 & 0 \\ 0 & 0 & 0 \\ 0 & 0 & 2.231775 \end{bmatrix}$$

$$ZERO := \begin{bmatrix} 0 & 0 & 0 \\ 0 & 0 & 0 \\ 0 & 0 & 0 \end{bmatrix}$$

$$ZERO2 := \begin{bmatrix} 0 & 0 \\ 0 & 0 \\ 0 & 0 \end{bmatrix}$$

$$A := [\,[\,-0.0946243929726694,\ 0.0379163622709622,\ 0.134998916217492,\ -0.,\ -0.,\ 1.00429068747098\,],$$
$$[\,0.00972214417204160,\ -0.282689992446031,\ -0.149357775302353,\ -0.,\ -0.,\ -1.11110982991803\,],$$
$$[\,0.0899992774783279,\ -0.388330215786119,\ -1.38262626279893,\ -0.,\ -0.,\ -10.2857024255269\,],$$
$$[\,1,\ 0,\ 0,\ 0,\ 0,\ 0\,],$$
$$[\,0,\ 1,\ 0,\ 0,\ 0,\ 0\,],$$
$$[\,0,\ 0,\ 1,\ 0,\ 0,\ 0\,]\,]$$

$$B := \begin{bmatrix} 1 & 0 \\ 0 & 1 \\ 0.6 & 0.1 \end{bmatrix}$$

$$C := \begin{bmatrix} 0.203124132428363 & -0.0936103595993719 \\ 0.250104829744499 & 0.412208992339286 \\ 2.31525613820622 & 0.958734671940820 \\ 0 & 0 \\ 0 & 0 \\ 0 & 0 \end{bmatrix}$$

2. Matrixes for the movement in the xy plane

```
restart;

m := 1.75;
a11 := 0.58;
zg := 0.13;
a33 := 1.49;
a22 := a33;
a44 := 0;
xg := 0.2;
yg := 0;
Iyy := 0.19;
a55 := 0.087;
a66 := a55;
g := 9.81;
l4 := 0.6;
l3 := 0.1;
Ixx := 0.072;
Izz := Iyy;
M := Matrix([[m + a22, -m·zg, m·xg], [-m·zg, Ixx + a44, 0], [m·xg,
    0, Izz + a66]]);
DD := Matrix([[0.78, 0, 0], [0, 0.3, 0], [0, 0, 0.3]]);
J := Matrix([[0, 1, 0], [0, 1, 0], [0, 0, 1]]);
G := Matrix([[0, 0, 0], [0, zg·m·g, 0], [0, -xg·m·g, 0]]);
ZERO := Matrix([[0, 0, 0], [0, 0, 0], [0, 0, 0]]);
ZERO2 := Matrix([[0, 0], [0, 0], [0, 0]]);
A := Matrix([[evalm(-M^-1&*DD), evalm(-M^-1&*G)], [J,
    ZERO]]);
B := Matrix([[1], [0.07], [-1.23]]);
C := Matrix([[evalm(M^-1&*B)], [0], [0], [0]]);
v1 := t→1;
v2 := t→1;
v3 := t→1;
v4 := t→1;
v5 := t→1;
v6 := t→1;
x := t→Vector_column([1, 1, 1, 1, 1, 1]);
u := t→1.8;


>
```

$$m := 1.75$$

$$a11 := 0.58$$

$$zg := 0.13$$

$$a33 := 1.49$$

$$a22 := 1.49$$

$$a44 := 0$$

$$xg := 0.2$$

$$yg := 0$$

$$Iyy := 0.19$$

$$a55 := 0.087$$

$$a66 := 0.087$$

$$g := 9.81$$

$$l4 := 0.6$$

$$l3 := 0.1$$

$$Ixx := 0.072$$

$$Izz := 0.19$$

$$M := \begin{bmatrix} 3.24 & -0.2275 & 0.350 \\ -0.2275 & 0.072 & 0 \\ 0.350 & 0 & 0.277 \end{bmatrix}$$

$$DD := \begin{bmatrix} 0.78 & 0 & 0 \\ 0 & 0.3 & 0 \\ 0 & 0 & 0.3 \end{bmatrix}$$

$$J := \begin{bmatrix} 0 & 1 & 0 \\ 0 & 1 & 0 \\ 0 & 0 & 1 \end{bmatrix}$$

$$G := \begin{bmatrix} 0 & 0 & 0 \\ 0 & 2.231775 & 0 \\ 0 & -3.43350 & 0 \end{bmatrix}$$

$$ZERO := \begin{bmatrix} 0 & 0 & 0 \\ 0 & 0 & 0 \\ 0 & 0 & 0 \end{bmatrix}$$

$$ZERO2 := \begin{bmatrix} 0 & 0 \\ 0 & 0 \\ 0 & 0 \end{bmatrix}$$

$$A := [[-0.375193923435399, -0.455964837508298, 0.182335286312677, -0., -5.47886376928219, -0.],$$
$$[-1.18550857752157, -5.60738889629358, 0.576128856057416, -0., -48.3085626043291, -0.],$$
$$[0.474071744412959, 0.576128856057416, -1.31342003685717, 0., 19.3180589142555, 0.],$$
$$[0, 1, 0, 0, 0, 0],$$
$$[0, 1, 0, 0, 0, 0],$$
$$[0, 0, 1, 0, 0, 0]]$$

$$B := \begin{bmatrix} 1 \\ 0.07 \\ -1.23 \end{bmatrix}$$

$$C := \begin{bmatrix} 1.33498431985878 \\ 5.19040184399823 \\ -6.12723650523673 \\ 0 \\ 0 \\ 0 \end{bmatrix}$$

$$v1 := t \rightarrow 1$$

$$v2 := t \rightarrow 1$$

$$v3 := t \rightarrow 1$$

$$v4 := t \rightarrow 1$$

$$v5 := t \rightarrow 1$$

$$v6 := t \rightarrow 1$$

$$x := t \rightarrow Vector_{column}([1, 1, 1, 1, 1, 1])$$

$$u := t \rightarrow 1.8$$

APPENDIX B

Maple codes for ripple currents in SMPS unit modelling.

```
> restart;
>
```

$$T := 8e-6;$$
$$D1 := 0.43;$$
$$D2 := 0.52;$$
$$D3 := 0.73;$$
$$I1jmen := 0.78;$$
$$I2jmen := 1.18;$$
$$I3jmen := 1.41;$$
$$\text{alpha} := 0;$$
$$\text{beta} := 0;$$

$$I1 := t \rightarrow piecewise\left((\text{t-alpha}) < T, \left(\text{Heaviside}(D1 \cdot T - (\text{t-alpha})) \cdot \left(0.6 \cdot I1jmen + \left(\frac{0.8 \cdot I1jmen}{D1 \cdot T} \cdot (\text{t-alpha}) \right) \right) + \text{Heaviside}((\text{t-alpha}) - \text{D1} \cdot \text{T}) \cdot \left(1.4 \cdot \text{I1jmen} - \left(\frac{0.8 \cdot I1jmen}{(1 - D1) \cdot T} \cdot ((\text{t-alpha}) - D1 \cdot T) \right) \right) \right), 0 \right);$$

$$I2 := t \rightarrow piecewise\left((\text{t} - \text{beta}) < T, \left(\text{Heaviside}(D2 \cdot T - (\text{t} - \text{beta})) \cdot \left(0.6 \cdot I2jmen + \left(\frac{0.8 \cdot I2jmen}{D2 \cdot T} \cdot (\text{t} - \text{beta}) \right) \right) + \text{Heaviside}((\text{t} - \text{beta}) - \text{D2} \cdot \text{T}) \cdot \left(1.4 \cdot \text{I2jmen} - \left(\frac{0.8 \cdot I2jmen}{(1 - D2) \cdot T} \cdot ((\text{t} - \text{beta}) - D2 \cdot T) \right) \right) \right), 0 \right);$$

$$I3 := t \rightarrow piecewise\left((\text{t}) < T, \left(\text{Heaviside}(D3 \cdot T - (\text{t})) \cdot \left(0.6 \cdot I3jmen + \left(\frac{0.8 \cdot I3jmen}{D3 \cdot T} \cdot (\text{t}) \right) \right) + \text{Heaviside}((\text{t}) - \text{D3} \cdot \text{T}) \cdot \left(1.4 \cdot \text{I3jmen} - \left(\frac{0.8 \cdot I3jmen}{(1 - D3) \cdot T} \cdot ((\text{t}) - D3 \cdot T) \right) \right) \right), 0 \right);$$

$$T := 0.000008$$
$$D1 := 0.43$$
$$D2 := 0.52$$
$$D3 := 0.73$$
$$I1jmen := 0.78$$
$$I2jmen := 1.18$$
$$I3jmen := 1.41$$
$$\alpha := 0$$
$$\beta := 0$$

$$I1 := t \to piecewise\left(t - \alpha < T, \text{Heaviside}\left(D1\,T - t + \alpha\right) \left(0.6\,I1jmen + \frac{0.8\,I1jmen\left(t - \alpha\right)}{D1\,T} \right) + \text{Heaviside}\left(t - \alpha - D1\,T\right) \left(1.4\,I1jmen + \frac{(-1)\cdot 0.8\,I1jmen\left(t - \alpha - D1\,T\right)}{(1 - D1)\,T} \right), 0 \right)$$

$$I2 := t \to piecewise\left(t - \beta < T, \text{Heaviside}\left(D2\,T - t + \beta\right) \left(0.6\,I2jmen + \frac{0.8\,I2jmen\left(t - \beta\right)}{D2\,T} \right) + \text{Heaviside}\left(t - \beta - D2\,T\right) \left(1.4\,I2jmen + \frac{(-1)\cdot 0.8\,I2jmen\left(t - \beta - D2\,T\right)}{(1 - D2)\,T} \right), 0 \right)$$

$$I3 := t \to piecewise\left(t < T, \text{Heaviside}(D3\,T - t) \left(0.6\,I3jmen + \frac{0.8\,I3jmen\,t}{D3\,T} \right) + \text{Heaviside}(t - D3\,T) \left(1.4\,I3jmen + \frac{(-1)\cdot 0.8\,I3jmen\left(t - D3\,T\right)}{(1 - D3)\,T} \right), 0 \right)$$

```
>
>
```

$$I1per := t \to I1\left(\text{alpha} + (\text{T} - 0)\cdot\text{frac}\left(\frac{(\text{t} - \text{alpha})}{\text{T} + \text{alpha}} \right) \right);$$
$$I2per := t \to I2\left(\text{beta} + (\text{T} - 0)\cdot\text{frac}\left(\frac{(\text{t} - \text{beta})}{\text{T} + \text{beta}} \right) \right);$$
$$I3per := t \to I3\left(0 + (\text{T} - 0)\cdot\text{frac}\left(\frac{(\text{t} - 0)}{\text{T} - 0} \right) \right);$$

$$I1per := t \to I1\left(\alpha + T\,\text{frac}\left(\frac{t - \alpha}{T + \alpha} \right) \right)$$
$$I2per := t \to I2\left(\beta + T\,\text{frac}\left(\frac{t - \beta}{T + \beta} \right) \right)$$
$$I3per := t \to I3\left(T\,\text{frac}\left(\frac{t}{T} \right) \right)$$

```
> plot([I1per(t), I2per(t), I3per(t)], t = 1e-5 ..6e-5);
```

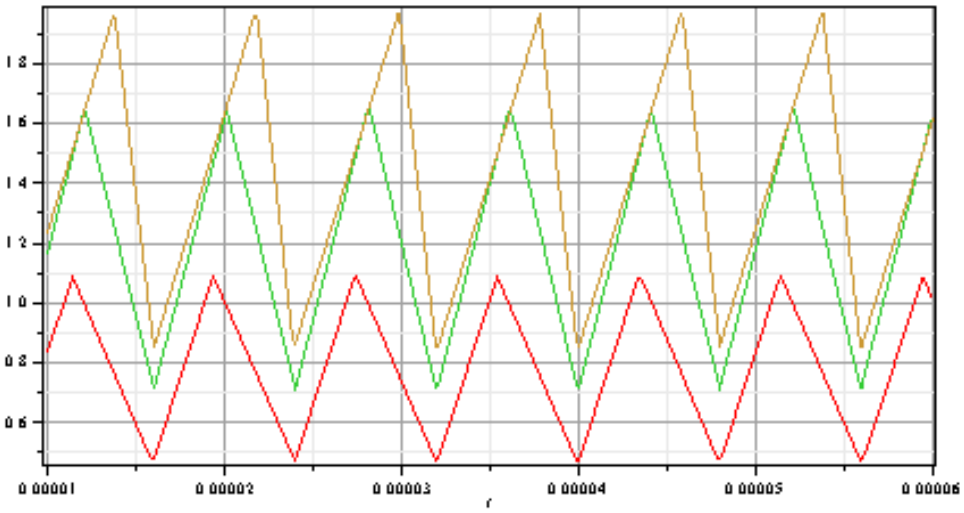

> $plot(I1per(t) + I2per(t) + I3per(t), t = 1e-5..6e-5);$

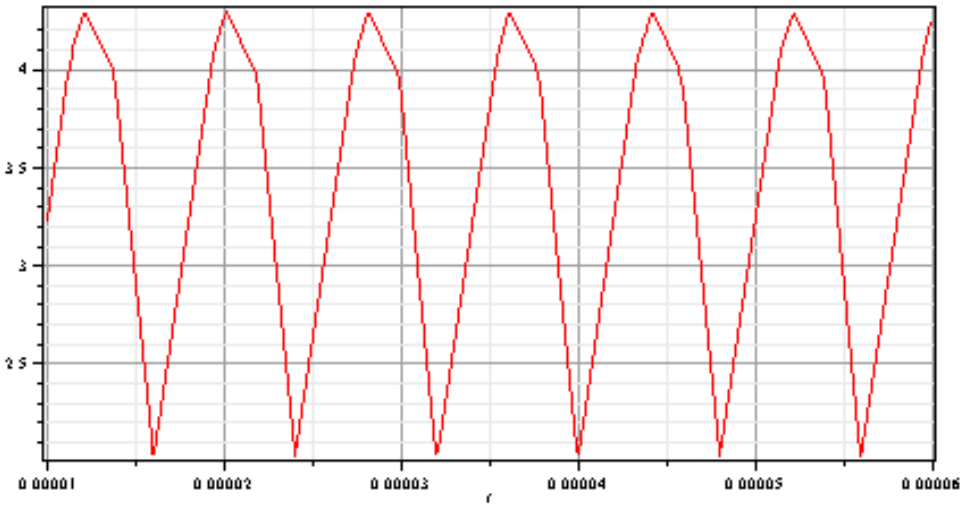

```
> restart;
>
```

$$T := 8e-6;$$
$$D1 := 0.43;$$
$$D2 := 0.52;$$
$$D3 := 0.73;$$
$$I1jmen := 0.78;$$
$$I2jmen := 1.18;$$
$$I3jmen := 1.41;$$
$$\text{alpha} := 0;$$
$$\text{beta} := 0;$$
$$A := 2.4e-6;$$
$$B := 4e-6;$$

$$I1 := t \rightarrow piecewise\left((t-\text{alpha}) < T, \left(\text{Heaviside}(D1 \cdot (T) - (t - \text{alpha})) \cdot \left(0.6 \cdot I1jmen + \left(\frac{0.8 \cdot I1jmen}{D1 \cdot (T)} \cdot (t - \text{alpha}) \right) \right) + \text{Heaviside}((t - \text{alpha}) - \text{D1} \cdot (\text{T})) \cdot \left(1.4 \cdot \text{I1jmen} - \left(\frac{0.8 \cdot I1jmen}{(1 - D1) \cdot T} \cdot ((t-\text{alpha}) - D1 \cdot (T)) \right) \right) \right), 0 \right);$$

$$I2 := t \rightarrow piecewise\left((t + \text{beta}) < T, \left(\text{Heaviside}(D2 \cdot T - (t + \text{beta})) \cdot \left(0.6 \cdot I2jmen + \left(\frac{0.8 \cdot I2jmen}{D2 \cdot T} \cdot (t + \text{beta}) \right) \right) + \text{Heaviside}((t + \text{beta}) - \text{D2} \cdot \text{T}) \cdot \left(1.4 \cdot \text{I2jmen} - \left(\frac{0.8 \cdot I2jmen}{(1 - D2) \cdot T} \cdot ((t + \text{beta}) - D2 \cdot T) \right) \right) \right), 0 \right);$$

$$I3 := t \rightarrow piecewise\left((t) < T, \left(\text{Heaviside}(D3 \cdot T - (t)) \cdot \left(0.6 \cdot I3jmen + \left(\frac{0.8 \cdot I3jmen}{D3 \cdot T} \cdot (t) \right) \right) + \text{Heaviside}((t) - \text{D3} \cdot \text{T}) \cdot \left(1.4 \cdot \text{I3jmen} - \left(\frac{0.8 \cdot I3jmen}{(1 - D3) \cdot T} \cdot ((t) - D3 \cdot T) \right) \right) \right), 0 \right);$$

$$T := 0.000008$$
$$D1 := 0.43$$
$$D2 := 0.52$$
$$D3 := 0.73$$
$$I1jmen := 0.78$$
$$I2jmen := 1.18$$
$$I3jmen := 1.41$$
$$\alpha := 0$$
$$\beta := 0$$
$$A := 0.0000024$$
$$B := 0.000004$$

$$I1 := t \to piecewise\left(t - \alpha < T, \text{Heaviside}(D1\,T - t + \alpha) \left(0.6\,I1jmen + \frac{0.8\,I1jmen\,(t - \alpha)}{D1\,T} \right) + \text{Heaviside}(t - \alpha - D1\,T) \left(1.4\,I1jmen + \frac{(-1)\cdot 0.8\,I1jmen\,(t - \alpha - D1\,T)}{(1 - D1)\,T} \right), 0 \right)$$

$$I2 := t \to piecewise\left(t + \beta < T, \text{Heaviside}(D2\,T - t - \beta) \left(0.6\,I2jmen + \frac{0.8\,I2jmen\,(t + \beta)}{D2\,T} \right) + \text{Heaviside}(t + \beta - D2\,T) \left(1.4\,I2jmen + \frac{(-1)\cdot 0.8\,I2jmen\,(t + \beta - D2\,T)}{(1 - D2)\,T} \right), 0 \right)$$

$$I3 := t \to piecewise\left(t < T, \text{Heaviside}(D3\,T - t) \left(0.6\,I3jmen + \frac{0.8\,I3jmen\,t}{D3\,T} \right) + \text{Heaviside}(t - D3\,T) \left(1.4\,I3jmen + \frac{(-1)\cdot 0.8\,I3jmen\,(t - D3\,T)}{(1 - D3)\,T} \right), 0 \right)$$

>

>

$$I1per := t \to I1\left(\text{alpha} + (\text{T} - 0)\cdot \text{frac}\left(\frac{(\text{t} - \text{alpha})}{\text{T} + \text{alpha}} \right) \right);$$

$$I2per := t \to I2\left(\text{beta} + (\text{T} + 0)\cdot \text{frac}\left(\frac{(\text{t} + \text{beta})}{\text{T} - \text{beta}} \right) \right);$$

$$I3per := t \to I3\left(0 + (\text{T} - 0)\cdot \text{frac}\left(\frac{(\text{t} - 0)}{\text{T} - 0} \right) \right);$$

$$I1per := t \to I1\left(\alpha + T\,\text{frac}\left(\frac{t - \alpha}{T + \alpha} \right) \right)$$

$$I2per := t \to I2\left(\beta + T\,\text{frac}\left(\frac{t + \beta}{T - \beta} \right) \right)$$

$$I3per := t \to I3\left(T\,\text{frac}\left(\frac{t}{T} \right) \right)$$

> $plot([I1per(t + B), I2per(t + A), I3per(t)], t = 1\text{e-}5 \,..6\text{e}-5);$

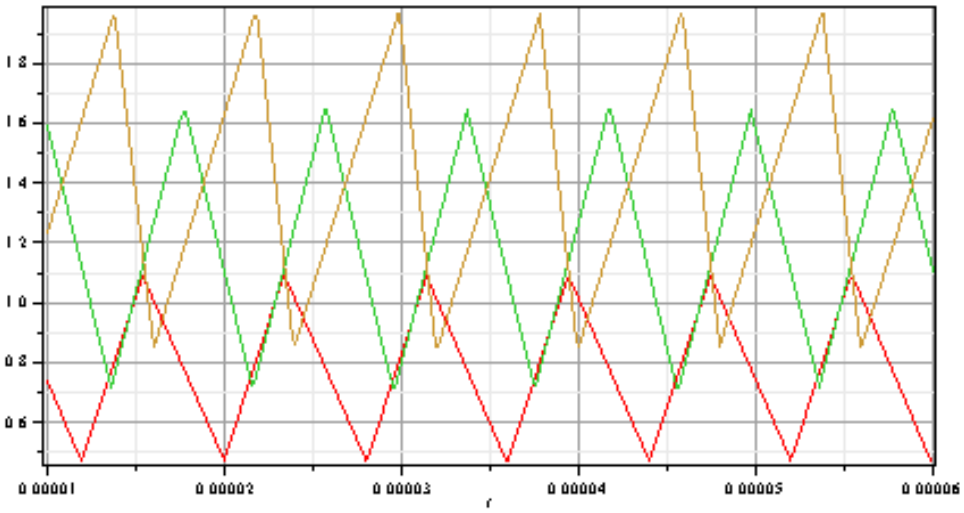

> $plot(I1per(t+B)+I2per(t+A)+I3per(t), t=1e-5..6e-5);$

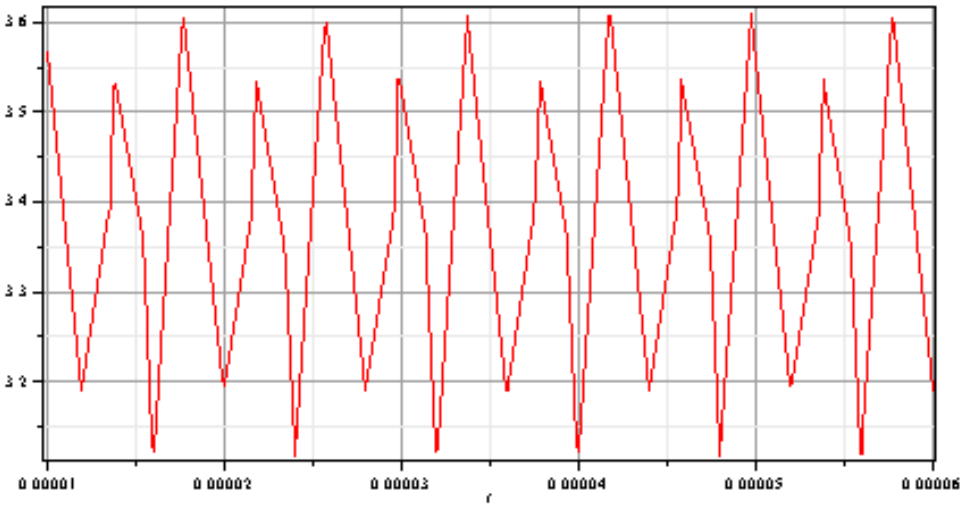

APPENDIX C

Motherboard circuit diagram

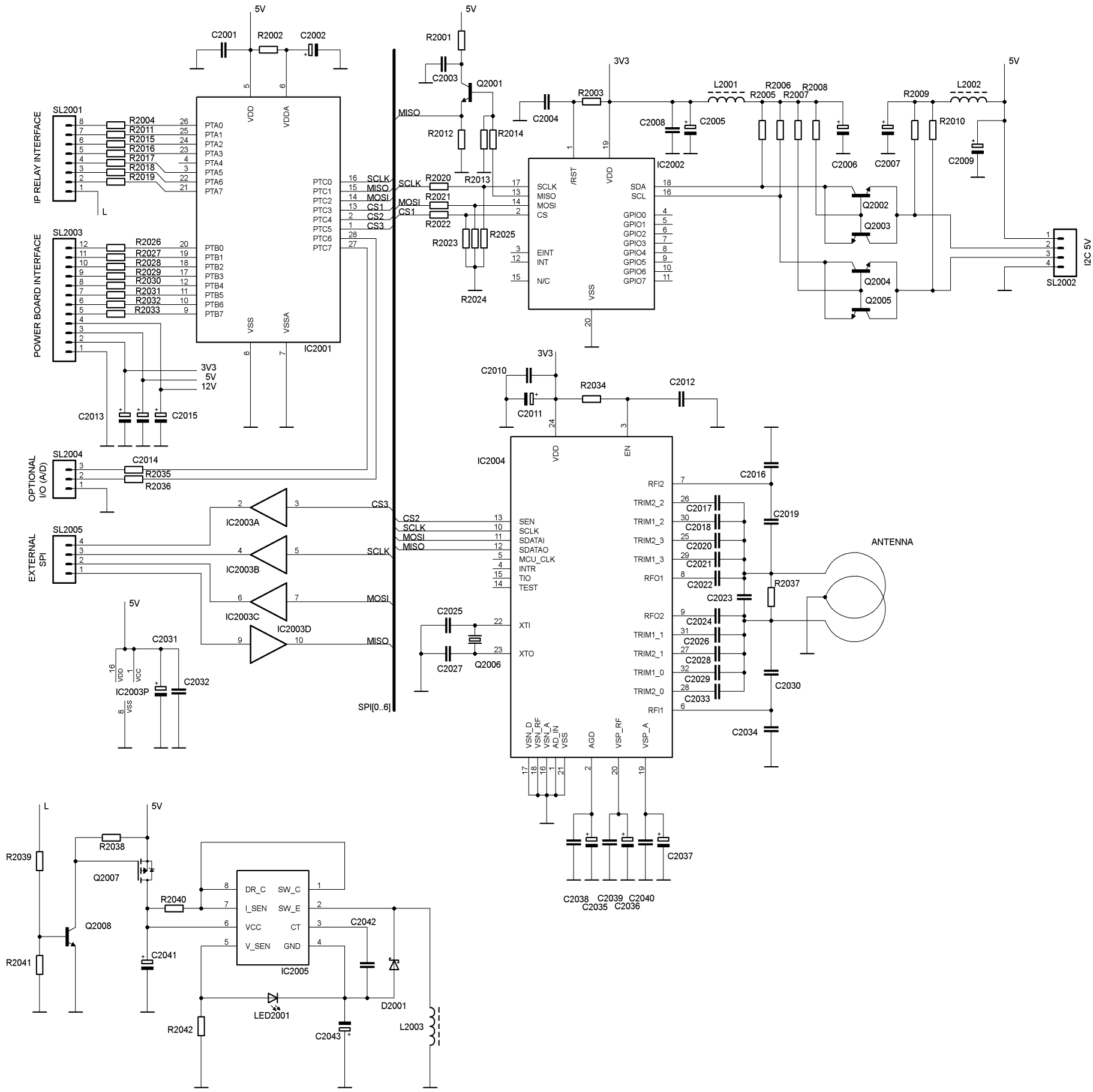

APPENDIX D

Power supply source circuit diagram